Development and Characterisation of a Zero-Moment Half-Metal

A dissertation submitted to the University of Dublin
for the degree of Doctor of Philosophy

Katarzyna Estera Siewierska
Trinity College Dublin, February 2021

SCHOOL OF PHYSICS
UNIVERSITY OF DUBLIN
TRINITY COLLEGE

Declaration

I declare that this thesis has not been submitted as an exercise for a degree at this or any other university and it is entirely my own work.

I agree to deposit this thesis in the University's open access institutional repository or allow the library to do so on my behalf, subject to Irish Copyright Legislation and Trinity College Library conditions of use and acknowledgement.

Name: Katarzyna Estera Siewierska

Signature: ..... **Date:** 31/12/2020

Summary

A dream material for spintronics would have low/zero net moment, no stray fields, high resonance frequency, low damping and be 100 % spin polarised. Such materials combine the best features of a ferromagnet and an antiferromagnet and are called zero moment half-metals (ZMHM).The first ZMHM is a Heusler alloy consisting of Manganese, Ruthenium and Gallium (MRG). The demonstration opened a new field of spintronics with no net moment, which has the potential to revolutionise magnetic data storage and data transfer.

One of the main challenges of incorporating MRG into a spintronic device is ensuring stability of MRG during annealing at temperatures up to $T = 350\,^{\circ}\mathrm{C}$. A detailed study of the effect of annealing of blanket MRG films epitaxially grown on MgO substrates, capped with a 3 nm amorphous layer of AlO_x, revealed little changes in material properties up to $T = 350\,^{\circ}\mathrm{C}$. Mn diffusion is the main concern for MRG-based device structures and this was addressed by selecting several potential diffusion barrier materials. Then their performance was tested by investigating the effects of annealing were studied in MRG based spin-valve structures with varying spacers. The most promising spacer was found to be Mo with a thickness of 2 nm which did not affect the crystal structure of MRG or the interfaces between the layers and maintained perpendicular magnetic anisotropy of the MRG. Mo also has a large spin diffusion length and can potentially be used as a dusting layer in magnetic tunnel junction devices.

Varying Mn content in MRG was found to vary Mn on 4*c* and 4*d* sites, thus increasing Mn content raises T_{comp}. Addition of Ru decreases both the Anomalous Hall angle and spin polarisation meaning the Fermi level is pushed upwards in the density of states. Comparison of AHE and SQUID

loops shows there is a 'soft component' in net moment, absent in AHE loops where R_{xy} is proportional to the Mn^{4c} sublattice magnetisation. This means the net moment is canted at zero fields. The canting of the net moment in zero-field could arise from sublattice non-collinearity due to competing exchange on the Mn^{4c} sublattice, as suggested by Heisenberg exchange energies found using mean field theory. This was investigated further by XMCD measurements of sublattice moments.

The imaging of domains directly by polar magneto-optic Kerr effect in a ZMHM was demonstrated for the first time. A detailed study demonstrates two thermally activated mechanisms of magnetisation reversal. In films with weak pinning, magnetisation reversal is dominated by domain wall motion. Magnetisation reversal by nucleation was found in films with strong pinning. In between the energy ranges, the reversal is not dominated by either process, but is rather a mixture of the two. Analysis of virgin domain patterns after thermal demagnetisation allow to visualise the prominent pinning sites. Their spacings are ≈ 240 nm, which provides an upper bound for the track-width of spin-torque domain-wall motion-based devices.

The sublattice specific moments were obtained as a function of applied field and temperature from x-ray magnetic circular magnetism measurements. Crossing of compensation and a spin-flop transition near compensation were observed. Using a simple uniaxial anisotropy model, anisotropy constants of sublattices were found to be of the order $10^6 \mathrm{Jm}^{-3}$. The Mn^{4a} and Mn^{4c} sublattice showed easy-axis and easy-plane anisotropies, respectively. Non-collinearity of sublattices was observed, with the canting angle of sublattices $(\theta^{4a,4c} - 180°) < \pm 10°$. The non-collinearity, unusually large anisotropy constant values as well as the apparent easy-plane anisotropy found for Mn^{4c} sublattice are most likely to originate from competing exchange on that sublattice. Data from neutron diffraction measurements of sublattice moments in three dimensions and a more complicated model will be a test of this hypothesis.

For my family, my friends and the readers of this work.

Acknowledgements

Firstly I would like to acknowledge two outstanding people I had the priviledge of working with in my PhD, my supervisor Prof. Michael Coey and co-supervisor Dr. Karsten Rode. Words cannot describe how both helped me in developing my scientific knowledge and skills. Without their exceptional expertise and experience this PhD would not have been possible.

I would like to thank the past and present members of the Magnetism and Spintronics group in Trinity College Dublin for all of their help and support throughout my PhD. They have transferred many valuable skills and knowledge to me, were always ready to offer help and advice when I needed it and working with them has been priviledge. During my PhD many of them have become my very close friends and with their support I have endured the challenges of the PhD.

I am grateful to the academic staff I met and worked with, during my studies and the PhD, at the school of physics and mathematics at Trinity College Dublin. In particular, I would like to thank Prof. Louise Bradley, Prof. Igor Shvets, Prof. James Lunney, Prof. Stefan Hutzler, Prof. Samson Shatashvili and Prof. Vesselin Tonchev (Faculty of Physics, Sofia University, Bulgaria), whom I had worked with on research projects that influenced my decision to pursue a PhD in the first place, and have provided me with an opportunity to work on research topics outside the scope of my PhD. Special thanks also to Prof. Eric Finch and Prof. Petros Florides, who have provided me with tonnes of motivation and for many interesting conversations, especially about physics and history.

Outside the School of Physics and Trinity College I had the opportunity to work with researchers to perform measurements for this PhD work. Their contribution is greatly appreciated and without them the research would

not be complete. XMCD measurements and analysis were performed with Dr. Davide Betto, our local contact and a past group member, at the ID32 in the European synchrotron radiation source where he worked with Dr. Nicholas Brookes. Dr. Kane Esien from Queen's University Belfast performed SQUID measurements while our system was not available for use. Prof. Michael Stock and Dr. Clara De Castro Amaral Siqueira from the School of Geology at TCD, performed ED-XRF measurements that were critical to determine compositions of our films and have succeed where many other techniques have failed. Prof. Rudolf Schaefer from Leibniz Institute for Solid State and Materials Research, provided intial MOKE measurements before our group commissioned a MOKE microscope. I have also been involved in teaching duties at the school of mathematics and would also like to thank the staff and academics for all care and support they provided me with.

The school of physics and CRANN would not function without he support of the non-academic staff who have been a great support with both technical and administration related issues. Working with them was a pleasure, both as an undergraduate and postgraduate student, because of their concern and dedication to help students by ensuring their safety in the labs, maintaining the research facilities, taking care that their paperwork is in order and informing about college matters.

Last but not least, I would like to thank all my friends and family members who have been with me during the progress of my PhD. They have accompanied me in sharing both good and difficult moments. Their presence in my life has has been invaluable and helped me build strength and confidence in myself.

List of Publications

1. Banerjee C., Teichert N., **Siewierska, K. E.**, Gercsi Z., Atcheson G. Y. P., Stamenov P., Rode K., Coey J. M. D. & Besbas J.
   "Single pulse all-optical toggle switching of magnetization without gadolinium in the ferrimagnet Mn_2Ru_xGa",
   Nature Communications **11** (1), 4444 (2020)

2. Bonfiglio G., Rode K., **Siewierska, K. E.**, Besbas J., Atcheson G. Y. P., Stamenov P., Coey J. M. D., Kimel A. V., Rasing T. & Kirilyuk A.
   "Magnetization dynamics of the compensated ferrimagnet Mn_2Ru_xGa",
   Physical Review B **100** (10), 104438 (2019)

3. Khan T. M., Lunney J. G., O'Rourke D., Meyer M.-C., Creel J. R., **Siewierska K. E.**
   "Various pulsed laser deposition methods for preparation of silver-sensitised glass and paper substrates for surface-enhanced Raman spectroscopy"
   Applied Physics A **125** (9), 659 (2019)

4. **Siewierska K. E.**, Teichert N., Schäfer R., Coey J. M. D.
   "Imaging Domains in a Zero-Moment Half Metal",
   IEEE Transactions on Magnetics **55** (2), p. 1-4 (2018)

5. Toktarbaiuly O., Usov V., Ó Coileáin C., **Siewierska K. E.**, Krasnikov S., Norton E., Bozhko S. I., Semenov V. N., Chaika A. N., Murphy B. E., Lübben O., Krzyżewski F., Załuska-Kotur M. A., Krasteva A., Popova H., Tonchev V., Shvets I. V.
   "Step bunching with both directions of the current: Vicinal W (110) surfaces

versus atomistic scale model"
Physical Review B **97** (3), 035436 (2018)

6. Gough J. J., **Siewierska K. E.**, Mehigan S., Hanlon D., Backes C., Gholamvand Z., Szydłowska B. M., Blau W. J., McCabe E., Bradley A. L.
"Influence of graphene oxide/Ag nanoparticle composites on the fluorescence properties of organic dyes"
Journal of Nanoscience and Nanotechnology **17** (12), p. 8901 - 8911 (2017)

7. Khan T. M., Mujawar M. A., **Siewierska K. E.**, Pokle A., Donnelly T., McEvoy N., Duesberg G. S., Lunney J. G.
"Atmospheric pulsed laser deposition and thermal annealing of plasmonic silver nanoparticle films"
Nanotechnology **28** (44), 445601 (2017)

8. **Siewierska K. E.**, Atcheson G., Borisov K., Venkatesan M., Rode K., Coey J. M. D.
"Study of the Effect of Annealing on the Properties of Mn_2Ru_xGa Thin Films",
IEEE Transactions on Magnetics **53** (11), p. 1-5 (2017)

9. **Siewierska K. E.**, Tonchev V.
"Scaling of the minimal step-step distance with the step-bunch size: Theoretical predictions and experimental findings"
Journal of the Japanese Association for Crystal Growth **4** (6), p. 204 - 212 (2016)

Contents

List of Figures

List of Tables

1 Introduction

1.1 Fundamentals of Magnetism

Magnetism is a family of natural phenomena which involve interactions mediated via magnetic fields. The word magnet originates from the word magnes which is the Latin for 'lodestone'. Lodestone was the first material that was used as a permanent magnet. Magnetism is a purely quantum mechanical effect due to the Bohr-van Leeuwen theorem, which states that *'in a constant magnetic field and in thermal equilibrium, the magnetisation of an electron gas in the classical Drude-Lorentz (DL) model is identically zero'*.[1] Hence, to understand the origin of magnetism in materials, the quantum mechanical descriptions of the electron and its angular momentum are required. Most interactions in magnetism are mediated by magnetic fields, therefore the properties, dynamics and origins of those fields must be well modelled and understood [2].

1.1.1 Magnetic Fields

A magnetic field is a force field around a magnet where electric charges and magnetic dipoles experience a force known as the Lorentz force. The magnitude and direction

of the Lorentz force is described by

$$\mathbf{F} = q(\mathbf{E} + \mathbf{v} \times \mathbf{B}) \tag{1.1}$$

where $\mathbf{F}$ is the Lorentz force, q is the charge of the particle, $\mathbf{E}$ is the electric field, $\mathbf{v}$ is the velocity of the particle and $\mathbf{B}$ is the magnetic field. To define the B-field, the expression for the Lorentz force in equation 1.1 can be used. In electrostatics, the force experienced by a charged particle is simply $\mathbf{F} = q\mathbf{E}$. If the charged particle moves near a current carrying wire it will experience a force that depends on its velocity. Hence the $\mathbf{B}$-field can be defined as the magnetic field required so that the force experienced by the particle satisfies equation 1.1.

Magnetic fields are generated from the motion of electric charges and their fundamental quantum property called spin. The behaviour of $\mathbf{B}$ magnetic field is described by Maxwell's equations in matter. The two important equations are Gauss's law for the $\mathbf{B}$-field and Ampere's law given by

$$\nabla \cdot \mathbf{B} = 0 \tag{1.2}$$

$$\nabla \times \mathbf{B} = \mu_0 \boldsymbol{j}_{\text{total}} \tag{1.3}$$

where $\mu_0 = 4\pi \times 10^{-7}$ TmA^{-1} is magnetic permeability of free space and the total current density $\mathbf{j}_{\text{total}}$ is the sum of the conduction current density in electrical circuits $\mathbf{j}_c$ and the magnetisation current density $\mathbf{j}_m$ associated with the magnetisation M of the material. The current density $\mathbf{j}_m$ cannot be measured, its nature is quantum mechanical and it is a representation of the intrinsic angular momentum of the electron, i.e. its spin. Analogously to equation 1.3, it is related to magnetisation by

$$\nabla \times \mathbf{M} = \mu_0 \boldsymbol{j}_m \tag{1.4}$$

For Ampere's law to remain in a practical form, we now define a new field called $\mathbf{H}$

$$\mathbf{H} = \frac{B}{\mu_0} - \mathbf{M} \tag{1.5}$$

where $\mathbf{H}$ has units of Am^{-1}, so that we get

$$\nabla \times \mathbf{H} = \boldsymbol{j}_c \tag{1.6}$$

In vacuum the two fields are proportional to each other, with the constant of propor-

tionality being μ_0. In matter those two fields are very different as can be seen in Figure 1.1. From equation 1.2, the divergence of the **B**-field is zero, i.e. it is a solenoidal

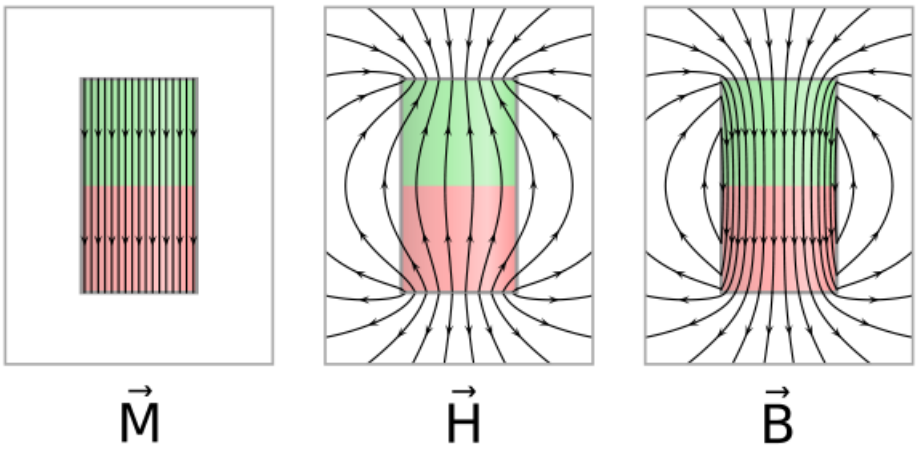

Figure 1.1: Magnetic field lines of the **B**-field, **H**-field and the direction of magnetisation of a bar magnet.

vector field. This means that the field lines have no start or end but form closed loops or extend into infinity, as shown in Figure 1.1. The H-field inside the magnet points in the opposite direction to the field outside and field lines point away from the north pole and towards the south pole. Therefore, the H-field is similar to the electric field, because the field lines appear to begin at a fictitious positive magnetic charge and end at negative magnetic charge. However, this is only a mathematical representation since magnetic monopoles do not exist. The H-field inside the magnet is called the demagnetising field and outside the stray field [2]. Magnetic fields are generated by moving electronic charges and by intrinsic magnetic moment, known as 'spin', which is a consequence of quantum mechanics. In the next section the orbital and spin moments of the electron and their coupling will be discussed.

1.1.2 Orbital and Spin moment of the electron

In the Bohr model of the atom, the electron orbiting the nucleus with velocity **v** and period T in a circular orbit can be thought of as a circular current loop with radius **r**, where the effective current I_e is given by

$$I_e = \frac{-e}{T} = \frac{-ev}{2\pi r} = \frac{-em_e vr}{2\pi m_e r^2}$$

Using this effective current, the magnetic moment can be deduced from the classical expression for a current loop

$$\boldsymbol{\mu}_l = I_e \mathbf{A} = \frac{-em_e vr}{2m_e}\hat{\boldsymbol{n}} = \frac{-e}{2m_e}\mathbf{l}$$

where $\mathbf{A} = \pi r^2 \hat{\boldsymbol{n}}$ is the area of the loop with the unit vector perpendicular to it and $\mathbf{l} = m_e \mathbf{r} \times \mathbf{v}$ is the angular momentum of the electron. The angular momentum of an electron is quantised in units of $\hbar$, that is Planck's constant divided by 2π, then the natural unit for electronic magnetism is the Bohr magneton μ_B, which in SI units is given by

$$\mu_B = \frac{e\hbar}{2m_e} = 9.27 \times 10^{-24}\ \mathrm{J\,T^{-1}}$$

Hence in the Bohr model an electron of mass m_e orbiting the nucleus in the ground state with an orbital momentum of $\hbar$ produces a magnetic dipole moment of approximately one μ_B. Now the quantisation of angular momentum according to quantum mechanics can be applied and the orbital magnetic moment can be expressed in terms of μ_B

$$\boldsymbol{\mu}_l = -\frac{e}{2m_e}\mathbf{l} = -g_l \mu_B \frac{\mathbf{l}}{\hbar} \tag{1.7}$$

where g_l is the orbital g-factor. Combining equation 1.7 and the expression for μ_B we find that $g_l = 1$. The angular momentum $\mathbf{l}$ is quantised in integer multiples of $\hbar$ and the associated quantum number is m_l with $m_l = 0, \pm 1, \pm 2, ..., m_l \leq \frac{|\mathbf{l}|}{\hbar}$. It can be shown that the electron has an intrinsic angular momentum, called spin, with values $\pm\frac{1}{2}\hbar$. A vector diagram of the electron spin is shown in Figure 1.2. Analogously to the expression for $\boldsymbol{\mu}_l$ in equation 1.7, the spin angular moment $\boldsymbol{\mu}_s$ can be expressed in terms of μ_B

$$\boldsymbol{\mu}_s = -g_s \mu_B \frac{\mathbf{s}}{\hbar} \tag{1.8}$$

where g_s is the spin g-factor and $\mathbf{s}$ is spin angular momentum. It is important to note that the spin angular momentum has the opposite orientation to spin moment, so when spin angular momentum is positive i.e. 'spin up', the corresponding spin moment is 'down' or negative. The spin momentum is also quantised in multiples of $\hbar$, but the associated quantum number is half-integer, i.e. $m_s = \pm\frac{1}{2}$. Hence, a quantum of the spin moment of an electron is approximately one μ_B. Protons and neutrons also have

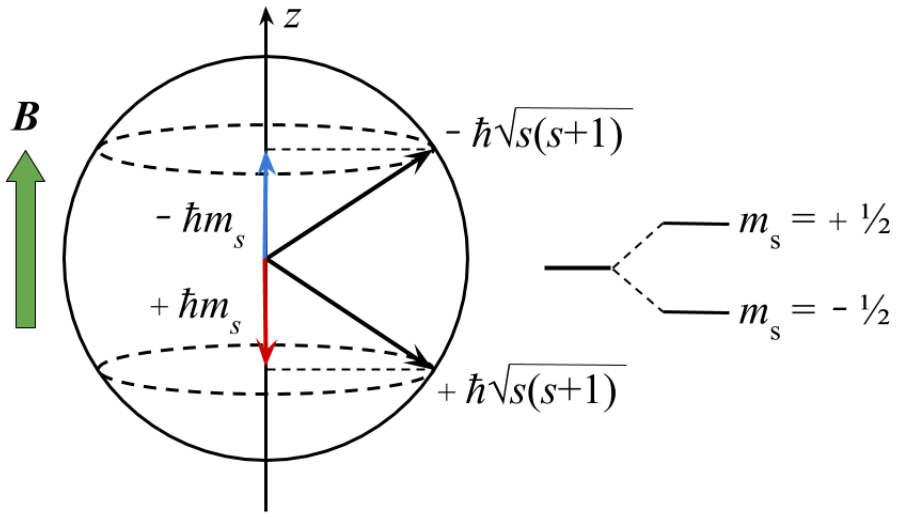

Figure 1.2: Vector diagram of the electron spin. An applied field **B** acts on the spin moment and causes the total spin vector to precess with Larmor frequency. It has two possible projections: spin down (blue arrow) and spin up (red arrow). On the right, the Zeeman splitting of the two magnetic levels into $m_s = \pm\frac{1}{2}$ in the presence of **B**, with $\Delta E = \mu_B B$ is shown.

spin of $\pm\frac{1}{2}\hbar$, but their rest mass is about 2000 times larger than that of an electron, and their contribution to the magnetic moment is negligible.

In general, every electron in an atom has orbital and spin angular momentum. There may be coupling between the two angular momenta via the spin-orbit interaction (SOI). SOI arises from the interaction of the spin of a moving particle with an electrical potential as described by relativistic quantum mechanics. To understand this, one can consider an electron moving in a magnetic field **B** with momentum **p**. This electron will experience the Lorentz force **F** perpendicular to its trajectory and will also posses Zeeman energy. According to classical electrodynamics and special relativity, if the electron moves in an electric field **E** it will experience an effective magnetic field in its rest frame, which will depend on the cross product of the momentum and the electric field. This effective magnetic field will also induce a momentum-dependent Zeeman energy, and this energy is the spin-orbit interaction. For an electron bound in a hydrogenic atom, in a spherically symmetric potential, using semi-classical electrodynamics and non-relativistic quantum mechanics, up to first order perturbation theory,

the spin-orbit interaction can be described by the following Hamiltonian [2]

$$\hat{\mathcal{H}}_{SO} = \frac{1}{2m_e^2c^2r}\frac{\mathrm{d}V(r)}{\mathrm{d}r}\mathbf{l}\cdot\mathbf{s} = \lambda\hat{\boldsymbol{l}}\cdot\hat{\boldsymbol{s}} \tag{1.9}$$

where c is the speed of light, $\hat{\boldsymbol{l}}$ and $\hat{\boldsymbol{s}}$ are respectively the orbital and spin angular momentum operators and $V(r)$ is the Coulomb potential given by

$$V(r) = \frac{-Ze^2}{4\pi\varepsilon_0 r} \tag{1.10}$$

where Z is the atomic number. Evaluating the r-dependant part of equation 1.9

$$\frac{1}{r}\frac{\mathrm{d}V(r)}{\mathrm{d}r} = \frac{Ze^2}{4\pi\varepsilon_0 r^3} \tag{1.11}$$

Since $r \simeq a_0/Z$ where a_0 is the Bohr radius, λ scales as Z^4, which means that spin-orbit interaction is weak for light elements, but becomes much stronger in heavy elements with high Z such as platinum or tungsten.

SOI gives rise to the total angular momentum $\mathbf{j} = \mathbf{l} + \mathbf{s}$. The magnetic moment associated with this momentum in terms of μ_B is given by

$$\boldsymbol{\mu}_j = -g_j\mu_B\frac{\boldsymbol{j}}{\hbar} \tag{1.12}$$

where g_j is the Landé-g factor. Then the macroscopic magnetisation M of the system is given by

$$\boldsymbol{M} = \frac{\boldsymbol{\mu}N}{V} \tag{1.13}$$

where μ is the net moment on each atom, N is the number of atoms in the material and V is the volume of the material. [2]

So far the discussion was limited to single-electron atoms, where the Schrödinger equation can be solved analytically. Now the treatment will be extended to multi-electron atoms. [3] The Hamiltonian H can be expressed as a sum of three parts

$$H = H_{\mathrm{CF}} + H_{\mathrm{Res}} + H_{\mathrm{SO}} \tag{1.14}$$

where H_{CF} is the central field Hamiltonian, H_{Res} is the residual Coulomb Hamiltonian and H_{SO} is the spin-orbit interaction Hamiltonian. Each part of the Hamiltonian

contains the following terms

- H_{CF}: the kinetic energy of all electrons, the Coulomb attraction between the nucleus and all electrons and the 'radial' (central) part of the Coulomb repulsion between all electrons.
- H_{Res}: the 'angular' (residual) part of Coulomb interaction between all electrons which couples the momenta of individual electrons, i.e. for N electrons the orbital and spin angular momenta are $\mathbf{L} = \sum_{i=1}^{N} \mathbf{l}_i$ and $\mathbf{S} = \sum_{i=1}^{N} \mathbf{s}_i$
- H_{SO}: the sum of all spin-orbit interactions.

It is important to note that only the total angular momentum $\mathbf{J}$, which is the sum of all coupled angular moments, is constant, however there are two ways of adding angular momenta to calculate $\mathbf{J}$. The conservation of $\mathbf{J}$, obtained by two different coupling (addition) schemes, is illustrated for a 2-electron atom in Figure 1.3.

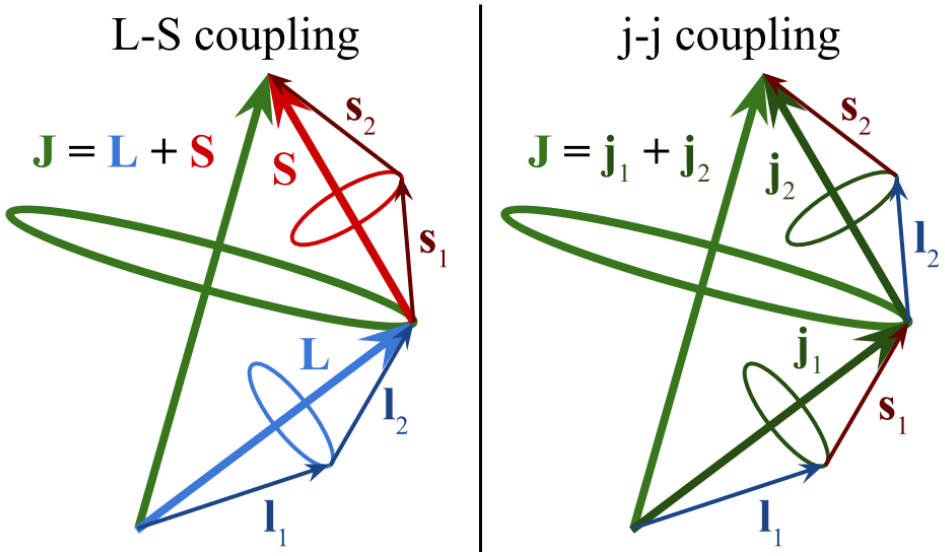

Figure 1.3: Vector addition diagrams for a 2-electron atom. L-S coupling where $\mathbf{J} = \mathbf{L} + \mathbf{S}$ and j-j coupling where $\mathbf{J} = \mathbf{j}_1 + \mathbf{j}_2$.

The Schrödinger equation is too complicated to solve analytically for atoms with more than one electron and the problem is simplified by application of perturbation theory. The order in which angular momenta are added depends on the perturbation order of H_{Res} and H_{SO}. For light atoms, the Coulomb interaction is stronger than the

spin-orbit interaction, i.e. $H_{\text{Res}} > H_{\text{SO}}$, then **L** and **S** couple to a total **J** known as L-S coupling. For heavy atoms $H_{\text{Res}} < H_{\text{SO}}$ and the angular momenta are added according to the j-j coupling scheme.

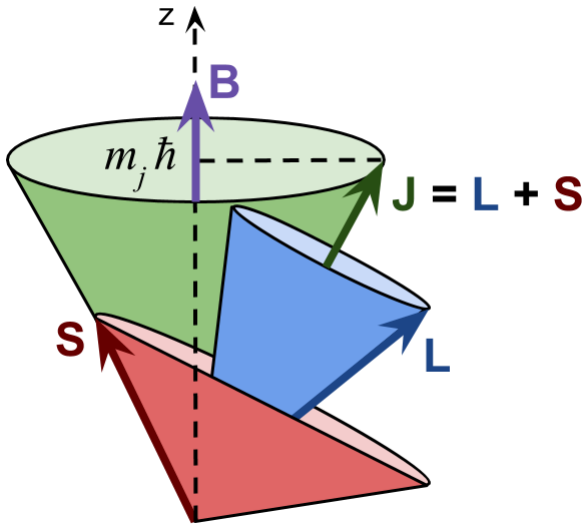

Figure 1.4: Vector cones of angular momenta. Precession of $\mathbf{J} = \mathbf{L} + \mathbf{S}$ around a weak magnetic field **B** applied along the z-axis. The cones arise due to uncertainty in measuring angular momentum components.

As mentioned before, **J** is a conserved quantity, however **L** and **S** are not. In quantum mechanics, if two observable operators do not commute, they cannot be measured simultaneously and satisfy the Heisenberg uncertainty principle. The commutation relations between angular momenta components, e.g. $\mathbf{L} = (L_x, L_y, L_z)$ are non-zero which follows from the canonical commutation relations. However, the operator $L^2 = L_x^2 + L_y^2 + L_z^2$, which corresponds to the magnitude of **L**, commutes with all components of **L**. The same rules apply to the components and magnitudes of **J** and **S**. In a weak magnetic field **B** applied along the z-axis, the total angular momentum will precess as illustrated in Figure 1.4. The z-component and magnitude of angular momenta are known, however the remaining x and y components are unknown. Therefore the vectors **J**, **L** and **S** lie on cones representing the uncertainty arising from the fact that their components do not commute.

1.1.3 Types of Magnetism

Five main types of magnetism are diamagnetism, antiferromagnetism, paramagnetism, ferromagnetism and ferrimagnetism, summarised in Table 1.1.

Type	Susceptibility	Characteristics
Diamagnetism	Negative and very small	No long-range order. In the presence of an applied field, moments align to oppose the field.
Paramagnetism	Positive and small	No long-range order. In zero field, atoms have randomly oriented magnetic moments and the net magnetisation is zero. In an applied field, moments align along the field direction.
Ferromagnetism	Positive and large, function of applied field and microstructure dependent.	Spontaneous parallel alignment of moments.
Ferrimagnetism	Positive and large, function of applied field and microstructure dependent.	Non-equal moments have mixed parallel and anti-parallel alignment. Net magnetisation present.
Antiferromagnetism	Positive and small	Equal moments have mixed parallel and anti-parallel alignment. No net magnetisation.

Table 1.1: Summary of five main types of magnetism.

The first type are diamagnetic materials, which in the presence of an external magnetic field induces an opposing field in the material causing a repulsive force. This property is present in all materials because it originates from the fact that electrons performing orbital motion produce a magnetic moment in the opposite direction to an externally applied field. In materials where all electronic shells are filled and there are no magnetic contributions, this weak effect dominates.

Materials that in the presence of an external magnetic field are weakly attracted to it are known as paramagnets. In contrast to diamagnets, the external magnetic field induces a field in the same direction inside the material. Paramagnetism occurs in

materials with unpaired electrons, so atoms with incompletely filled atomic orbitals are usually, but not always, paramagnetic. The unpaired electrons have a dipole moment but are randomly oriented, hence the net magnetisation is zero. In the presence of a magnetic field, the dipoles align and a net positive moment is induced in the direction of the applied field and the magnetisation is proportional to the density of unpaired electrons.

Magnetism is most commonly associated with materials that exhibit spontaneous magnetisation in the absence of external fields, below the magnetic ordering temperature, Curie temperature T_C. Such materials are either ferromagnetic or ferrimagnetic. Ferromagnets are materials where all magnetic atomic species have their moments aligned in the same direction and hence all positively contribute to the magnetisation. In ferrimagnetic materials, some magnetic species are anti-aligned and hence subtract from the net magnetisation. Ferromagnetism occurs in metals when the spin-up and spin-down states in the conduction band split in zero field. This in general is unfavourable, but when the density of states at Fermi level is high and the band is sufficiently narrow, the cost of exchange splitting is overcome and spontaneous magnetic order appears. Above T_C, thermal perturbations destroys the spontaneous magnetic order and the material behaves like a paramagnet.

Antiferromagnetic materials have atoms arranged in crystallographically equivalent sublattices. The net moments on the sublattices are equal in magnitude but opposite in direction, hence there is no stay field. This is antiferromagnetic ordering, which occurs in materials below their magnetic ordering temperature, the Néel temperature T_N. Above T_N, the moments are disordered due to thermal perturbations and the materials exhibit paramagnetic behaviour. [2]

1.1.4 Magnetic Anisotropy

The first person to describe the compass needle was the Chinese polymath and statesman Shen Kuo in his 'Dream Pool Essays' written in 1088 [4; 5]. The most iconic horseshoe shaped magnet was popularised by Swiss physicist Daniel Bernoulli in 1743 [6]. The bar magnets are the most commonly used shape of magnets in everyday life and they were exhibited by Gowind Knight before the Royal Society in 1744 [7]. The three different shapes are depicted in Figure 1.5. Up to 1951 it was not possible to

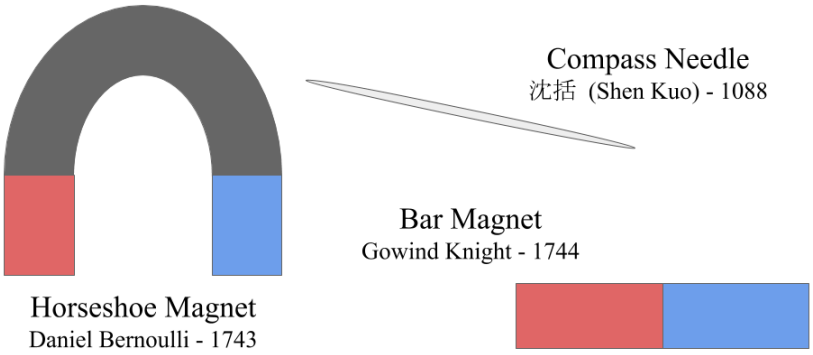

Figure 1.5: Before the breaking of the shape barrier in 1951, magnets were made in complicated shapes such as needles, horseshoes and bars to maximise their stray field.

manufacture permanent magnets in any desired shape, because they would easily self-demagnetise. For a uniformly magnetised ellipsoid, the demagnetising field $\mathbf{H}_d$ is related to the magnetisation $\mathbf{M}$ via the demagnetising factor $\mathcal{N}$, such that

$$\mathbf{H}_d = \mathcal{N}\mathbf{M} \tag{1.15}$$

where $0 \leq \mathcal{N} \leq 1$ depending on the shape of the object and direction of $\mathbf{M}$. For a permanent magnet, the coercive field $\mathbf{H}_c$ must be grater than $\mathbf{H}_d$ and the coercivity is limited by the anisotropy. Magnetic anisotropy is a consequence of the fact that magnetic properties of magnets are direction dependent. The shapes of magnets in the past had to be chosen so that $\mathbf{H}_c > \mathbf{H}_d$ and this is known as the shape barrier. The shape barrier was broken in 1951 with the advent of hexagonal ferrites, a new class of magnetic materials developed by the company Phillips in the Netherlands. In those materials, coercivity exceeds the spontaneous magnetisation allowing for any shape of magnet to be made opening a new world of technological applications. Few decades later samarium-cobalt (1970's) and neodymium-iron (1980's) rare-earth magnets were invented and are the strongest permanent magnets available, in particular the neodymium magnets can produce a stray field of over 1.4 T. [7]

The two main types of magnetic anisotropy are shape and magnetocrystalline anisotropies and will be discussed in detail. Other types of anisotropy include surface anisotropy e.g. where ultra thin films can overcome the shape barrier and produce perpendicular magnetic anisotropy (PMA), and exchange-related anisotropy e.g. at

a ferromagnet/antiferromagnet interface resulting in unidirectional anisotropy which manifests itself as exchange bias [8; 9; 10].

Shape anisotropy is related to the magnetostatic self energy E_s

$$E_s = -\frac{1}{2}\mu_0 \int_V \mathbf{H}_d \cdot \mathbf{M}\, d^3r \tag{1.16}$$

where the integral is taken over the volume of the magnet V. Let $|\mathbf{M}| = M_s$ then substituting expression 1.15 into the integrand and evaluating the integral, the magnetostatic self energy expression becomes

$$E_s = -\frac{1}{2}\mu_0 V \mathcal{N} M_s^2 \tag{1.17}$$

The anisotropy energy is the difference in the self-energy when the ellipsoid is magnetised along its easy and hard axes. For the easy and hard directions, the demagnetisation factors are $\mathbb{N}_{easy} = \mathcal{N}$ and $\mathcal{N}_{hard} = \frac{1}{2}(1-\mathcal{N})$, respectively. Then the difference in of self-energies ΔE_s is given by

$$\begin{aligned} \Delta E_s &= \frac{1}{2}\mu_0 V M_s^2 \left(\frac{1}{2}(1-\mathcal{N}) - \mathcal{N}\right) \\ \Delta E_s &= \frac{1}{4}\mu_0 V M_s^2 (1-3\mathcal{N}) \end{aligned} \tag{1.18}$$

Then for the ellipsoid, the shape anisotropy constant K_{sh}, with SI units [J m^{-3}] can be expressed in terms of $\mathcal{N}$

$$K_{sh} = \frac{1}{4}\mu_0 M_s^2 (1-3\mathcal{N}) \tag{1.19}$$

For a sphere which is symmetric in all directions, $\mathcal{N} = \frac{1}{3}$ and $K_{sh} = 0$ as expected. For non-ellipsoidal shape of a magnet, an effective demagnetising factor is used to approximate it. In thin films, the demagnetising factor for $\mathbf{M}$ along the in-plane and out-of-plane directions are 0 and 1, respectively. This means that this shape will always prefer the magnetisation to lie in the plane of the thin film. Thin films out-of-plane easy axis are possible when the shape anisotropy is overcome by magnetocrystalline anisotropy.

The magnetocrystalline anisotropy has two distinct sources. The first is the single-ion contribution where the orbital motion of the electron around the atomic nucleus couples to the crystal field. The second two-ion anisotropy contribution arises from

the mutual interaction of dipoles. Magnetocrystalline anisotropy energy densities (E_a) for cubic and tetragonal crystal symmetries:

Cubic symmetry

$$\begin{aligned} E_a &= K_{1c}(\alpha_1^2\alpha_2^2 + \alpha_2^2\alpha_3^2 + \alpha_3^2\alpha_1^2) + K_{2c}(\alpha_1^2\alpha_2^2\alpha_3^2) \\ E_a &\approx K_{1c}(\sin^4(\theta)\cos^2(\phi)\sin^2(\phi) + \cos^2(\theta)\sin^2(\theta)) \end{aligned} \tag{1.20}$$

where K_{1c} and K_{2c} are the respective first and second order anisotropy constants, and α_1, α_2, α_3 are the direction cosines of the magnetisation.

Tetragonal symmetry

$$E_a = K_1\sin^2(\theta) + K_2\sin^4(\theta) + K_2^{'}\sin^4(\theta)\cos(4\phi) + O(\sin^6(\theta)) \tag{1.21}$$

where K_1, K_2 and $K_2^{'}$ are the first, second and third order anisotropy constants. The cubic Heusler alloy Mn_2Ru_xGa thin film is epitaxially grown on MgO(100) single crystal substrate producing a 1 % tetragonal distortion of the unit cell due to non-volume conserving biaxial strain and the thin film has PMA. [2]

Uniaxial anisotropy

Taking equation 1.21 and keeping the first order term gives a special case of magnetocrystalline anisotropy known as uniaxial anisotropy. In this case, the magnetisation is constrained to lie along the easy-axis in the absence of an applied field. The anisotropy energy density E_u is

$$E_u = K_u\sin^2(\theta) \tag{1.22}$$

where K_u is the uniaxial anisotropy constant and θ is the angle between the easy-axis and **M**. The coercivity is limited by anisotropy such that

$$H_c < \frac{2K_u}{\mu_0 M_s} \tag{1.23}$$

where M_s is saturation magnetisation. Increasing the anisotropy will increase the coercive field and hence make the material more demagnetisation resistant.

1.1.5 Magnetic Domains and Domain Walls

The basis of the modern theory of magnetic domains is the minimisation of internal energy. In a ferromagnetic material, a large region with constant magnetisation will

produce a large stray field and requires a lot of magnetostatic energy. To reduce the energy, this region can split up into smaller oppositely magnetised regions called magnetic domains thus reducing the stray field. Further splitting of larger domains into smaller domains with magnetisation oriented occurs until the stray field and hence the magnetostatic energy are minimised. For a crystal of a magnetic material, the internal energy to be minimised is described by Landau-Lifshitz free energy E_{L-L} equation [11; 12]

$$E_{L-L} = E_{ex} + E_D + E_\lambda + E_A + E_Z \tag{1.24}$$

where E_{ex} is the exchange energy, E_D is magnetostatic energy, E_λ is magnetoelastic anisotropy energy, E_A is magnetocrystalline anisotropy energy and E_Z is Zeeman energy.
Examination of each contribution to the free energy in more detail:

- E_{ex}: In ferromagnetic, ferrimagnetic and antiferromagnetic materials, exchange energy describes the interactions between magnetic dipoles. This energy is minimised when all dipoles are aligned, hence it is responsible for the magnetisation.

- E_D: The self-energy in magnetic materials is due to the magnetic field created by the magnetisation. This is the stray field on the outside and the demagnetising field on the inside of the material. In the context of magnetic domains, this energy is minimised when the length of the 'loops' of the stray field is reduced which is achieved when the magnetised regions split into different domains as described above.

- E_λ: This energy is due to magnetostriction refering to changes in the crystal lattice dimensions of the crystal when magnetised inducing an elastic strain. The directions of magnetisation that reduce the strain minimise the energy and favour the axis of magnetisation of domains to be parallel.

- E_A: Magnetocrystalline anisotropy implies that the crystal lattice has 'easy' and 'hard' directions along which it can be magnetised. This energy is minimised when magnetisaton lies along the easy-axis direction of the crystal lattice. A polycrystalline material consists of distinctly oriented grains and hence domain magnetisation of the grains will point along the easy axis of the local crystal orientation.

- E_Z: The interaction of the magnetic material with an externally applied field results in this energy term that is added/subtracted to the self energy. Magnetic domains will tend to align with an externally applied field. For hard magnetic materials, there is a critical field known as the coercive field that is needed to trigger magnetisation reversal. Increasing the external field further leads towards saturation of magnetisation meaning all domains are aligned along the applied field direction.

Magnetic domains are separated by finite regions, where magnetic moments undergo a gradual reorientation known as domain walls. [2] The domain wall energy E_W is the difference in energy of magnetic moments before and after the domain wall has been created. Both E_W and domain wall width (δ_w) depend on the exchange and magnetocrystalline anisotropy energies. The anisotropy energy minimisation favours narrow domain walls because it favours magnetic moments aligned with the crystal lattice. On the other hand, minimisation of exchange favours parallel alignement of magnetic moments which makes domain walls wider. The two opposing energies are minimised to reach an equilibrium and set the width of the domain wall. There are two main types of domain walls, Bloch and Néel domain walls, illustrated in Figure 1.6.

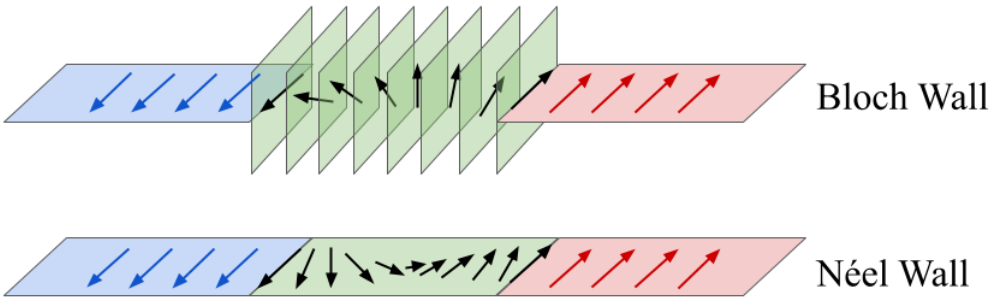

Figure 1.6: Diagram of Bloch and Néel domain walls.

In a Bloch domain wall the magnetisation rotates along the normal direction of the domain wall, i.e. magnetisation lies along the domain wall plane as shown in the top of Figure 1.6. The Bloch type domain walls were named after F. Bloch and occur in bulk materials and thin films. In the Néel wall, named after L. Néel, the magnetisation rotates about a line that is orthogonal to the magnetisations of the domain walls. Hence,

the moments smoothly rotate within the plane of the wall, as depicted at the bottom of Figure 1.6. The rotation varies strongly at the core, where the moment point close to the hard axis. Towards the edges of the wall, the rate of change of rotation decays logarithmically. This type of wall is common in ultra thin films where the exchange length is large relative to film thickness.

1.1.6 Magnetic Hysteresis and Magnetisation Reversal

Magnetic hysteresis is the essential characteristic of ferromagnetic and ferrimagnetic materials. Hysteresis loops are plots of the irreversible macroscopic average magnetisation **M** response to an externally applied magnetic field **H**. Figure 1.7 depicts a hysteresis loop of a hard ferromagnet with critical points with their corresponding magnetic domain orientations indicated on the diagram.

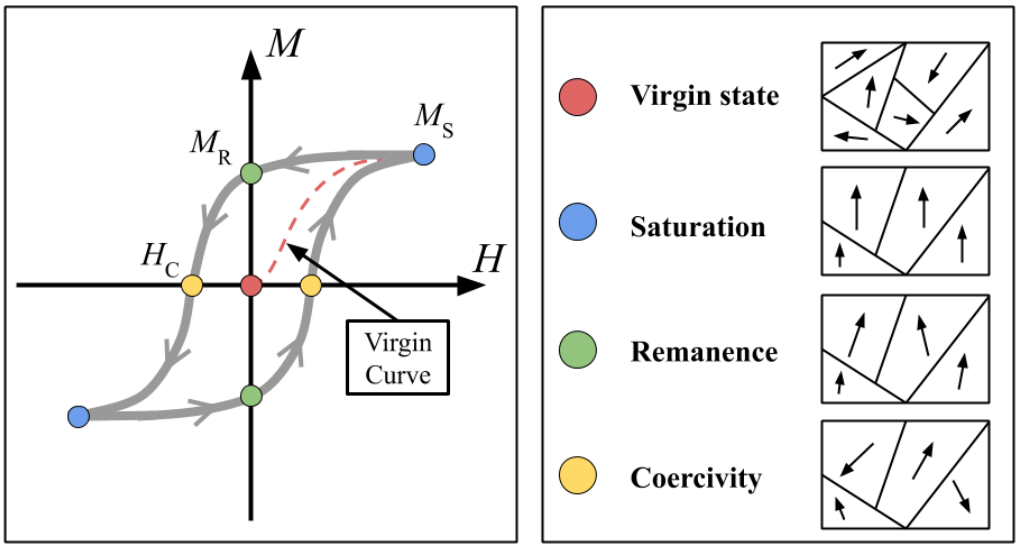

Figure 1.7: Right: Hysteresis loop and the virgin curve for a hard ferromagnetic material. Left: The domain orientations corresponding to the virgin state, saturation, remanence and coercivity.

Initially the ferromagnet is in an unmagnetised, unique multi-domain 'virgin' state. As the magnetic field is applied, magnetisation increases following the virgin curve and reaches the saturation state. This process is irreversible and the initial multi-domain

state cannot be recovered, unless the sample is heated above the Curie temperature (T_C), that is the temperature above which the spontaneous magnetisation vanishes. At saturation, all magnetic domains are aligned with the applied field direction and magnetisation is maximal (M_S). When **H** is zero, the ferromagnet is in a metastable remanent state with a non-zero net magnetisation (M_R), with domains are not perfectly aligned. Note that removing the applied field does not mean $\mathbf{H} = 0$, because of the demagnetising field. Increasing **H** in the opposite direction to the magnetisation, triggers the process of magnetisation reversal and the point at which $\mathbf{M} = 0$ is known as coercivity and domains are oriented to cancel net magnetisation. Further increasing the applied field saturates the sample and the magnetisation is fully reversed.

The processes involved in magnetisation reversal are illustrated in Figure 1.8.

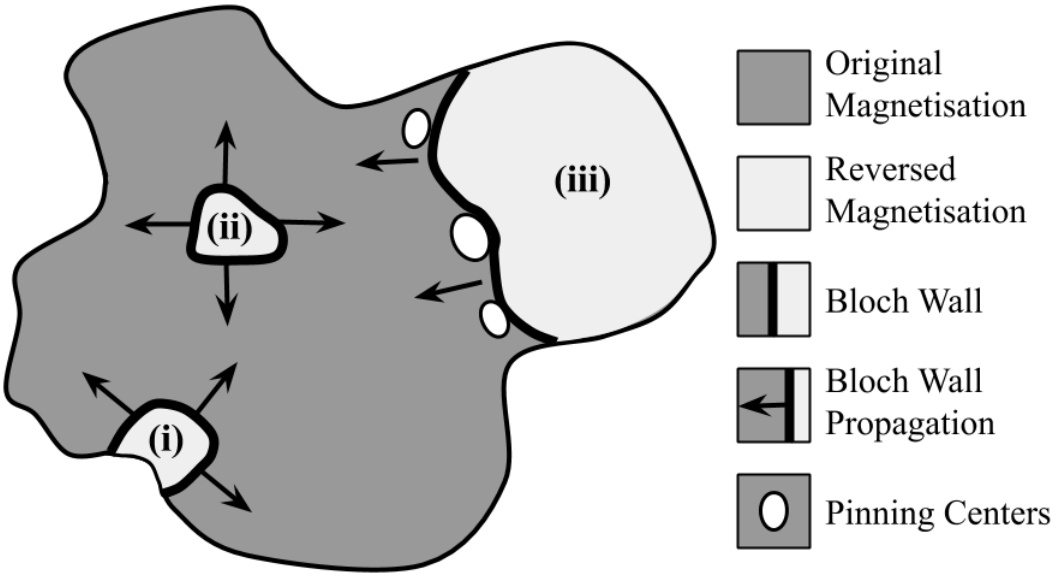

Figure 1.8: Magnetisation reversal processes: (i) reverse domain in the bulk nucleated at a defect such as a crystal dislocation or from a spontaneous thermal fluctuation, (ii) reverse domain, which has grown by domain wall propagation but is now trapped by present pinning centers (iii) reverse domain nucleated at a surface asperity e.g. region of high roughness or scratch.

Polycrystalline samples have grains and the grain boundaries host defects such as crystal dislocations/misfits. Such defects can act as sites for domain nucleation because the distortions of the crystal lattice locally modify the anisotropy and hence the

coercivity. Nucleation can also occur stochastically due to thermal fluctuations. The crystal dislocations can also act as pinning centers, which force a moving domain wall into a local energy minimum and get 'stuck'. To overcome the energy barrier, more external field is applied and this is known as depinning of a domain wall. Surface asperities such as scratches or regions of high surface roughness are regions of strong demagnetising fields. As a result they act as nucleation centers because the reverse externally applied **H** field is enhanced in their vicinity. [2] In this work, the discussion will be focused on thin films with perpendicular magnetic anisotropy, where magnetisation reversal is dominated by either of two processes:

1. **Domain wall motion:** nucleation of a few isolated domains which expand with time via Bloch wall propagation.

2. **Domain nucleation:** magnetisation reversal occurs by nucleation only.

1.1.7 Weiss Molecular Field Theory

The first modern theory of ferromagnetism is the molecular field theory proposed by P. Weiss in 1906. [2] The theory can be derived by applying a mean field approximation to the Heisenberg Hamiltonian given by

$$H = -\sum_{ij} \mathscr{J}^{ij} S^i \cdot S^j - g\mu_B \sum_i S^i \cdot \mu_0 H = -g\mu_B \sum_i S^i \cdot \left(\frac{1}{g\mu_B} \sum_j \mathscr{J}^{ij} S^j + \mu_0 H \right) \quad (1.25)$$

where in the first term J^{ij} are positive (negative) for ferromagnetic (antiferromagnetic) nearest neighbour coupling between spins S and the second term is the external applied field. The Hamiltonian can be rewritten to resemble a system of spins in an effective field ($\mu_0 H_{\text{eff}}$)

$$H = -g\mu_B \sum_i S^i \cdot \mu_0 H_{\text{eff}} \quad \text{where} \quad \mu_0 H_{\text{eff}} = \frac{1}{g\mu_B} \sum_j \mathscr{J}^{ij} S^j + \mu_0 H \quad (1.26)$$

Mean field approximation replaces the effective field operator with its thermodynamic mean value (multiples of a half). The mean effective field in the Weiss theory is an enormous internal molecular field proportional to the magnetisation, with the constant of proportionality known as Weiss coefficient. Modelling the temperature dependence of spontaneous magnetisation in a ferromagnet with zero external field can be achieved

using the Weiss molecular field theory. The magnetisation is modelled by the Brillouin function

$$B_J(x) = \frac{2J+1}{2J}\coth\left(\frac{2J+1}{2J}x\right) - \frac{1}{2J}\coth\left(\frac{1}{2J}x\right) \tag{1.27}$$

and the magnetisation at $T = 0$ K is given by $M_0 = \rho g \mu_B J$ where ρ is the number of atoms per unit volume, g is the Landé g factor and J is total angular momentum quantum number.

The molecular field theory can also be applied to ferrimagnets. A ferrimagnet can be regarded as an antiferromagnet with unequal moments. Let the two antiferromagnetically coupled sublattices be labelled A and B, then equations for the internal molecular fields $\mathbf{H}_{int}$ for each sublattice in an external field $\mathbf{H}$ are

$$\mathbf{H}^A_{int} = n^{AA}_W \mathbf{M}^A + n^{AB}_W \mathbf{M}^B + \mathbf{H} \tag{1.28}$$

$$\mathbf{H}^B_{int} = n^{AB}_W \mathbf{M}^A + n^{BB}_W \mathbf{M}^B + \mathbf{H} \tag{1.29}$$

where n^{AA}_W, n^{AB}_W, and n^{BB}_W are the Weiss coefficients. The magnitude of the magnetisation is modelled by the Brillouin function. At equilibrium, magnetisation direction is parallel to the internal molecular field, given by unit vectors $\mathbf{h}^{A,B}_{int}$

$$\mathbf{M}^A = M^A_0 B_J(x^A)\mathbf{h}^A_{int} \tag{1.30}$$

$$x^A = \frac{3C^A|\mathbf{H}^A_{int}|}{\rho^A g \mu_B (J^A+1)T} \tag{1.31}$$

$$\mathbf{h}^A_{int} = \frac{\mathbf{H}^A_{int}}{|\mathbf{H}^A_{int}|} \tag{1.32}$$

$$\mathbf{M}^B = M^B_0 B_J(x^B)\mathbf{h}^B_{int} \tag{1.33}$$

$$x^B = \frac{3C^B|\mathbf{H}^B_{int}|}{\rho^B g \mu_B (J^B+1)T} \tag{1.34}$$

$$\mathbf{h}^B_{int} = \frac{\mathbf{H}^B_{int}}{|\mathbf{H}^B_{int}|} \tag{1.35}$$

where $C^{A,B}$ are Curie constants for each sublattice given by

$$C^A = \frac{\mu_0 \rho^A m^A_{\text{eff}}}{3k_B} \tag{1.36}$$

$$m^A_{\text{eff}} = g\mu_B\sqrt{J^A(J^A+1)} \tag{1.37}$$

$$C^B = \frac{\mu_0 \rho^B m^B_{\text{eff}}}{3k_B} \tag{1.38}$$

$$m^B_{\text{eff}} = g\mu_B\sqrt{J^B(J^B+1)} \tag{1.39}$$

where J^A and J^B are half-integer sublattice quantum numbers.

The Curie temperature T_C for the ferrimagnet can be expressed in terms of the Weiss

coefficients and Curie constants

$$T_C = \frac{1}{2}\left((C^A n_W^{AA} + C^B n_W^{BB}) + \sqrt{(C^A n_W^{AA} - C^B n_W^{BB})^2 - 4C^A C^B (n_W^{AB})^2}\right) \tag{1.40}$$

The Weiss coefficients n_W can be converted to Heisenberg exchange coupling constants $\mathscr{J}$ using the following expression

$$\mathscr{J}^{ij} = n_W^{ij} \rho \mu_0 (g\mu_B)^2 \tag{1.41}$$

The Weiss molecular field model is can be used to fit magnetometry data of spontaneous magnetisation in zero field as a function of temperature to obtain the Weiss coefficients and obtain the sublattice magnetisation behaviour. The strength of this model its simplicity and that it can be easily implemented numerically. However there are also weak points that must be considered:

- The magnetometry data should be collected over a wide range of temperatures and T_C should be experimentally determined to ensure the accuracy of Weiss constants.
- The mean field approximation is not accurate at low temperatures and around T_C and provides an over-estimation of T_C.
- It does not take account of anisotropy, which is usually much weaker than exchange. An anisotropy term can be implemented, but this creates convergence problems at low temperatures.
- The model does not account for non-collinear sublattice moments.

1.2 Spin Electronics

Spin electronics or spintronics is the marriage of electronics which is based on the manipulation of charge of the electron and magnetism where the intrinsic spin of the electron plays the main role. The goal of spintronics is to develop devices that exploit electron spin to create new functionalities. [13; 14; 15] The spintronic dream includes

universal memory, THz data transfer speeds and electronics with ultra-low power consumption. Traditional electronics ignored the spin of the electron, but when high-quality metallic films became available in the 1970s with thickness in the nanometer range, it became feasible to manipulate spin polarized electronic currents. Unlike charge, spin is not conserved in scattering events, with about 1 in 100 events causing a spin flip, so the spin diffusion length (λ_s) is about ten times the mean free path. Therefore for spintronic devices thin magnetic films are required, where layer thickness is comparable to λ_s ($1-20$ nm). The magnetic properties of thin films vary dramatically from those of the bulk. Fabricating thin film heterostructures, e.g. several alternating layers of material thin films with different magnetic and electrical properties gives rise to phenomena such as exchange bias, perpendicular magnetic anisotropy, spin polarisation, spin current generation, giant and tunnel magnetoresistance. Those phenomena form the basic principles of operation of spintronic devices. [2] Two key features of spintronic materials which will be discussed in this section are spin polarisation and spin currents.

1.2.1 Spin Polarisation

As mentioned above, spintronics is about building devices that manipulate the spin of the electron. Therefore, one of the key properties important for spintronic materials is high spin polarisation. Spin polarisation is the degree to which spins are oriented along a specific direction. Different types of materials can produce spin polarised currents as the electrons pass through them. Let P be the degree of spin polarisation of the conduction electrons at the Fermi energy E_F

$$P = \frac{D_{up} - D_{down}}{D_{up} + D_{down}} \tag{1.42}$$

where D_{up} and D_{down} are the densities of spin-up and spin-down states at Fermi level, respectively. Figure 1.9 depicts the band structures of a non-magnetic metal, ferromagnetic metal and a half-metal. For a non-magnetic metal, the conduction bands are the same for spin-up and spin-down electrons. Hence the current passing through has no spin polarisation at zero field, i.e. $P = 0$. In ferromagnetic materials the spin-up and spin-down are exchange split due to Coulomb interaction, hence depending on the material the current emerging from it will be to some degree spin polarised, i.e. $0 <$ P

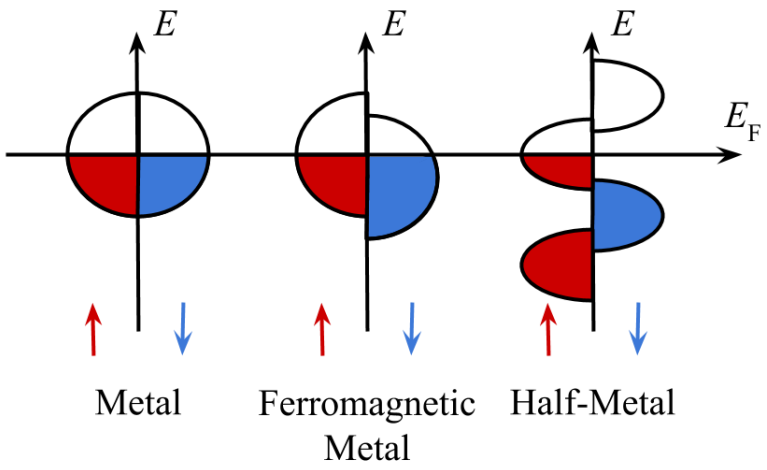

Figure 1.9: Band structure diagrams for a metal, ferromagnetic metal and a half-metal.

< 1. There is also a very interesting class of materials called half-metals. Here there exists a spin gap in the band structure and if the Fermi level is located in the spin gap, 100% spin polarisation can be achieved, i.e. $P = 1$ at $T = 0$ K in materials with no SOI. In practice the current emerging from a half-metal is not fully spin polarised but it is to a very high degree and such materials are desirable in spintronic devices.

1.2.2 Spin Polarised Currents

An electrical current I_C is the flow of electronic charges in the presence of a potential difference or voltage V. The electrons flowing in a non-magnetic conductor have their spins randomly oriented hence the net flow of angular momentum is zero. However, in a ferromagnet or a half-metal it is possible to generate a spin polarised current and hence have a non-zero flow of angular momentum. Analogously to the charge current, the spin current I_S is the flow of spins (angular momentum) in the presence of a chemical potential μ. Table 1.2 is a summary of types of currents and their main characteristics.

Manipulation and exploitation of electron spin is at the heart of operation of spintronic devices. Efficient generation of spin polarised charge and pure spin currents as well as spin-charge conversion are of critical importance. Figure 1.10 is a diagram summarising the many ways in which spin polarised currents are generated. The most

Type	Characteristics
Unpolarised charge current	Flow of charges only in non-magnetic metals.
Spin polarised current	Flow of both charge and angular momentum e.g. inside a ferromagnetic/ferrimagnetic metal or a half-metal.
Spin current	Flow of angular momentum, but no net charge flow, carried by conduction electrons in metals and by magnons (spin waves) in insulators.

Table 1.2: Summary of types of currents and their main characteristics.

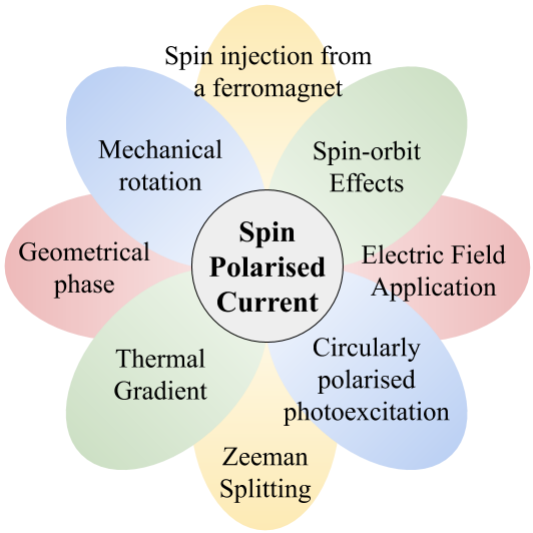

Figure 1.10: Diagram summarising methods of spin polarised current generation.

common method to generate a spin polarised current in a non-magnetic metal (NM) is spin injection from a ferromagnet (FM). In this case a heterostructure of a ferromagnetic thin film and a non-magnetic metal are in contact. In the presence of an electric field the electrons are injected from FM into NM. The two materials have different density of states as illustrated in Figure 1.9, with the FM having exchange-split spin up and spin down bands. As a result there will be an accumulation of one type of spin at the interface of the two materials, characterised by the chemical potential difference $\Delta\mu$. For this purpose, the FM can be replaced with a half-metallic ferro- or ferrimagnetic material to potentially increase the degree of spin polarisation. Other ways to produce spin accumulation and spin polarised currents include spin-orbit scattering, spin Seebeck and Nernst effects in the presence of a thermal gradient, Zeeman split-

ting, presence of a magnetic field or an electrical field, spin motive force, circularly polarised photoexcitation, a thermal gradient, Berry phase curvature and mechanical rotation. [16]

1.3 Magneto-Transport Phenomena

Transport in magnetic conductors is very different from non-magnetic conductors. Many fascinating magneto-transport phenomena occur in ferromagnetic and ferrimagnetic thin films and thin film heterostructures. Those include various Hall and magnetoresistive effects. Magnetoresistance (MR) is the variation in resistance measured in the presence of an applied magnetic field and without it given by

$$MR = \frac{\rho(\mathbf{B}) - \rho(0)}{\rho(0)} \tag{1.43}$$

where $\rho(\mathbf{B})$ and $\rho(0)$ are electrical resistivities in the presence and absence of a magnetic field, respectively. Three main magnetoresistance effects are anisotropic, giant and tunnel magnetoresistance.

For $3d$ ferromagnets, the $3d$ band is exchange split into spin up and down subbands. At the Fermi level conduction electrons coexist in s-like and d-like states. The s-band is not spin-split, however the s states hybridise with the d states and thus can aquire predominantly spin up or down character. The s-electrons are delocalised with high mobility and carry most of the current. The d-electrons are localised and ineffective current carriers due to high effective mass and low mobility. In strong ferromagnets, spin down s-electrons scattering dominates because they can only scatter into $3d$ spin down states, assuming negligible spin-flip scattering. The Hall resistivity of metallic ferromagnets, in addition to ordinary Hall effect, acquires a contribution from spin dependent scattering. This is known as the anomalous Hall effect (AHE), which is empirically proportional to the magnetisation of the sample.

1.3.1 Anisotropic Magnetoresistence

Anisotropic magnetoresistance (AMR) in ferromagnets, discovered in 1856 by W. Thompson [17], is defined as the difference in longitudinal resistance (ρ_{xx}) measured with spontaneous magnetisation $\mathbf{M}$ oriented parallel ($\rho_{\parallel}$) and perpendicular ($\rho_{\parallel}$) to the

applied current **I**, and originates from spin-orbit interaction. [18] The AMR ratio is given by

$$\begin{aligned} \mathrm{AMR} &= \frac{(\rho_{\parallel} - \rho_{\perp})}{\rho_{\parallel}} \\ \mathrm{AMR}(\phi) &= \rho_{\perp} + (\rho_{\parallel} - \rho_{\perp}) \cos^2(\phi) \end{aligned} \tag{1.44}$$

where ϕ the angle between the spontaneous magnetisation and the applied current, i.e. $\phi = 0$ for $\mathbf{M} \parallel \mathbf{I}$ and $\phi = \frac{\pi}{2}$ for $\mathbf{M} \perp \mathbf{I}$ and the direction of magnetisation is varied by an externally applied magnetic field. The AMR ratio is a few percent (up to $\approx 3\%$) higher when the current and magnetisation directions are colinear because the spin-flip scattering is most efficient in this orientation. The greatest sensitivity of to change of resistance occurs for $\phi = \frac{\pi}{4}$ calculated from the condition $\frac{d^2\mathrm{AMR}(\phi)}{d\phi^2} = 0$, which is exploited in AMR based spintronic sensors.

1.3.2 Giant Magnetoresistence

Surprisingly large magnetoresistance was first demonstrated in epitaxial antiferromagnetically coupled Fe-Cr multilayers hence the name giant magnetoresistance (GMR). It was independently discovered by two research groups led by A. Fert in France [19] and P. Grünberg in Germany [20] in 1988. Their discovery led to the development of spin-valve sensors and both physicists were awarded the 2007 Nobel Prize in Physics for the discovery. The magnetisations of ferromagnetic Fe layers align antiparallel (AP) in zero-field, when the thickness of the Cr layers that separates them is adjusted. Applying and external magnetic field can force the magnetisations to align parallel (P). The GMR ratio is given by

$$\mathrm{GMR} = \frac{R_{AP} - R_P}{R_P} \times 100\% \tag{1.45}$$

Measurements on the Fe-Cr heterostructure showed that at 4.2 K resistivity was reduced by almost a factor of 2. To force all Fe layers into a parallel alignment a field of 2 T was required. Figure 1.11 illustrates the low resistance (R_P) and high resistance (R_{AP}) configurations in a tri layer spin valve and their corresponding density of state (DOS) diagrams. The high and low resistance states can be explained by considering Mott's two-current model of conduction, neglecting spin-flip scattering and scattering at the ferromagnet/conductor interfaces. In $3d$ ferromagnets such as Fe, electron-atom

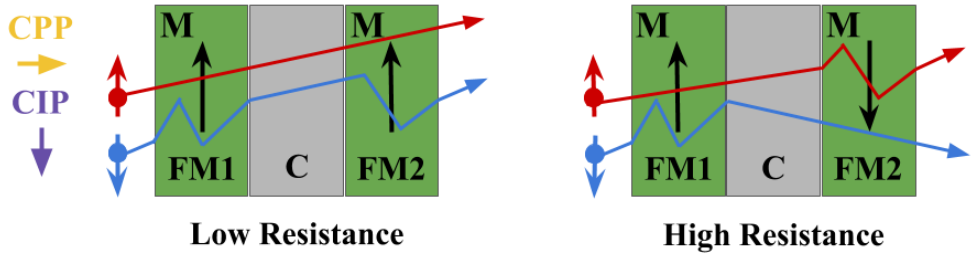

Figure 1.11: GMR: Low resistance parallel magnetisation alignment of FM layers (FM1 & FM2) and high resistance antiparallel magnetisation alignment of FM layers separated by a non-magnetic conductor (C).

scattering depends on the electron spin orientation and the filling of the exchange-split $3d$ band responsible for the magnetic properties of the material. As mentioned before, at the Fermi level conduction electrons coexist in s-like and d-like states. The s-band is not spin-split, however the s states hybridise with the d states and thus can aquire predominantly spin up or down character. The transport of the majority spins at Fermi level has s-like character in ferromagnets and is therefore similar to that in non-magnetic metals. However for minority spins, the s and d states are hybridised, the Fermi level lies within the $3d$ band resulting in stronger scattering. Therefore the mean free path λ of minority spins is shorter than that of majority spins. The role of FM1 is to produce a spin polarised current that is then injected into the sufficiently thin non-magnetic conductor thickness. The low resistance state arises because in both FM1 and FM2 the spin dependent conductivity is the same and there is little scattering. However if the magnetisation of FM2 is reversed relative to FM1, spin dependent conductivity for minority and majority spins in FM1 is the opposite in FM2 giving rise to a lot of spin dependent scattering and a high resistance state.

GMR heterostructures can be fabricated for measurements in two geometrical configurations, current parallel to plane (CIP) and current perpendicular to plane (CPP), as indicated in Figure 1.11. In the two geometries GMR has a distinct origin and characteristic length scale for which it can be observed. The factors that contribute to CIP-GMR bulk spin-dependent scattering within FM and C layers and at interfaces as well as interfacial specular reflections of the electron wave function. [21; 22] In CPP-GMR, the current passing perpendicularly to the layers gives rise to a build up of spin polarisation near the FM/C interfaces, known as spin accumulation. In the case of CIP

that length scale is the mean free path λ and for CPP it is the spin diffusion/relaxation length l_s. This means that thicker conductor layers are allowed in CPP geometry since $l_s > \lambda$.

1.3.3 Tunnel Magnetoresistence

Magnetic tunnel junctions (MTJ's) are thin film trilayer structures, similar to the spin valve but the non-magnetic conductor is replaced by an insulator material, e.g. crystalline MgO. The insulator introduces a potential barrier that electrons can tunnel through with the probability of tunnelling proportional to the insulator thickness ($\approx 1-2$ nm). It was originally discovered by the French physicist M. Jullière in 1975 [23]. In the model by Jullière, the tunneling current is proportional to the product of the DOS at Fermi level of the two ferromagnetic layers. The tunnel magnetoresistance effect is illustrated in Figure 1.12.

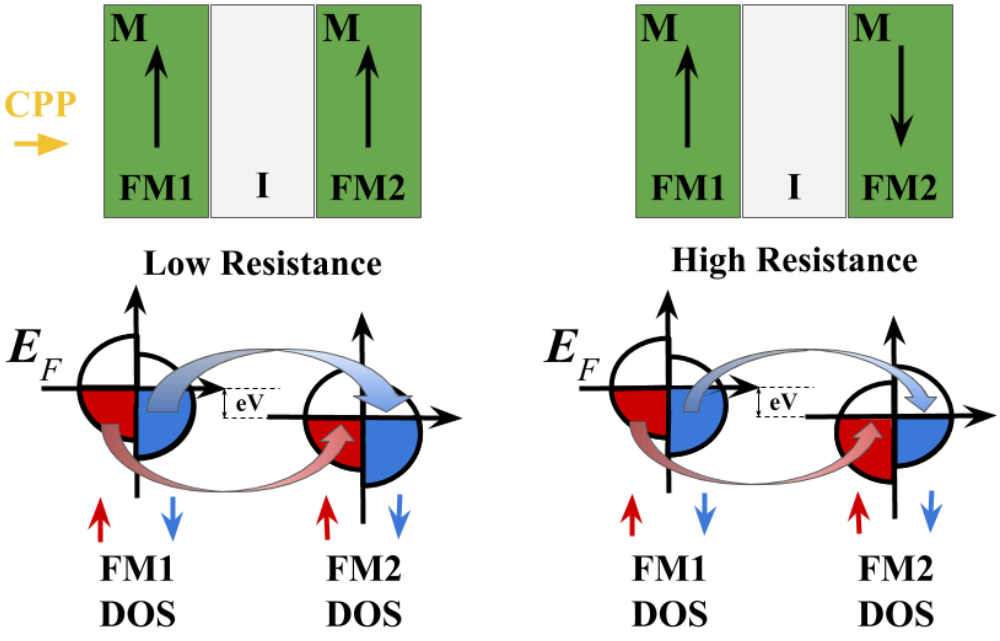

Figure 1.12: TMR: Diagram showing the low resistance parallel magnetisation alignment of FM layers (FM1 & FM2) and high resistance antiparallel magnetisation alignment of FM layers separated by a non-magnetic insulator (I) with corresponding diagrams of density of states (DOS) and a potential barrier eV.

The picture is similar to CPP-GMR with the key difference in due to the replacement of the conductor with and insulator (I), which introduces a potential barrier $\Phi = eV$ where e is electron charge and V is the bias voltage. During tunnelling, electrons preserve their spin orientation and are only allowed to tunnel into the $3d$ sub-band with the same spin orientation. In the parallel magnetisation state, electrons have a higher probability to tunnel through the barrier because of strong overlap of the spin-resolved DOS of FM1 and FM2, resulting in a low resistance state. In the anti-parallel magnetisation orientation, the band splitting is reversed leading to a poor overlap of spin-resolved DOS of FM1 and FM2 and higher resistance. The TMR ratio in terms of the spin polarisation of the two FM electrodes is given by

$$\text{TMR} = \frac{R_{AP} - R_P}{R_P} \times 100\% = \frac{2P_{FM1}P_{FM2}}{1 - P_{FM1}P_{FM2}} \times 100\% \tag{1.46}$$

This model works well in the cases of incoherent tunnelling where the band structure of the barrier can be neglected, e.g. amorphous AlO_x barrier. MTJ's with 3d ferromagnets as electrodes and an amorphous AlO_x barrier yield TMR ratios of up to 70 % at 300 K [24]. The highest recorded TMR ratio of about 1010 % at 5 K was in CoFeB/MgO/CoFeB MTJ's reported by researchers in the H. Ohno group of Tohoku University in Japan [25]. They also demonstrate that at 300 K, TMR ratios as large as 500 % can be achieved. In this case, the MgO tunnel barrier is highly crystalline and facilitates coherent tunneling of electrons between the FM electrodes. As a consequence, Jullière's model is no longer valid and the tunnelling probability depends on the symmetries of the electron states.

1.3.4 Ordinary and Anomalous Hall Effects

In 1879 Edwin H. Hall discovered that electrons in a current carrying non-magnetic conductor in a magnetic field acquire a transverse velocity which 'presses' them against one side of the conductor due to the Lorentz force. For the experiment he used a 'flat spiral of German silver wire' [26]. About a year later, Hall reported that the effect was ten times larger in ferromagnetic iron [27]. Both discoveries were remarkable, but here we will focus on the second one which is known as the anomalous Hall effect (AHE).

It was observed that the Hall resistivity ρ_{xy}, measured for a sample with the magnetic field applied perpendicular to the plane of the conductor H_z, shows very different

behaviour for magnetic and non-magnetic conductors. In the case of a non-magnetic conductor, ρ_{xy} is proportional to H_z with the constant of proportionality is R_0 which depends on carrier density. This linear relationship is expected from the Lorentz force. For magnetic materials, it was found that ρ_{xy} depends on the magnetisation of the material M_z through an empirical formula

$$\rho_{xy} = R_0 H_z + R_S M_z \tag{1.47}$$

where R_S is a constant that depends on various parameters of the specific material, but mainly on longitudinal resistivity ρ_{xx} and it is one order of magnitude larger than R_0 in most $3d$ ferromagnets. [28] Before proceeding to the modern theory of AHE, it is important to first find the expressions that will allow to express ρ_{xy} in terms of ρ_{xx} as well as σ_{xy} in terms of σ_{xx}. The derivation of these relations begins with Ohm's Law in metals

$$\mathbf{j} = \hat{\sigma} \cdot \mathbf{E}$$

where $\mathbf{j}$ is the in-plane current density $\hat{\sigma}$ is the conductivity tensor and $\mathbf{E}$ is the electric field. The equation can be rewritten with the tensor in the form of a 2×2 matrix.

$$\mathbf{j} = \begin{bmatrix} \sigma_{xx} & \sigma_{xy} \\ \sigma_{yx} & \sigma_{yy} \end{bmatrix} \cdot \mathbf{E}$$

Since conductivity is the reciprocal of resistivity, the equations above can be rearranged to obtain

$$\hat{\rho} \cdot \mathbf{j} = \mathbf{E}$$

where $\hat{\rho}$ is the resistivity tensor and $\mathbf{E}$ is the electric field. The equation can also be rewritten with the tensor in the form of a 2×2 matrix

$$\begin{bmatrix} \rho_{xx} & \rho_{xy} \\ \rho_{yx} & \rho_{yy} \end{bmatrix} \cdot \mathbf{j} = \mathbf{E}$$

Now using the fact that the conductivity tensor is equal to the inverse of the resistivity tensor, the components of the conductivity tensor can be expressed in terms of the components of the resistivity tensor. Noting that $\sigma_{xx} = \sigma_{yy}$, $\sigma_{xy} = -\sigma_{yx}$, $\rho_{xx} = \rho_{yy}$ and $\rho_{xy} = -\rho_{yx}$ one obtains

$$\hat{\sigma} = \begin{bmatrix} \sigma_{xx} & \sigma_{xy} \\ -\sigma_{xy} & \sigma_{xx} \end{bmatrix} = \hat{\rho}^{-1} = \frac{1}{\rho_{xx}^2+\rho_{xy}^2} \begin{bmatrix} \rho_{xx} & \rho_{xy} \\ -\rho_{xy} & \rho_{xx} \end{bmatrix}$$

Comparing the elements and considering that $\rho_{xy}^2 << \rho_{xx}^2$

$$\sigma_{xx} = \frac{\rho_{xx}}{\rho_{xx}^2+\rho_{xy}^2} \approx \frac{1}{\rho_{xx}} \quad (1.48) \qquad \sigma_{xy} = \frac{\rho_{xy}}{\rho_{xx}^2+\rho_{xy}^2} \approx \frac{\rho_{xy}}{\rho_{xx}^2} = \rho_{xy}\sigma_{xx}^2 \quad (1.49)$$

Now using these relations, it will be possible to easily express σ_{xy} in terms of ρ_{xx} and studying the dependence of these quantities on each other is a tool to study the origins of AHE in materials. For over a century since its discovery, AHE was an enigma of physics due to the complicated quantum nature of the phenomenon. The mathematical description required sophisticated theoretical tools in topology, such as Berry phase curvature, which were developed in the late-twentieth century. Still today the origins of AHE are under debate, however three main mechanisms have been identified. There are two extrinsic mechanisms, known as skew scattering and side-jump, and an intrinsic deflection mechanism [28].

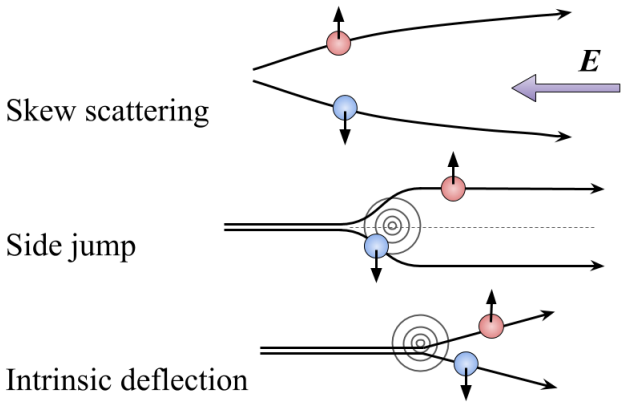

Figure 1.13: Graphic representation of skew scattering, side jump and intrinsic deflection, that are believed to give rise to AHE.

- **Skew scattering:** due to effective SOI of the electron or an impurity in the material the electron experiences asymmetric scattering.
- **Side-jump:** upon approaching or leaving an impurity in the material, the electron velocity is deflected in opposite directions by the electric fields. The time-integral of of the velocity deflection is the side-jump.

- **Intrinsic deflection:** electrons acquire an anomalous velocity perpendicular to the electric field based on Berry phase curvature, that is an effective magnetic field in the rest frame of the electron, which depends on the band structure of the material [28].

The total anomalous Hall conductivity σ_{xy} is a sum of the conductivities that arise from each type of mechanism

$$\sigma_{xy} = \sigma_{xy,\phi_B} + \sigma_{xy,\text{Skew}} + \sigma_{xy,\text{Side}} \tag{1.50}$$

Each term has a different dependence on σ_{xx}. First, the summary of the dependences of the anomalous Hall relativities ρ_{xy} for each mechanisms on ρ_{xx} is given in the Table 1.3 below. From the data in Table 1.3, the expression for ρ_{xy} in terms of ρ_{xx} becomes

Mechanism	$\rho_{xy} \propto \rho_{xx}^n$	$\sigma_{xy} \propto \sigma_{xx}^n$
Intrinsic deflection	$n = 2$	$n = 0$
Skew Scattering	$n = 1$	$n = 1$
Side Jump	$n = 2$	$n = 0$

Table 1.3: Summary of contributions to AHE and the dependences of ρ_{xy} on ρ_{xx} and σ_{xy} on σ_{xx} [28]

$$\rho_{xy} = \alpha_{\phi_B}\rho_{xx}^2 + \alpha_{\text{Skew}}\rho_{xx} + \alpha_{\text{Side}}\rho_{xx}^2 \tag{1.51}$$

where α_{ϕ_B}, α_{Skew} and α_{Side} are constants. Then using the relations derived above we arrive at the expression of σ_{xy} in terms of σ_{xx}

$$\sigma_{xy}^{AHE} = \alpha_{\phi_B} + \alpha_{\text{Skew}}\sigma_{xx} + \alpha_{\text{Side}} \tag{1.52}$$

By studying the dependence of σ_{xy} on σ_{xx} for different materials as a function of temperature, etc. the dominance of any mechanism can be determined. The ratio of the AHE transverse resistivity ρ_{xy} to longitudinal resistivity ρ_{xx} values are used to calculate what is known as the Anomalous Hall angle θ_{AH}. This quantity is related to the degree of spin-dependent scattering in the magnetic material, as θ_{AH} is proportional to the cross product of the polarisation of the fermi level and the magnetisation direction of the 4*c* sublattice since its electrons are in metallic *s*-like states and contribute to the

transport. Materials with a high Hall angle can be expected to have a high spin polarisation which is a very desirable property for spintronic device application. However, verify the spin polarisation other techniques such as point contact Andreev reflection (PCAR) measurements must be performed [29].

1.4 Zero-Moment Half-Metallic Heusler Ferrimagnets

1.4.1 Background and Research Objectives

The new challenge for spin electronics relates to data rate. It has not enjoyed the same exponential increase as magnetic recording density, which has facilitated the storage of enormous quantities of data in server farms. If the big data revolution is to advance, this bottleneck has to be addressed. The vision is that this will be achieved with a new generation of spintronics that enables electronic chip-to-chip communications in the currently inaccessible 'terahertz gap' of the electromagnetic spectrum, thereby underpinning the big data revolution for another 25 years. The 'terahertz gap' is the frequency space between 0.1 and 10 THz shown in Figure 1.14. In this frequency range, semiconductor technology is limited by carrier mobility and mm-wave optical or electronic solutions based on Josephson junctions are impractical to integrate with chip-based electronics operating in ambient conditions.

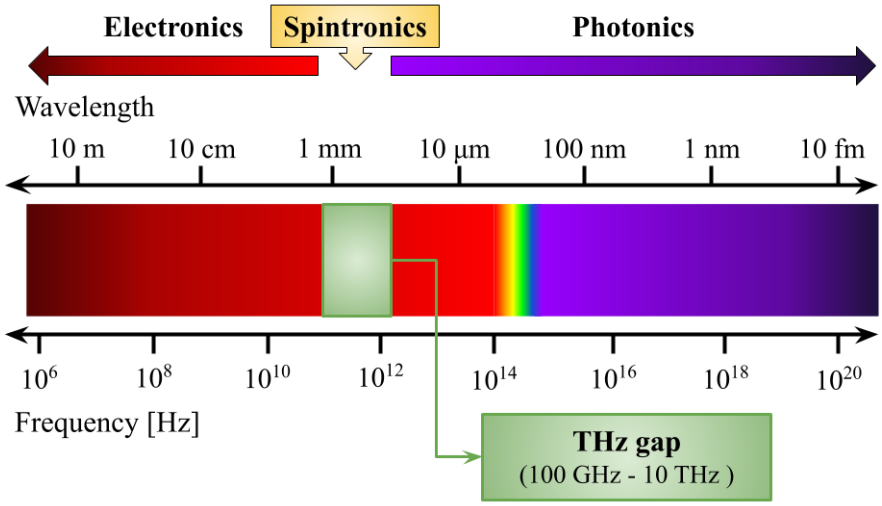

Figure 1.14: Diagram of the electromagnetic spectrum indicating the frequency region known as the THz gap.

The prospect of electrical excitation of THz radiation is related to a new type of magnetic material proposed by van Leuken and de Groot in 1954, which they called a 'half-metallic antiferromagnet' [30]. Like a ferromagnetic half-metal [31; 32], it is fully spin polarised, with electrons of only one spin present at the Fermi level. The magnet was composed of two inequivalent crystallographic sublattices, with precisely compensating magnetisation in the ground state. The terms 'zero-moment half-metal' (ZMHM) or 'compensated ferrimagnetic half-metal' are used because the symmetry element that would make the sublattices equivalent is missing, hence they are not antiferromagnets. Such materials combine the best features of a ferromagnet and an antiferromagnet, offering immunity to external fields and demagnetising effects, while half-metallicity preserves high spin polarisation. ZMHMs look non-magnetic from the outside, yet ferromagnetic from the inside. Most interesting is the magnetic resonance, at a Larmor frequency $f_L = \mu_0 \gamma H_{\text{eff}}$. Two fundamental modes are the anisotropy-controlled ferromagnetic mode and the antiferromagnetic-like exchange mode. It should be possible to excite both by spin currents. The former depends on the anisotropy field, $H_{\text{eff}} \approx 2K/Ms$ and the resonance frequency becomes large as the magnetisation M_S goes to zero. For the latter, $H_{\text{eff}} \approx (2H_K H_{\text{ex}})^{1/2}$, where H_{ex} is the inter-sublattice exchange field ($\approx 10^8 - 10^9$ Am^{-1}). Respective frequencies are ≈ 500 GHz and ≈ 3 THz. [33]

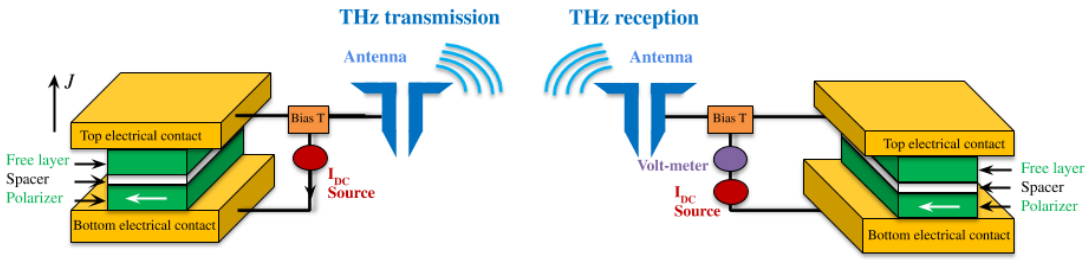

Figure 1.15: Chip-based heterodyne THz transceiver, based on zero-moment half-metal spin-torque oscillators.

Current 4G technology provides smartphones with rates of order 10 Mb/s. The next 5G and 6G technology aims be 1000 times faster, meaning that carrier frequencies have to be increased to avoid band saturation. The higher carrier frequencies imply reduced cell size. Data rates in computers are currently stuck at about 1 - 3 Gb/channel, and the

current fix is to use multiple channels (like multiple platters on a hard disk). Wireless communications in the 1 - 10 m range, and particularly in the very short range < 1 m leads us into the THz gap. Bandwidth is critical on the smallest scale, for example on and between chips and in the banks of servers in data centres. Wireless communications are critical between controllers of RAID (redundant array of independent disks) arrays, and more generally between the dense distributed networks of nodes in the internet of things (IoT), where it is envisioned that any node may have to be repurposed and may need to respond fast with a huge bandwidth. It has proved very difficult to integrate optics (for speed) with silicon electronics. Photonic integrated circuits are bulky [34]. This is precisely where spintronics can come to the rescue, with high-frequency auto oscillators based on the ferrimagnetic and exchange mode resonances of new materials, driven by spin transfer or spin-orbit torque. The terahertz oscillators can be integrated with silicon in a back-end process developed for MRAM, and can potentially exhibit wide tunability and band hopping capabilities. Figure 1.15 illustrates the short-range chip-to-chip concept.

1.4.2 Mn_2Ru_xGa: First Zero-Moment Half-Metal

Heusler alloys are a rich family of materials, with over a thousand compounds synthesised from over 40 elements. Figure 1.16 shows the cubic crystal structures of (a) half-Heusler (XYZ), (b) regular full-Heusler (X_2YZ) and (c) inverse full-Heusler (XY_2Z) compounds. X and Y are transition metals, where X is more electropositive than Y, and Z is a main group element. The diagram illustrates how addition of X or Y in the chemical formula of a half-Heusler leads to one of the two types of full-Heusler structures. Heusler alloys exhibit many properties relevant to spintronics including half-metallicity and ferrimagnetism. Therefore, this material class was a promising place to start in the search for zero moment half-metals.[35]

In the past two decades, a number of candidate ZMHM materials have been proposed on the basis of density functional theory electronic structure calculations, such as $C1_b$ CrMnSb, $L2_1$ Fe_2VGa or $D0_3$ Mn_3Ga [36; 37; 38]. They all either crystallised in the wrong structure with no spin gap e.g. Mn_3Ga [39], decomposed into a mixture of simpler phases e.g. CrMnSb, or turned out to have non-magnetic (or very weak itinerant ferromagnetic) sublattices e.g. Fe_2VGa [40]. It began to look as if there was some

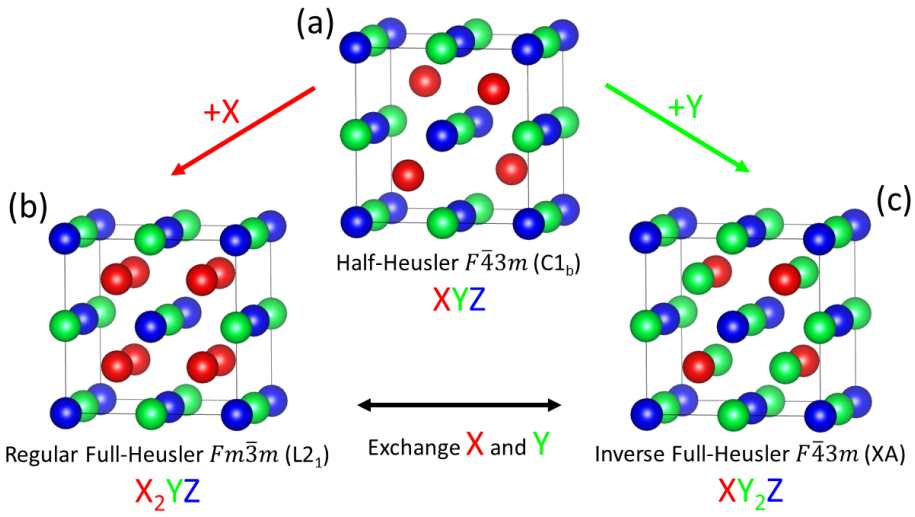

Figure 1.16: Three cubic crystal structures of Heusler compounds. (a) Half-Heusler (XYZ), (b) regular full-Heusler (X_2YZ) and (c) inverse full-Heusler (XY_2Z), where X and Y are transition metals and Z is a main group element.

fundamental reason why the ZMHM was so elusive [37]. In 2014 researchers at the magnetism and spintronics group at Trinity College Dublin succeeded in making thin films of a new material that showed evidence of the long-sought magnetic behaviour. [41] It belonged to the extensive, 1500-member, family of cubic Heusler alloys, which between them, exhibit almost every possible type of electronic ground state [42; 43] - insulating, topologically insulating, semiconducting, metallic, superconducting, ferromagnetic, ferrimagnetic, antiferromagnetic and half-metallic. The original X_2YZ Heusler compound, Cu_2MnSn, caused a mild sensation in 1903 because it was ferromagnetic, yet contained no ferromagnetic element (Mn is antiferromagnetic).

A characteristic of the ground state of a stoichiometric half metal, arising from the spin-gap in one of the sub-bands, is the integral number of unpaired electron spins. The number of minority spins per formula unit is an integer, because the $\downarrow$ bands are either full or empty. The total number of electrons is an integer, hence the number of $\uparrow$ electrons as well as the difference $\uparrow$ - $\downarrow$ are also integers. The latter is the spin moment m in Bohr magnetons per formula. Ignoring any orbital contribution, spin mixing due to spin-orbit coupling, and magnetic excitations at finite temperature, the expectation is that m will be an integer: 0, 1, 2, 3... μ_B/fu. The idea is nicely illustrated by Slater-

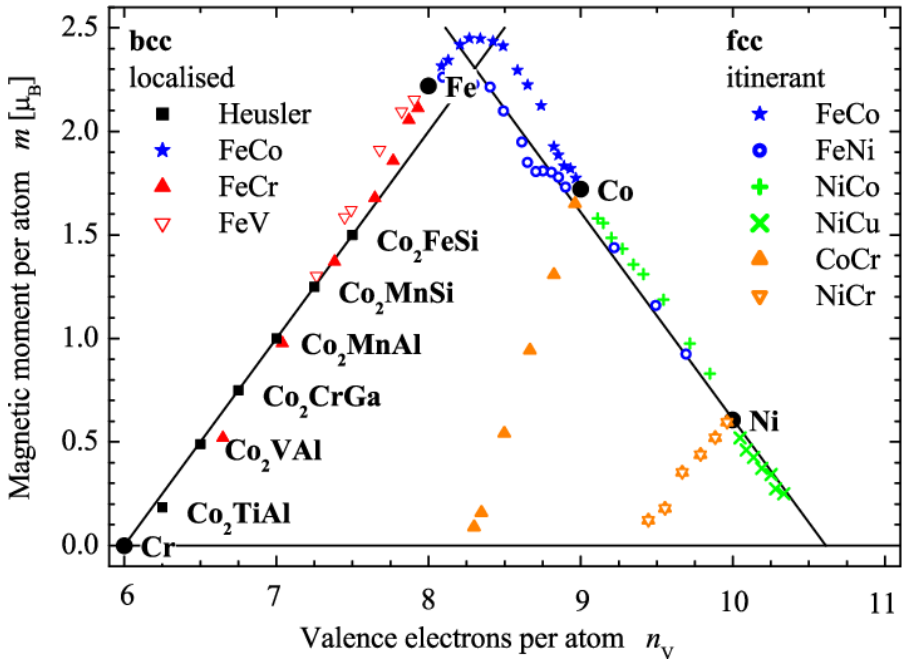

Figure 1.17: Slater-Pauling curve for 3*d* transition metals: the average magnetic moment per atom versus valence electron count for a series of Co_2YZ Heusler compounds. The rising branch has slope 1, as expected for half-metals. Taken from [44]

Pauling curve for the series of Co-based Heuslers [44] in Figure 1.17. The graph relates the average magnetic moment per atom to the number of valence electrons per atom (n_v). To calculate n_v, first the number valence electrons of each elemental species in the compound and sum over the sites in the primitive unit cell. The total is divided by the number of atoms (see example below). The Slater-Pauling rules for half-metallic full-Heusler and half-Heuser alloys are $m = 24 - z$ and $m = 18 - z$, respectively, where z is the number of valence electrons. There is evidence that Co_2MnSi and $Co_2FeAl_{0.5}Si_{0.5}$ are highly spin polarised [45], however, all attempts to synthesise a 24-electron cubic Heusler or an 18-electron half-Heusler with zero moment had proven unsuccessful.

Calculation of n_v for Co_2MnAl:

$$\begin{aligned} \text{Co} &= 9 \text{ valence electrons} \\ \text{Mn} &= 7 \text{ valence electrons} \\ \text{Al} &= 3 \text{ valence electrons} \\ \therefore z &= 9+9+7+3 = 28 \text{ valence electrons} \\ \therefore n_v &= \frac{z}{4} = \frac{28}{4} \\ n_v &= 7 \text{ valence electrons per atom} \end{aligned}$$

The first member of ZMHM material class was the Heusler alloy $Mn_2Ru_{0.5}Ga$, 21-valence electrons half-metallic compensated ferrimagnet in thin film form, which orders magnetically below $\approx$ 500 K. [41] Other members of ZMHM material class have been demonstrated in thin film [46] and in bulk [47]. The path to discovery of $Mn_2Ru_{0.5}Ga$ began with the preparation of thin films of the tetragonal $D0_{22}$ structure $Mn_{3-x}Ga$ alloys [48; 49]. The cubic Mn_3Ga could be stabilised on MgO substrates but turned out to have a small net moment - the Fermi level was not quite in the spin gap, but lay 0.4 eV higher. Cubic films of Mn_2Ru_xGa were then prepared, to push E_F into the spin gap with increasing x [41]. Mn_2Ru_xGa (MRG) crystallises in a cubic inverse full-Heusler structure (XA), space group $F\bar{4}3m$, with two crystallographically inequivalent magnetic Mn sites with 4a and 4c Wyckoff positions and each sublattice is non-centrosymmetric.

Highly textured MRG thin films are grown epitaxially on single crystal MgO (001) by DC magnetron sputtering. A small ($\approx$ 1 %) tetragonal distortion due to the bi-axial substrate strain induces perpendicular magnetic anisotropy of the net moment. [41] The in-plane lattice parameter (a) is constrained by the substrate while the out-of-plane parameter (c) varies with Ru content. A small net magnetic moment in MRG is due to the compensating effect of antiferromagnetically coupled inequivalent Mn magnetic sublattices. At compensation, the net moment vanishes and hence magnetically the material resembles an antiferromagnet, while half-metallicity preserves high spin polarisation of up to 60 % [41] in MRG as measured by PCAR. This leads to immunity to externally applied fields and absence of demagnetising fields. As the net moment tends to zero, anisotropy field becomes large, therefore high frequency

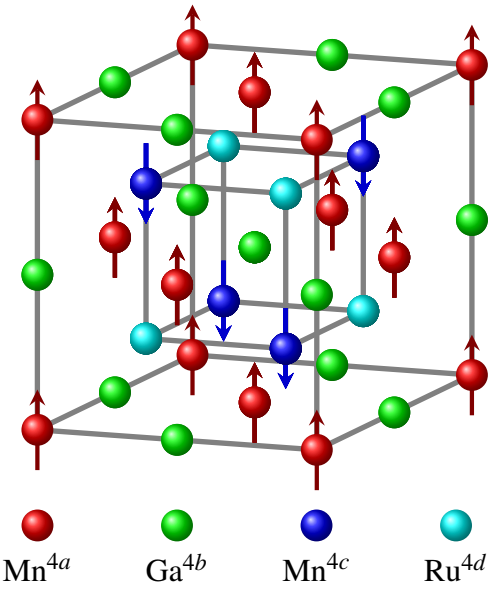

Figure 1.18: Crystal structure of cubic full inverse-Heusler Mn_2RuGa.

spin dynamics and low Gilbert damping can be achieved. For MRG, maximum zero-applied-field resonance frequency $\approx$ 160 GHz and Gilbert damping $\alpha \approx 0.02$ have so far been demonstrated. [50; 51]

MRG also offers efficiency and ease of detection and manipulation of the magnetic state. Remarkably efficient generation of spin-orbit fields $\mu_0 H_{\text{eff}}$ was measured in single-layers of MRG, where $\mu_0 H_{\text{eff}}$ approaches 0.1×10^{-10} Tm^2/A in the low-current density limit. This is almost a thousand times the Oersted field and one to two orders of magnitude greater than $\mu_0 H_{\text{eff}}$ in heavy metal/ferromagnet bilayers [52]. Transport in MRG is dominated by the Mn^{4c} sublattice which has a non-vanishing moment at compensation. This allows for observation of magnetic domains in MRG close to compensation by MOKE [53]. Most recent results demonstrate thermal single-pulse toggle switching in MRG, making it the first non-Gd based material to exhibit this effect [54; 55].

1.5 My PhD Project

The overreaching research objective is to develop new spintronic materials that will advance communication rates from GHz to THz, and demonstrate the functionality required for generating terahertz radiation electrically in ambient conditions.

My PhD project aims to contribute to fulfilling the research objectives related to the demonstration of ZMHM based spin-torque oscillators, as outlined in the section above. The research is based on a new class of materials, the zero-moment half metals (ZMHMs), and specific objectives include:

- To achieve high Curie temperature ($T_C > 500$ K), Fermi-level spin polarisation (> 50 % at room temperature) and low Gilbert damping ($\alpha \leq 0.01$) in MRG compensated ferrimagnetic alloys.
- Investigate ways to control Mn diffusion in MRG-based heterostructures.
- Gain a deeper understanding of the physics at play in MRG and characterise the films by previously unexplored techniques.

Firstly, the effect of magnetic annealing of blanket MRG thin films as well as MRG-based spin-valve heterostructures will be discussed in Chapter 3. In the magnetic annealing study of thin films it was found that heat treatment of 1 hour in $\leq 350\,^{\circ}$C does not influence the properties of the thin films. However significant diffusion and loss of anisotropy is observed by annealing at 400 °C.[56] For heterostructures, a variety of spacers have been selected to investigate their performance as a diffusion barrier while maintaining MRG properties. The study showed Hf and Mo are most effective spacers.

In order to optimise MRG thin films for a variety of applications, thin films with varying Mn and Ru composition were prepared and thoroughly investigated. Variation of Mn content in Mn_2Ru_xGa thin films influences chemical disorder and crystal structure, which strongly impact material properties. It was found in Chapter 4, that Mn variation manipulates the population of the Mn^{4c} sublattice. Molecular mean field theory model was used to fit thermal out-of-plane net moment of MRG thin films

to extract Weiss coefficients and calculate Heisenberg exchange energies. Comparison of anomalous Hall effect and SQUID magnetometry loops suggests canting of the net moment relative to the anisotropy axis in zero field. The origin of the canting is hypothesised to be due to non-collinearity of the Mn^{4c} sublattice moments, via a competing exchange mechanism between negative nearest and positive next-nearest intra-sublattice interactions.

Magneto-transport is dominated by the *s*-like electronic states of the Mn^{4c} sublattice, the Kerr rotation in magneto-optic Kerr effect is proportional to M_z^{4c}, hence it is possible to observe magnetic domains of MRG thin films in the compensated and near compensated state. Chapter 5 includes the first report of the magnetic domain structure of a ZMHM and the investigation of magnetic reversal and pinning.[53] The magnetic reversal was found to be domain wall motion or nucleation dominated, depending on film deposition conditions.

In Chapter 6, an extensive X-ray magnetic circular dichroism study performed on thin films is presented. Site specific moment was measured at a variety of temperatures and applied field. For a sample with compensation at 145 K, spin-flop transition was observed. Angular scans allowed to construct projections of magnetic moments onto the m_x - m_z plane. Using the simple uniaxial anisotropy model, anisotropy constants for each Mn sublattice were determined.

Finally, the dissertation will end with the main conclusions arising from my research and and outlook for future work in Chapter 7.

References

[1] B. Savoie, "A rigorous proof of the Bohr–van Leeuwen theorem in the semi-classical limit," *Rev. Math. Phys.*, vol. 27, no. 08, p. 1550019, 2015. (Cited on page: 1)

[2] J. Coey, *Magnetism and Magnetic Materials*. Cambridge University Press, New York, 2010. (Cited on page: 1, 3, 6, 10, 13, 15, 18, 21)

[3] D. J. Griffiths, *Quantum mechanics*. Pearson, Cambridge University Press, 1995. (Cited on page: 6)

[4] J. Needham, *Science & Civilisation in China*, vol. IV:1. Cambridge: Cambridge University Press, 2008. (Cited on page: 10)

[5] J. Makeham, *China: The World's Oldest Living Civilization Revealed*. London: Thames & Hudson, 2008. (Cited on page: 10)

[6] A. Kloss, *Geschichte des Magnetismus*. Germany: VDE-Verlag, 2004. (Cited on page: 10)

[7] J. M. D. Coey, "Hard magnetic materials: A perspective," *IEEE Trans. Magn.*, vol. 47, no. 12, pp. 4671–4681, 2011. (Cited on page: 10, 11)

[8] W. H. Meiklejohn and C. P. Bean, "New magnetic anisotropy," *Phys. Rev.*, vol. 102, pp. 1413–1414, Jun 1956. (Cited on page: 12)

[9] W. H. Meiklejohn, "Exchange Anisotropy - A Review," *J. Appl. Phys.*, vol. 33, no. 3, pp. 1328–1335, 1962. (Cited on page: 12)

[10] J. Nogués and I. K. Schuller, "Exchange bias," *J. Magn. Magn. Mater.*, vol. 192, no. 2, pp. 203 – 232, 1999. (Cited on page: 12)

[11] D. Wei, *Micromagnetics and Recording Materials*. Springer Briefs in Applied Sciences and Technology, Springer Berlin Heidelberg, 2012. (Cited on page: 14)

[12] R. Carey and E. Isaac, *Magnetic domains and techniques for their observation*. London: The English University Press Ltd., 1966. (Cited on page: 14)

[13] S. A. Wolf, D. D. Awschalom, R. A. Buhrman, J. M. Daughton, S. von Molnár, M. L. Roukes, A. Y. Chtchelkanova, and D. M. Treger, "Spintronics: A spin-based electronics vision for the future," *Science*, vol. 294, no. 5546, pp. 1488–1495, 2001. (Cited on page: 20)

[14] I. Žutić, J. Fabian, and S. Das Sarma, "Spintronics: Fundamentals and applications," *Rev. Mod. Phys.*, vol. 76, pp. 323–410, Apr 2004. (Cited on page: 20)

[15] C. Chappert, A. Fert, and F. Van Dau, "The emergence of spin electronics in data storage," *Nat. Mat.*, vol. 6, pp. 813 – 823, 2007. (Cited on page: 20)

[16] A. Hirohata, K. Yamada, Y. Nakatani, I.-L. Prejbeanu, B. Diény, P. Pirro, and B. Hillebrands, "Review on spintronics: Principles and device applications," *J. Magn. Magn. Mater.*, vol. 509, p. 166711, 2020. (Cited on page: 24)

[17] W. Thomson, "On the electro-dynamic qualities of metals:—Effects of magnetization on the electric conductivity of nickel and of iron," *R. Soc. Lond.*, vol. 8, pp. 546 – 550, 1856. (Cited on page: 24)

[18] T. McGuire and R. Potter, "Anisotropic magnetoresistance in ferromagnetic 3d alloys," *IEEE Trans. Mag.*, vol. 11, pp. 1018 – 1038, 1975. (Cited on page: 25)

[19] M. N. Baibich, J. M. Broto, A. Fert, F. N. Van Dau, F. Petroff, P. Etienne, G. Creuzet, A. Friederich, and J. Chazelas, "Giant magnetoresistance of (001)fe/(001)cr magnetic superlattices," *Phys. Rev. Lett.*, vol. 61, pp. 2472–2475, Nov 1988. (Cited on page: 25)

[20] G. Binasch, P. Grünberg, F. Saurenbach, and W. Zinn, "Enhanced magnetoresistance in layered magnetic structures with antiferromagnetic interlayer exchange," *Phys. Rev. B*, vol. 39, pp. 4828–4830, Mar 1989. (Cited on page: 25)

[21] R. E. Camley and J. Barnaś, "Theory of giant magnetoresistance effects in magnetic layered structures with antiferromagnetic coupling," *Phys. Rev. Lett.*, vol. 63, pp. 664–667, Aug 1989. (Cited on page: 26)

[22] J. Barnaś, A. Fuss, R. E. Camley, P. Grünberg, and W. Zinn, "Novel magnetoresistance effect in layered magnetic structures: Theory and experiment," *Phys. Rev. B*, vol. 42, pp. 8110–8120, Nov 1990. (Cited on page: 26)

[23] M. Julliere, "Tunneling between ferromagnetic films," *Phys. Lett. A*, vol. 54, no. 3, pp. 225 – 226, 1975. (Cited on page: 27)

[24] T. Miyazaki and N. Tezuka, "Giant magnetic tunneling effect in Fe/Al_2O_3/Fe junction," *J. Magn. Magn. Mater.*, vol. 139, no. 3, pp. L231 – L234, 1995. (Cited on page: 28)

[25] S. Ikeda, J. Hayakawa, Y. Ashizawa, Y. M. Lee, K. Miura, H. Hasegawa, M. Tsunoda, F. Matsukura, and H. Ohno, "Tunnel magnetoresistance of 604 % at 300 K by suppression of Ta diffusion in CoFeB/MgO/CoFeB pseudo-spin-valves annealed at high temperature," *App. Phys. Lett.*, vol. 93, no. 8, p. 082508, 2008. (Cited on page: 28)

[26] E. H. Hall, "On a New Action of the Magnet on Electric Currents," *Am. J. Math.*, vol. 2, no. 3, pp. 287–292, 1879. (Cited on page: 28)

[27] E. H. Hall, "On the new action of magnetism on a permanent electric current," *Am. J. Sci.*, vol. 20, pp. 161–186, 1880. (Cited on page: 28)

[28] N. Nagaosa, J. Sinova, S. Onoda, A. H. MacDonald, and N. P. Ong, "Anomalous Hall effect," *Rev. Mod. Phys.*, vol. 82, no. 2, pp. 1539–1592, 2010. (Cited on page: xxxi, 29, 30, 31)

[29] K. Borisov, D. Betto, Y. C. Lau, C. Fowley, A. Titova, N. Thiyagarajah, G. Atcheson, J. Lindner, A. M. Deac, J. M. D. Coey, P. Stamenov, and K. Rode, "Tunnelling magnetoresistance of the half-metallic compensated ferrimagnet mn2ruxga," *Appl. Phys. Lett.*, vol. 108, no. 19, p. 192407, 2016. (Cited on page: 32)

[30] H. van Leuken and R. de Groot, "Half-metallic antiferromagnets," *Phys. Rev. Lett.*, vol. 74, no. 7, pp. 1171–1173, 1995. (Cited on page: 33)

[31] R. A. de Groot, F. M. Mueller, P. G. v. Engen, and K. H. J. Buschow, "New class of materials: Half-metallic ferromagnets," *Phys. Rev. Lett.*, vol. 50, pp. 2024–2027, Jun 1983. (Cited on page: 33)

[32] M. I. Katsnelson, V. Y. Irkhin, L. Chioncel, A. I. Lichtenstein, and R. A. de Groot, "Half-metallic ferromagnets: From band structure to many-body effects," *RMP*, vol. 80, no. 2, pp. 315–378, 2008. (Cited on page: 33)

[33] D. Betto and *et al.*, "The zero-moment half metal: How could it change spin electronics?," *AIP Adv.*, vol. 6, no. 5, p. 055601, 2016. (Cited on page: 33)

[34] W. Liu, M. Li, R. Guzzon, E. J. Norberg, J. S. Parker, M. Lu, L. A. Coldren, and J. Yao, "A fully reconfigurable photonic integrated signal processor," *Nat. Photonics*, vol. 10, p. 190–195, Mar 2016. (Cited on page: 34)

[35] K. Manna, Y. Sun, L. Muechler, J. Kübler, and C. Felser, "Heusler, Weyl and Berry," *Nat. Rev. Mater.*, vol. 3, no. 244-256, 2018. (Cited on page: 34)

[36] S. Wurmehl and *et al.*, "Valence electron rules for prediction of half-metallic compensated-ferrimagnetic behaviour of heusler compounds with complete spin polarization," *J. Phys. Cond. Mat.*, vol. 18, no. 27, p. 6171, 2006. (Cited on page: 34)

[37] X. Hu, "Half-metallic antiferromagnet as a prospective material for spintronics," *Adv. Mater.*, vol. 24, no. 2, pp. 294–298, 2012. (Cited on page: 34, 35)

[38] I. Galanakis, P. Mavropoulos, and P. Dederichs, "Electronic structure and slater–pauling behaviour in half-metallic heusler alloys calculated from first principles," *J. Phys. D Appl. Phys.*, vol. 39, no. 5, p. 765, 2006. (Cited on page: 34)

[39] P. Kharel and *et al.*, "Structural and magnetic transitions in cubic Mn_3Ga," *Journal of Physics: Condensed Matter*, vol. 26, no. 12, p. 126001, 2014. (Cited on page: 34)

[40] M. Hakimi and *et al.*, "The zero-magnetization heusler ferrimagnet," *J. Appl. Phys*, vol. 113, no. 17, p. 17B101, 2013. (Cited on page: 34)

[41] H. Kurt, K. Rode, P. Stamenov, M. Venkatesan, Y. C. Lau, E. Fonda, and J. M. D. Coey, "Cubic Mn_2Ga thin films: Crossing the spin gap with ruthenium," *Phys. Rev. Lett.*, vol. 112, no. 2, p. 027201, 2014. (Cited on page: 35, 37)

[42] T. Graf, C. Felser, and S. Parkin, "Simple rules for the understanding of heusler compounds," *Prog. Solid State Chem.*, vol. 39, p. 50, 2011. (Cited on page: 35)

[43] C. Felser and A. Hirohata, *Heusler Alloys*, vol. 222. Springer International Publishing, 1 ed., 2016. (Cited on page: 35)

[44] B. Balke, S. Wurmehl, G. H. Fecher, C. Felser, and J. Kübler, "Rational design of new materials for spintronics: Co_2FeZ (Z=Al, Ga, Si, Ge)," *Sci. Technol. Adv. Mat.*, vol. 9, no. 1, p. 014102, 2008. PMID: 27877928. (Cited on page: xviii, 36)

[45] S. Mitani, *Magnetic Tunnel Junctions Using Heusler Alloys*, vol. 222, ch. 17, pp. 401–412. Springer International Publishing, 1 ed., 2016. (Cited on page: 36)

[46] M. E. Jamer, Y. J. Wang, G. M. Stephen, I. J. McDonald, A. J. Grutter, G. E. Sterbinsky, D. A. Arena, J. A. Borchers, B. J. Kirby, L. H. Lewis, B. Barbiellini, A. Bansil, and D. Heiman, "Compensated ferrimagnetism in the zero-moment heusler alloy Mn_3Al," *Phys. Rev. Appl.*, vol. 7, no. 6, 2017. (Cited on page: 37)

[47] R. Stinshoff, G. H. Fecher, S. Chadov, A. K. Nayak, B. Balke, S. Ouardi, T. Nakamura, and C. Felser, "Half-metallic compensated ferrimagnetism with a tunable compensation point over a wide temperature range in the Mn-Fe-V-Al Heusler system," *AIP Adv,*, vol. 7, no. 10, p. 105009, 2017. (Cited on page: 37)

[48] H. Kurt, K. Rode, M. Venkatesan, P. Stamenov, and J. M. Coey, "Mn3-xga ($0<x<1$): Multifunctional thin film materials for spintronics and magnetic recording," ... *status solidi (b)*, vol. 2344, pp. 2338–2344, 2011. (Cited on page: 37)

[49] K. Rode, N. Baadji, D. Betto, Y.-C. Lau, H. Kurt, M. Venkatesan, P. Stamenov, S. Sanvito, J. M. D. Coey, E. Fonda, E. Otero, F. Choueikani, P. Ohresser, F. Porcher, and G. André, "Site-specific order and magnetism in tetragonal Mn_3Ga thin films," *Phys. Rev. B*, vol. 87, no. 18, p. 184429, 2013. (Cited on page: 37)

[50] D. Betto, K. Rode, N. Thiyagarajah, Y.-C. Lau, K. Borisov, G. Atcheson, M. Žic, T. Archer, P. Stamenov, and J. M. D. Coey, "The zero-moment half metal: How could it change spin electronics?," *AIP Adv.*, vol. 6, no. 5, p. 055601, 2016. (Cited on page: 38)

[51] G. Bonfiglio, K. Rode, K. Siewerska, J. Besbas, G. Y. P. Atcheson, P. Stamenov, J. M. D. Coey, A. V. Kimel, T. Rasing, and A. Kirilyuk, "Magnetization dynamics of the compensated ferrimagnet Mn_2Ru_xGa," *Phys. Rev. B*, vol. 100, p. 104438, Sep 2019. (Cited on page: 38)

[52] S. Lenne, Y.-C. Lau, A. Jha, G. Y. P. Atcheson, R. E. Troncoso, A. Brataas, J. M. D. Coey, P. Stamenov, and K. Rode, "Giant spin-orbit torque in a single ferrimagnetic metal layer," 2019. (Cited on page: 38)

[53] K. E. Siewierska, N. Teichert, R. Schäfer, and J. M. D. Coey, "Imaging domains in a zero-moment half metal," *IEEE Trans. Mag.*, vol. 55, no. 2, pp. 1–4, 2019. (Cited on page: 38, 40)

[54] C. Banerjee, N. Teichert, K. Siewierska, Z. Gercsi, G. Atcheson, P. Stamenov, K. Rode, J. M. D. Coey, and J. Besbas, "Single pulse all-optical toggle switching of magnetization without gadolinium in the ferrimagnet Mn_2Ru_xGa," *Nat. Commun.*, vol. 11, p. 4444, 2020. (Cited on page: 38)

[55] C. S. Davies, G. Bonfiglio, K. Rode, J. Besbas, C. Banerjee, P. Stamenov, J. M. D. Coey, A. V. Kimel, and A. Kirilyuk, "Exchange-driven all-optical magnetic switching in compensated 3*d* ferrimagnets," *Phys. Rev. Res.*, vol. 2, p. 032044, Aug 2020. (Cited on page: 38)

[56] K. E. Siewierska, G. Atcheson, K. Borisov, M. Venkatesan, K. Rode, and J. M. D. Coey, "Study of the Effect of Annealing on the Properties of Mn_2Ru_xGa Thin Films," *IEEE Trans. Magn.*, vol. 53, no. 11, pp. 1–5, 2017. (Cited on page: 39)

2
Experimental Methods

2.1 Magnetron Sputtering Thin Film Deposition

Magnetron sputtering is a plasma vapour deposition process used for fast and highly scalable growth of thin films from various materials. The earliest sputtering and ion etching experiments were described by W.R. Grove in 1852 [1; 2] and the investigation into using magnetic fields for controlling a DC glow discharge plasma was presented by Albert Hull in 1921 [3; 4]. The first use of magnetron, with a cylindrical geometry, was reported in mid 1936 by Frans Penning [5] and he was granted a US patent for his device in 1939 [6].

Sputtering requires a plasma in a vacuum and a negative electronic bias on the target material to attract heavy positive ions. The ions bombard the target material, allowing the surface atoms to gain sufficient momentum and be removed from the surface. The plasma is confined by an array of magnets behind the target. For non-reactive sputtering, inert gases such as argon can be used to generate the plasma. For reactive sputtering, usually a mixture of an inert gas and a reactive gas such as nitrogen or oxygen are used. The two main types are direct current (DC) and radio frequency (RF) magnetron sputtering. [7]

2.1.1 Direct Current Magnetron Sputtering

DC Magnetron sputtering is a technique used for epitaxial growth of thin films from conductive materials. The basic mechanism of DC magnetron sputtering is shown in Figure 2.1. In the magnetron sputtering tool, a static electric field is applied between the target (cathode) and the substrate (anode). A gas is released into the chamber, e.g. argon, at a high pressure to ignite and sustain a plasma over the target. Once the plasma is stable, the gas pressure can be decreased. The positively charged ions in the plasma are accelerated in the static electric field towards the negatively charged target. The ions bombard the target with sufficient force to cause the ejection of atoms from the surface of the target. Atoms travel away from the surface of the target and condense on a rotating substrate located above the target in close proximity. The plate rotates to ensure uniformity of the thin film. The deposition process occurs at a relatively high pressure and the mean free path of the sputtered atoms is much shorter than the target-substrate distance, hence this technique is not very directional, which means that films can be deposited over relatively larger areas. Underneath the target, permanent

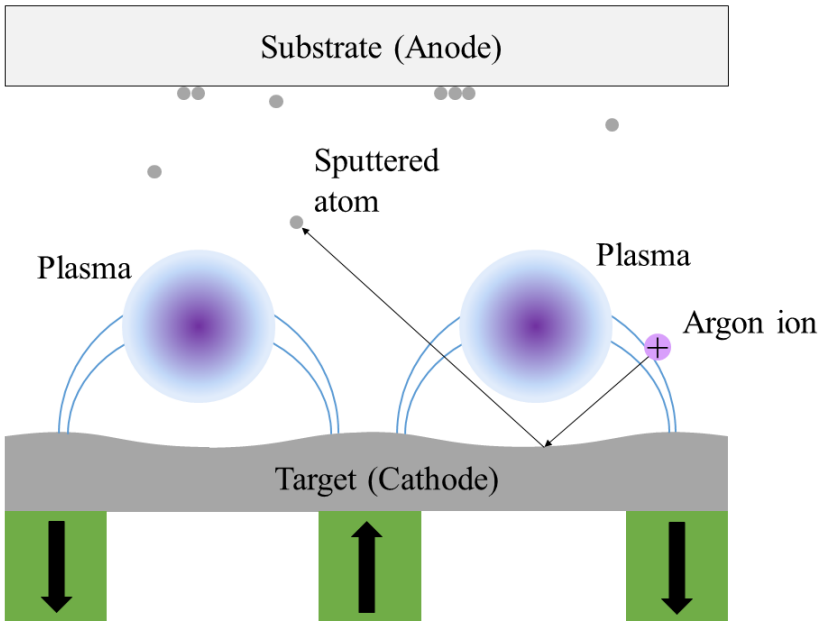

Figure 2.1: Illustration of the basic mechanism of DC magnetron sputtering.

magnets are placed to create a magnetic field above it. The magnetic field traps elec-

trons that participate in the sputtering process and inhibits substrate bombardment by the electrons which may cause overheating and damage to the film. The magnetic flux causes the electrons to move around a circular path on top of the target enhancing ionisation rate and sustain the plasma at lower pressures. However, leads to the formation of a 'race track' on the target and uneven material consumption. Magnetic targets are usually thinner than non-magnetic ones to maximise the stray field. DC sputtering is limited to depositing metals, because dielectrics are non-conducting and charge builds up on the target. This can result in arcing of the plasma and an unstable deposition process. To avoid this problem, radio frequency sputtering is used.

2.1.2 Radio Frequency Magnetron Sputtering

Radio Frequency (RF) magnetron sputtering involves replacing the DC power supply with an RF power supply (50 Ω) and an impedance matching network. No net current flows in the target hence a non-conducting target can be sputtered. An alternating electrical potential runs through a Noble gas, e.g. argon, in a vacuum chamber at the radio frequency of 13.56 MHz. Electrons are much lighter than the Ar ions and can easily oscillate with the applied RF source. In the positive cycle as shown in Figure 2.2, the electrons are attracted towards the target hence inducing a negative bias. The magnets behind the target trap the electrons so they are not free to bombard it. In the negative portion of the cycle, the Ar ions bombard the target and material is sputtered off. Charge build-up is prevented because of the alternating of the electrical power, which cleans the surface after each cycle reducing arcing of the plasma. RF magnetron sputtering can be employed for both metallic and dielectric targets. Thin films produced by the RF technique are generally smoother and more dense, because the plasma can be sustained at relatively lower pressures. Using an RF source instead of a DC source also means that deposition rates are much slower and higher voltages are required for sputtering. The width and depth of the race track is reduced, because the electrons are less confined by the magnetic field and the plasma is more spread out over the target. This provides a more efficient utilisation of the target material.

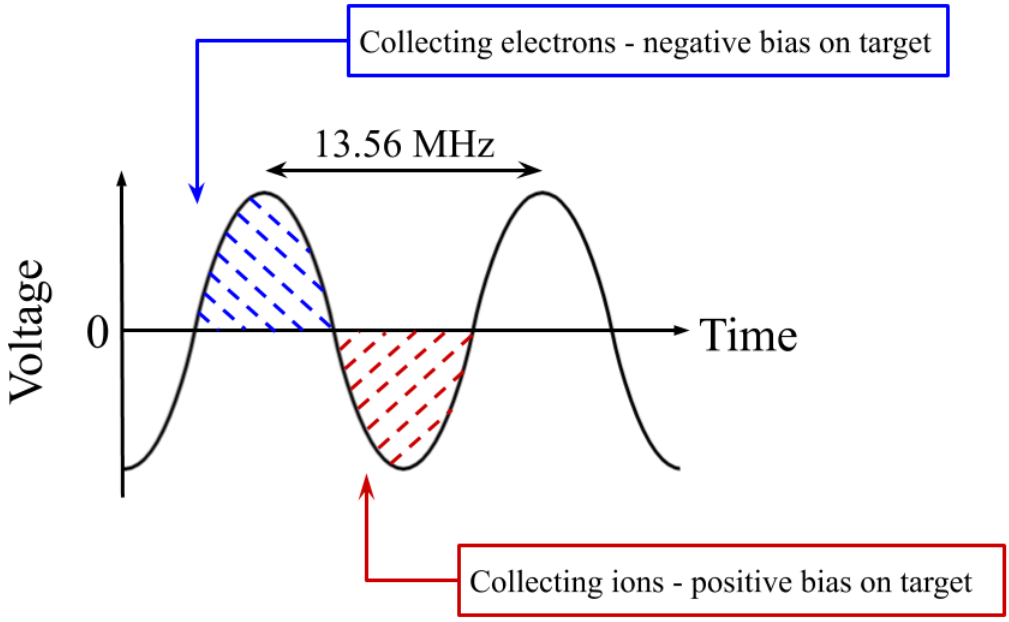

Figure 2.2: Illustration of the cycle in RF magnetron sputtering.

2.1.3 Sputter Yields and Rates

The sputter yield is the statistical average for the number of atoms ejected from the surface of a cathode target per incident sputter ion. It depends on the atomic masses of both target and sputtering ion species, the kinetic energy of the ion and the surface bonding energy of the target. For each element or a compound the sputter yield is constant in a given energy field. Once the energy of the sputtering ions is higher than the surface bonding energy of the target, it is possible to dislodge atoms from the target surface. The sputtering of single element targets means all atoms have the same binding energy, but for alloy targets the binding energy varies for different atomic species. The question arises: When sputtering from an alloy target, is the chemical composition of the thin film the same as that of the target?

Based on sputter yield calculations, atoms with weaker bonding energies are sputtered faster than those with stronger bonding. This depletes the number of weakly bonded atoms at the surface of the target available for sputtering. After a short time, the surface portion of the target reaches an equilibrium chemical composition which is in direct proportion to the reciprocal of the sputter yields of each element. As a re-

sult, the proportion of each atomic species available for sputtering enables the resultant film composition to be exactly the same as that of the original homogeneous chemical composition of the target. This highlights the importance of running a pre-sputtering process before the actual deposition process. The sputter rate of a material is the thickness deposited per unit time. For a fixed target to substrate distance, the rate depends on the gas pressure and target power. For depositions that involve co-sputtering from multiple targets, the gas pressure is fixed and target power is varied to achieve films of a desired chemical composition and thickness.

2.1.4 Shamrock Sputtering System

The original Shamrock sputtering system consists of the cassette module (CM), transfer module and the process module known as chamber A developed by Sputtered Films, Inc. designed for the growth of high quality metal thin films. Chamber B (Plassys MP900) was connected to the TM via one of the available ports. A schematic diagram of the arrangement of the chambers and what they contain is shown in Figure 2.3. The sputtering system is located in a class 10000 clean room. Most of the samples I have worked on during the course of my PhD were deposited in the Shamrock.

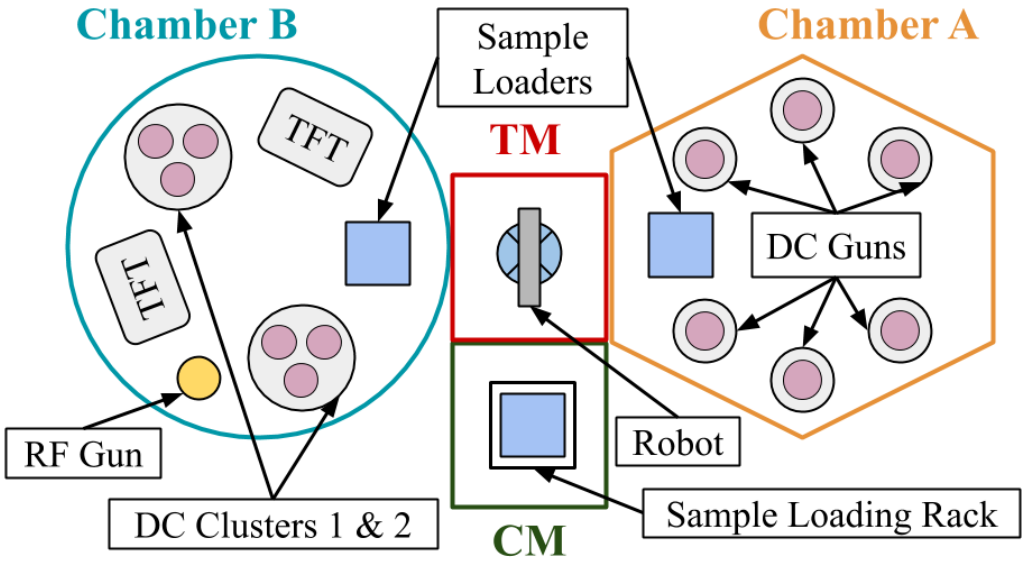

Figure 2.3: Diagram of Chambers A and B, Transfer module (TM) and Cassette module (CM) in the Shamrock magnetron sputtering system.

The Shamrock Sputtering System:

- **Cassette Module (CM):** High vacuum load lock with a sample loading rack that can hold 16 wafers up to 6 inches in diameter.
- **Transfer Module (TM):** High vacuum chamber containing the semi-automatic Genmark GB3 vacuum robot system. The robotic arm allows for transfer of wafers from CM to Chambers A and B.
- **Chamber A:** Planetary style batch tool with a hexagonal vacuum chamber maintained at a base pressure of 3×10^{-7} Torr with 6 DC magnetron sputter guns. The system is equipped with a turntable fitted with four planets, hence simultaneous deposition on four wafers at ambient temperature is possible. Each planet has an array of permanent magnets to produce a uniform magnetic field (10 mT) to bias films in-plane, which defines the easy-axis in materials with in-plane anisotropy. Reactive sputtering in O_2 is available and typical pressure during the deposition is 2 mTorr. The main advantage of the system is loading and unloading of wafers is fully automated and various recipes for depositions of multilayered stacks can be programmed and run in sequence mode.
- **Chamber B:** Large vacuum chamber developed by Plassys, with a base pressure of 1×10^{-8} Torr contains two clusters with 3 DC sputter guns each, 2 target-facing-target (TFT) RF sputter guns, and one normal incidence RF sputter gun. The sputter rate is typically varied with the target current for a particular Ar flow rate, which is usually set to the lowest flow rate which maintains plasma stability on the target. The system is semi-automated and requires a user to load and unload a wafer into the chamber in between depositions. Home-made oxygen compatible heater is fitted over the planet which holds the wafer allowing for a temperature range of 20 °C to 500 °C during depositions.

2.1.5 Trifolium Dubium Deposition & Characterisation System

Trifolium Dubium (TD) is a new €3.2 million is a state of the art tool for the deposition and characterisation of thin films located in CRANN in a class 10000 clean room. The system was funded by SFI, available for use from January 2019 and is a National

Access Facility. Figure 2.4 depicts the various chambers of the TD assembly: two magnetron sputtering chambers, a pulsed laser deposition (PLD) chamber and molecular beam epitaxy (MBE) chamber, all developed by DCA Instruments (Finland) as well as an X-ray photoelectron spectrometer (XPS) from SPECS (Germany). In my PhD I have produced some films in TD by magnetron sputtering, but did not use other deposition techniques, so the detailed description of the tool is focused on the sputter chambers.

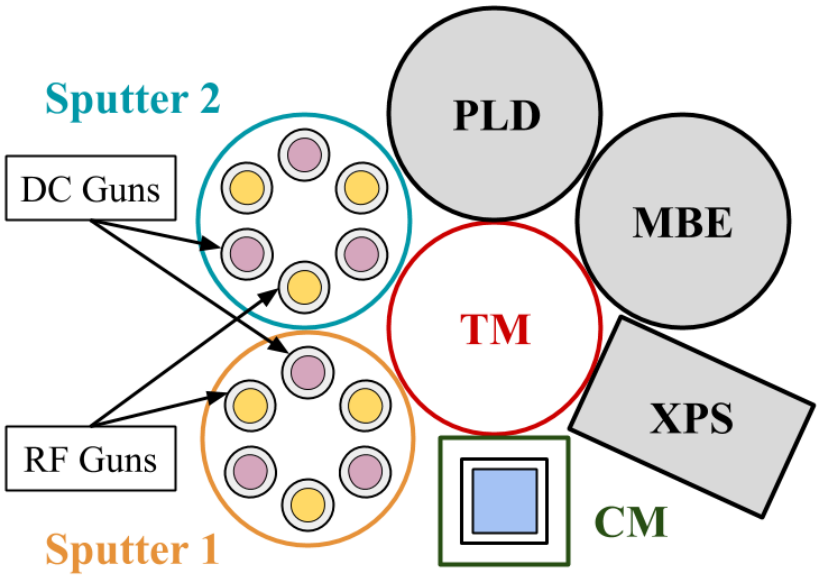

Figure 2.4: Diagram of Sputter 1 and 2, PLD, MBE, XPS, Transfer Module (TM), and Cassette Module (CM) in the Trifolium Dubium (TD) deposition & characterisation system.

Trifolium Dubium Sputtering System:

- **Cassette Module (CM):** High vacuum load lock with a sample loading rack that can hold 10 wafers up to 4 inches in diameter. Wafers are backed out at 500 °C for an hour before being transferred out of the CM.
- **Transfer Module (TM):** UHV central hub containing a fully automated robotic unit for transferring wafers between the CM and all other chambers.
- **Sputter (SP) 1 & 2:** Two UHV (base pressure $< 1 \times 10^{-9}$) sputtering chambers with 6 magnetrons each arranged confocally with adjustable tilt angle. There are

3 RF and 3 DC guns which can be switched between the magnetrons and co-sputtering from up to 3 magnetrons is possible. Sample holders of various sizes made from metals with high melting points are available and process temperature range is 15 °C - 1000 °C. SP 1 is primarily used for sputtering metals, where SP 2 is used for both metal and dielectric material sputtering. Gas pressure can be controlled in either the upstream or downstream regulation. Downstream regulation is based on maintaining a constant Ar flow rate and the pressure is controlled by a opening/closing of a throttle valve. In the upstream regulation, the pressure is controlled by varying the Ar gas flow through a valve. Ar flow and gas pressure are critical factors influencing the quality of thin films and with both pressure control modes available, deposition processes can be further optimised. The typical pressure during the deposition is between $1-5$ mTorr. Additional features include target-facing-target (TFT) sputtering for high quality dielectric thin films, reactive sputtering (in O_2 or N_2 gas), wedge deposition for thickness variation across a single sample, substrate biasing, high temperature oxygen-compatible heaters, natural and plasma oxidation/nitridation of metal layers, with quartz crystal monitoring (QCM) of deposition rates.

2.2 Crystallography

Crystallography is the study of crystal structure, grain size and defects in materials which determine their properties. Crystallographic methods involve the analysis of diffraction patterns of samples irradiated with different types of beam sources. There are three diffraction sources in crystallography which are X-rays, electrons and neutrons since their wavelengths are about 1-2 Å which is comparable to d-spacing of crystals. More details about the three diffraction sources are summarised in Table 2.1. In crystallography lattice planes in a crystal are represented by 3 integers h, k, and l called the Miller indices. Coordinates in square brackets such as $[hkl]$ denote a direction vector given by the sum $h\mathbf{a}_1 + k\mathbf{a}_2 + l\mathbf{a}_3$ where a_i for $i = 1,2,3$ are basis vectors in real space ($\mathbb{R}$). Coordinates in angle brackets such as $< hkl >$ denote a family of directions which are related by symmetry operations. A plane of a crystal lattice with regular repetitions for a particular spacing is denoted by the indices in parentheses (hkl). A family of lattice planes are given by the indices in curly brackets $\{hkl\}$. It is

Type	Mechanism	Energy	Cost & Availability
X-ray Diffraction	X-rays interact with spatial distribution of the valence electrons of atoms	$\approx 10^4$ eV	X-ray diffractometers are relatively cheap. It is convenient and very commonly used.
Electron Diffraction	Electrons are negatively charged and interact via the Coulomb force. Inside the material they interact with both negative charged electrons and positively charged nuclei of atoms	≈ 40 eV	Transmission electron microscopes are more expensive, special sample preparation is needed and not as common as XRD.
Neutron Diffraction	Neutrons have no charge but have spin. They are scattered by both atomic nuclei held together via the strong nuclear force and by magnetic fields	≈ 0.08 eV	Neutron beam sources are limited, they are considered to be very special tools and are very expensive.

Table 2.1: Summary of diffraction techniques with X-ray, electron and neutron beams as a source.

often convenient to perform a Fourier transform on the lattice in $\mathbb{R}$ into its reciprocal space $\mathbb{R}^*$, also known as k-space or momentum space. Each set of (hkl) lattice planes in $\mathbb{R}$ is represented by a point (hkl) in $\mathbb{R}^*$. The concept of reciprocal space is fundamental to the theory of diffraction. The next section will be focused on the theory of X-ray diffraction.

2.2.1 X-ray Diffraction Theory

X-ray diffraction (XRD) is a commonly used technique to study the crystal structure of the materials prepared as thin films or powders. The basic mechanism of XRD, briefly described in Table 2.1, is the elastic scattering of unpolarised X-ray radiation by the valence electrons known as Thomson scattering. The scattering is elastic meaning the magnitude of the diffraction vector in $\mathbb{R}^*$ is conserved. The Thomson scattering cross

section σ_T in SI units is given by

$$\sigma_T = \frac{8\pi}{3}\left(\frac{q^2}{4\pi\varepsilon_0 mc^2}\right)^2 = \frac{8\pi}{3}\left(\frac{\alpha\lambda_C}{2\pi}\right)^2 = \frac{8\pi}{3}\left(\frac{\alpha\hbar}{mc}\right)^2 \tag{2.1}$$

where q is the charge on the particle, ε_0 is the permittivity of free space, m is the mass of the particle, c is the speed of light in free space, α is the fine structure constant, λ_C is the Compton wavelength and $\hbar$ is the reduced Planck's constant. The classical radius of a point particle with mass m and charge q is $r_e = \frac{q^2}{4\pi\varepsilon_0 mc^2}$, so the scattering cross section σ_T depends on the square of the radius, i.e. an area of a disk, meaning the point particle behaves like a solid sphere. For an electron $\sigma_T = 66.52\,(\text{fm})^2$. Another important point is that cross section is independent of the wavelength of incident radiation. Lastly, note that σ_T is inversely proportional to the square of mass m. Considering the mass of the electron m_e and proton m_p we have $m_p = 1836 m_e$. Therefore the contribution to Thomson scattering [8] by the nucleus is negligible. The model of X-ray diffraction

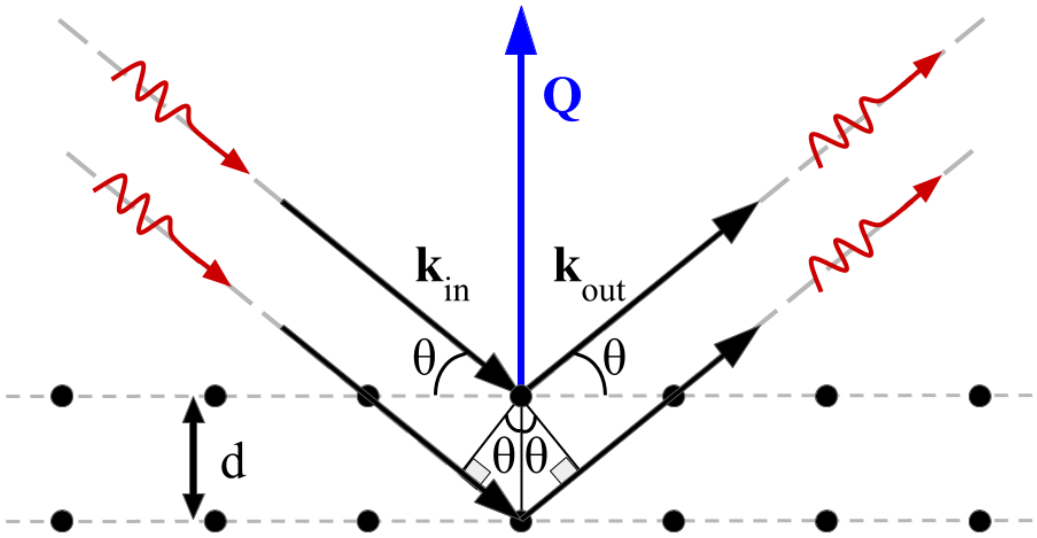

Figure 2.5: Schematic diagram of Bragg diffraction Law. X-ray radiation incident at an angle θ is reflected from parallel atomic planes with spacing d. The **Q**, $\mathbf{k}_{\text{in}}$ and $\mathbf{k}_{\text{out}}$ are vectors in reciprocal space shown to demonstrate the equivalence of Bragg and von Laue formulations.

is as was proposed by William H. Bragg and William L. Bragg and it is illustrated in

Figure 2.5. The incident radiation is reflected from semi-transparent atomic planes at an angle θ. The waves can interfere with each other. The condition for constructive interference is a phase shift of a multiple of 2π between two reflected waves. The scattered X-rays are detected at a large distance. The mathematical expression known as the Bragg Law [9] is given by

$$n\lambda = 2d\sin(\theta) \tag{2.2}$$

where n is a positive integer indicating diffraction order, λ is the wavelength of x-rays (e.g. Cu K_α is 0.154056 nm), d is atomic lattice spacing and θ is the scattering angle. An X-ray diffraction pattern is a series of peaks that correspond to constructive interference. Using equation 2.2, the out-of-plane lattice parameter (c) of the crystal unit cell of a thin film can be calculated by taking the 2θ position of the (n00) peak. Further analysis of the peaks in the diffraction pattern can provide more information about the crystal structure of the material. Shifts in peak positions are related to the strain of the material, ratios of specific peak intensities can be related to the chemical ordering out-of-plane in the crystal and FWHM of a peak can be related to the grain size τ by the Scherrer equation [10] given by

$$\tau = \frac{K\lambda}{\Delta(2\theta)\cos(\theta_B)} \tag{2.3}$$

where K is a shape factor (for thin films $K = 0.9$), λ is the X-ray wavelength, $\Delta(2\theta)$ is the integral breadth of a peak at position 2θ and θ_B is the Bragg angle of the peak. For new materials prepared in bulk form with an unknown structure, Rietveld refinement [11] performed on the diffraction pattern from powder scan can determine the crystal properties. The Bragg diffraction Law is a special case of the von Laue formulation,

$$\mathbf{Q} = \mathbf{k}_{\text{out}} - \mathbf{k}_{\text{in}} \in \mathbb{R}^* \tag{2.4}$$

where $\mathbf{Q}$ is the diffraction vector, $\mathbf{k}_{\text{in}}$ is the incident wave vector and $\mathbf{k}_{\text{out}}$ is the scattered wave vector in reciprocal space as shown in Figure 2.2. As mentioned before, in $\mathbb{R}^*$ lattice planes are represented by a grid of points of equal symmetry. The crystal structure, lattice parameters and wavelength (λ) of the X-ray radiation determine the angle at which constructive interference will occur. Lattice planes in which diffraction

will occur for a particular λ can be determined using the sphere of reflection, more commonly known as Ewald's sphere named after Paul P. Ewald who proposed it. [12] The Ewald's sphere is a geometrical construction which demonstrates the relationship

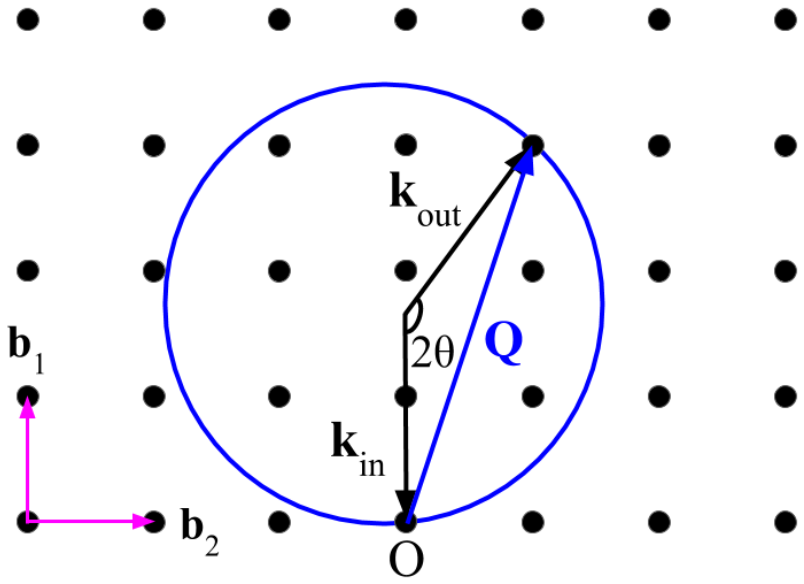

Figure 2.6: Ewald's circle construction in reciprocal space $\mathbb{R}^*$.

between $\mathbf{Q}$, $\mathbf{k}_{\text{in}}$, $\mathbf{k}_{\text{out}}$, 2θ and the reciprocal lattice of the crystal for a particular λ. An example of an Ewald's sphere for a cubic symmetry is demonstrated in Figure 2.6. The incident plane wave has a wave vector $\mathbf{k}_{\text{in}} = \frac{2\pi}{\lambda}$ and the the diffracted wave has a wave vector $\mathbf{k}_{\text{out}}$. As mentioned before, the diffraction process is assumed to be elastic, i.e. energy is conserved, then $|\mathbf{k}_{\text{in}}| = |\mathbf{k}_{\text{out}}|$ and hence the diffraction vector $\mathbf{Q}$, defined in equation 2.4, must lie on the surface of a sphere with radius $r = |\mathbf{k}_{in}|$ i.e. the Ewald's sphere. In the 2-D projection which is a circle, the origin of the reciprocal lattice is placed at the tip of the $\mathbf{k}_{\text{in}}$ wave vector as shown in Figure 2.6 and diffraction occurs at points that lie on circumference of the circle. When the crystal is rotated relative to the radiation source, this corresponds to a translation of the Ewald's sphere in $\mathbb{R}^*$. A point in $\mathbb{R}^*$ which passes through the Ewald's sphere at least once will be recorded as a diffraction peak, provided the diffracted wave hits the detector which depends on the diffraction limit of the crystal i.e. d-spacing. Since the radius of the Ewald's sphere is inversely proportional to λ, the radius increases for shorter wavelengths.

The Bragg and von Laue conditions must be satisfied for diffraction to occur, however they are not always sufficient. To fully determine which diffractions are allowed or forbidden, the crystal space group symmetry and the Renninger effect must also be considered. In short, the Renninger effect is multiple diffraction which may result in a decrease in the intensity of a diffraction peak due to a simultaneous presence of two reciprocal lattice points on the surface of the Ewald's sphere. [13] The diffracted beam intensity for a monocrystalline material (I_{diff}) is the square of the diffraction amplitude as a function of diffraction vector $\mathbf{Q} \in \mathbb{R}^*$ which can be expressed in terms of two contributions as

$$I_{\text{diff}} = |A(\mathbf{Q})|^2 \propto |S(\mathbf{Q})|^2 |f(\mathbf{Q})|^2 \tag{2.5}$$

where $S(\mathbf{Q})$ is the geometrical structure factor and $f(\mathbf{Q})$ is the atomic form factor. The geometrical structure factor quantifies the extent to which interference of waves from identical ions in the crystal lattice reduces the intensity of the Bragg peak associated with the reciprocal diffraction vector $\mathbf{Q}$ in the diffraction pattern. For a monoatomic crystal with n-atom basis at positions $\mathbf{d}_1, ..., \mathbf{d}_n$ in the primitive unit cell, the expression for $S(\mathbf{Q})$ is

$$S(\mathbf{Q}) = \sum_{j=1}^{n} e^{i\mathbf{Q}\cdot\mathbf{d}_j} \tag{2.6}$$

For a polyatomic crystal, $S(\mathbf{Q})$ has the form

$$S(\mathbf{Q}) = \sum_{j=1}^{n} f_j(\mathbf{Q}) e^{i\mathbf{Q}\cdot\mathbf{d}_j} \tag{2.7}$$

where now the atomic form factor is included because it is proportional to the Fourier transform of the electronic charge distribution $\rho(\mathbf{r})$ that will vary for different atomic species. The expression for $f_j(\mathbf{Q})$ for $j = 1, .., n$ can be written as

$$f_j(\mathbf{Q}) = -\frac{1}{e} \int \rho_j(\mathbf{r}) e^{i\mathbf{Q}\cdot\mathbf{r}} d^3\mathbf{r} \tag{2.8}$$

The structure factor can be sensitive to site occupancy of different atomic species in the crystal lattice, provided the constituting elements of the material have sufficiently distinct electronic charge distributions. Hence, the crystal ordering can be related to the ratio of peak intensities.

2.2.2 X-ray Diffraction Methods

A basic XRD measurement geometry is shown in Figure 2.7.

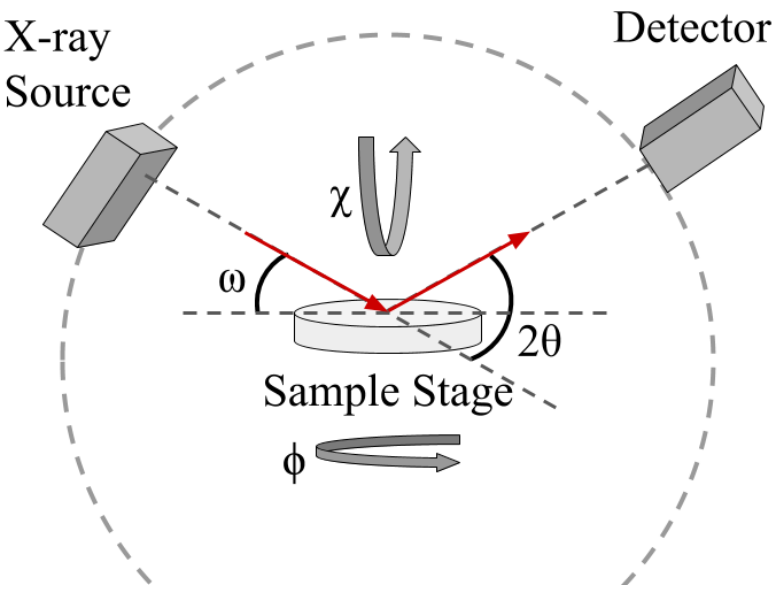

Figure 2.7: Basic XRD measurement geometry: X-ray source, detector and the sample stage. All relevant angles ω, 2θ, ϕ and χ are shown.

The three main types of XRD methods are Von Laue, rotating crystal and powder diffraction and a brief summary is given in Table 2.2.

Method	Crystal Type	Source	Angle
Von Laue	Monocrystalline	Polychromatic Beam	Fixed
Rotating crystal	Monocrystalline	Monochromatic Beam	Variable
Powder	Polycrystalline	Monochromatic Beam	Variable

Table 2.2: Summary of X-ray diffraction methods.

In my PhD I used the powder method because all samples I prepared were highly textured but polycrystalline metal alloys. The typical scan is 2θ - ω with $\omega = \frac{2\theta}{2}$ and the diffraction pattern of intensity versus 2θ is obtained. Another common measurement is a pole figure scan where for the system is aligned to a peak and the ϕ angle is varied. This scan demonstrates the symmetry of the crystal e.g. for a cubic crystal, the 0° - 360° scan will show a peak every 90°. For bulk materials prepared in pellets

by arc melting for example, the material must first be crushed into a fine powder using mortar and pestle. The powder is then spread out and flattened on a glass slide for XRD measurements in a X-ray diffractometer with a divergent beam. It is important to use such beam type as the crystallites in the powder have a random orientation, hence Bragg diffraction of the X-rays at different incidence angles relative to the sample stage is achieved. In the case of thin films, high resolution measurements using an X-ray diffractometer with a parallel beam is preferable. This is due to the fact that thin films are highly textured and very flat.

2.2.3 Reciprocal Space Mapping

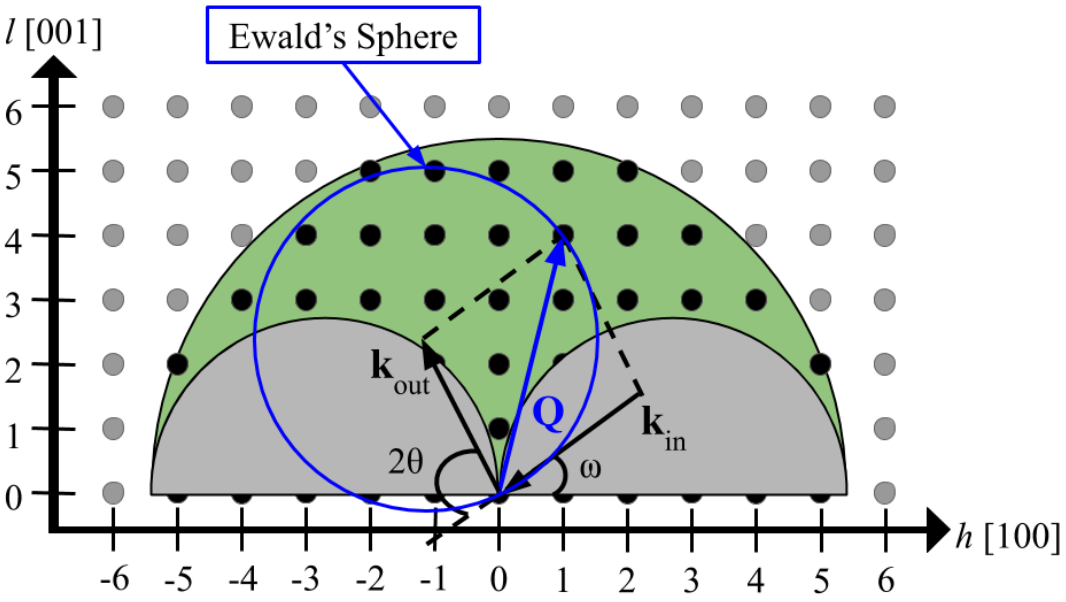

Figure 2.8: Diagram of the regions in reciprocal space where the beam is transmitted (grey) and where diffraction of X-rays with wavelength λ will occur (green).

A 2-D map of a portion of the reciprocal space (Q_x, Q_z) can be obtained by reciprocal space mapping (RSM) technique. The lattice planes that can be probed are limited by the fact that the beam must enter and exit through the top of the sample. Figure 2.8 demonstrates the regions where the beam is transmitted (grey) and the region where diffraction is possible and the condition to be satisfied is $0 < \omega < 2\theta$. The maximum

magnitude of the diffraction vector in reciprocal space for X-ray radiation with wavelength λ is $|\mathbf{Q}| = 2 \times \frac{2\pi}{\lambda}$. This limits the radius of the large green semi-circle centered at the origin. The two smaller grey semi-circles are regions that cannot be probed because of the geometry of Bragg scattering i.e. X-ray cannot be transmitted through the sample. The remaining region is green and can be probed. Performing an ω scan also known as a rocking curve, with 2θ fixed keeps $|\mathbf{Q}|$ constant but varies its direction which traces out an arc centered at the origin. Keeping ω fixed and performing a detector scan, meaning variation of 2θ angle, will result in tracing out an arc along the Ewald's sphere. A reciprocal space map can be either an ω scan over a range of 2θ or a 2θ scan for a range of ω. To obtain a good-signal to noise ratios scans are much more time consuming as compared to a standard XRD scan. However, the RSM is a powerful technique which provides information on both the out-of-plane and in-plane crystal properties such as lattice parameters, strain and grain size. It is important to obtain a map of the monocrystalline substrate and thin film peak next to each other, i.e. the diffraction planes from the two crystals are parallel, because the substrate lattice parameters are known and can be used to calculate the lattice parameter of the thin film.

2.2.4 X-ray Reflectivity

X-ray reflectivity (XRR) is a measurement technique used to study the properties of thin films such as thickness, density and interfacial roughness in both crystalline and amorphous materials. The principle of XRR is the refraction and specular reflection experienced by the X-ray incident on an interface with different refraction indices. The X-ray radiation hits the air/thin film interface at grazing incidence θ. According to Snell's law of refraction, there is a critical angle θ_c where for $\theta < \theta_c$ the radiation is totally reflected, and at θ_c the X-rays penetrate into the sample reflecting from the interfaces between thin film layers. The emerging X-rays undergo interference hence the resulting XRR is a periodic oscillation which decays at higher angles. Figure 2.9 shows an XRR pattern and a corresponding fit for a bilayer thin film of $Mn_2Ru_{0.7}Ga$ capped with AlO_x on a MgO substrate.

The information that can be obtained from the XRR pattern:

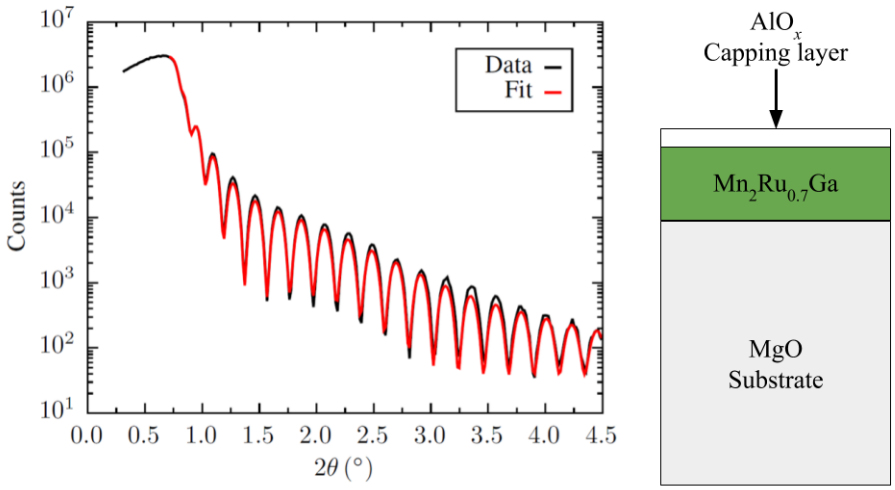

Figure 2.9: Left: Example of an XRR pattern plotted on a semi-logarithmic scale with a fit for a $Mn_2Ru_{0.7}Ga$ thin film (39.3 nm) on MgO (001) single crystal substrate (0.5 mm), capped with AlO_x (3 nm). Right: Diagram of the bilayer thin film on a substrate.

- **Electronic density:** The critical angle θ_c is related to the electronic density of the material which for smooth and continuous films is within $\approx$ 10 % of the actual material density. The amplitude of the oscillations is related to the density contrast. If two adjacent layers have a similar density, e.g. SiO_2 and Si_3N_4, it will be difficult to distinguish between the two signals and to fit the pattern. For thickness calibration to determine sputtering rates, it is useful to deposit a heavy metal on an Si wafer of a known thickness and then deposit Si_3N_4 on top to get a good density contrast.

- **Thickness:** The period of oscillation $\Delta 2\theta$ is related to the thickness of the thin film via the Fourier transform. Thickness is inversely proportional to the oscillation period. The upper bound for the thickness that can be measured by XRR is related to the coherence of the beam and can reach hundreds of nm.

- **Surface and interface roughness:** The intensity and oscillation decay rate at higher angles are related to the surface and interface roughness of the layers. Higher surface and interface roughness will smear the refracted beam resulting in a higher decay rate.

2.2.5 XRD Diffractometers

During the course of my PhD, XRD measurements were performed on either of two diffractometers. The first is the Phillips Panalytical X'Pert Pro used mainly for standard XRR and XRD and the second a Bruker D8 High Resolution XRD system for high resolution XRD and reciprocal space mapping on thin films only. Both diffractometers are equipped with multi-strip detectors to allow for the integration of each point along 2θ over the detector array for fast acquisition. The systems have a Cu-tube as the X-ray radiation source where the most intense emission line is K_α with wavelength $\lambda = 0.154056\,\text{nm}$. The Bruker High Resolution uses a double-bounce asymmetric channel-cut Ge(220) monochromator and a Göbel mirror to filter the weaker K_β line and to provide a parallel beam shape. In the Phillips, both lines are present and the beam is divergent hence it is suitable for powder samples.

2.3 Magneto-transport

The study and understanding of magneto-transport properties of magnetic metals is important to fundamental research but also for future technological applications of such materials in devices. Magneto-transport measurements were performed on blanket thin films. In this section, I will discuss the Van der Pauw method used to find the sheet resistance of a thin film and briefly describe the magneto-transport measurement systems.

2.3.1 Van der Pauw Method

The Van der Pauw method is a very simple and quick method of measuring the resistivity of a thin film of material. It was proposed by Leo J. Van der Pauw in 1958 [14; 15]. This is a four point contact method with the contacts around the perimeter of the sample which provides an averaged resistivity over the entire film. Here, most films are either square or rectangular in shape and hence contacts are always placed in the four corners of the sample. The contacts are made from indium metal. It is very soft at room temperature and hence can be moulded and cold welded onto the surface of the thin film. Such contacts can also be easily removed after the measurement. However for measurements preformed at low temperatures in a cryostat, the sample is contacted

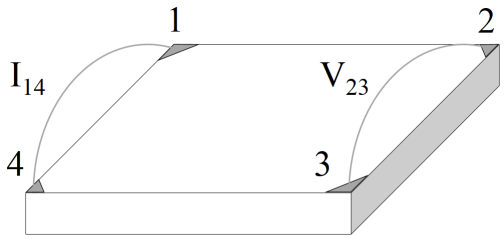

Figure 2.10: Van der Pauw method contact arrangement for square thin films.

with silver paint to prevent detachment. Such contacts can be removed using acetone. The method is very effective at producing an accurate measurement provided that the following five conditions are satisfied:

- The film must be a thin film of uniform thickness.
- The film must be isotropic, homogeneous and free of holes.
- The four contacts must be bonded to the corners of the film (Figure 2.10).
- The area of the contacts should be at least an order of magnitude smaller than the area of the thin film.

The measurement method consists of passing a small current, e.g. $1-5$ mA, between contacts 1 and 4 (I_{14}) and voltage is measured between contacts 2 and 3 (V_{23}). Then by Ohm's Law we can find the resistance $R_{14,23}$ using

$$R_{14,23} = \frac{V_{23}}{I_{14}}$$

This is the resistance along the vertical direction. To increase the accuracy, the same measurement is performed with the current of reversed polarity (I_{41}) and also along the opposite edge. Then all of the resistances are averaged over

$$R_v = \frac{R_{14,23}+R_{41,32}+R_{23,14}+R_{32,41}}{4}$$

The same procedure is applied for the other two edges to obtain the resistance along the horizontal direction

$$R_h = \frac{R_{12,43}+R_{21,34}+R_{34,21}+R_{43,12}}{4}$$

Then the Van der Pauw equation is applied to calculate the sheet resistance (R_s).

$$e^{\frac{-\pi R_v}{R_s}} + e^{\frac{-\pi R_h}{R_s}} = 1 \tag{2.9}$$

If $R_v \neq R_h$ equation 2.9 can be solved for R_s by approximating it using the Newton-Raphson Method. In the case where $R_v = R_h = R$, the equation can be solved analytically and the sheet resistance is given by

$$R_s = \frac{\pi R}{\ln 2}$$

When R_s is known, the longitudinal resistivity ρ_{xx} can be calculated using

$$\rho_{xx} = R_s t \tag{2.10}$$

where t is the thickness of the thin film. To find the Hall resistivity ρ_{xy} of a ferrimagnet, AHE measurements are performed on the magnetic thin film. The current is passed along the diagonal of the sample (I_{13} and I_{24}) and the voltage is measured perpendicularly to the current flow. A magnetic field is applied normal to the sample. Positive field is first applied to saturate the sample, then it is swept from negative to positive and back to negative again. The Anomalous Hall voltage is proportional to the z-component of magnetisation of the sample at a fixed temperature. For magnetic materials, the resulting graph of the Hall voltage (V_{xy}) versus applied magnetic field ($\mu_0 H$) is a hysteresis loop. Due to the square symmetry of the sample, we cannot distinguish vertical and horizontal directions, so we can consider the case of $R_v = R_h = R$ where R is

$$R = \left(\frac{ln(2)}{\pi}\right)\frac{\Delta V}{I}$$

where $\Delta V = \frac{1}{2}\left(V_{xy}(+\mu_0 H_S) - V_{xy}(-\mu_0 H_S)\right)$ i.e. half the difference between transverse voltages taken at positive and negative saturation field $\mu_0 H_S > \mu_0 H_C$, I is the current passed along the diagonal (I_{13} and I_{24}) and the prefactor $(\frac{ln(2)}{\pi})$ takes account of the measurement geometry. Then ρ_{xy} is given by

$$\rho_{xy} = Rt \tag{2.11}$$

The Anomalous Hall angle (θ_{AH}), which is a measure of spin dependent scattering by impurities or large spin-orbit interaction defects via the side-jump or skew-scattering

mechanism [16], is given by the ratio

$$\theta_{AH} = \frac{\rho_{xy}}{\rho_{xx}} \tag{2.12}$$

In conventional ferromagnetic metals such as $L1_0$ FePt $\theta_{AH} \approx 0.1$. [17]

2.4 Magnetometry

Superconducting QUantum Interference Device (SQUID) magnetometry is a high-sensitivity technique employed to measure the absolute moment of magnetic samples. It was first demonstrated experimentally in 1963 by P.W. Anderson and J.M. Rowell [18]. SQUID magnetometry is a high-sensitivity technique employed to measure the absolute moment of magnetic samples. In DC mode, SQUID can detect moments as low as 10^{-10} A m^2 and in AC mode the sensitivity increases further with the capability of measuring moments down to 10^{-12} A m^2.

In my PhD work magnetometry measurements were performed in a Quantum Design MPMS XL-5 SQUID magnetometer. For thin films, the sample must be diced to a size $\approx 4\times4$ mm^2 to fit into a non-magnetic plastic straw. The sample can be placed horizontally or vertically in the straw for out-of-plane and in-plane applied magnetic field measurements, respectively. The temperature range is from 4 K - 400 K and a field of up to 5 T can be applied.

2.4.1 Direct Current SQUID magnetometry

DC SQUID magnetometry operates on the basis of the DC Josephson effect [19]. A Josephson junction consists of a superconducting loop with weak contacts, such as an insulator or non-superconducting material, as shown in Figure 2.11. Electrical current I_{tot} enters the loop and splits into two currents I_1 and I_2 with equal magnitudes $I_1 = I_2 = \frac{1}{2}I_{\text{tot}}$, but opposite directions in the loop. The direct current can cross the insulating barrier in the absence of externally applied electromagnetic fields, because of quantum mechanical tunnelling. The Josephson current magnitude $I(t)$ is

$$I(t) = I_c \sin(\phi(t)) \tag{2.13}$$

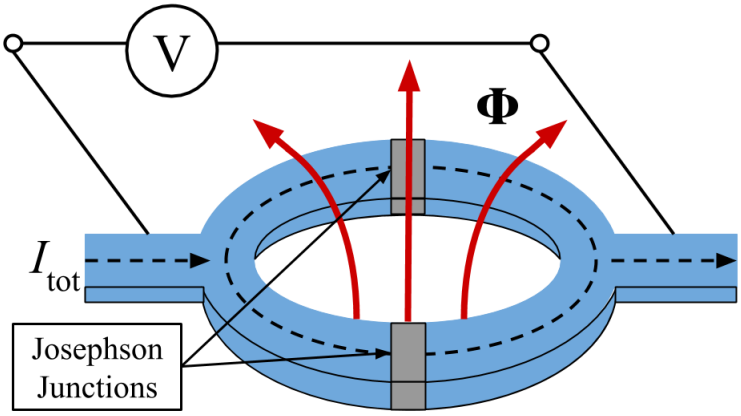

Figure 2.11: Illustration of a DC SQUID: A superconducting loop with two Josephson junctions in parallel. Total current (I_{tot}) enters the loop and splits into two paths. Voltage (V) is measured across the loop and Φ is the externally applied magnetic flux (pale red arrows).

where I_c is the critical current and $\phi(t)$ is the Josephson phase. When the magnetic flux Φ is externally applied, it will generate a screening current I_S to cancel it and generates an additional Josephson phase proportional to Φ. Inside the loop, I_S will be in the same direction as I_2 say, and oppose I_1. As a result when sufficient magnetic flux is applied, the critical current I_c can be reached in either of the branches producing a voltage drop across the junction. The relation between the current variation in time to the voltage can easily be derived from two Josephson relations [20]

$$\frac{\partial I}{\partial \phi} = I_c \cos(\phi); \qquad \frac{\partial \phi}{\partial t} = \frac{2\pi}{\Phi_0} V(t) \tag{2.14}$$

where $\Phi_0 = \frac{2\pi\hbar}{2e}$ is the magnetic flux quantum. Then by applying the Chain rule

$$\frac{\partial I}{\partial t} = \frac{\partial I}{\partial \phi} \cdot \frac{\partial \phi}{\partial t} = \left(I_c \cos(\phi) \right) \cdot \left(\frac{2\pi}{\Phi_0} V(t) \right) \tag{2.15}$$

and rearranging the above expression the current-voltage characteristic is given by

$$V = \frac{\Phi_0}{2\pi \cos(\phi)} \frac{\partial I}{\partial t} = L(\phi) \frac{\partial I}{\partial t} \tag{2.16}$$

where $L(\phi)$ is the kinetic inductance expressed in terms of the Josephson phase. For $\phi = 0$, we obtain $L_J = L(0) = \frac{\Phi_0}{2\pi}$ known as Josephson inductance, a characteristic pa-

rameter of the Josephson junction. In a SQUID there is a pickup coil which forms a

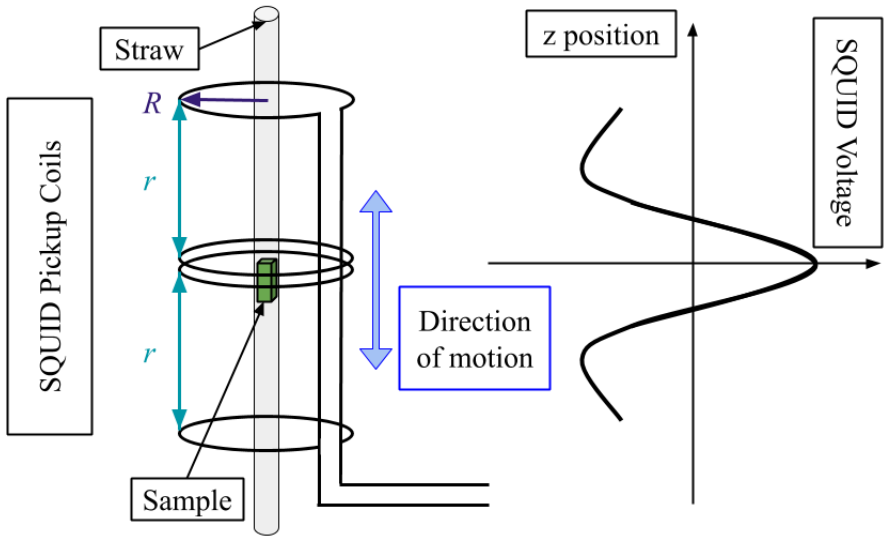

Figure 2.12: Left: Schematic of the SQUID pickup coil geometry, forming a second order gradiometer, demonstrating sample position and direction of motion. **Right:** Typical response of the SQUID pickup coil showing the voltage as a function of z position of the point dipole (sample) with respect to the pickup coil.

second order gradiometer as shown in Figure 2.12. The sample is displaced along its vertical axis inside a non-magnetic plastic straw. The induced current is converted to a voltage which can be related to the magnetic moment. A point like sample approximation applies as long as the sample measured is smaller than the radius (R) of the pick up coil and the coil separation (r).

2.5 Atomic Force Microscopy

Atomic force microscopy (AFM) is a scanning probe microscopy technique developed by G. Binnig, C. F. Quate and Ch. Gerber in 1986. [21] It employs an atomically sharp tip attached to an cantilever that is scanned across a surface and is capable of sensing the extremely small forces (10^{-12} - 10^{-8} N) between the tip and the surface. The deflection of the cantilever is monitored using a photodiode detector, split into 4 quadrants. The deflection is monitored by recording the voltage difference of either the top and bottom or the right and left diodes. The measurements are typically performed

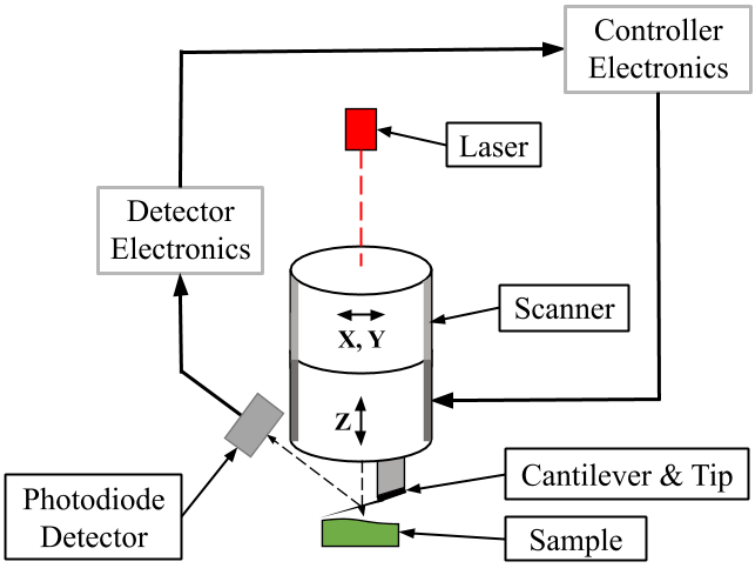

Figure 2.13: Schematic of an atomic force microscopy apparatus.

in ambient conditions but also in liquid. Figure 2.13 depicts a schematic diagram of an AFM apparatus. The contact and tapping modes of AFM are commonly used to image the topography of a thin film surface and obtain the average surface roughness.

In contact mode, the tip snaps into contact with the sample surface due to the adsorbed fluid layer on it. Constant deflection is maintained between the sample surface and the cantilever via a feedback loop which controls a piezoelectric stepper to vary the vertical position (Z) of the scanner at each (X,Y) data point. A constant deflection means a constant force is kept between the tip and the surface. A computer records the distance the scanner moves vertically at each (X,Y) data point and forms a topographic image of the surface of the sample.

For tapping mode measurement, the cantilever is tuned to oscillate close to its resonance frequency with an amplitude ranging between 20 nm to 100 nm. The tip lightly taps on the sample surface and the constant oscillation amplitude is achieved using a feedback loop which maintains a constant root mean square (RMS) amplitude signal acquired by the split photodiode detector. The stepper varies the vertical position (Z) of the scanner at each (X,Y) data point in order to maintain a constant amplitude and the image of the sample surface is formed. A constant tip-sample interaction is

maintained during imaging is achieved by keeping the oscillation amplitude constant.

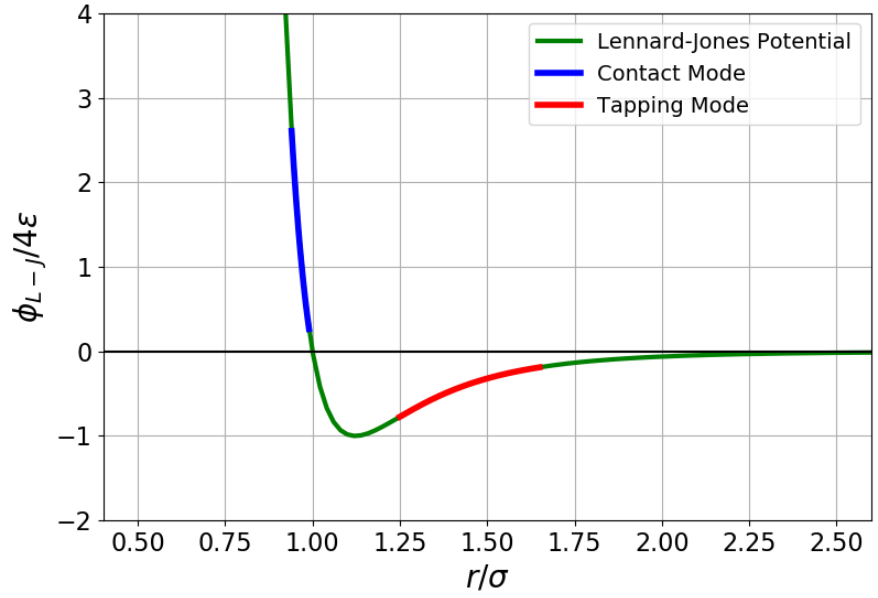

Figure 2.14: Lennard-Jones potential $(\phi_{\text{L-J}}/4\varepsilon)$ versus inter-particle distance (r/σ). The red and blue curved of the potential indicate the contact mode and tapping mode regions, respectively.

The forces acting during the operation of the contact and tapping AFM modes can be approximated by the Lennard-Jones potential $\phi_{\text{L-J}}$, which describes the intermolecular potential energy between a pair of neutral atoms [22], and is given by

$$\phi_{\text{L-J}}(r) = 4\varepsilon\left[\left(\frac{\sigma}{r}\right)^{12} - \left(\frac{\sigma}{r}\right)^{6}\right] \tag{2.17}$$

where ε is the depth of the potential well, σ is finite distance at which the inter-particle potential vanishes and r is the distance between the particles. Figure 2.14 shows a graph of the Lennard-Jones potential versus inter-particle distance. The force F is given by the negative of the derivative of the potential with respect to r. For contact mode, $F > 0$ hence the force is repulsive, calculated from Hooke's law, and the potential energy curve is concave up (blue curve). For tapping mode, $F < 0$ meaning the force is attractive and potential energy curve is concave down (red curve).

2.6 Magneto-Optic Kerr Effect Microscopy

The presence of a magnetic field can alter the optical properties of a material. This was first discovered in 1845 by M. Faraday, who observed that when a linearly polarised propagated through a piece of glass positioned between two poles of a magnet, as depicted in Figure 2.15, the plane of polarisation of transmitted light was rotated. [23] This is known as Faraday effect and it is a circular magnetic birefringence. Linear polarisation can be treated as a superposition of left- and right-handed circularly polarisations (LCP & RCP). In the presence of a magnetic field, the LCP and RCP waves experience different refractive indices inside the dielectric material. Difference in refractive indices implies that the LCP and RCP waves will travel through the material at different speeds introducing a phase shift between them. The emerging radiation is elliptically polarised with the major axis rotated by the Faraday rotation angle θ_F.

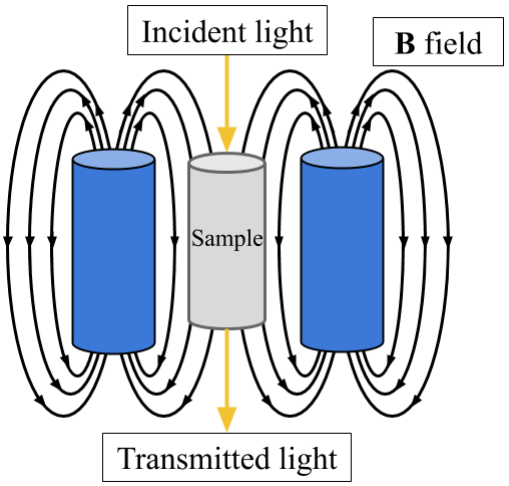

Figure 2.15: Schematic diagram of the Faraday effect experiment. The dielectric sample is located between two magnetic poles and the **B** field lines and the direction is indicated. The linearly polarised light wave is incident normal to the sample surface and parallel to the **B** field.

Reflecting a linearly polarised light wave from the surface of a ferromagnetic or ferrimagnetic material also results in a rotation of the plane of polarisation by the Kerr angle θ_K. This is the magneto-optical Kerr effect (MOKE) discovered by J. Kerr in 1877.[24] This technique is surface sensitive, with typical penetration depth of 25 nm. [25] In MOKE, three geometries depicted in Figure 2.16 are usually considered. They differ in the relative orientation of the magnetisation **M** to the wave vector **k** of incident linearly polarised radiation. The magnetisation directions, polarisation variation and detection principles for each geometry are summarised in Table 2.3.

The magneto-optics is relativistic quantum effect which results from the interplay of spin-orbit interaction (SOI) and band exchange splitting (BES). The SOI energy level splitting is attributed to the interaction between the electron spin S and the orbital

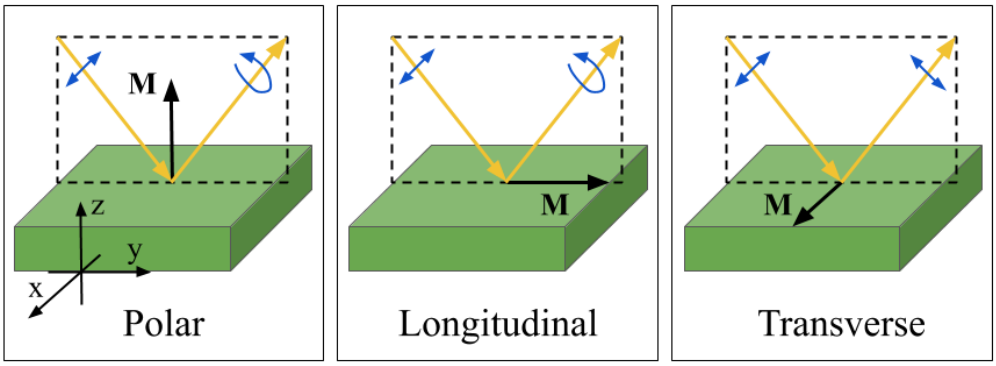

Figure 2.16: Magneto-optic Kerr effect measurement geometries.

Type	Polar	Longitudinal	Transverse
Magnetisation direction	Out-of-plane	In-plane	In-plane
Polarisation variation	Linear to Elliptic	Linear to Elliptic	None
Detection	Polarisation Analysis	Polarisation Analysis	Intensity Measurement

Table 2.3: Summary of Magneto-optic Kerr effect measurement geometries.

angular momentum L and allows for the coupling of incident circularly polarised photons to the orbital motion of the spin-polarised electrons. BES is induced by either an external magnetic field, i.e. the Zeeman effect, or the spontaneous magnetisation of ferromagnetic or ferrimagnetic materials. Both SOI and BES cause the lifting of energy level degeneracy associated with magnetic quantum number m_l. This implies that the responses LCP ($m_l = +1$) and RCP ($m_l = -1$) photons will be different, e.g. LCP photon may be able to excite an electron to some empty state with an appropriate m_l value, but the RCP photon may not as the corresponding $-m_l$ state may be occupied.

The macroscopic description for the magneto-optical phenomena is based on the classical theory of electromagnetism by J.C. Maxwell & O. Heaviside. [8] In Maxwell's equations, the displacement field **D**, also known as electric induction, represents the impact of the electric field **E** on the arrangement of charges in a medium. They are related by permittivity ε. The presence of a magnetic field can induce a change in the ε second rank tensor, making it anisotropic. The form of the tensor will depend on the geometry and ε_z ε_y and ε_x show the forms of permittivity tensors in the lowest

order of spin orbit coupling, for polar, longitudinal and transverse MOKE geometries, respectively

$$\varepsilon_z, \varepsilon_y, \varepsilon_x = \begin{bmatrix} \kappa_1 & \kappa_2 & 0 \\ -\kappa_2 & \kappa_1 & 0 \\ 0 & 0 & \kappa_1 \end{bmatrix}, \begin{bmatrix} \kappa_1 & 0 & -\kappa_2 \\ 0 & \kappa_1 & 0 \\ \kappa_2 & 0 & \kappa_1 \end{bmatrix}, \begin{bmatrix} \kappa_1 & 0 & 0 \\ 0 & \kappa_1 & \kappa_2 \\ 0 & -\kappa_2 & \kappa_1 \end{bmatrix} \tag{2.18}$$

where κ_1 and κ_2 are the complex first and second order permittivity constants, respectively. The anisotropy in the ε tensor in the presence of a magnetic field is a consequence of the symmetry of the Lorentz force $\mathbf{F}_L$.

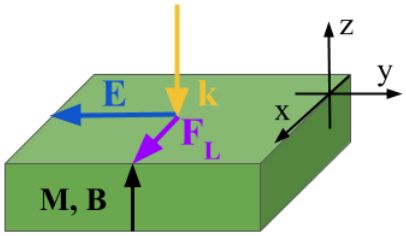

Figure 2.17: Diagram of the arrangement of the **E**, **k**, **B**, **M** and $\mathbf{F}_L$ vectors in the polar MOKE geometry.

Consider the simplest case of the polar geometry (magnetised along z-axis) and a linearly polarised light along the y-axis (s-polarised), incident normal to the surface of a ferromagnet and the magnetic field applied along the z-axis. The electric field will excite the electrons into oscillatory motion along the y-axis. In the Lorenz force $\mathbf{F}_L$ formula, the magnetic field contribution is expressed in the cross-product $\mathbf{F}_L = e(\mathbf{v}_e \times \mathbf{B})$, hence it is acting along the x-axis, orthogonal to both **E** and **B** as illustrated in Figure 2.17. This means there is electronic acceleration along both x and y which will contribute to the outgoing light. This results in the reflected electric field being polarised mainly along the y-axis (s-polarised) but also having a small component along the x-axis (p-polarisation), and combining the two leads to elliptic polarisation.

Both Faraday and Kerr effects are observed in magneto-optical Kerr effect microscopy, which is a technique used to image magnetic domains in ferromagnetic and ferrimagnetic materials. In my PhD, I have studied the magnetic domains of perpendicularly magnetised MRG thin film in the polar MOKE geometry.

2.6.1 Basic Theory of Magneto-Optic Phenomena

The expressions for the Faraday and Kerr rotations can be derived in terms of refractive indices using Fresnel formulas for reflection and transmission of EM waves. First the refractive indices (eigenvalues) and the corresponding normal modes (eigenvectors)

will be found by solving Maxwell's equations in matter and using the correct form of the ε tensor. [26]

Consider the polar MOKE geometry, where the magnetic field **B** and magnetisation **M** are parallel to the z-axis, and the **E** electric field is transverse to it. Up to the lowest order in spin-orbit coupling, the compact form of the ε tensor components is

$$\varepsilon_{ij} = \kappa_1 \delta_{ij} + \kappa_2 \varepsilon_{ijk} u_k \tag{2.19}$$

where κ_1 and κ_2 are complex first and second order permittivity constants, respectively, and **u** is the unit vector parallel to **M**. The first step is solving Maxwell equations in matter (SI units) given by

$$\begin{aligned} \nabla \cdot \mathbf{D} &= \rho & \nabla \times \mathbf{H} &= \mathbf{J} + \frac{\partial \mathbf{D}}{\partial t} \\ \nabla \cdot \mathbf{B} &= 0 & \nabla \times \mathbf{E} &= -\frac{\partial \mathbf{B}}{\partial t} \end{aligned} \tag{2.20}$$

where for a linear medium

$$\mathbf{D} = \varepsilon \mathbf{E}, \qquad \mathbf{J} = \sigma \mathbf{E}, \qquad \mathbf{B} = \mu \mathbf{H} \tag{2.21}$$

where ε, σ and μ are second rank permittivity, conductivity and permeability tensors, respectively. Considering an incident plane wave characterised by **E** and **H** transverse components given by

$$\mathbf{E}(\mathbf{r},t) = \mathbf{E}_0 e^{i(\mathbf{k}\cdot\mathbf{r}-\omega t)} \quad \text{and} \quad \mathbf{H}(\mathbf{r},t) = \mathbf{H}_0 e^{i(\mathbf{k}\cdot\mathbf{r}-\omega t)} \tag{2.22}$$

Substituting into the relevant Maxwell equation from 2.20 and using relations in 2.21

$$\begin{aligned} \nabla \times \mathbf{H} &= \sigma(\omega)\mathbf{E} + \varepsilon(\omega)\frac{\partial \mathbf{E}}{\partial t} \\ \nabla \times \mathbf{H} &= (\sigma(\omega) - i\omega\varepsilon(\omega))\mathbf{E} \end{aligned}$$

using the above equation, the dielectric function $\varepsilon(\omega)$ can be redefined in terms of conductivity $\sigma(\omega)$ to

$$\varepsilon(\omega) = 1 + \frac{i\sigma(\omega)}{\omega} \tag{2.23}$$

hence the Maxwell equation can be rewritten as

$$\boldsymbol{\nabla} \times \mathbf{H} = \varepsilon(\omega)\frac{\partial \mathbf{E}}{\partial t} \tag{2.24}$$

Considering the next Maxwell equation and taking the curl of both sides leads to the wave equation with solutions 2.22

$$\begin{aligned}
\boldsymbol{\nabla} \times (\boldsymbol{\nabla} \times \mathbf{E}) &= -\mu\frac{\partial(\boldsymbol{\nabla} \times \mathbf{H})}{\partial t}, \quad \text{but} \quad \mu \approx 1 \\
\nabla(\boldsymbol{\nabla} \cdot \mathbf{E}) - \nabla^2\mathbf{E} &= -\varepsilon\frac{\partial^2 \mathbf{E}}{\partial t^2}, \quad \text{Wave Equation} \\
-\mathbf{k}(\mathbf{k} \cdot \mathbf{E}) + k^2\mathbf{E} &= \omega^2\varepsilon\mathbf{E}, \quad \text{let} \quad k_0 = \frac{\omega}{c} \\
\therefore k^2\mathbf{E} - \mathbf{k}(\mathbf{k} \cdot \mathbf{E}) &= c^2k_0^2\mathbf{D}
\end{aligned}$$

hence an equation relating the $\mathbf{E}$ and $\mathbf{D}$ fields is obtained. $\mathbf{E} \perp \mathbf{k}$ implies $\mathbf{k} \cdot \mathbf{B} = 0$. Then using $\mathbf{E} = \varepsilon^{-1}\mathbf{D}$ and the final expression

$$\varepsilon^{-1}\mathbf{D} = \left(\frac{c}{n}\right)^2\mathbf{D} \tag{2.25}$$

where $n = \frac{k}{k_0}$ is the refractive index. The inverse of the permittivity tensor ε_{ij}^{-1} can be easily found to be

$$\varepsilon_{ij}^{-1} \approx \frac{1}{\kappa_1}\delta_{ij} + \frac{\kappa_2}{\kappa_1^2}\varepsilon_{ijk}u_k \tag{2.26}$$

where the approximation $\kappa_2^2 \ll \kappa_1^2$ was applied. Solving the eigenvalue problem in equation 2.25 and considering the upper 2x2 block, the refractive indices and normal modes are derived. Let $x = (\frac{c^2}{n^2})$, $a = \frac{1}{\kappa_1}$ and $b = \frac{\kappa_2}{\kappa_1}u_z$, then the characteristic polynomial $f(x)$ can be solved in the following way

$$\begin{aligned}
f(x) = x^2 - 2ax + a^2 + (ab)^2 = (x-a)^2 + (ab)^2 = 0 \\
\therefore x = a \pm iab
\end{aligned}$$

where $i = \sqrt{-1}$. Filling back in for the variables x, a and b

$$\frac{c^2}{n^2} = \left(\frac{1}{\kappa_1} \pm iu_z\frac{\kappa_2}{\kappa_1^2}\right) = \left(\frac{\kappa_1 \pm iu_z\kappa_2}{\kappa_1^2}\right)$$

and the refractive indices can be found

$$\frac{n^2}{c^2} = \left(\frac{\kappa_1^2}{\kappa_1 \pm iu_z\kappa_2}\right) = \left(\frac{\kappa_1^2}{\kappa_1 \pm iu_z\kappa_2}\right)\left(\frac{\kappa_1 \mp iu_z\kappa_2}{\kappa_1 \mp iu_z\kappa_2}\right) = \left(\frac{\kappa_1^3 \mp iu_z\kappa_1^2\kappa_2}{\kappa_1^2 - u_z\kappa_2^2}\right)$$

$$\frac{n^2}{c^2} \approx \kappa_1 \mp i\kappa_2$$

The eigenvalues and eigenvectors which correspond to the refractive indices and normal modes are

$$n_\pm^2 = \kappa_1 \pm i\kappa_2 \quad \text{and} \quad \mathbf{D}_\pm = \hat{x} \pm i\hat{y} \tag{2.27}$$

where for simplicity the κ_1 and κ_2 are redefined to contain the speed of light constant squared c^2.It follows that the two normal modes correspond to the circularly polarised modes, $\mathbf{D}_+$ (LCP) and $\mathbf{D}_-$ (RCP). Each mode, experiences a different refractive index, n_+ or n_-, and this is the basic origin of magneto-optical phenomena. Faraday effect occurs in transmission and the Kerr effect in reflection. Fresnel coefficients relate the reflected and transmitted waves to the incident waves, and can be used to derive the rotation of polarisation angles. The case of normal incidence will be considered because it corresponds to how measurements are performed in the MOKE microscope.

2.6.1.1 Polar Kerr Effect at Normal Incidence

Following from the derivation above in the polar MOKE geometry, consider an incident s-polarised light wave normal to the surface of the ferromagnetic or ferrimagnetic material, i.e. $\mathbf{k} \parallel \hat{\mathbf{u}}$, where $\mathbf{u} = (0,0,1)$. At normal incidence and in the absence of magneto-optic coupling, the Fresnel reflection coefficients for s-polarised and p-polarised light, r_{ss} and r_{pp}, respectively, are the same and given by

$$r_{ss} = r_{pp} = \frac{1-n}{1+n} \tag{2.28}$$

where n is the refractive index. Electric field $\mathbf{E}$ of linearly polarised wave with magnitude $2E_0$, being a superposition of LCP and RCP polarised waves, $\mathbf{E}_+$ and $\mathbf{E}_-$, is expressed as a linear combination of s-polarised and p-polarised waves

$$E_+ = E_0(\hat{x} + i\hat{y}) \quad \text{and} \quad E_- = E_0(\hat{x} - i\hat{y}) \tag{2.29}$$

and the refractive indices associated with LCP and RCD are n_+ and n_-, respectively. Then the electric field of the wave reflected from the surface $\mathbf{E}^r$ is a linear combination of the Fresnel coefficients for LCP and RCP given by

$$\begin{aligned} E^r &= \left(\frac{1-n_+}{1+n_+}\right)\mathbf{E}_+ + \left(\frac{1-n_-}{1+n_-}\right)\mathbf{E}_- \\ E^r &= E_0\left(\frac{(1-n_+)(1+n_-)(\hat{x}+i\hat{y})+(1-n_-)(1+n_+)(\hat{x}-i\hat{y})}{(1+n_+)(1-n_+)}\right) \\ E^r &= 2E_0\left(\frac{(1-n_+n_-)\hat{x}+i(n_--n_+)\hat{y})}{(1+n_+)(1-n_+)}\right) = \alpha_x\hat{x}+\alpha_y\hat{y} \end{aligned} \tag{2.30}$$

The tangent function of the angle of rotation of polarisation ϕ is given by the ratio $\frac{\alpha_y}{\alpha_x}$

$$\tan(\phi) = \frac{\alpha_y}{\alpha_x} = \frac{i(n_- - n_+)}{(1-n_+n_-)} \tag{2.31}$$

for small ϕ, $\tan(\phi) \approx \phi$ and using the expressions for $n_\pm = \kappa_1 \pm i\kappa_2$, where $\kappa_2^2 \ll \kappa_1^2$, ϕ becomes

$$\begin{aligned} \phi &= \frac{i(n_- - n_+)}{1-n_+n_-} = \frac{\sqrt{i\kappa_2-\kappa_1}-\sqrt{-i\kappa_2-\kappa_1}}{1-\sqrt{\kappa_1^2+\kappa_2^2}} \approx \frac{\sqrt{i\kappa_2-\kappa_1}-\sqrt{-i\kappa_2-\kappa_1}}{1-\kappa_1} \\ &= \frac{\sqrt{\kappa_1}}{\sqrt{\kappa_1}}\left(\frac{\sqrt{i\kappa_2-\kappa_1}-\sqrt{-i\kappa_2-\kappa_1}}{1-\kappa_1}\right) = \frac{\sqrt{i\kappa_2\kappa_1-\kappa_1^2}-\sqrt{-i\kappa_2\kappa_1-\kappa_1^2}}{\sqrt{\kappa_1}(1-\kappa_1)} \\ &= \frac{\sqrt{i\kappa_2\kappa_1-\kappa_1^2+(\frac{1}{4}\kappa_2^2-\frac{1}{4}\kappa_2^2)}-\sqrt{-i\kappa_2\kappa_1-\kappa_1^2+(\frac{1}{4}\kappa_2^2-\frac{1}{4}\kappa_2^2)}}{\sqrt{\kappa_1}(1-\kappa_1)} \\ &= \frac{\sqrt{(i\kappa_1+\frac{1}{2}\kappa_2)^2-\frac{1}{4}\kappa_2^2}-\sqrt{(i\kappa_1-\frac{1}{2}\kappa_2)^2-\frac{1}{4}\kappa_2^2}}{\sqrt{\kappa_1}(1-\kappa_1)} \approx \frac{i\kappa_1+\frac{1}{2}\kappa_2-i\kappa_1+\frac{1}{2}\kappa_2}{\sqrt{\kappa_1}(1-\kappa_1)} \\ \therefore \phi &\approx \frac{\kappa_2}{\sqrt{\kappa_1}(1-\kappa_1)} \end{aligned}$$

To obtain the Kerr rotation θ_K, the above constants are replaced by permittivity constants, i.e. $\kappa_1, \kappa_2 = \varepsilon_{xx}, \varepsilon_{xy}$ and using equation 2.23 ϕ is expressed in terms of conductivities σ_{xx}, σ_{xy}

$$\phi = \frac{\kappa_2}{\sqrt{\kappa_1}(1-\kappa_1)} = \frac{\varepsilon_{xy}}{\sqrt{\varepsilon_{xx}}(1-\varepsilon_{xx})} = \frac{-\sigma_{xy}}{\sigma_{xx}\sqrt{1+\frac{i\sigma_{xx}}{\omega}}} \tag{2.32}$$

The angle ϕ is a complex angle, with the Kerr angle $\theta_K = Re[\phi]$ given by

$$\theta_K = Re[\phi] = \frac{-\sigma_{xy}}{\sigma_{xx}\left(\sqrt{1+\frac{\sigma_{xx}^2}{\omega^2}}\right)}\left[\sqrt{\frac{1}{2}\left(\sqrt{1+\frac{\sigma_{xx}^2}{\omega^2}}+1\right)}\right] \tag{2.33}$$

and the ellipticity $\varepsilon_K = Im[\phi]$ is

$$\varepsilon_K = Im[\phi] = \frac{\sigma_{xy}}{\sigma_{xx}\left(\sqrt{1+\frac{\sigma_{xx}^2}{\omega^2}}\right)}\left[\sqrt{\frac{1}{2}\left(\sqrt{1+\frac{\sigma_{xx}^2}{\omega^2}}-1\right)}\right] \tag{2.34}$$

The Kerr signal is proportional to the magnetisation components making it useful for studying the hysteretic behaviour of thin film samples. The hysteresis loops measured in Kerr are related to those measured by AHE.

2.6.2 Faraday Effect

The Faraday effect is observed in the MOKE microscope because the light passes through the objective lens which is, unfortunately, inside the magnetic field. The derivation of θ_F is very similar to the one described above for MOKE. Consider the linearly polarised wave as a superposition of LCP ($\mathbf{E}_+$) and RCP ($\mathbf{E}_-$) waves. Each experiences a different refractive index inside the medium in the presence of a magnetic field. This results in the two polarisations propagating at different speeds inside a material. Let the distance travelled inside the material be L, then the times taken to travel this distance for $\mathbf{E}_+$ and $\mathbf{E}_-$ are

$$t_\pm = \frac{L}{v_\pm} = \frac{Ln_\pm}{c} \tag{2.35}$$

The angle of rotation of a circularly polarised wave after travelling through a material is simply $\theta = \omega t$, hence for $\mathbf{E}_+$ and $\mathbf{E}_-$ the angles are

$$\theta_\pm = \omega\frac{Ln_\pm}{c} \tag{2.36}$$

It is important to note that $\mathbf{E}_+$ and $\mathbf{E}_-$ will rotate in opposite directions, anticlockwise and clockwise. This leads to the expression for the Faraday rotation angle θ_F

$$\begin{aligned} \theta_+ - \theta_F &= \theta_- + \theta_F \\ \therefore \theta_F &= \frac{1}{2}(\theta_+ - \theta_-) = \frac{\omega L}{2c}(n_+ - n_-) \end{aligned} \tag{2.37}$$

The Faraday rotation is proportional to L and but also to the difference in refractive indices $(n_+ - n_-)$, which depends linearly on the applied magnetic field $\mathbf{B}$.

2.6.3 MOKE Microscope

MOKE measurements were performed with an Evico Magnetics high-end wide-field Kerr microscope [27], equipped with

- **Light Source:** Kerr-LED lamp based on eight light-emitting diodes with the choice of monochromatic (white light) or dichromatic (blue and red light) wavelengths. The light is guided from the source to the microscope by optical fibers.
- **Zeiss Optics:** objective lenses ranging from 1.25x, 20x, 50x and 100x (with oil immersion), optical zoom lenses 1x, 2.5x and 4x for magnification.
- **Magnets:** A rotatable water-cooled electromagnet for in-plane field measurements up to 1.4 T and a water-cooled electromagnet for out-of-plane measurements up to 950 mT.
- **Sample Stage:** Manual xy stage with an xyz piezo stage for compensation of lateral and focus drift. Manual x-y sample shift up to $\pm$ 14 mm and manual sample rotation. Samples of up to 35 mm in size can be measured.
- **Optical Components:** Rotatable polariser, rotatable analyser and a compensator module.
- **Detection:** Sensitive low noise digital cooled CCD camera with a frame rate between 8.8 - 115 frames/s and maximal pixel resolution of 960 $\times$ 600.
- **Software Features:** Computer controlled choice of Kerr sensitivity and compensation of parasitic Faraday effect in the objective lens. [28]

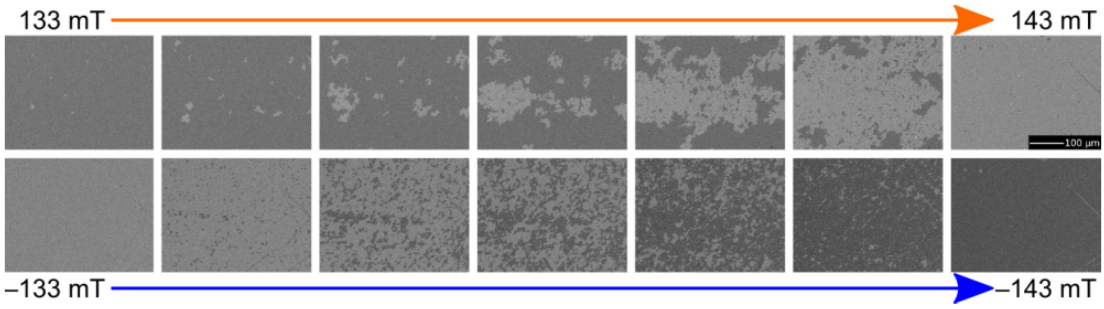

Figure 2.18: MOKE images of $Mn_2Ru_{0.4}Ga$ thin films obtained via Kerr microscopy near coercivity.

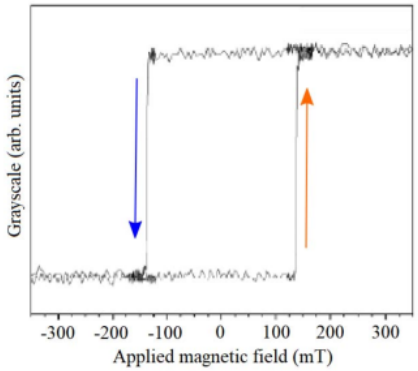

Figure 2.19: Hysteresis loop of $Mn_2Ru_{0.4}Ga$ thin films obtained via Kerr microscopy.

In order to measure a hysteresis loop, the sample is first saturated in positive saturation field $\mathbf{B}_S$. A background image is capture and subtracted from the data. This allows for the topology of the sample surface to be removed and only MOKE signal is observed. Next the magnetic field is swept from + $\mathbf{B}_S$ to - $\mathbf{B}_S$, then back to + $\mathbf{B}_S$ at a desired increment. To correct for the Faraday effect in the objective lens caused by the field applied perpendicular to the film, a compensation module is utilised to readjust the analyser position using a non-magnetic mirror as a reference.

In the case of MRG, it is possible to use the MOKE microscope to image domains directly, despite the fact that the material does not produce a stray field. At or near compensation, MRG is insensitive to external fields and demagnetising effects, yet electronically it resembles a spin polarised ferromagnetic metal. The films exhibit perpendicular magnetic anisotropy due to a small ≈ 1 % tetragonal elongation of the cubic unit cell induced by biaxial substrate-induced strain. The electronic band structure exhibits a spin gap, and it is the Mn^{4c} sublattice that predominantly contributes spin polarised conduction electrons at the Fermi energy. It follows that direct imaging of the domains of MRG by polar MOKE is possible. [29] An example of a Kerr loop of $Mn_2Ru_{0.4}Ga$ thin film is shown in Figure 2.19. Close to coercivity, the switching of magnetic domains can be observed in the images as demonstrated in Figure 2.18.

2.7 Synchrotron X-ray Radiation Techniques

To gain a deeper understanding of the magnetic properties of the zero-moment half metallic thin films, the X-ray magnetic circular dichroism (XMCD) measurements were performed on a soft X-ray beamline ID32 shown in Figure 2.20, at the European Synchrotron Radiation Facility (ESRF) in Grenoble, France. The dichroism arises because the magnetic state of the material modifies the absorption coefficients of circularly polarised X-rays with different helicities. XMCD is element specific due to defined energy of the absorption edges. In the case of MRG, the Mn sublattices can be distinguished because they are crystallographically inequivalent, giving rise to a ≈ 1 eV difference in absorption energy.

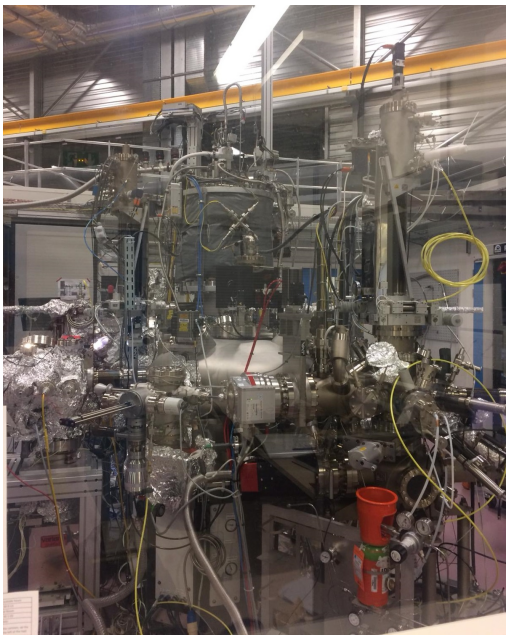

Figure 2.20: Soft X-Ray spectroscopy beamline (ID32) high field magnet assembly at ESRF.

2.7.1 Synchrotron Radiation Source

The principle on which synchrotron radiation sources are based is that charged particles, such as electrons, emit electromagnetic (EM) radiation when accelerated. Figure 2.21 shows the main components of a synchrotron radiation source. The electron gun is the source of the electrons, which enter a linear accelerator where they can reach energies of MeV. Next, the electrons enter the booster synchrotron which further accelerates them up to the required GeV energies, before they are injected in bunches into the main storage ring.

The storage ring contains bending dipole magnets. The electrons travelling through the magnetic field experience the Lorenz force causing centripetal acceleration, which results in bending of their trajectories, maintaining a circular orbit, and emission of EM radiation. The power loss per revolution for acceleration perpendicular to the direction

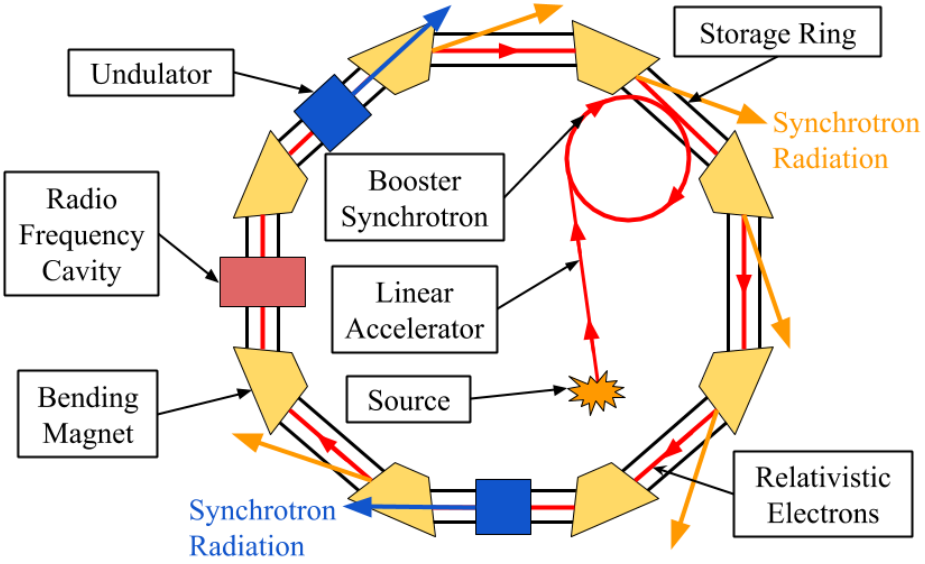

Figure 2.21: Schematic diagram of the basic components of a synchrotron radiation source.

of particle propagation is given by

$$P = \frac{2e^2 c\gamma^4}{12\pi\varepsilon_0\rho^2}, \quad \gamma = \frac{E}{m_0 c^2} \tag{2.38}$$

where ρ is the radius of the storage ring and m_0 is the rest mass of the charged particle. It is important to note that since the mass of the electron is 1836 times smaller than the mass of the proton, it means that electrons lose energy $\approx 10^{13}$ times faster than protons. This is why electrons are used to harvest the power in synchrotron light sources, whereas protons are used in the large hadron collider (LHC) where energy losses are minimised. To calculate the energy loss per turn ΔE, the power loss per revolution P is integrated with respect to time,

$$\Delta E = \oint P dt = P t_b = P\frac{2\pi\rho}{c} \tag{2.39}$$

where t_b is the time it takes for the particles to travel through bending magnets.

Radio-frequency (RF) cavities are units used to synchronously resupply the energy lost by electrons, due to emission of radiation as they circulate in the storage ring. The RF cavities require electrons to be split into bunches ($\approx$ 7 cm long) separated by the

wavelength of the cavities ($\approx$ 60 cm), because acceleration of the electrons can only occur during half of the oscillation period of the RF cavity. This is the reason why the electrons are not continuously injected into the storage ring.

An undulator is a structure located on the storage ring, which consists of periodic arrays of small dipole permanent magnets. The main feature of the undulator is that it can force the electron trajectory to oscillate. Compared to a simple bending magnet, the beam of radiation generated by the undulator has several orders of magnitude higher flux. The oscillating trajectory of the electrons can cause an interference in the emitted radiation which leads to narrow energy bands. The radiation from the undulator is coherent when the oscillation frequency exceeds the cyclotron frequency Ω_c given by

$$\Omega_c = \frac{eB}{2\pi m_e} \tag{2.40}$$

where e is the electron charge, B is the magnitude of a uniform magnetic field and m_e is the mass of the electron. Varying the spacing between the top and bottom magnet rows ('gap') alters the energy of the electrons in the ring. The undulator also controls the polarisation of radiation by varying the trajectory of the electrons. Linearly polarised light is generated when the oscillation of the electron trajectory is confined to a plane, where a helical trajectory of the electrons will produce circularly polarised light.

2.7.2 Beam Line Experimental Apparatus

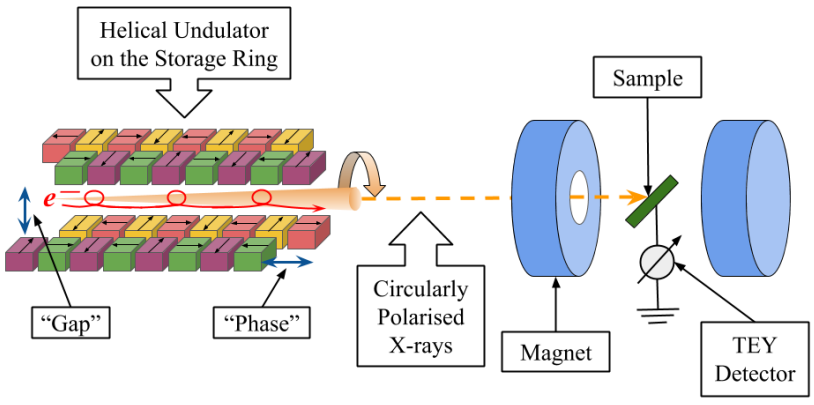

Figure 2.22: Schematic diagram of XMCD experimental apparatus at a beamline.

The basic components of the experimental set up at the beam line are depicted in Figure 2.22. The helical undulator located on the storage ring controls the energy of the electrons by varying the 'gap', as mentioned before. The relative movement of the permanent magnet arrays ('phase') forces the electrons into helical trajectories to produce circularly polarised radiation. The circularly polarised X-rays travel through various optical components and slits, which were omitted from the diagram, before reaching the sample. The optical components include a variable line spacing plane grating monochromator for wavelength selection and different types of mirrors to deflect, focus and filter the radiation. Thin film samples are attached to a copper sample holder mounted on a rod, which can be rotated and translated along two axes perpendicular to the beam. The sample is positioned directly in the beam path, in an ultra high vacuum chamber. Two pairs of liquid helium-cooled superconducting coils surround the chamber so that fields can be applied parallel (max. 9 T) and perpendicular (max. 4 T) relative to the beam direction. The X-ray absorption spectra are quantified by total electron yield (TEY), where the signal is given by the sample drain current, which is needed to replace the electrons ejected out of the material due to X-ray absorption. The electron yield is normalised relative to a gold foil target. The TEY detection method of X-ray absorption has a better signal-to-noise ratio in comparison to the fluorescence detection, where the X-rays emitted from the sample after electron-hole recombination are counted. However, the measurement is more surface sensitive and sampling depths range from 2 nm to 10 nm. This means that capping layers should be around 2 nm thick, to ensure the probing of the magnetic material thin film below it.

2.7.3 Theory of X-ray Absorption Spectroscopy and X-ray Magnetic Circular Dichroism

X-ray magnetic circular dichroism (XMCD) is the difference spectrum of two X-ray absorption spectra (XAS), one performed with left-handed circularly polarised (LCP) X-rays and, the other with right-handed circularly polarised (RCP) X-rays in a magnetic field. XMCD probes the spin anisotropy in exchange split bands at Fermi level to obtain the orbital and spin moments of the magnetic atomic species in a material. [30] To determine the magnetic properties of the Mn (transition metal) species in MRG thin

films, XAS is performed at the L-edge by probing in the region of 400-900 eV. In L-edge absorption, the core electrons are resonantly excited from $2p$ states to unoccupied valence states in the $3d$ band.

The degeneracy of the 2p band is lifted due to strong spin-orbit interaction (SOI). The total angular momentum number $j = |l \pm s|$ and for the 2p band $l = 1$ and $s = \frac{1}{2}$ hence it splits into $2p_{\frac{3}{2}}$ (4-fold degenerate $m_l = \pm\frac{3}{2}, \pm\frac{1}{2}$) and $2p_{\frac{1}{2}}$ (2-fold degenerate $m_l = \pm\frac{1}{2}$), with the opposite SOI. The 3d band is exchange split into 3d↑ and 3d↓ states and the unoccupied 3d valence states largely determine the magnetic behaviour of the material. The 3d band is also split by SOI, with $l = 2$ and $s = \frac{1}{2}$ into $3d_{\frac{5}{2}}$ (6-fold degenerate $m_l = \pm\frac{5}{2}, \pm\frac{3}{2}, \pm\frac{1}{2}$) and $3d_{\frac{3}{2}}$ (4-fold degenerate $m_l = \pm\frac{3}{2}, \pm\frac{1}{2}$). It is important to note that $\Delta E^{SOI}_{2p} \approx 10$ eV and $\Delta E^{SOI}_{3d} \approx 10$ meV, i.e. SOI of the 3d band is three orders of magnitude weaker than SOI of 2p band. As a result, the two XAS edges observed known as L_3 and L_2 correspond to exciting the Mn atom from its ground state, $^2S_{\frac{5}{2}}$ calculated from Hund's Rules, to the $^2P_{\frac{3}{2}}$ and $^2P_{\frac{1}{2}}$ excited states, respectively. The ratio of L_3 peak to L_2 peak is two for an isolated atom. However for an atom in a crystal, effects such as orbital hybridisation and SOI of the 3d band reduce this ratio. To measure the difference in the number of 3d valence holes with up and down spin, XAS must be spin dependent, hence circularly polarised x-ray radiation is used. The circularly polarised photons have the magnetic quantum number m_l = +1 and -1 for LCP and RCP, respectively. For a photoelectron originating from a SOI split level, $2p_{\frac{3}{2}}$ or $2p_{\frac{1}{2}}$, the angular momentum of the photon can be transferred in part to the spin via SOI. In the simple L-S coupling scheme, the transitions must satisfy the electric dipole selection rules:

$$\Delta l = \pm 1, \quad \Delta m_l = \pm 1, \quad \Delta s = 0, \quad \Delta m_s = 0 \tag{2.41}$$

In electric dipole transitions spin flips are forbidden ($\Delta m_s = 0$), hence spin up and down photoelectrons from the $2p$ band can only be excited to spin up and down unoccupied $3d$ valence states, respectively. In this way the exchange-split $3d$ valence band can be considered as a detector for the spins of the excited photoelectrons and the transition intensity is simply proportional to the number of unoccupied states of a particular spin. Using the one electron model and the selection rules above, the probabilities of

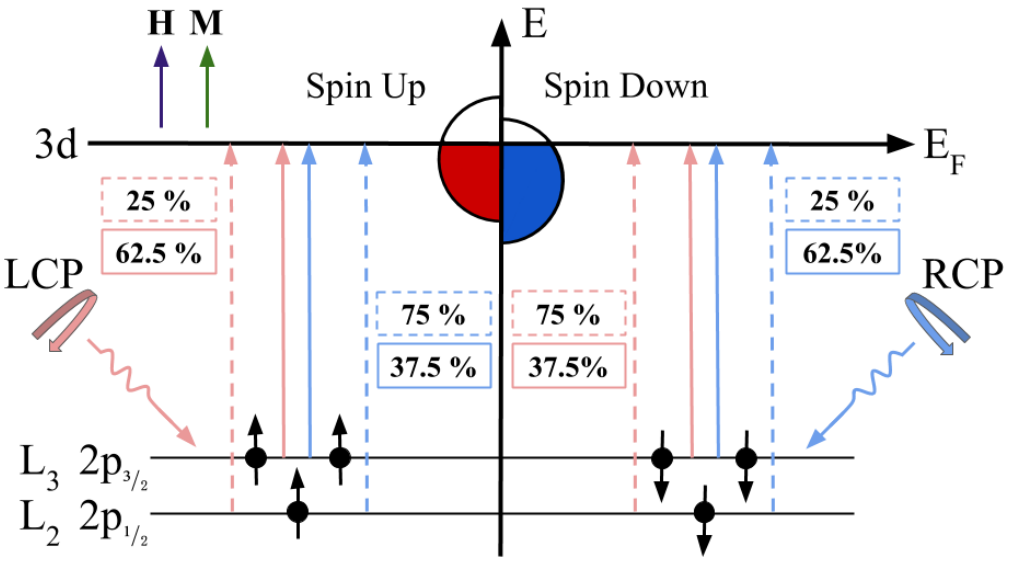

Figure 2.23: L-edge absorption one electron picture: transitions from $2p_{\frac{3}{2}}$ (solid line) and $2p_{\frac{1}{2}}$ (broken line) energy levels to the $3d$ band which is exchange split into $3d\uparrow$ and $3d\downarrow$. The SOI split $2p$ band emits spin polarised electrons when excited with circularly polarised X-rays, and the exchange split $3d$ band acts as a spin-detector. Transition probabilities for LCP ($\Delta m_l = +1$) and RCP ($\Delta m_l = -1$) are given in percentages.

transitions can be calculated from Fermi's Golden Rule

$$\sigma_{i\to f} = \frac{2\pi}{\hbar}|\langle\Phi_f|\hat{T}|\Phi_i\rangle|^2\rho_f(\hbar\omega - E_i) \tag{2.42}$$

where $\sigma_{i\to f}$ is the probability of transition from an initial core state $|\Phi_i\rangle$ to a final valence state $|\Phi_f\rangle$ by an absorption of an X-ray photon with energy $\hbar\omega$, $|\langle\Phi_f|\hat{T}|\Phi_i\rangle|$ is the matrix element of the electromagnetic field operator, ρ_f is the density of valence states above the Fermi energy and E_i is the core-level binding energy. The allowed transitions for an electron excited from the SOI split $2p$ energy levels to the exchange split $3d$ band and their probabilities are illustrated in Figure 2.23. Since the $p_{\frac{3}{2}}$ and $p_{\frac{1}{2}}$ energy levels have opposite SOI, the spin polarisation will be opposite at the corresponding L_3 and L_2 edges. This is reflected in the transition probabilities.

The quantisation axis of the $3d$ valence band 'detector' is determined by the magnetisation direction, and the size of the dichroism is proportional to $\mathbf{k}\cdot\mathbf{M} = |k||M|\cos(\theta)$ where θ is the angle between the wave vector of the incoming photon $\mathbf{k}$ and the magnetisation $\mathbf{M}$. Maximum dichroism is achieved for $\theta = 0, \pi$, i.e. the photon wave

vector and magnetisation are arranged in a parallel and anti-parallel configuration. For $\theta = \frac{\pi}{2}$ the intensities of the L_3 and L_2 peaks lie in between those obtained for parallel and anti-parallel alignment of photon wave vector and magnetisation.

Typical L-edge Mn XAS spectra for LCP (μ_+) and RCP (μ_-) X-ray radiation are shown in Figure 2.24 with the two characteristic L_3 and L_2 broad peaks. The XMCD

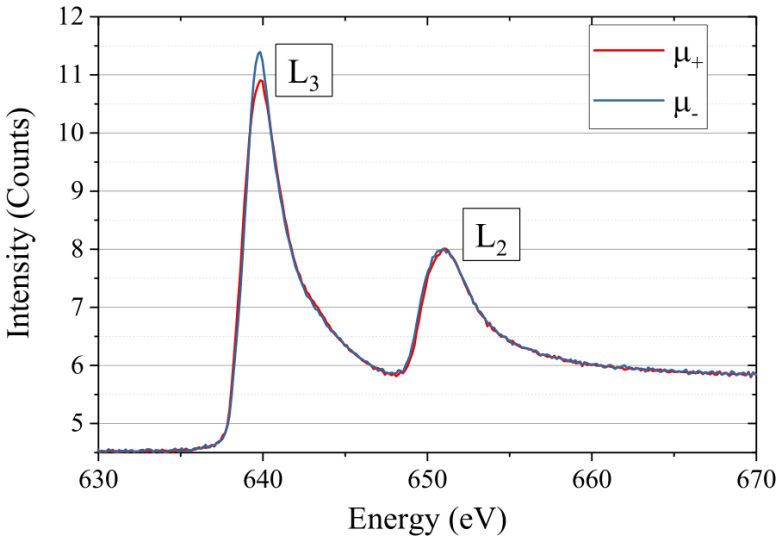

Figure 2.24: Mn L-edge XAS spectra performed with LCP (μ_+) and RCP (μ_-) X-rays.

spectrum is the difference of the μ_+ and μ_- XAS spectra and the average XAS spectrum μ_0 is approximated by $\frac{1}{2}(\mu_+ + \mu_-)$. A two-step background, which approximates the contribution from the unoccupied s, p states, is subtracted from the XAS spectrum before integration. The function $I(E)$ used for the background is given by

$$I(E) = I_0\left(\frac{1}{2} + \frac{1}{3}\tanh\left(\frac{E - E_{L_2}}{\Delta}\right) + \frac{1}{6}\tanh\left(\frac{E - E_{L_3}}{\Delta}\right)\right) \tag{2.43}$$

where I_0 is the intensity taken on the right hand side of the L_2 peak where the intensity begins to plateau (at 660 eV for Mn), E_{L_2} and E_{L_3} are the peak energies of the absorption edges and Δ is a broadening term. The integrated average XAS and XMCD spectra are used to quantitatively determine the ground state orbital and spin angular momenta via the sum rules [31; 32; 33]

$$\langle L_z \rangle = \left(\frac{2l(l+1)(4l+2-n)}{l(l+1)+2-c(c+1)}\right)\left(\frac{\int_{j_+ + j_-}(\mu_+ - \mu_-)d\omega}{\int_{j_+ + j_-}(\mu_+ + \mu_0 + \mu_-)d\omega}\right) \tag{2.44}$$

$$\langle S_z\rangle^{\text{eff}} = c_1(n)\langle S_z\rangle + c_2(n)\langle T_z\rangle = \frac{\int_{j_+}(\mu_+ - \mu_-)d\omega - (\frac{c+1}{c})\int_{j_-}(\mu_+ - \mu_-)d\omega}{\int_{j_+ + j_-}(\mu_+ + \mu_0 + \mu_-)d\omega} \quad (2.45)$$

with coefficients $c_1(n)$ and $c_2(n)$

$$c_1(n) = \frac{l(l+1)-2-c(c+1)}{3c(4l+2-n)}$$

$$c_2(n) = \frac{l(l+1)[l(l+1)+2c(c+1)+4]-3(c-1)^2(c+2)^2}{6lc(l+1)(4l+2-n)}$$

where for X-rays incident along the $\hat{z}$ direction, $\langle L_z\rangle$, $\langle S_z\rangle$ and $\langle T_z\rangle$ are the expectation values of the orbital momentum, spin momentum and magnetic dipole operators, respectively. There are integers: l is the orbital quantum number of the valence state, c is the orbital quantum number of the core state and n is number of electrons in the valence state. The spectra μ_+, μ_- and μ_0 are absorption spectra obtained with LCP, RCP and linearly polarised (parallel to the quantisation axis) X-ray radiation, respectively. The j_+ and j_- refer to the absorption edges with $j_+ = l + s$ and $j_- = |l - s|$.

For the $L_{3,2}$-edges of Mn, c = 1 (2p) and l = 2 (3d), so the equations 2.44 & 2.45 simplify to

$$\langle L_z\rangle = 2(10-n)\left(\frac{\int_{L_3+L_2}(\mu_+ - \mu_-)d\omega}{\int_{L_3+L_2}(\mu_+ + \mu_0 + \mu_-)d\omega}\right) \quad (2.46)$$

$$\langle S_z\rangle^{\text{eff}} = \langle S_z\rangle + \frac{7}{2}\langle T_z\rangle = \frac{3(10-n)}{2}\left(\frac{\int_{L_3}(\mu_+ - \mu_-)d\omega - 2\int_{L_2}(\mu_+ - \mu_-)d\omega}{\int_{L_3+L_2}(\mu_+ + \mu_0 + \mu_-)d\omega}\right) \quad (2.47)$$

Then substituting the expression for μ_0, using

$$\int_{L_2}(\mu_+ - \mu_-)d\omega = \int_{L_3+L_2}(\mu_+ - \mu_-)d\omega - \int_{L_3}(\mu_+ - \mu_-)d\omega$$

and recalling the orbital and spin angular momentum g-factors, $g_l = 1$ and $g_s = 2$, the expressions for the orbital and spin magnetic moments become

$$\mu_l = -g_l\langle L_z\rangle = -\frac{4(10-n)}{3}\left(\frac{\int_{L_3+L_2}(\mu_+ - \mu_-)d\omega}{\int_{L_3+L_2}(\mu_+ + \mu_-)d\omega}\right) \quad (2.48)$$

$$\mu_s = -g_s\langle S_z\rangle^{\text{eff}} = -(10-n)\left(\frac{6\int_{L_3}(\mu_+ - \mu_-)d\omega - 4\int_{L_3+L_2}(\mu_+ - \mu_-)d\omega}{\int_{L_3+L_2}(\mu_+ + \mu_-)d\omega}\right) \quad (2.49)$$

The sum rules assume that the transition from $2p$ core states to $3d$ valence states are well defined and that the $3d$ valence states are separable from other final states. This means that the L_3 and L_2 peaks are well separated as well as pure $2p_{\frac{3}{2}}$ and $2p_{\frac{1}{2}}$. However, in reality these conditions are only approximately satisfied with L_3 and L_2 absorption edges are not pure in character. Therefore, errors in the calculated orbital and spin moments from the sum rules are between 5-10 % [34; 35].

The anisotropies of the sublattice moments can be obtained by performing angle dependent measurements and applying an external magnetic field. Choosing the appropriate sample tilt angles, enables the construction of 2-D projections of magnetic moments. By balancing the torques the moment experiences in the presence of a magnetic field applied along the hard axis, the anisotropy constants can be calculated. The measurements and analysis is described in detail in Chapter 6.

References

[1] W. R. Grove, "Vii. on the electro-chemical polarity of gases," *Philosophical Transactions of the Royal Society of London*, vol. 142, pp. 87–101, 1852. (Cited on page: 47)

[2] J. E. Greene, "Review Article: Tracing the recorded history of thin-film sputter deposition: From the 1800s to 2017," *J. Vac.*, vol. 35, no. 5, p. 05C204, 2017. (Cited on page: 47)

[3] A. W. Hull, "The magnetron," *Journal of the A.I.E.E.*, vol. 40, no. 9, pp. 715–723, 1921. (Cited on page: 47)

[4] A. W. Hull, "The effect of a uniform magnetic field on the motion of electrons between coaxial cylinders.," *Phys. Rev.*, vol. 18, pp. 31–57, Jul 1921. (Cited on page: 47)

[5] F. Penning, "Die glimmentladung bei niedrigem druck zwischen koaxialen zylindern in einem axialen magnetfeld," *Physica*, vol. 3, no. 9, pp. 873 – 894, 1936. (Cited on page: 47)

[6] F. M. Penning, "Coating by cathode disintegration," U.S. patent 2,146,025 (7 February 1939). (Cited on page: 47)

[7] I. V. Tudose, F. Comanescu, P. Pascariu, S. Bucur, L. Rusen, F. Iacomi, E. Koudoumas, and M. P. Suchea, "Chapter 2 - chemical and physical methods for multifunctional nanostructured interface fabrication," in *Functional Nanostructured Interfaces for Environmental and Biomedical Applications* (V. Dinca and M. P. Suchea, eds.), Micro and Nano Technologies, pp. 15 – 26, Elsevier, 2019. (Cited on page: 47)

[8] J. D. Jackson, *Classical electrodynamics*. New York, NY: Wiley, 3rd ed. ed., 1999. (Cited on page: 56, 73)

[9] N. Ashcroft and N. Mermin, *Solid State Physics*. Philadelphia: Saunders College, 1976. (Cited on page: 57)

[10] A. L. Patterson, "The Scherrer Formula for X-Ray Particle Size Determination," *Phys. Rev.*, vol. 56, pp. 978–982, Nov. 1939. (Cited on page: 57)

[11] H. M. Rietveld, "A profile refinement method for nuclear and magnetic structures," *Journal of Applied Crystallography*, vol. 2, pp. 65–71, Jun 1969. (Cited on page: 57)

[12] P. P. Ewald, "Die Berechnung optischer und elektrostatischer Gitterpotentiale," *Annalen der Physik*, vol. 369, pp. 253–287, Jan. 1921. (Cited on page: 58)

[13] M. Renninger, "Umweganregung, eine bisher unbeachtete wechselwirkungserscheinung bei raumgitterinterferenzen," *Z. Phys.*, vol. 106, pp. 141–176, 1937. (Cited on page: 59)

[14] L. J. van der Pauw, "A method of measuring specific resistivity and hall effect of discs of arbitrary shape," *Philips Research Reports*, vol. 13, pp. 1–9, 1958. (Cited on page: 64)

[15] L. J. van der Pauw, "A method of measuring the resistivity and hall coefficient on lamellae of arbitrary shape," *Philips Research Reports*, vol. 20, pp. 220–224, 1958. (Cited on page: 64)

[16] N. Nagaosa, J. Sinova, S. Onoda, A. H. MacDonald, and N. P. Ong, "Anomalous Hall effect," *Rev. Mod. Phys.*, vol. 82, no. 2, pp. 1539–1592, 2010. (Cited on page: 67)

[17] T. Seki, S. Iihama, T. Taniguchi, and K. Takanashi, "Large spin anomalous Hall effect in $L1_0-$FePt: Symmetry and magnetization switching," *Phys. Rev. B*, vol. 100, p. 144427, Oct 2019. (Cited on page: 67)

[18] P. W. Anderson and J. M. Rowell, "Probable observation of the josephson superconducting tunneling effect," *Phys. Rev. Lett.*, vol. 10, pp. 230–232, Mar 1963. (Cited on page: 67)

[19] B. Josephson, "Possible new effects in superconductive tunnelling," *Physics Letters*, vol. 1, no. 7, pp. 251 – 253, 1962. (Cited on page: 67)

[20] A. Barone and G. Paterno, *Physics and Applications of the Josephson Effect*. New York: John Wiley & Sons, 1982. (Cited on page: 68)

[21] G. Binnig, C. F. Quate, and C. Gerber, "Atomic force microscope," *Phys. Rev. Lett.*, vol. 56, pp. 930–933, Mar 1986. (Cited on page: 69)

[22] J. E. Jones, "On the determination of molecular fields. —ii. from the equation of state of a gas," *Proc. R. Soc. Lond. Series A*, vol. 106, no. 738, pp. 463–477, 1924. (Cited on page: 71)

[23] M. Faraday, "On the magnetization of light and the illumination of magnetic lines of force," *Reprinted in Experimental researches in electricity, vol. III, ser. XIX*, pp. 2146–2242, 1855. (Cited on page: 72)

[24] J. Kerr, "Xliii. on rotation of the plane of polarization by reflection from the pole of a magnet," *The London, Edinburgh, and Dublin Philosophical Magazine and Journal of Science*, vol. 3, no. 19, pp. 321–343, 1877. (Cited on page: 72)

[25] S. Pathak and M. Sharma, "Polar magneto-optical kerr effect instrument for 1-dimensional magnetic nanostructures," *J. Appl. Phys.*, vol. 115, no. 4, p. 043906, 2014. (Cited on page: 72)

[26] A. Chtchelkanova, S. Wolf, and Y. Idzerda, *Magnetic Interactions and Spin Transport*. Springer, 01 2003. (Cited on page: 75)

[27] E. M. GmbH, "Magneto-optical kerr microscope and magnetometer - standard microscope." `http://www.evico-magnetics.de/Standard.html`, 2020. (Cited on page: 80)

[28] I. V. Soldatov and R. Schäfer, "Advanced MOKE magnetometry in wide-field kerr-microscopy," *J. Appl. Phys.*, vol. 122, no. 15, p. 153906, 2017. (Cited on page: 80)

[29] K. E. Siewierska, N. Teichert, R. Schäfer, and J. M. D. Coey, "Imaging domains in a zero-moment half metal," *IEEE Trans. Mag.*, vol. 55, no. 2, pp. 1–4, 2019. (Cited on page: 81)

[30] G. Schütz, W. Wagner, W. Wilhelm, P. Kienle, R. Zeller, R. Frahm, and G. Materlik, "Absorption of circularly polarized x rays in iron," *Phys. Rev. Lett.*, vol. 58, pp. 737–740, Feb 1987. (Cited on page: 85)

[31] B. T. Thole, P. Carra, F. Sette, and G. van der Laan, "X-ray circular dichroism as a probe of orbital magnetization," *Phys. Rev. Lett.*, vol. 68, pp. 1943–1946, Mar 1992. (Cited on page: 88)

[32] M. Altarelli, "Orbital-magnetization sum rule for x-ray circular dichroism: A simple proof," *Phys. Rev. B*, vol. 47, pp. 597–598, Jan 1993. (Cited on page: 88)

[33] P. Carra, B. T. Thole, M. Altarelli, and X. Wang, "X-ray circular dichroism and local magnetic fields," *Phys. Rev. Lett.*, vol. 70, pp. 694–697, Feb 1993. (Cited on page: 88)

[34] W. L. O'Brien and B. P. Tonner, "Orbital and spin sum rules in x-ray magnetic circular dichroism," *Phys. Rev. B*, vol. 50, pp. 12672–12681, Nov 1994. (Cited on page: 90)

[35] C. Piamonteze, P. Miedema, and F. M. F. de Groot, "Accuracy of the spin sum rule in xmcd for the transition-metal *l* edges from manganese to copper," *Phys. Rev. B*, vol. 80, p. 184410, Nov 2009. (Cited on page: 90)

3
Magnetic Annealing Effects

3.1 Magnetic Annealing of Mn_2Ru_xGa Thin Films

The effect of vacuum annealing thin films of the compensated ferrimagnetic half-metal Mn_2Ru_xGa at temperatures from 250 °C to 400 °C is investigated. If MRG is to be integrated into a device manufactured using silicon-based CMOS technology, the MRG layer will have to be able to survive the relevant processing conditions without modification of properties, and must be smooth. A major concern is the potential diffusion of elements in and from the MRG layer [1]. It is also important to understand how the properties of MRG may change due to the annealing at various temperatures. More fundamentally, there is an opportunity to examine the relation between the net magnetisation M and Hall resistivity ρ_{xy} for one sublattice in a half-metallic ferrimagnet [2]. The 39.3 nm films deposited on (100) MgO substrates exhibit perpendicular magnetic anisotropy due to a small $\sim 1\%$ tetragonal elongation induced by the substrate strain. The main change on annealing is a modification in the compensation temperature T_{comp}, which first increases from 50 K for the as-deposited $Mn_2Ru_{0.7}Ga$ thin film to 185 K after annealing at 250 °C, and then falls to 140 K after annealing at 400 °C. There are minor changes in the atomic order, coercivity, resistivity, and anomalous Hall effect (AHE), but the net magnetisation measured by SQUID magnetometry with the

field applied in-plane or perpendicular-to-the-plane changes more significantly. It saturates at $20-30$ kA m^{-1} at room temperature, and a small soft component is seen in the perpendicular SQUID loops, which is absent in the square AHE hysteresis loops. This is explained by the half-metallic nature of the compound; the AHE probes only the 4*c* Mn sublattice that provides the spin-polarised electrons at the Fermi level, whereas the SQUID measures the sum of the oppositely aligned 4*c* and 4*a* sublattice magnetisations.

3.1.1 Sample Preparation

An epitaxial thin film of MRG was grown by DC magnetron sputtering, using our Shamrock sputtering system, on a $25\,\text{mm}^2 \times 25\,\text{mm}^2$ (100) MgO substrate. The film was co-sputtered in argon from two $75\,\text{mm}^2$ targets of Mn_2Ga and Ru onto the substrate maintained at 380 °C. The chosen composition was $Mn_2Ru_{0.7}Ga$, which exhibits compensation below room temperature. The film was capped in situ with a 3 nm layer of AlO_x deposited at room temperature in order to prevent oxidation. The large sample was diced into four equal squares, and smaller pieces for subsequent treatment and measurements. Pieces of the thin film were annealed in a vacuum of 10^{-6} mbar in a perpendicular magnetic field of 800 mT for 1 h. The annealing temperatures chosen were 250 °C, 300 °C, 350 °C, and 400 °C. Provided the annealing temperature is kept below 400 °C, the cubic inverted Heusler (*XA*) crystal structure of MRG is maintained and Mn diffusion out of the film is minimised.

3.1.2 Structural Characterisation

A Bruker D8 X-ray diffractometer was used to determine the diffraction patterns of the thin films. Low angle X-ray reflectivity was measured using a Panalytical X'Pert Pro diffractometer, and thickness was found by fitting the interference pattern using X'Pert Reflectivity software with a least square fit. X-ray data on the films are shown in Figures 3.1 & 3.2. Fitting the X-ray reflectivity in Figure 3.1 gives a film thickness of 39.3 nm. There are no significant differences among four samples taken from different parts of the large film. The diffraction patterns in Figure 3.2 of the as-deposited $Mn_2Ru_{0.7}Ga$ film and samples annealed at 250 °C, 300 °C, 350 °C, and 400 °C in the

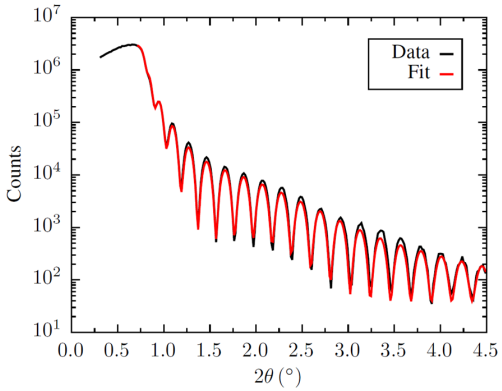

Figure 3.1: XRR of the as-deposited $Mn_2Ru_{0.7}Ga$ thin film. Fitting for a thickness of 39.3 nm and a density of 8.3 g cm^{-3}.

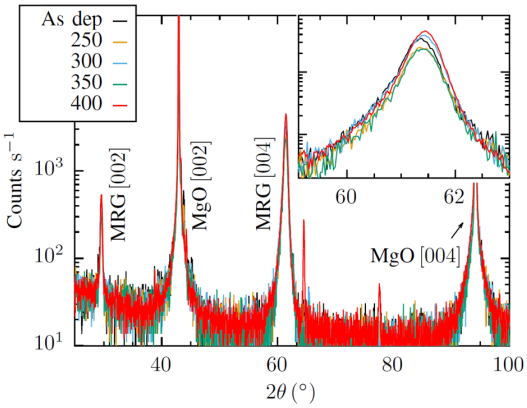

Figure 3.2: XRD pattern of $Mn_2Ru_{0.7}Ga$ thin films on MgO substrate at different anneal temperatures. Inset: (004) peak of MRG

perpendicular magnetic field exhibit (002) and (004) reflections from the MRG, together with peaks from the MgO substrate. There are only small changes in the relative (002) and (004) peak intensities $\left(\frac{I(002)}{I(004)}\right)$ on annealing, in the range 0.11-0.14 (Table 3.1). This small value is indicative of a high degree of atomic order in the inverted cubic Heusler structure (*XA*) [2]. The broadening of the (002) reflection is consistent with the measured MRG film thickness. Peak shifts on annealing are very small, and the *c* parameter of 604.2 pm decreases by only about 0.6 pm (Table 3.1).

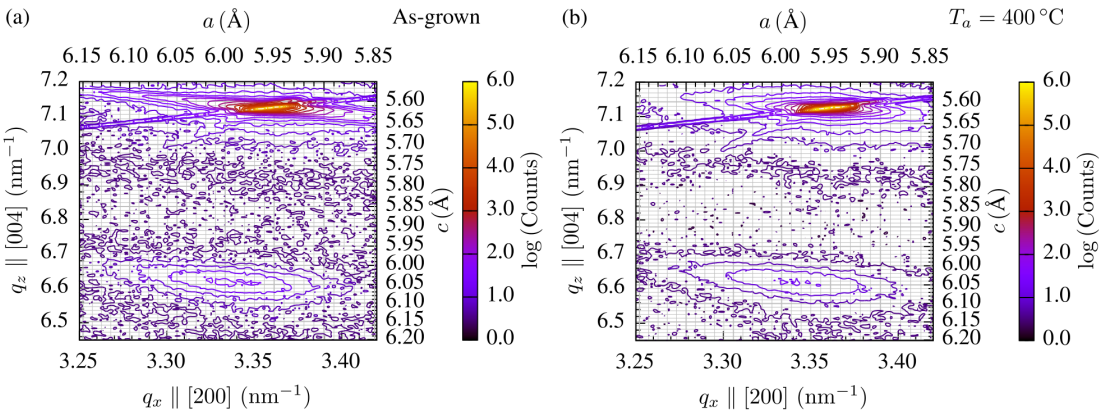

Figure 3.3: RSM of MgO (113) peak and (a) as-deposited MRG(204) peak and (b) MRG annealed at $T_a = 400\,°C$ (204) peak. The lattice parameters are calculated with respect to the MRG unit cell.

A reciprocal space map, shown in Figure 3.3 (a), of the as-deposited film confirms the c parameter, and shows a distribution of a parameters around the central value of 595.8 pm, which corresponds to that of MgO, to 604 pm. The map for the film annealed at 400 °C, in Figure 3.3 (b), is very similar showing that the crystal structure is practically unchanged by annealing. The ≈ 1 % substrate-induced tetragonal expansion of the cubic *XA* cell is responsible for the perpendicular magnetic anisotropy of the films.

3.1.3 Magnetotransport and Magnetisation Characterisation

Longitudinal and Hall resistivity were measured using the four-point Van der Pauw method with indium contacts and an applied current of 5 mA. For $Mn_2Ru_{0.7}Ga$ films, the calculated longitudinal ρ_{xx} and anomalous Hall ρ_{xy} resistivity values show no significant variation on annealing. The Hall angle was 0.7%, and did not vary significantly from sample to sample. The almost perfectly square anomalous Hall loops are shown in Figure 3.4, where the coercivity H_c^{AHE} is close to 450 mT, regardless of annealing temperature. Measurements of the magnetisation with the magnetic field applied perpendicular or parallel to the surface of the films were carried out using a 5 T Quantum Design SQUID. Hysteresis loops were measured in fields up to 5 T, at temperatures between 100 K and room temperature. These data were corrected for the diamagnetism of the substrate. Thermal scans in 30 mT after saturation of the magnetisation at room temperature were used to determine the compensation temperatures of the annealed and unannealed films. Those scans were performed on three of the samples, which are as-deposited MRG and MRG annealed at 250 °C and 400 °C. Data in Figure 3.5 show a compensation temperature T_{comp} of about 50 K for the as-deposited sample. There is a large Curie law upturn coming from a few ppm of Fe^{2+} in the MgO substrate, and the magnetisation of the film, therefore, does not cross zero. Compensation shifts to 185 K for a sample annealed at 250 °C, and is at 140 K in the sample annealed at 400 °C (Table 3.1). The measurements are performed in a small magnetic field. The magnetic moment of the substrate was found to be about -24.5 pAm^2 and the shift in T_{comp} due to this moment is about 0.15 K, which is negligible. In the SQUID measurements performed at room temperature (Figure 3.6), the as-deposited sample exhibits a square perpendicular hysteresis loop with a coercivity of 466 mT,

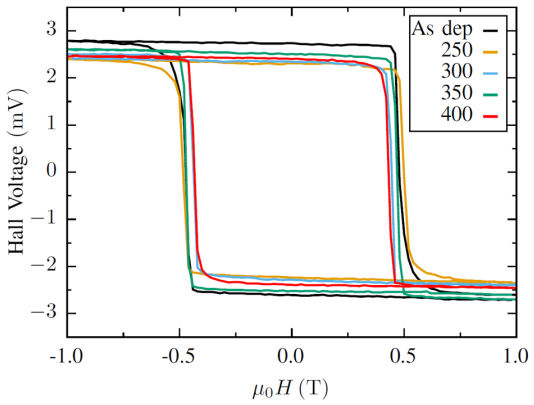

Figure 3.4: Anomalous Hall effect measured at room temperature in $Mn_2Ru_{0.7}Ga$ annealed at various temperatures. The data have been vertically centered.

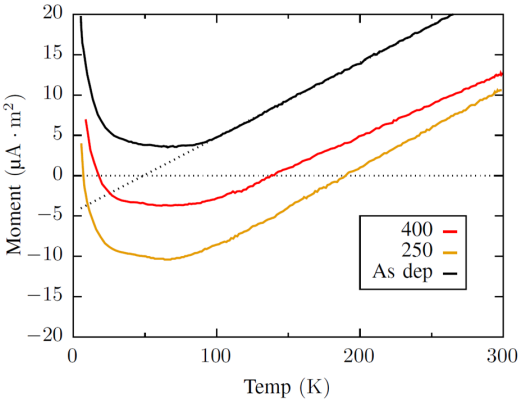

Figure 3.5: Temperature dependence of moment, measured at remanence (small applied field of 30 mT) of as-deposited $Mn_2Ru_{0.7}Ga$ thin film, and annealed at 250 °C and 400 °C.

but with clear signs of an easily saturating component, which was not seen in the AHE data of Figure 3.4. The parallel magnetisation also shows an easily saturated in-plane component and the net magnetisation approaches saturation in fields of order 5 T. The magnetocrystalline anisotropy constant K_u is given by $K_u = \frac{1}{2}\mu_0 H_a M_s$, where μ_0 is the vacuum permeability, H_a is the anisotropy field, and M_s is saturation magnetisation. Assuming an anisotropy field of 5 T and a net magnetisation of 20 kA m^{-1}, we find K_u to be 50 kJm^{-3}. After annealing at 250 °C, the coercivity decreases and the hysteresis is a little squarer, although the shape of the loop changes with temperature. The easily saturated component is larger and appears in the perpendicular loops of the films annealed at 300 °C and 350 °C, but vanishes in the film annealed at 400 °C. There the coercivity is only 265 mT, or just over half of the original value, and strikingly different from that measured by AHE in smaller fields (Table 3.1). The easily saturated in-plane component increases in magnitude with annealing, becoming almost equal to the out-of-plane moment. The overall decrease in coercivity and the features of the hysteresis loops may be related to the variation in concentration of Ru across the thickness MRG film, with more Ru found closer to the capping layer as found by transmission electron microscopy. The AHE measurement was repeated in 5 T saturation field and shows a coercivity of 207 mT, as shown in Figure 3.7.

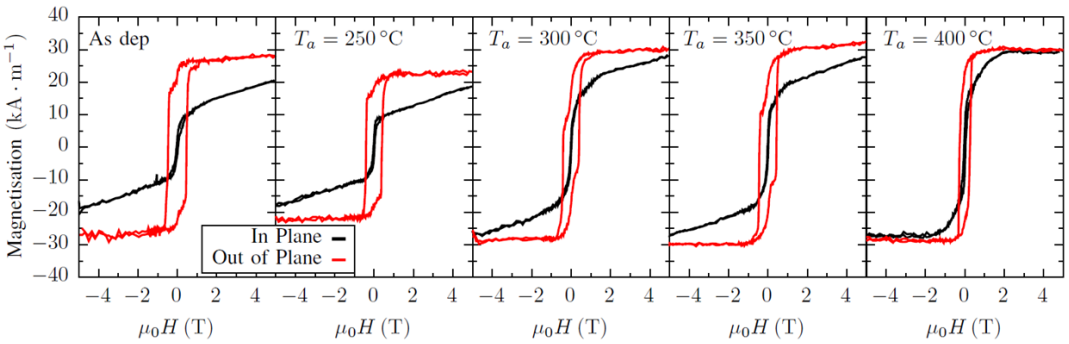

Figure 3.6: Magnetisation versus applied field, perpendicular and parallel to the surface of the $Mn_2Ru_{0.7}Ga$ thin films.

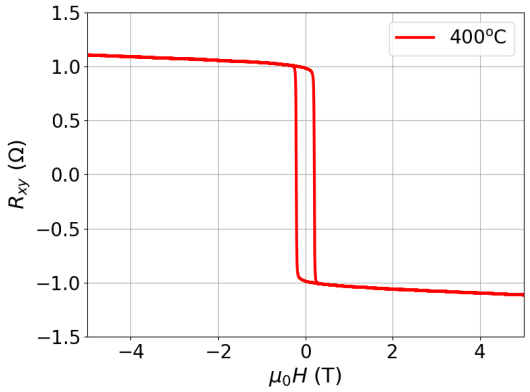

Figure 3.7: Anomalous Hall effect measured at room temperature in $Mn_2Ru_{0.7}Ga$ annealed 400 °C with +5 T saturation. The data has been vertically centered.

T_a (°C)	$\frac{I_{(002)}}{I_{(004)}}$	c (pm)	$H_c^{M(H)}$ (mT)	H_c^{AHE} (mT)	$\frac{H_c^{AHE}}{H_c^{M(H)}}$	T_{comp} (K)
-	0.140	604.1	466	485	1.04	50
250	0.143	604.4	413	495	1.20	185
300	0.119	603.6	406	441	1.09	-
350	0.145	603.8	432	475	1.10	-
400	0.119	603.6	265	434, 207*	1.64	140

Table 3.1: Data for as-deposited and annealed $Mn_2Ru_{0.7}Ga$ films

*After saturation in 5 T

3.1.4 Conclusion

Our studies of the effects of annealing the compensated ferrimagnetic half-metal have shown changes in c-lattice parameter of $0.1 - 0.2$ %, with minor modifications of the perpendicular anisotropy in films annealed up to 350 °C for one hour. The compensation temperature can vary, however, by as much as 130 K. Since T_{comp} depends on the balance between the two manganese sublattices, it is very sensitive to slight changes in site population due to redistribution of magnetic Mn and non-magnetic Ga or Ru atoms on the two different sites. The issue of diffusion in a multilayer structure is addressed in Section 3.2. The 4c sublattice moment shows near-perfect square minor loops in the 1 T AHE measurements, but this does not persist after saturation in 5 T. The hysteresis of the net magnetisation measured by SQUID magnetometry, which reflects the difference of the two sublattice moments, is more complex and it reflects the misalignment of the 4a moment with the c-axis. The minor changes in the structure of MRG and its AHE measured in small fields bodes well for its use in devices annealed at temperatures up to 350 °C.

3.2 Magnetic Annealing of Mn_2Ru_xGa based Spin-valves with Varying Spacers

The effects of annealing in magnetoresistive devices has been demonstrated with serendipitous outcomes. The crystallisation of MgO/CoFeB interfaces results in a drastic increase of TMR ratio due to coherent tunnelling, while the diffusion of Ta and other species into the active portion of the device can have deleterious consequences [3; 4; 5; 6]. The MgO/CoFeB electrode structure is the industry choice for TMR applications. Annealing temperatures for crystallisation of CoFeB into bcc structure are typically above 320 °C, depending on boron content. A major concern with incorporating Mn_2Ru_xGa(MRG) into device structures, is diffusion of Mn which can affect the crystal structure, magnetic properties as well as interfaces within a device. Recently, it was demonstrated that an ultrathin Ta dusting layer can be used to mitigate the effects of diffusion between MRG and an MgO barrier [7], though this impacts the TMR of the device due to the short diffusion length of Ta. There is a need for other materials which can minimise Mn diffusion and maintain the structural and magnetic

properties of MRG during an annealing process. The aim of this study is to prepare spin-valve structures where MRG and Co/Pt multilayer serve as a fixed and free layers, respectively. The two layers will be separated by a spacer layer with thickness $t = 1.4$, 2.0 nm. Five spacer materials have been selected for the study based on their close lattice match to MRG as well as their potential use as a diffusion barrier. The crystalline and magnetotransport properties of the heterostructures will be investigate pre- and post- annealing at at 350 °C to determine the performace of each material as a diffusion barrier.

3.2.1 Sample Preparation

Spin-valve structures of the form

$$\text{MgO//Mn}_2\text{Ru}_{0.7}\text{Ga(30 nm)/}y(t)\text{/ [Co(0.4 nm)/ Pt(0.8 nm)]}_8\text{/Co(0.4 nm)/Pt(3 nm)}$$

were prepared with the spacer layer, y, with $t = 1.4$ nm and 2 nm. The structure uses a Co/Pt multilayer as the free layer so as to produce perpendicular anisotropy without requiring lattice matching as in the MgO/CoFeB system. The materials selected for the study are given in Table 3.2.

Material $y(t)$	Comment
TiN	Known diffusion barrier, close lattice matching to MgO should allow for crystalline growth on MRG at high temperature
Hf	Ultrathin layers previously shown to promote coupling between MRG and CoFeB [1]
HfO_x	Used as high-k barrier (gate dielectric) in the semiconductor industry
V	Known as a getter for Al
Mo	Low affinity for alloying with Mn

Table 3.2: Summary of selected spacer materials.

All films deposited onto single crystal MgO (001) substrates in a SFI Shamrock sputter tool by DC sputtering except TiN which was deposited by RF sputtering. Base pressure was $< 2 \times 10^{-8}$ Torr. MRG is deposited at 320 °C by co-sputtering from an Mn_2Ga target and a Ru target. The particular stoichiometry of MRG used here was

chosen as it had a T_{comp} below room temperature (RT), with an as-deposited coercivity of $H_C \approx 380$ mT. All other materials were deposited after cooling down to room temperature, except for two spacer layers of TiN grown immediately after MRG at its deposition temperature. HfO_x was formed by natural oxidation of metallic Hf films. Magnetic annealing (MA) is carried out at 350 °C for 1 hour in a perpendicular field of 800 mT.

3.2.2 Results

Structural properties, such as XRD and XRR, were measured using a Panalytical X'Pert tool using Cu K_α radiation. Crystallographic data was analysed by fitting a Voigt function to the peak, taking into consideration $K_{\alpha 2}$ and instrumental broadening characterised using NIST 1976b. As-deposited MRG is single textured, with c-axis orientation perpendicular to the substrate surface. This gives us two diffraction peaks in our range of 2θ, namely (002) and (004). The magnetic properties are dependent on the crystalline characteristics, hence any changes in the magnetotransport should be relatable to changes in parameters such as the out-of-plane lattice parameter c, crystal coherence length L_c perpendicular to the film (using the Scherrer formula) and the ratio of intensities of the two peaks $I(002)/I(004)$. The (004) is significantly more intense than the (002) due to the situation of the strongly scattering Ru^{4d} site within this set of planes, making analysis much simpler using this peak primarily. This also gives us a metric for the degree of disorder within the crystal, as Ru moving to other sites will increase the intensity of the (002) peak. Magnetotransport is measured using Van der Pauw method in a 1 T GMW magnet. Squareness of the Hall signal, i.e. the ratio of Hall voltage at saturation to that at remanence, is used an indicator of its perpendicular anisotropy.

3.2.2.1 Co/Pt superlattice

The magnetic properties of a Co/Pt superlattice are strongly dependent on the quality of the interfaces between the various layers, i.e. the roughness and degree of intermixing. The Pt layer induces an interfacial anisotropy which gives rise to a perpendicular magnetic moment, and is independent of the crystal structure of the superlattice. The superlattice peaks are determined by the strain at interfaces between the Co and Pt

which result in a d-spacing which is found between the expected values for each [8]. This can be controlled by changing the thickness of each layer, thereby altering the propagation of strain through the superlattice. This means we can achieve PMA independently of the seed layer used, which was the case for all films as-deposited despite a variety of superlattice peaks present as shown in Table 3.3.

Material $y(t)$	Peaks present before MA	Peaks present after MA	PMA present after MA
HT TiN(1.4 nm)	Co/Pt(200)	Co/Pt(200)	No
HT TiN(2.0 nm)	Co/Pt(200)	Co/Pt(200)	No
RT TiN(1.4 nm)	Co/Pt(200)	Co/Pt(200)	No
RT TiN(2.0 nm)	Co/Pt(200)	Co/Pt(200)	No
Hf(1.4 nm)	-	-	No
Hf(2.0 nm)	-	-	No
HfO_x(1.4 nm)	-	Co/Pt(200)	No
HfO_x(2.0 nm)	-	-	No
V(1.4 nm)	Co/Pt(200) Co/Pt(111)	Co/Pt(200)	No
V(2.0 nm)	Co/Pt(200) Co/Pt(111)	Co/Pt(200)	No
Mo(1.4 nm)	Co/Pt(200)	Co/Pt(200)	No
Mo(2.0 nm)	Co/Pt(220)	Co/Pt(220)	Yes

Table 3.3: Summary of crystalline structure changes in Co/Pt multilayers, before and after magnetic annealing (MA).

3.2.2.2 Titanium Nitride (TiN)

The lattice parameter of TiN is closely matched to the MgO (4.24 vs. 4.212 Å). Due to this, it has a high potential as a spacer material for MRG-based GMR devices. TiN is widely used in the semiconductor and spintronics industries as a diffusion barrier and should be capable of withstanding the typical temperatures used during wafer processing. A crystalline spacer can be grown at high temperature (same as the deposition temperature of MRG), or amorphous at room temperature. Both have been investigated for their suitability.

The XRD patterns of the spin-valve structure with TiN spacers, both crystalline and amorphous, before and after magnetic annealing, for two thicknesses of 2 nm and

1.4 nm are shown in Figures 3.8 and 3.9. There is a small sharp peak at 40.5°, which

correspond to the Pt (111) reflection. The as-deposited state shows minor variation in

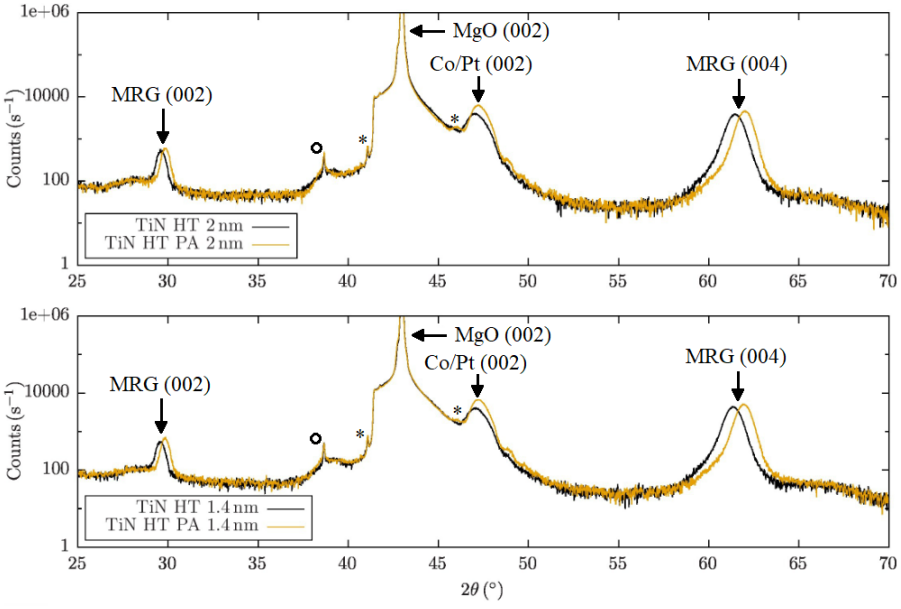

Figure 3.8: XRD of spin-valve structures with a TiN spacer layer, deposited at 320 °C high temperature (HT), with spacer thickness t = 1.4, 2.0 nm, pre- and post-annealing (PA). The peaks labelled with a * are bbc Pt peaks and a ○ are sample holder peaks.

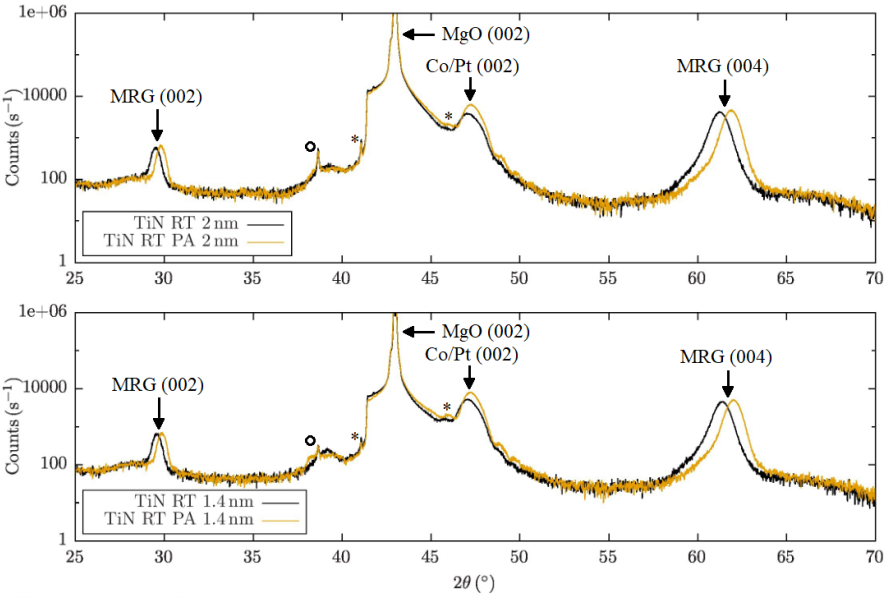

Figure 3.9: XRD of spin-valve structures with a TiN spacer layer, deposited at room temperature (RT), with spacer thickness $t = 1.4$, 2.0 nm, pre- and post-annealing (PA). The peaks labelled with a * are bbc Pt peaks and a ○ are sample holder peaks.

the MRG (004) peak position, with an additional peak at 47.056° that can be attributed to Pt (200). The TiN (002) peak for the crystalline spacers is not visible due to the close proximity of the MgO (002) peak. After magnetic annealing, MRG (004) peak in all XRD patterns has shifted to higher angles, indicating a reduction in the d-spacing. We can also note the increased intensity and shift of the Pt (200) peak, as well as the emergence of Kiessig fringes around the peak, all of which suggests a greater degree of ordering.

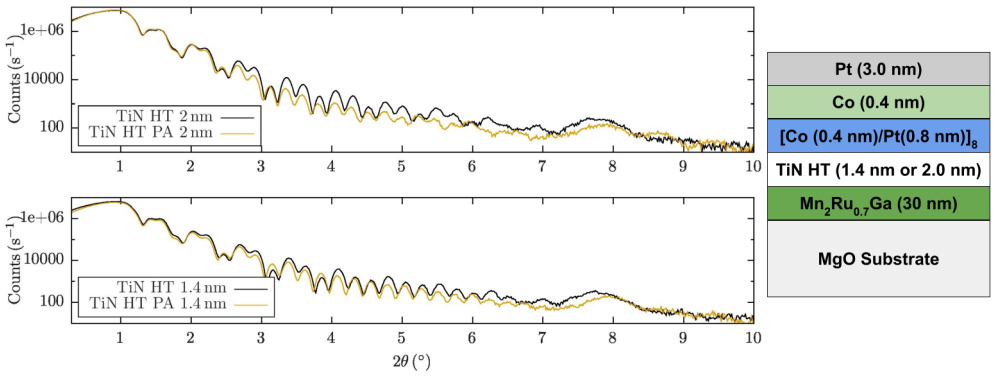

Figure 3.10: Left: XRR of spin-valve structures with a TiN spacer layer, deposited at 320 °C high temperature (HT), with spacer thickness $t = 1.4$, 2.0 nm, pre- and post-annealing (PA). **Right**: Illustration of the stack.

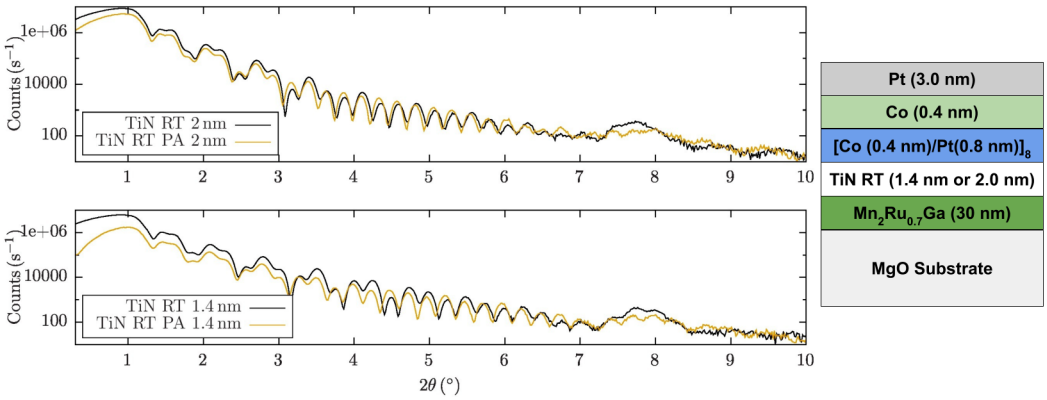

Figure 3.11: Left: XRR of spin-valve structures with a TiN spacer layer, deposited at room temperature (RT), with spacer thickness $t = 1.4$, 2.0 nm, pre- and post-annealing (PA). **Right**: Illustration of the stack.

The XRR patterns of the stacks are shown in Figures 3.10 and 3.11. We can see that the interfacial structure is well maintained, with only minor changes in the spectrum that can arise from changes in interface roughness. This is particularly clear in the amorphous RT TiN stacks. This suggests that there is little diffusion across the TiN spacer, however the characteristic multilayer node at $\approx 8°$ appears shifted to higher angles in the case of HT TiN and gains some fine detail in the RT TiN stacks.

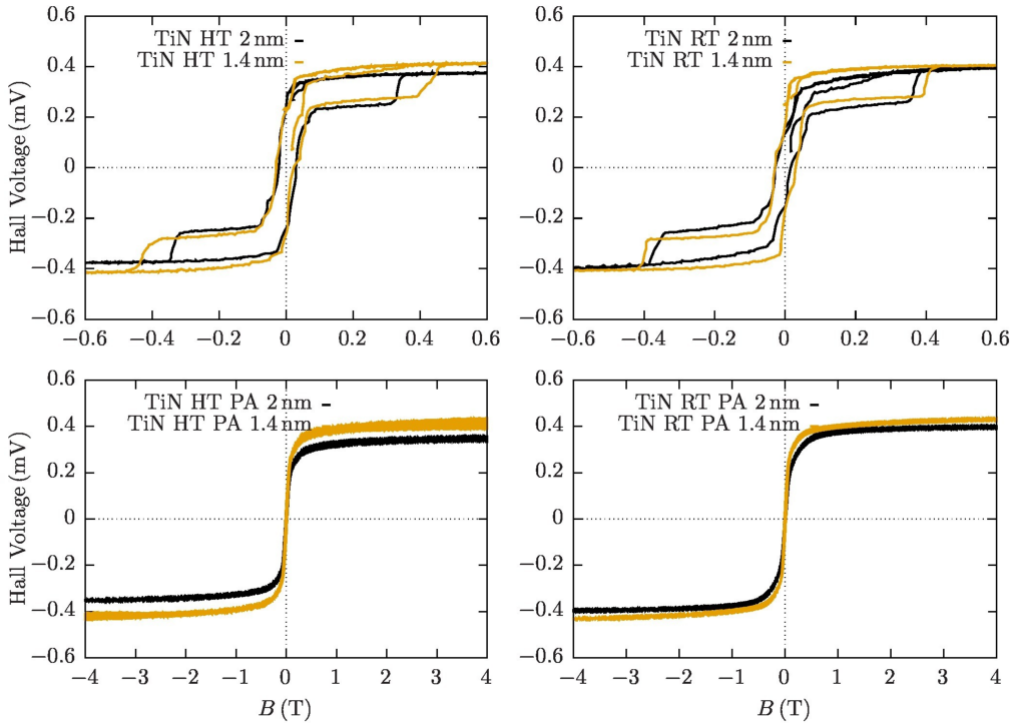

Figure 3.12: AHE of spin-valve structures with a TiN spacer layer, deposited at high (HT) and room (RT) temperature, with spacer thickness $t = 1.4$, 2.0 nm, pre- and post-annealing (PA).

Anomalous Hall effect (AHE) measurements are shown in Figure 3.12. Before annealing, the switching fields for both the Co/Pt and MRG layers are clearly visible, with coercivity of ≈ 50 mT and ≈ 400 mT respectively. The Co/Pt appears to have partially in-plane anisotropy due to the emergence of bulk order of the Pt layers of the stacks. The HT TiN stacks appear to have a more square free layer switch as compared to the RT TiN stacks. After annealing, the MRG no longer switches even up to fields of 4 T. The shift in MRG(004) peak in XRD data suggests that the MRG is no longer tetragonally distorted leading to in-plane anisotropy and hence it produces no observable hysteresis. At this point, the Co/Pt appears to lie almost totally in-plane. The change in MRG can be attributed to the loss of Mn from the film, which may be due to alloying with Ti or N from the spacer layer. Both phase diagrams indicate a degree of solubility at the annealing temperature. In summary, annealing causes significant disruption to the crystal quality of the MRG layer leading an to in-plane moment of MRG. There is little diffusion, however Mn is lost due to intermixing at

the MRG/TiN interface. Co/Pt begins slightly in-plane already due to development of Pt(200) texture, reducing local *XA* structure at Co/Pt interface.

3.2.2.3 Hafnium (Hf)

Hf has a similar lattice constant to MgO (a = 4.44 Å in the fcc phase). It is expected to be a good candidate to form an epitaxial film on MRG. It has been demonstrated to allow for a form of exchange coupling between MRG and a ferromagnetic layer as a dusting layer between them. [1]

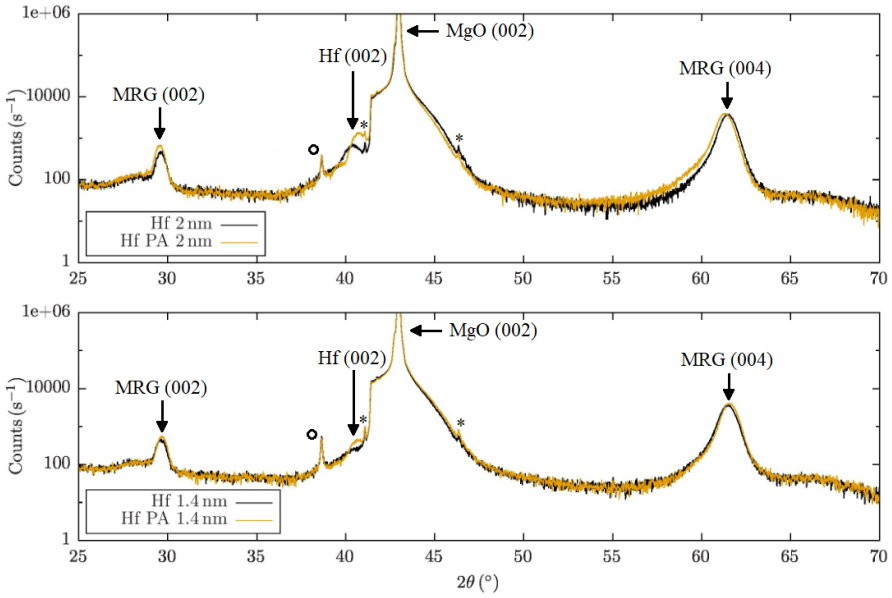

Figure 3.13: XRD of spin-valve structures with a Hf spacer layer, with thickness t = 1.4, 2.0 nm, pre- and post-annealing (PA). The peaks labelled with a * are bbc Pt peaks and a ○ are sample holder peaks.

In XRD patterns in Figure 3.13, the MRG(004) is present and stable between the two stacks. Hf (002) peak is visible in the stack with the 2 nm thick Hf spacer. Co/Pt peaks are absent from the pattern suggesting that an interfacial requirement to promote a crystalline texture within the Co/Pt has not been satisfied. After annealing, there is a minor shift in the MRG (004) position, however there is a strong improvement in the ordering of the Hf. This is indicated by the emergence of the Hf (002) peak in the $t = 1.4$ nm stack, as well as the development of Kiessig fringes around the peak in the $t = 2$ nm stack.

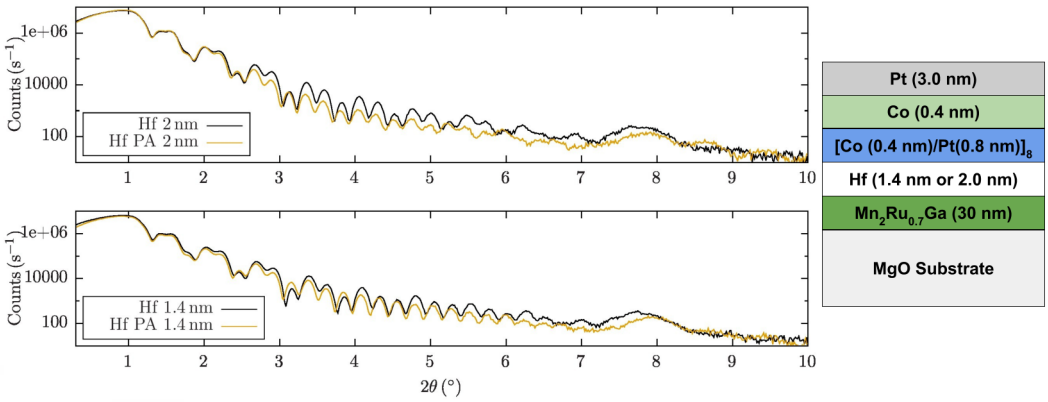

Figure 3.14: Left: XRR of spin-valve structures with a Hf spacer layer, with thickness $t = 1.4$, 2.0 nm, pre- and post-annealing (PA). **Right**: Illustration of the stack.

The stability of the MRG(004) peak suggests that there is a very little diffusion occurring in the stack, which is supported by the XRR pattern, shown in Figure 3.14. Similar to the TiN spacers, the interfacial structure appears to be intact after annealing. The $t = 2$ nm stacks appear to be less stable than the $t = 1.4$ nm stack, which may be related to an increase in roughness between Co and Pt layers. The characteristic multilayer node at 7.5° does not present with any fine detail after annealing in either case, which suggests the Co/Pt film has no preferred texture, though it does shift slightly.

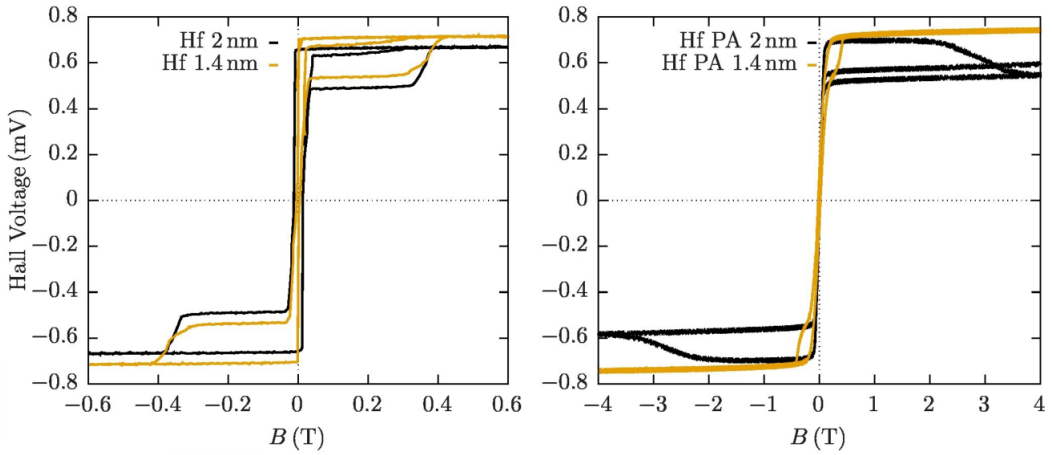

Figure 3.15: EHE of spin-valve structures with a Hf spacer layer, with thickness $t = 1.4$, 2.0 nm, pre- and post-annealing (PA).

Prior to annealing, the heterostructure exhibits a very square response in AHE from

both the Co/Pt free layer with coercivity < 50 mT and the MRG film appears to be almost identical in each stack with coercivity ≈ 350 mT, as shown in Figure 3.15. This suggests that the as-deposited MRG/Hf bottom layer is a very suitable seed for Co/Pt. However, after annealing the hysteresis of the Co/Pt free layer is less square. In the case of $t = 1.4$ nm stack, the MRG switches at roughly the same coercive field, which is in agreement with the very small shift to higher angles in the MRG peak observed in XRD. In contrast, the MRG layer in the $t = 2$ nm stack appears to be now switching in the opposite direction to the free layer. This is because the sign in AHE has changed, which is indicative of increase in T_{comp} from below to above RT. This is also in agreement with XRD data where a small shift to lower angles was observed, increasing tetragonality and hence strain in the sample which influences T_{comp}. In general, the structure and transport properties of Hf-based stacks are relatively robust, which suggests that Hf may be a good candidate as spacer for MRG-based GMR devices. The disadvantage here was the reduction of PMA in Co/Pt after annealing, likely due to Pt-Co interface roughness.

3.2.2.4 Hafnium Oxide (HfO_x)

HfO_x is used extensively in the semiconductor industry as a gate oxide for transistor applications. There is a large body of work already established in the optimisation and deposition of such materials. Here, natural oxidation has been used to produce the oxide layer, by exposing a hafnium layer to atmosphere after depositing a Hf metal layer with 80 % of the expected total thickness. As a result there is some uncertainty in the final thickness. While there are potential flaws with this method, e.g. as not fully oxidising the Hf metal layer or oxidation of MRG at the interface. The optimisation of an oxidation process is a task on its own hence the results presented here describe a first attempt at producing a novel oxide barrier for TMR devices.

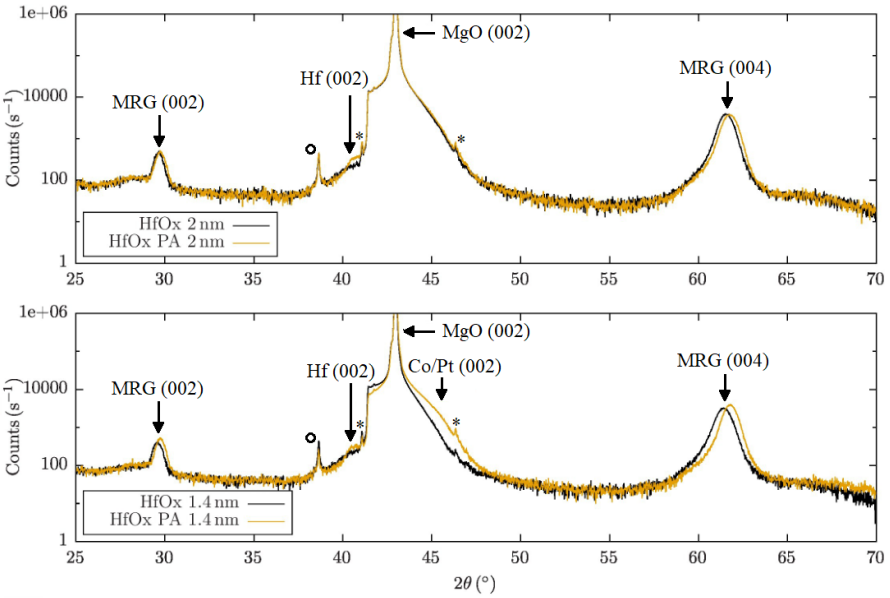

Figure 3.16: XRD of spin-valve structures with a HfO_x barrier layer, with thickness t = 1.4, 2.0 nm, pre- and post-annealing (PA). The peaks labelled with a * are bbc Pt peaks and a ○ are sample holder peaks.

XRD of the as-deposited stacks, shown in Figure 3.16, indicates that the MRG has not been affected by the oxidation process, indicated by the presence of the MRG (004) peak. This peak appears to be at a lower intensity in the structure with the $t = 1.4$ nm HfO_x barrier, which suggests that some oxidation may have occurred at the interface. There is no indication of a crystalline Co/Pt or Hf layer in the structure. After annealing, a shift towards higher angles is observed for MRG(004) peak, indicating a loss of tetragonality and hence we expect loss of PMA. This shift is larger in the stack with $t = 1.4$ nm, and combined with the emergence of a Hf(002) peak at 40.5°, means the Hf is precipitating as the MRG takes up the oxygen instead. Additionally, emergence of a bump around the expected Pt(200) peak at $\approx 47°$ suggests that alloying is occurring between the HfO_x and Co/Pt free layer.

XRR patterns shown in Figure 3.17 provides more evidence for the presence of alloying, as the multilayer peak at 7.5° almost disappears after annealing. The fringe pattern of the barrier layer appears to shift, indicating that the interfaces of the HfO_x with either MRG or Co/Pt are somewhat mixed, consistent with XRD.

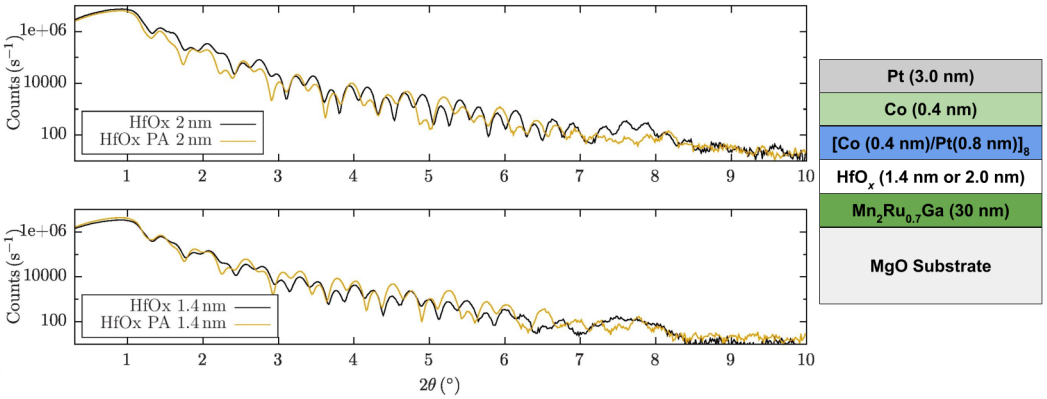

Figure 3.17: Left: XRR of spin-valve structures with a HfO_x barrier layer, with thickness $t = 1.4$, 2.0 nm, pre- and post-annealing (PA). **Right**: Illustration of the stack.

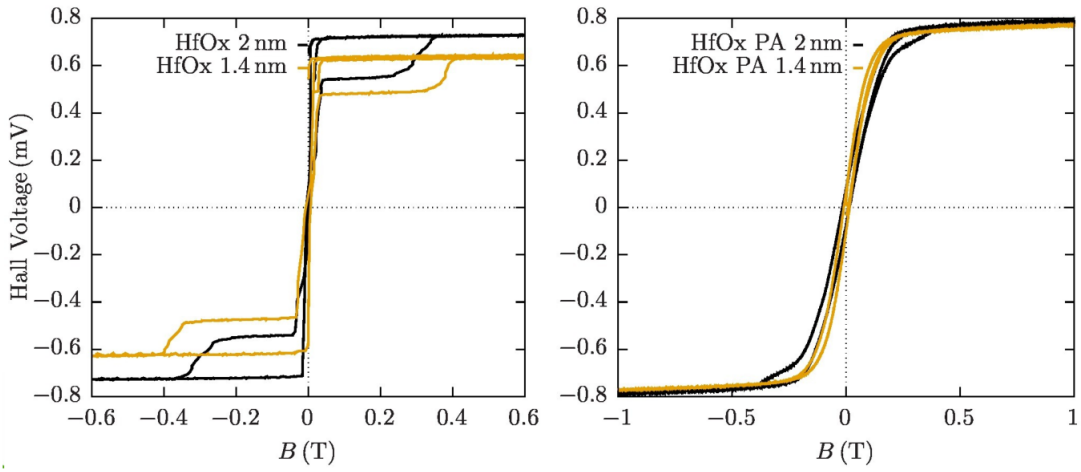

Figure 3.18: EHE of spin-valve structures with a HfO_x barrier layer, with thickness $t = 1.4$, 2.0 nm, pre- and post-annealing (PA).

Figure 3.18 shows the AHE data of the stacks. Firstly, annealing results in the Co/Pt free layer has lost most of its PMA, with the remnance reduced to almost zero. The anisotropy of Co/Pt is primarily influenced by the quality of interfaces between the multilayers, the result suggests that diffusion of material upwards in the stack has occurred, along with some bulk ordering of the Pt. It is not immediately obvious which atomic species are diffusing in the stacks. The primary suspects are the oxygen from the barrier and/or potentially Mn from the bottom of the stack. In the $t = 2$ nm HfO_x stack, there is a slight hysteresis around 0.4 T, which is likely to be from the MRG

layer. Due to the reduced tetragonal distortion observed in XRD, the MRG net moment is partially in-plane. This small hysteresis is absent in the $t = 1.4$ nm HfO_x stack and the MRG cannot be saturated even at fields up to 4 T. This can be attributed to the much larger MRG(004) peak shift seen in XRD, resulting in a fully in-plane net moment. In summary, thinner HfO_x barrier layer is not stable during annealing, and may not be suitable for use in devices. The $t = 2$ nm is still of interest, however oxidation process must be optimised to avoid precipitation of Hf and oxidation of MRG. Also, this barrier is not suitable for the Co/Pt multilayer, hence other free layers should be explored.

3.2.2.5 Vanadium (V)

Vanadium has previously seen applications in Gd-based Schottky junctions as a diffusion barrier for the aluminium interconnects. [9] It additionally has a bcc structure with lattice parameter a = 3.0274 Å, which is close to half the in-plane lattice parameter of MRG. Hence there is potential for epitaxial growth of V on MRG, under compressive strain. It must be noted that there is also an fcc structure with $a = 3.79$ Å.

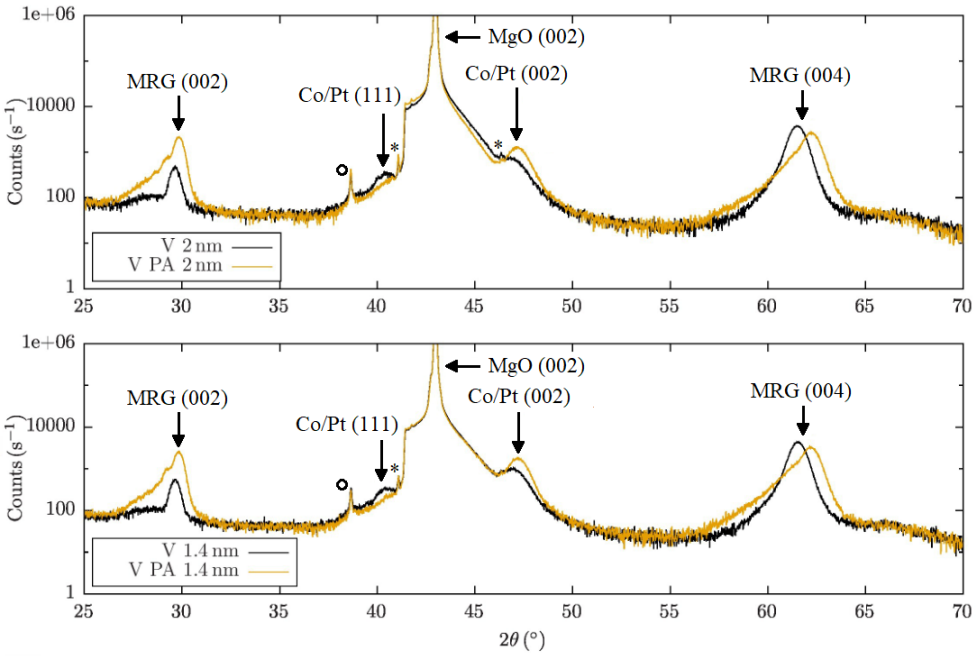

Figure 3.19: XRD of spin-valve structures with a V spacer layer, with spacer thickness $t = 1.4$, 2.0 nm, pre- and post-annealing (PA). The peaks labelled with a * are bbc Pt peaks and a ○ are sample holder peaks.

The XRD patterns in Figure 3.19, in the as-deposited stacks the MRG is well crystallised. There is no peak associated with the Co/Pt multilayer at 45°. There is a small peak at 47.04°, which corresponds with the Pt (200) peak and a small peak at 40.5°, which corresponds to the Pt (111) peak of the bcc crystal. Due to the extreme mismatch between these crystals, the V is unlikely to be epitaxially grown on the MRG. Upon annealing, the XRD patterns suggest that the vanadium is recrystallised, with the bcc V(100) and V(200) peaks appearing at 29.28° and 61.08°, respectively, while the (111) bcc peak has disappeared. The Pt(200) peak appears stronger, suggesting improved crystallisation. Meanwhile, the MRG (004) peak has shifted significantly to higher angles, indicating a large reduction in the tetragonal distortion of the films and loss of PMA. This could be due to the formation of a V-Mn alloy at the interface, which is removing Mn from the MRG film.

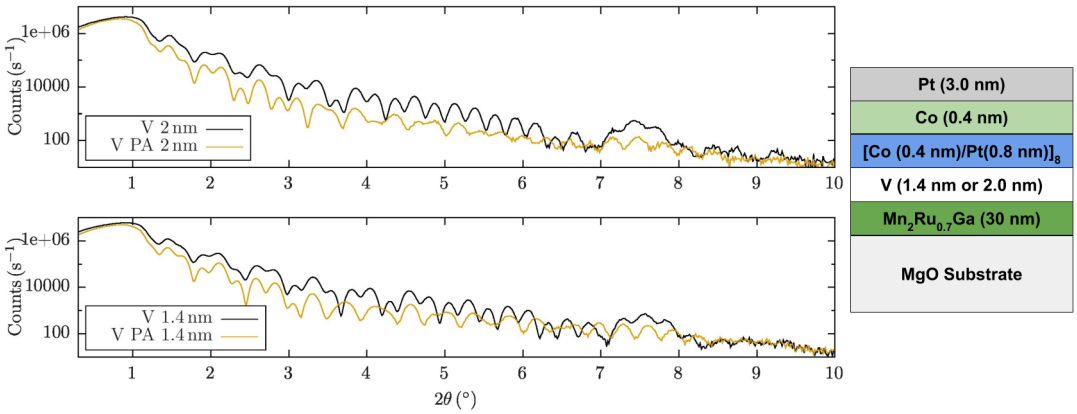

Figure 3.20: Left: XRR of spin-valve structures with a V spacer layer, with spacer thickness $t = 1.4$, 2.0 nm, pre- and post-annealing (PA). **Right**: Illustration of the stack.

The XRR patterns in Figure 3.20, demonstrate a moderate change in the quality of the interfaces. This is particularly evident for the $t = 1.4$ nm V stack, where the wide fringe associated with the V layer has become indeterminate by 3.5°, indicating intermixing at the interfaces. The more narrow fringes appear to be better defined, which suggests a reduction in roughness at some of the interfaces. However at higher angles the Co/Pt multilayer related interfaces appear significantly rougher, which can be attributed to the recrystallisation of the vanadium from the 111 texture to the 100.

AHE measurements in Figure 3.21 show that V is initially a good candidate material as a seed for Co/Pt, with a very square hysteresis in the as-deposited state. For

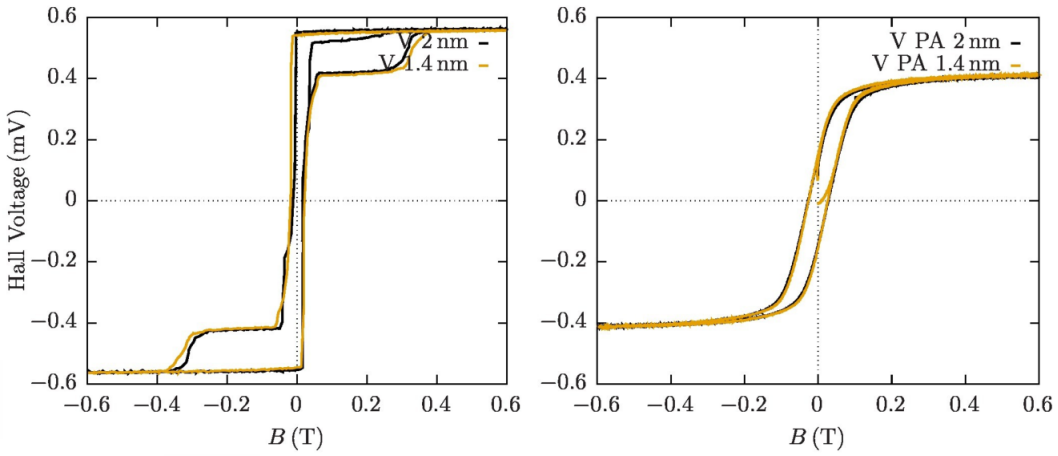

Figure 3.21: EHE of spin-valve structures with a V spacer layer, with spacer thickness $t = 1.4$, 2.0 nm, pre- and post-annealing (PA).

both thicknesses, little difference in the coercivity of both Co/Pt and MRG are observed. Upon annealing however, the Co/Pt loses significant perpendicular anisotropy with a remnance that is less than one third of the initial value and the net moment of MRG appears to be fully in plane since there no evidence of MRG saturation even at fields of up to 4 T. This is consistent with the reduction in tetragonality due to the MRG(004) peak shift seen in XRD.

3.2.2.6 Molybdenum (Mo)

Mo is known to have a low affinity for alloying relative to many other d-block materials, and this is especially the case with Mn. It has been employed as a diffusion barrier in solar cells [10], and has a relatively low resistivity ($\approx 3\times$ that of Cu). The Mo FCC crystal phase with a lattice parameter of a = 4.03 Å.

From the XRD shown in Figure 3.22, differences in the MRG are already observed before annealing. This may be due to target inhomogeneities/flaking due to long periods of sputtering. In the $t = 1.4$ nm Mo-based stack, the Pt (200) peak at 47.04° appears again. Interestingly, it is not present at in the $t = 2$ nm Mo stack which has a peak at 68.4° instead. This peak corresponds strongly with the $CoPt_3$(220) reflection. Upon annealing the MRG layer shows little change in structure, with the (004) peak shifting only slightly to higher angles for the $t = 1.4$ nm stack. In comparison, the Pt and $CoPt_3$ peaks have grown in intensity. This suggests the Mo induces precipitation of

Pt rich alloys in the free layer, which will in turn shift the Co/Pt into a softer magnetic phase.

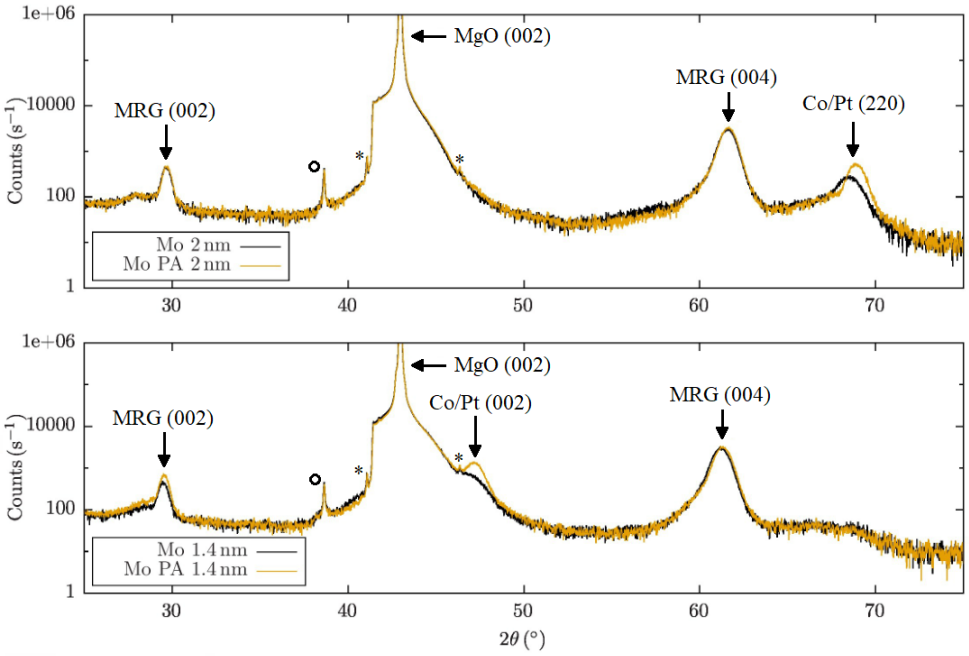

Figure 3.22: XRD of spin-valve structures with a Mo spacer layer, with thickness t = 1.4, 2.0 nm, pre- and post-annealing (PA). The peaks labelled with a * are bbc Pt peaks and a ○ are sample holder peaks.

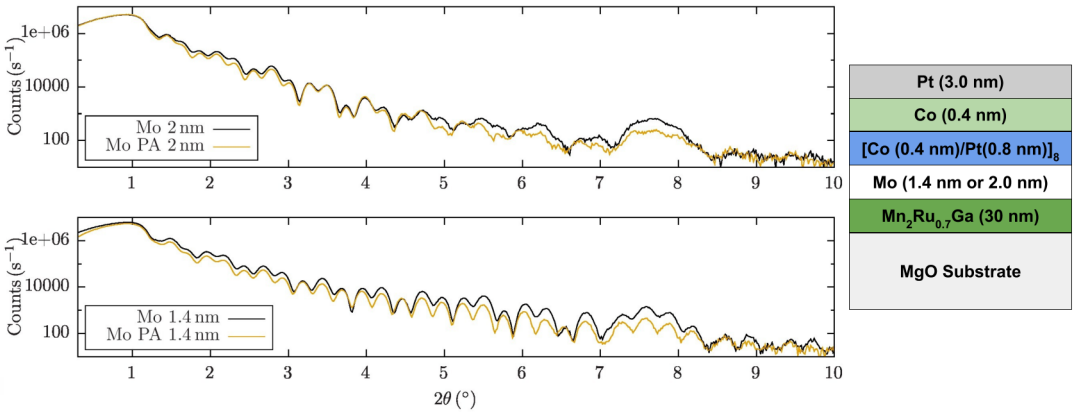

Figure 3.23: Left: XRR of spin-valve structures with a Mo spacer layer, with thickness t = 1.4, 2.0 nm, pre- and post-annealing (PA). **Right**: Illustration of the stack.

The XRR patterns in Figure 3.23, show very little change in either case after annealing, suggesting that the interfaces are well maintained during the annealing process.

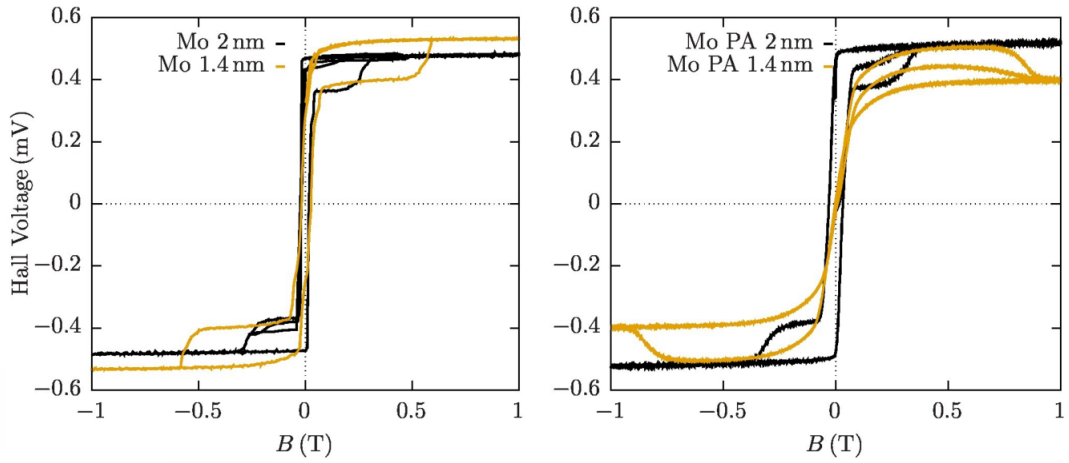

Figure 3.24: EHE of spin-valve structures with a Mo spacer layer, with thickness $t =$ 1.4, 2.0 nm, pre- and post-annealing (PA).

The AHE data in Figure 3.24 show that the $t = 1.4$ nm stack exhibit less perpendicular anisotropy in the free layer than the $t = 2$ nm stack. There is also a difference in the coercivity of the MRG layer, attributable to the different initial c-spacing between the two samples as seen from XRD. After annealing, the Co/Pt loses almost all PMA in the $t = 1.4$ nm Mo stack, whereas it is well maintained in the $t = 2$ nm stack with a small increase in coercivity. Additionally, the MRG is largely unaffected in the $t = 2$ nm stack, though it appears to be partially coupled to the Co/Pt layer. In the $t = 1.4$ nm nm stack it still has PMA, but appears to have moved through compensation, since the switch occurs in the other direction.

The proposed mechanism is that the Co is capable of disolving small percentages of Mo, thus the first Co layer of the superlattice is able to alloy partially. In the $t = 1.4$ nm stack, this induces a loss of local $L2_1$ order at the Co/Pt interface. The $L2_1$ local order is essential for the development of PMA in such multilayer ferromagnets. Loss of local order at interface then causes the Pt to favour a 100 texture in the first few repetitions of the superlattice. Annealing promotes the propagation of the 100 texture through the superlattice resulting in a total loss of PMA. In the $t = 2$ nm stack there is enough Mo available to reduce the Co:Pt ratio sufficiently to induce the formation of a $CoPt_3$ phase.

Once again, annealing favour this phase to be propagated throughout the superlattice and from AHE the $CoPt_3$ appears to maintain PMA.

3.2.2.7 Mn_2Ru_xGa

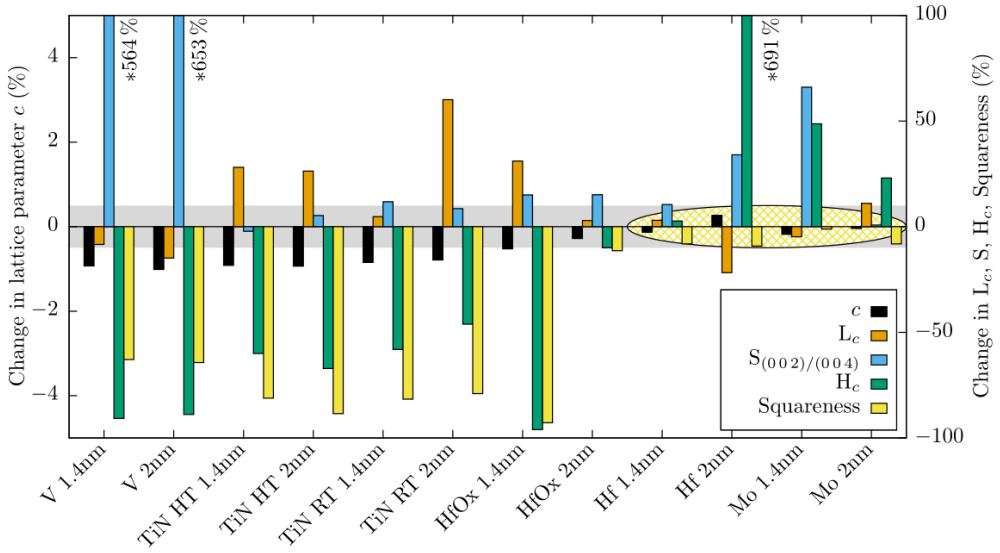

Figure 3.25: Relative change of c lattice parameter, coherence length, intensity ratio, coercivity, and squareness in MRG after annealing. The grey box indicates a threshold of 10 % change in squareness as a metric for potential use in applications. The yellow ellipse indicates the best two candidate spacers.

The relative change of characteristic parameters of MRG thin films after annealing have been collated in Figure 3.25. There is a very clear correlation between a reduction in c and the loss of both squareness and coercivity. In cases where squareness was maintained within 10 % of the original value, c-parameter has not been reduced to destroy both the tetragonal distortion ($c/a \leq 1$) and the PMA.

Introduction of the TiN spacer induces an increase in L_c, suggesting that annealing has reduced the defect density of the crystal structure. Given TiN's use as a diffusion barrier, it is unlikely that any atoms have diffused into defect positions and is more likely caused by the reordering of crystal sites which is corroborated with the increase in $I(002)/I(004)$. This suggests that the inherent crystal defects induced by the inclusion of Ru on the 4d sites help to stabilise the strain of the crystal in order to promote perpendicular anisotropy. It is worth noting that when the TiN spacer is grown at the

same deposition temperature as MRG, the results are more consistent. One possibility is that the interface between MRG and TiN is crystalline, resulting in an additional strain on the MRG.

In contrast to all other materials, it appears that the $t = 2$ nm Hf spacer has induced an increase in the c parameter of MRG, leading to T_{comp} increasing to above RT indicated by a change of sign of AHE at 300 K. The shift in T_{comp} caused the coercivity to increase significantly due to its divergent nature close to T_{comp} which is now closer to 300 K than before MA. The increase in c is accompanied by a decrease in L_c, indicating an increase in diffusion based defects. Considering the binary phase diagrams [11], Hf is likely to acts as a source for filling defects within MRG, though only to a small degree as Hf absorption into both Mn and Ga is limited to ≈ 1 % at., while maintaining crystal structure. The filling of defects leads to an increase in electronic pressure in the crystal, leading to an increase in the biaxial strain hence an increase of c. This accounts for the reduced effects seen in the HfO_x $t = 2$ nm and Hf $t = 1.4$ nm based heterostructures, where the counter-diffusion into the Hf layer limits the available atoms to fill defect sites. HfO_x barrier with $t = 1.4$ nm performs poorly due to near complete loss of PMA, whereas for $t = 2$ nm it maintains coercivity and squareness. If the $t = 1.4$ nm HfO_x is fully oxidised ($x \approx 2$), then diffusion into MRG either across the barrier or from the barrier itself will be reduced. However, data presents a strong likelihood of oxidation of MRG at the interface. This results in a similar effect as observed with TiN. The thicker HfO_x spacer is probably not fully oxidised, which leads to some inter-diffusion. Hf spacers appear to work quite well, with the $t = 1.4$ nm spacer showing only a small change in all properties.

Using a V spacer is accompanied by a significant increase of S and decrease of L_c indicating inter-diffusion of V into the crystal has occurred. Additional peaks near the MRG(002) and MRG(004) peaks with d-spacing of ≈ 0.3058 nm and 0.1511 nm are present after MA, with satellites for each, making fitting for the MRG peak difficult. These d-spacings correspond well to either RuV (100) = 0.298 nm, RuV (200) = 0.148 nm or Ga_5V_2 (220) = 0.317 nm, Ga_5V_2 (530) = 0.1537 nm. Given the phase diagrams for Ga-V and Ru-V [11], it is substantially more likely for the crystalline compound to be a Ga-V binary such as Ga_5V_2 or Ga_41V_8, both of which form readily at 300 K. From the substantial increase in $I(002)/I(004)$, when can then assume

that reordering of Ru from the Heusler 4*d* site occurs forming an unspecified highly disordered cubic alloy, likely with B2 symmetry.

Mo spacers appear to have similar properties to Hf, and phase diagrams again show a range of absorption up to 4 % at. in Mn and 16 % at. in Ga.[11] Counter-diffusion is limited to Mn, as the Mo does not appear to absorb much Ga at the annealing temperature (350 °C). Given the increase in S for the $t = 1.4$ nm Mo heterostructure, reordering of the Ru is expected which strongly impacts magnetic properties. The results demonstrate that the squareness is mostly maintained and the coercivity increases, suggesting that T_{comp} has increased despite a lower c parameter. Diffusion of Mo into MRG defect sites must therefore induce an additional moment on one of the Mn sublattices. This effect is less prominent with the $t = 2$ nm Mo heterostructure, but still an increase in T_{comp} is observed and L_c has increased without any change in $I(002)/I(004)$. With more material to diffuse, it is possible that the additional Mo inclusions in the MRG help to maintain ordering of the Ru^{4d} site.

3.2.3 Conclusion

Substrate induced strain has an significant influence on the properties of MRG thin films. DFT calculations have highlighted the role of crystalline defects as a source of electronic doping that maintains strain within the lattice [12]. Annealing of MRG thin films promotes the removal of crystalline defects, which relaxes the lattice, however it is not possible to identify the defects from XRD. Spacer materials were selected based on their lattice parameter and potential to act as a diffusion barrier. At one extreme is the case of a TiN spacer layer in which no diffusion is possible, resulting in loss of PMA due to relaxation. At the other extreme is a V spacer layer, in which atomic species diffuse strongly resulting in a complete disordering of the crystal and full loss of PMA. Hf and Mo represent a compromise, as a small degree of inter-diffusion stabilises the crystal structure by filling the defects. A fully or mostly oxidised HfO_x spacer layer appears to behave similarly to TiN, whereas the partially oxidised Hf spacer layer more resembles the Hf heterostructure in behaviour due to available diffusive species. Both Hf and Mo may be useful as thin protective layers in future active devices and attract interest into investigating potential effects of Mo doping on the crystalline and magnetic properties of MRG itself. From the perspective of the Co/Pt

free layer, it seems that most stable texture is the (110) orientation which was promoted by the $t = 2$ nm thick Mo layer. Also, Mo has a long spin diffusion length ≈ 235 nm [13] so it could a more suitable as an ultra-thin dusting layer in MgO based magnetic tunnel junctions, as compared to Ta. The study demonstrates that particular material thin films incorporated into a spin-valve structure with MRG, either as a capping layer or as part of a heterostructure, can have positive impacts on some material properties of MRG at the expense of others.

References

[1] K. Borisov, G. Atcheson, G. D'Arcy, Y.-C. Lau, J. M. D. Coey, and K. Rode, "Exchange coupling of a perpendicular ferromagnet to a half-metallic compensated ferrimagnet via a thin hafnium interlayer," *Appl. Phys. Lett.*, vol. 108, no. 19, p. 192407, 2017. (Cited on page: 95, 102, 109)

[2] H. Kurt, K. Rode, P. Stamenov, M. Venkatesan, Y. . Lau, E. Fonda, and J. M. D. Coey, "Cubic Mn_2Ga thin films: Crossing the spin gap with ruthenium," *Phys. Rev. Lett.*, vol. 112, no. 2, 2014. (Cited on page: 95, 97)

[3] H. Kurt, K. Rode, K. Oguz, M. Boese, C. C. Faulkner, and J. M. D. Coey, "Boron diffusion in magnetic tunnel junctions with MgO (001) barriers and CoFeB electrodes," *Appl. Phys. Lett.*, vol. 96, no. 26, p. 262501, 2010. (Cited on page: 101)

[4] S. Ikeda, J. Hayakawa, Y. Ashizawa, Y. M. Lee, K. Miura, H. Hasegawa, M. Tsunoda, F. Matsukura, and H. Ohno, "Tunnel magnetoresistance of 604 % at 300 K by suppression of Ta diffusion in CoFeB/MgO/CoFeB pseudo-spin-valves annealed at high temperature," *App. Phys. Lett.*, vol. 93, no. 8, p. 082508, 2008. (Cited on page: 101)

[5] Y. Fukumoto, K.-i. Shimura, A. Kamijo, S. Tahara, and H. Yoda, "High thermal stability of magnetic tunnel junctions with oxide diffusion barrier layers," *Appl. Phys. Lett.*, vol. 84, no. 2, pp. 233–235, 2004. (Cited on page: 101)

[6] Y. Yang, W. X. Wang, Y. Yao, H. F. Liu, H. Naganuma, T. S. Sakul, X. F. Han, and R. C. Yu, "Chemical diffusion: Another factor affecting the magnetoresistance ratio in Ta/CoFeB/MgO/CoFeB/Ta magnetic tunnel junction," *Appl. Phys. Lett.*, vol. 101, no. 1, p. 012406, 2012. (Cited on page: 101)

[7] A. Titova, C. Fowley, E. Clifford, Y. C. Lau, K. Borisov, D. Betto, G. Atcheson, R. Hübner, C. Xu, P. Stamenov, M. Coey, K. Rode, J. Lindner, J. Fassbender, and A. M. Deac, "Effect of insertion layer on electrode properties in magnetic tunnel junctions with a zero-moment half-metal," *Sci. Rep.*, vol. 9, no. 1, p. 4020, 2019. (Cited on page: 101)

[8] I. S. Pogosova, J. V. Harzer, B. Hillebrands, G. Güntherodt, D. Guggi, D. Weller, R. F. C. Farrow, and C. H. Lee, "Interface analysis of (110)-oriented Co/Pt superlattices with large magnetic anisotropies using x-ray diffraction," *J. App. Phys.*, vol. 76, no. 2, pp. 908–913, 1994. (Cited on page: 104)

[9] M. Eizenberg, R. D. Thompson, and K. N. Tu, "A study of vanadium as diffusion barrier between aluminum and gadolinium silicide contacts," *J. Appl. Phys.*, vol. 53, no. 10, pp. 6891–6897, 1982. (Cited on page: 114)

[10] P. Blösch, F. Pianezzi, A. Chirilă, P. Rossbach, S. Nishiwaki, S. Buecheler, and A. N. Tiwari, "Diffusion barrier properties of molybdenum back contacts for Cu(In,Ga)Se_2 solar cells on stainless steel foils," *J. Appl. Phys.*, vol. 113, no. 5, p. 054506, 2013. (Cited on page: 116)

[11] R. W. Cahn, "Binary Alloy Phase Diagrams–Second edition. T. B. Massalski, Editor-in-Chief; H. Okamoto, P. R. Subramanian, L. Kacprzak, Editors. ASM International, Materials Park, Ohio, USA. December 1990. xxii, 3589 pp., 3 vol., hard- back. $995.00 the set," *Adv. Mater.*, vol. 3, no. 12, pp. 628–629, 1991. (Cited on page: 120, 121)

[12] M. Žic, K. Rode, N. Thiyagarajah, Y.-C. Lau, D. Betto, J. M. D. Coey, S. Sanvito, K. J. O'Shea, C. A. Ferguson, D. A. MacLaren, and T. Archer, "Designing a fully compensated half-metallic ferrimagnet," *Phys. Rev. B*, vol. 93, no. 14, p. 140202, 2016. (Cited on page: 121)

[13] S. Liang, H. Yang, P. Renucci, B. Tao, P. Laczkowski, S. Mc-Murtry, G. Wang, X. Marie, J.-M. George, S. Petit-Watelot, A. Djeffal, S. Mangin, H. Jaffrès, and Y. Lu, "Electrical spin injection and detection in molybdenum disulfide multilayer channel," *Nat. Commun.*, vol. 8, no. 14947, 2017. (Cited on page: 122)

4

Varying Mn Content in Mn_2Ru_xGa Thin Films

4.1 Background

Zero-moment ferrimagnetic half-metals (ZMHM) are attractive materials for applications in spintronic devices. [1; 2] They offer advantages over their antiferromagnetic or half-metallic ferromagnetic counterparts.[3] As the net moment tends to zero, anisotropy field becomes large, therefore high frequency spin dynamics and low Gilbert damping can be achieved. For MRG, maximum zero-applied-field resonance frequency of $\approx$ 160 GHz and Gilbert damping constant $\alpha \approx 0.02$ have been demonstrated. [1; 4] MRG also offers efficiency and ease of detection and manipulation of the magnetic state.

Remarkably efficient charge/spin conversion and large spin-orbit fields per current density $\frac{\mu_0 \boldsymbol{H}_{\text{eff}}}{j}$ related to spin currents have recently been measured in single thin films of MRG, where $\frac{\mu_0 \boldsymbol{H}_{\text{eff}}}{j}$ approaches 0.1×10^{-10} T/Am^{-2} in the low-current density limit. This is almost a thousand times the Ørsted field and one to two orders of magnitude greater than $\frac{\mu_0 \boldsymbol{H}_{\text{eff}}}{j}$ in heavy metal/ferromagnet bilayers. [5] The efficiency of current induced spin-orbit torque switching in Ru/MRG/MgO has been found to be simi-

lar to that of a ferromagnet, e.g. Ta/CoFeB/MgO [6] or Pt/Co/AlO_x [7], despite larger MRG film thickness and coercivity [8]. Furthermore, thermal single-pulse all-optical toggle switching at ultra short timescales ($<$ 10 ps) has been recently demonstrated in MRG, making it the first non-Gd based material to exhibit this effect. [9; 10; 11] MRG-based devices could offer a practical solution to the current problem of chip-to-chip generation and detection of electromagnetic radiation in the 0.1 THz - 10 THz frequency range, known as the 'THz gap', provided sufficiently high magnetoresistive effects can be achieved. [1; 12]

Each spintronic application requires a specific set of material properties. For example, efficient single-pulse all optical toggle switching (SPAOS) at room temperature (RT) in MRG films requires T_{comp} to be just above RT. [9] High spin polarisation and perfectly crystalline films with smooth surfaces are desirable for MRG-based magnetic tunnel junctions. Earlier studies have investigated the variation of some of these properties with x in Mn_2Ru_xGa. [13; 14; 15; 16] The results show that an increase in Ru content increases tetragonal distortion of the cubic unit cell on MgO and improves the wetting of the film. These qualities are useful for all applications, and particularly for the fabrication of nanostructured devices. [14; 15]

The goal of the present work is to help identify compositions which exhibit the best combinations of properties for specific applications. Thin thin films are prepared with varying Ru and Mn content, while keeping the Ga content fixed. The dominant contribution of Mn^{4c} sites to the density of states at the Fermi level allows us to disentangle net and sublattice magnetisations with the aim of establishing non-collinearity of the Mn^{4c} sublattice moments, which results in the canting of net moment.

The crystalline and structural properties of the thin films were determined by x-ray diffraction, reciprocal space mapping and x-ray reflectivity. Net magnetisation as a function of temperature and field loops at $T = 300$ K were measured by SQUID magnetometry. Spin-polarisation at the Fermi level was found by point contact Andreev reflection (PCAR) on selected samples. Anomalous Hall effect (AHE) measurements $T = 300$ K show hysteresis loops which can be compared to magnetometry loops. Magneto-optic Kerr microscopy (MOKE) measurements of Kerr contrast versus temperature in the range $300\,\mathrm{K} - 500\,\mathrm{K}$ were performed on selected samples. Temperature dependence of the net magnetisation was modelled by Weiss molecular mean

field (MFT) for a two sublattice ferrimagnet to extract Weiss coefficients and calculate Heisenberg exchange constants.

4.2 Methodology

Epitaxial thin films of Mn_yRu_xGa (MRG) with $x+y \approx 3$ were grown by DC magnetron sputtering on 10×10 mm^2 (100) MgO substrates in our Shamrock sputtering system [1; 13]. The base pressure of the system was 10^{-8} Torr. Films were co-sputtered in argon onto single-side polished substrates maintained at 350 °C from three 75 mm targets of Mn_2Ga, Ru and either MnGa or Mn_3Ga. Deposition rates from each target were calibrated and used to determine the values of x and y in the formula. Films were capped in-situ with a 3 nm layer of AlO_x deposited at room temperature to prevent further oxidation. Film thickness and rms roughness were determined by low- angle X-ray scattering in a Panalytical X'Pert Pro diffractometer, and thickness was found by fitting the interference pattern using X'Pert Reflectivity Software. A Bruker D8 Discovery X-ray diffractometer with a copper tube (K_α wavelength = 154.06 pm) and a double-bounce Ge [220] monochromator on the primary beam was used to determine the diffraction patterns of the thin films. Reciprocal space maps were obtained on the same diffractometer around the (113) MgO reflection.

Magnetisation measurements with the field applied perpendicular or parallel to the surface of films mounted in a straw were made using a 5 T Quantum Design SQUID magnetometer. Data included hysteresis loops and thermal scans from 10 K - 400 K. They were corrected for the magnetism of the substrate. Thermal scans in zero field after saturation of the magnetisation at room temperature were used to determine the compensation temperatures of the films. For Kerr imaging, an Evico Magnetics wide-field Kerr microscope with a 10x/0.25 objective lens was used. All loops were measured with polar sensitivity and red LED light with a field applied out-of-plane. Faraday rotation was compensated during the measurement using a feature which readjusts the analyser position relative to a mirror reference.[17] Samples were heated from 300 K - 500 K on a temperature-controlled microscope stage.

Electrical measurements were made in a 1 T GMW electromagnet under ambient conditions. Silver wires were cold-welded to the films with indium and the current used was 5 mA. High field data were obtained in a 14 T Quantum Design Physical Property

Measurement System (PPMS^{TM}). The films there were contacted with silver paint. The 4-point Van der Pauw geometry was used to determine both the Hall resistivity and the longitudinal resistivity of the films.

Point contact Andreev reflection (PCAR) measurements were made in the PPMS using a mechanically sharpened Nb tip. Landing the tip onto the sample surface is controlled by an automated vertical Attocube piezo-stepper. Two horizontal Attocube^{TM} steppers are used to move the sample laterally to probe a pristine area. The differential conductance spectra were fitted using a modified Blonder-Tinkham-Klapwijk model, as detailed elsewhere.[18; 19]

4.3 Results

Three Ru series of Mn_yRu_xG thin films were prepared for $x = 0.5$, 0.7 and 0.9 and $1.2 \leq y \leq 2.6$. Here in the results section, the main focus will be on samples which exhibit a compensation within the measurable temperature range, namely $0 < T < T_C$ where T_C is the Curie temperature. A summary of sample compositions which satisfy this condition is given in 4.1, with the only exception of $Mn_{2.2}Ru_{0.5}Ga$ which has a virtual compensation point below $T = 0$ K. It has been included to keep 3 distinct Mn composition per series for the systematic study.

Series 1	Series 2	Series 3
$Mn_{2.2}Ru_{0.5}Ga$	$Mn_{2.0}Ru_{0.7}Ga$	$Mn_{1.8}Ru_{0.9}Ga$
$Mn_{2.4}Ru_{0.5}Ga$	$Mn_{2.2}Ru_{0.7}Ga$	$Mn_{2.0}Ru_{0.9}Ga$
$Mn_{2.6}Ru_{0.5}Ga$	$Mn_{2.4}Ru_{0.7}Ga$	$Mn_{2.2}Ru_{0.9}Ga$

Table 4.1: Compositions of the thin films derived from sputtering rates, where Mn is varied in three Ru series. All films show compensation, with the exception of $Mn_{2.2}Ru_{0.5}Ga$.

The results section will begin with subsection 4.3.1 on crystallography showing the XRD, RSM and XRR data and the extracted parameters. Subsection 4.3.2 shows SQUID magnetometry scans of net magnetisation for the three Ru series. This data will be used to find T_{comp} and net magnetisation extrapolated to $T = 0$ K. AHE loops measured at temperatures below, close and above T_{comp} will demonstrate the signature magnetic characteristics associated with ZMHM. A comparison of AHE and magnetometry out-of-plane hysteresis loops measured at $T = 300$ K will be shown, followed by the results of spin polarisation and θ_{AH} values as a function of Mn and Ru content. Lastly, subsection 4.3.3 summarises the mean field theory fitting of temperature scans of the out-of-plane net moment which allows to calculate sublattice magnetisations and exchange constants. The Kerr contrast data as a function of temperature provides an experimental value of T_C for selected samples.

4.3.1 Crystallography

The diffraction patterns of MRG thin films are presented in Figure 4.1. The MRG (002) and MRG (004) peaks as well as the MgO (002) substrate are labelled. From the 2θ position of the (004) peak the c lattice parameter is calculated. The ratio of

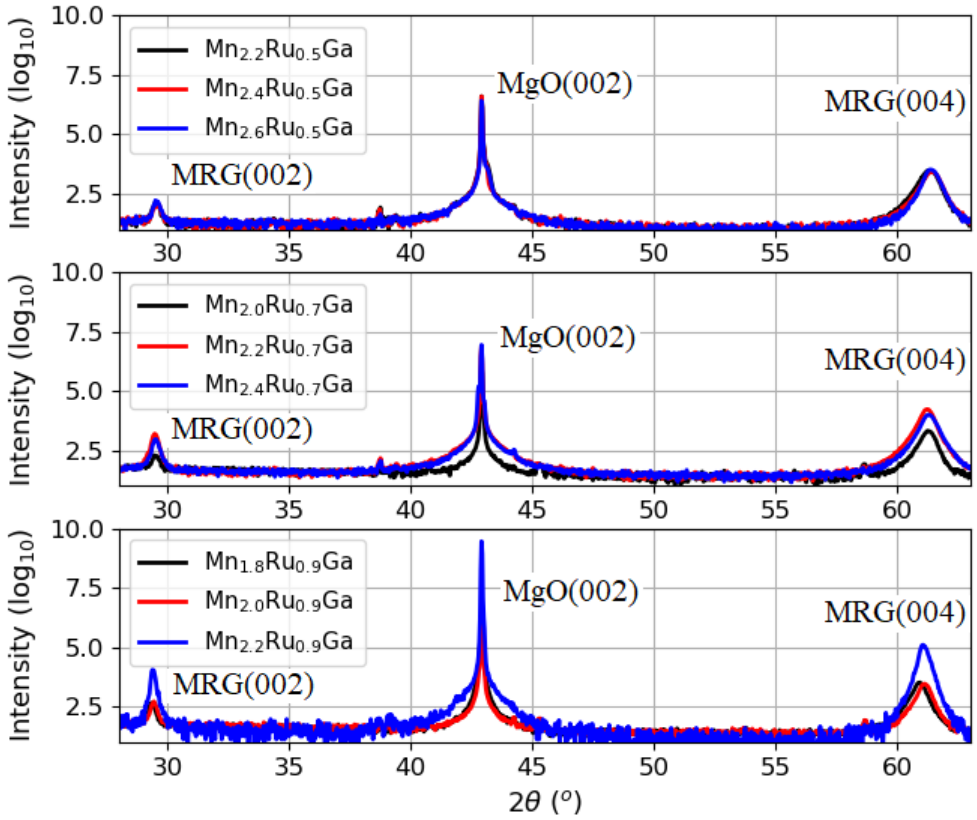

Figure 4.1: XRD data of MRG thin films on MgO(001) substrate from three Ru Series. The MRG(002), MgO(002) and MRG(004) peaks are labelled.

(002) and (004) peak intensities $\left(\frac{I(002)}{I(004)}\right)$ is related to the degree of atomic order out-of-plane in the inverted Heusler *XA* structure [20]. Both *c* and *a* lattice parameters were calculated, with respect to the MRG unit cell, from the MRG (206) peak shown in RSM data in Figures 4.2, 4.3 and 4.4. The *c* parameters from both methods were compared and found to be the same, as expected. From the fitting of XRR spectra, the average MRG thicknesses and densities were found. The average thicknesses of MRG and AlO_x layers were 50 nm and 3 nm, respectively. All findings are summarised in Table 4.2.

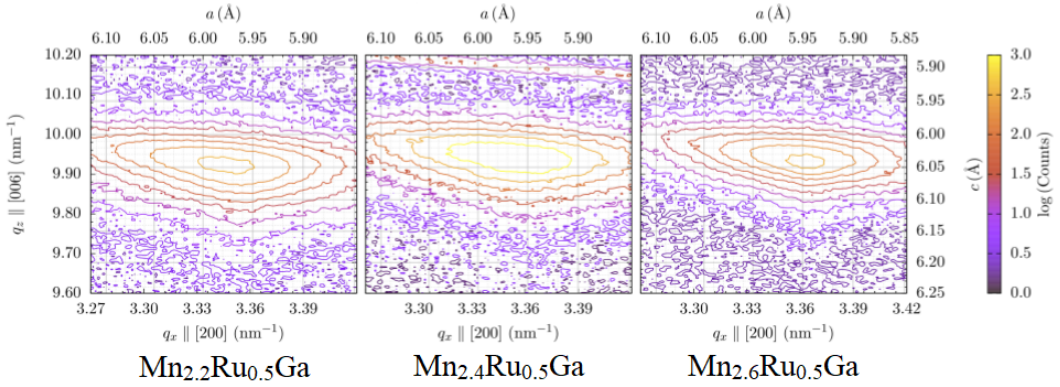

Figure 4.2: RSM data of the MRG(206) peak of $Mn_{2.2}Ru_{0.5}Ga$, $Mn_{2.4}Ru_{0.5}Ga$ and $Mn_{2.6}Ru_{0.5}Ga$ thin films.

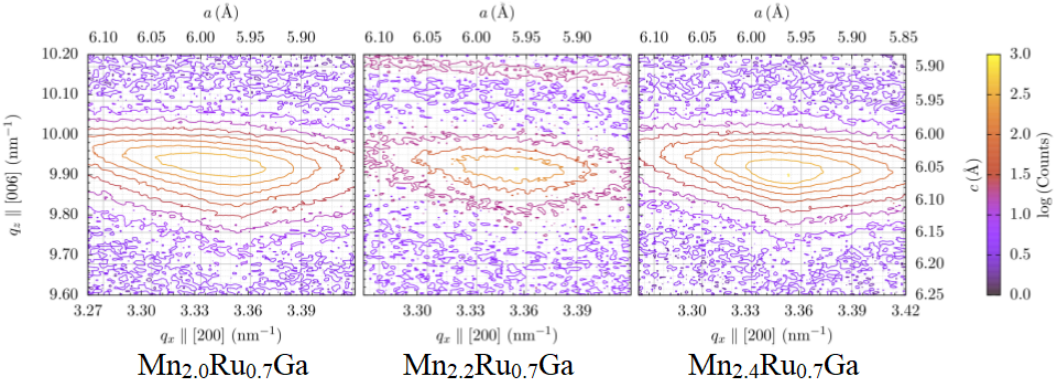

Figure 4.3: RSM data of the MRG(206) peak of $Mn_{2.0}Ru_{0.7}Ga$, $Mn_{2.2}Ru_{0.7}Ga$ and $Mn_{2.4}Ru_{0.7}Ga$ thin films.

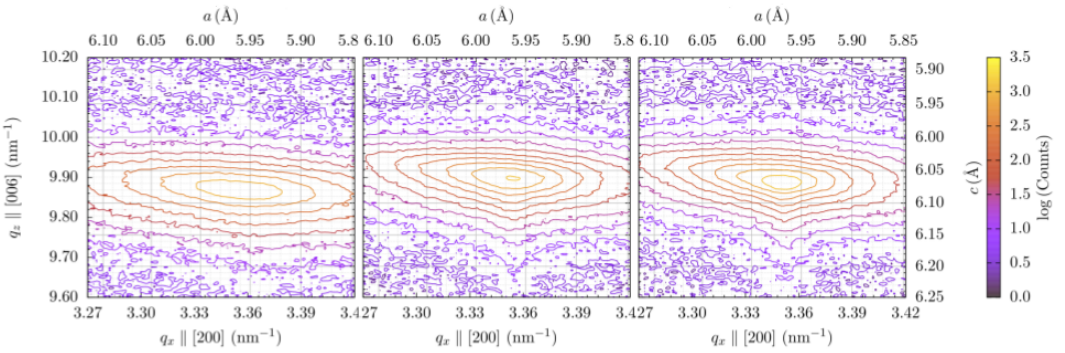

Figure 4.4: RSM data of the MRG(206) peak of $Mn_{1.8}Ru_{0.9}Ga$, $Mn_{2.0}Ru_{0.9}Ga$ and $Mn_{2.2}Ru_{0.9}Ga$ thin films.

The differences in the shapes of the MgO (002) peaks between samples is due to the fact that films were deposited on MgO substrates from different supplier since they were not all made at the same time. Reciprocal space maps of the MRG (206) reflection show a distribution of a parameters around the central value of $\sqrt{2}a_{MgO} = 595$ pm. The wide range of a parameters comes from the fact that the films are ≈ 50 nm in thickness, which means the crystal lattice relaxes, and also due to twinning in the MgO substrate. The substrate-induced tetragonal expansion of the cubic unit cell is responsible for the PMA of the films. The $\frac{c}{a}$ ratio increases as more Ru is added to the films from 1.01 to 1.02 meaning the tetragonal distortion is in the range $1-2$ %.

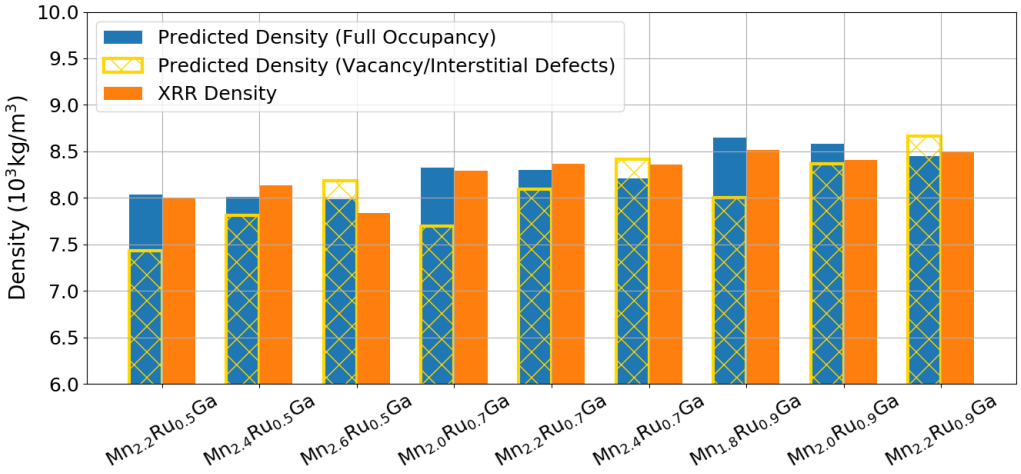

Figure 4.5: Calculated (blue) and experimental (orange) densities for the nine MRG films. The yellow crossed bars show densities predicted if there were vacancies/interstitials in the structure.

The densities of the films were obtained from the low angle X-ray reflectivity data. Theoretical densities are calculated from the atomic formulae reduced to exactly four atoms per formula unit, using the experimentally determined a- and c-parameters to determine the cell volume. Calculating densities for $Mn_2Ru_{0.5}Ga$, for example, by assuming full occupancy or two vacancies per unit cell unit gives 7900 kg/m^3 or 7100 kg/m^3, respectively. The density obtained from fitting the XRR pattern was 7800 kg/m^3. This shows that the vacancy assumption underestimates the density by 9 %, whereas the experimental density agrees with that calculated for full occupancy to within about 1 %. A comparison of experimental and calculated densities of nine

films for full occupancy is shown in Figure 4.5, where it is seen that the values agree to within 3 %. The densities predicted for the formulae with 0.3 or 0.1 vacancies and 0.1 interstitial Mn atoms are marked by yellow crossed bars. We conclude that all the crystallographic sites in MRG really are close to fully occupied. Overall, the density increases with increasing Ru content as expected. The number of valence electrons n_v per formula unit is included in Table 4.2.

	Series 1			Series 2			Series 3		
Mn	2.2	2.4	2.6	2.0	2.2	2.4	1.8	2.0	2.2
n_v	24.2	24.4	24.6	24.4	24.6	24.8	24.6	24.8	25.0
$\frac{I(002)}{I(004)}$	0.05	0.04	0.05	0.10	0.09	0.09	0.29	0.18	0.11
c (pm)	605	604	604	605	605	606	608	606	607
a (pm)	597	596	595	598	596	596	596	596	597
$\frac{c-a}{a} \times 100$	1.3	1.3	1.5	1.2	1.5	1.7	2.0	1.7	1.7
Density (kg/m^3)	8003	8135	7840	8296	8365	8359	8513	8409	8496

Table 4.2: Number of valence electrons (n_v), $\frac{I(002)}{I(004)}$ ratio, out-of-plane (c), in-plane (a) lattice parameters and density of the MRG thin films.

4.3.2 Magneto-transport and Magnetometry

Temperature scans of the out-of-plane component of the net magnetic moment are shown in Figure 4.6. Compensation temperatures were deduced from the change of sign of the remanent magnetisation in zero applied field found from thermal scans, after saturating in 5 T at 400 K. All samples bar one exhibited a compensation point. The scans were performed without any applied field to avoid magnetic signal from the MgO substrate. Curie temperatures (T_C) were all above 400 K, the temperature limit of our SQUID measurements, however an estimation of T_C was found from mean field fits of magnetisation curves. All magnetic parameters are summarised in Table 4.3.

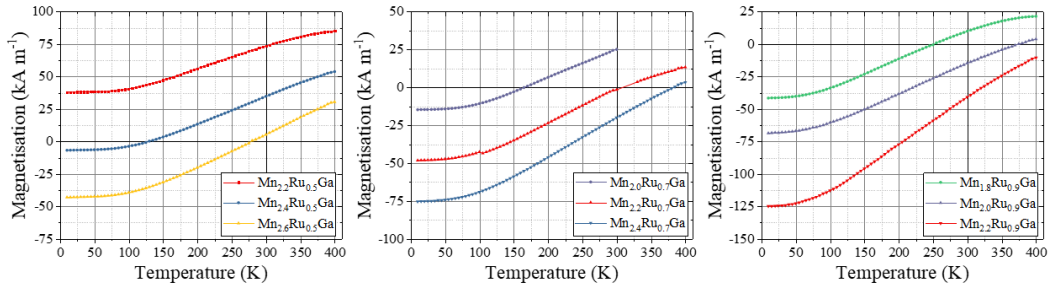

Figure 4.6: Magnetisation versus temperature scans in the out-of-plane geometry with no applied external field for all MRG samples.

	Series 1			Series 2			Series 3		
Mn	2.2	2.4	2.6	2.0	2.2	2.4	1.8	2.0	2.2
M_0^{Net} (kA/m)	34	6	38	13	43	67	36	61	111
M_0^{Net} (μ_B/Mn)	0.20	0.03	0.22	0.08	0.25	0.39	0.21	0.35	0.65
T_{comp} (K)	-	130	278	165	311	381	253	375	436
T_C (K)	550	577	592	530	543	494	478	513	491

Table 4.3: Summary of magnetic parameters of the MRG thin films: net magnetisation at $T = 4$ K (M_0^{Net}) and compensation temperature (T_{comp}) and Curie temperatures (T_C).

The Mn^{4c} sublattice electrons are mainly contributing to the Fermi level in the density of states and hence dominate magnetotransport. It follows that in AHE measurements, the transverse resistance (R_{xy}) is proportional to the z-component of the Mn^{4c} sublattice magnetisation, i.e. $R_{xy} \propto M_z^{4c}$. The transverse (ρ_{xy}) and longitudinal (ρ_{xx}) resistivities can be calculated from AHE as described in Chapter 2 subsection 2.3.1. The ratio ρ_{xy}/ρ_{xx} gives the anomalous Hall angle (θ_{AH}), which is a measure of spin dependent scattering. [21]

One of the main characteristics of MRG is that the coercivity diverges as the net moment tends to zero at compensation. Figure 4.7 shows AHE R_{xy} versus $\mu_0 H$ at three temperatures. The data confirms that the coercive field increases when the measurement temperature approaches the compensation point. The Anomalous Hall coefficient of the hysteresis loop changes sign when T_{comp} is crossed. This is due to the change of spin polarisation of the carriers with respect to the net magnetisation. [15] The AHE measurement at 300 K which is very close to the compensation point of $Mn_{2.6}Ru_{0.5}Ga$ shows a huge coercivity > 12 T. The sign convention in this paper sets R_{xy} to be positive (negative), in $\mu_0 H > 0$, at temperatures below (above) T_{comp}.

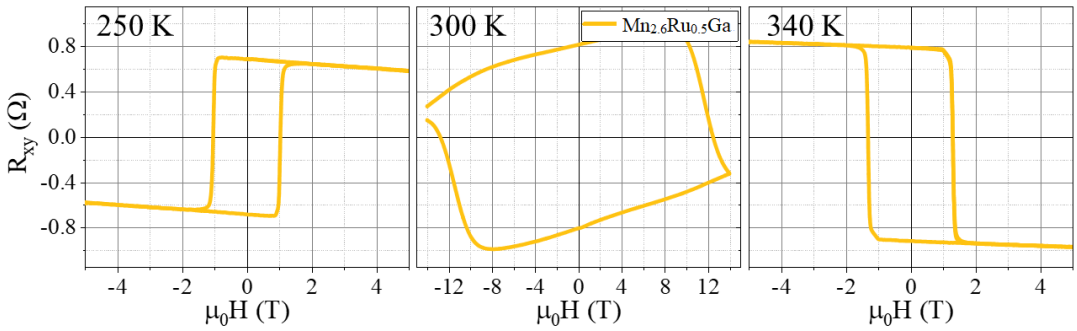

Figure 4.7: AHE loops of $Mn_{2.6}Ru_{0.5}Ga$ thin film, with T_{comp} = 275 K, measured at T = 250 K, 300 K and 340 K.

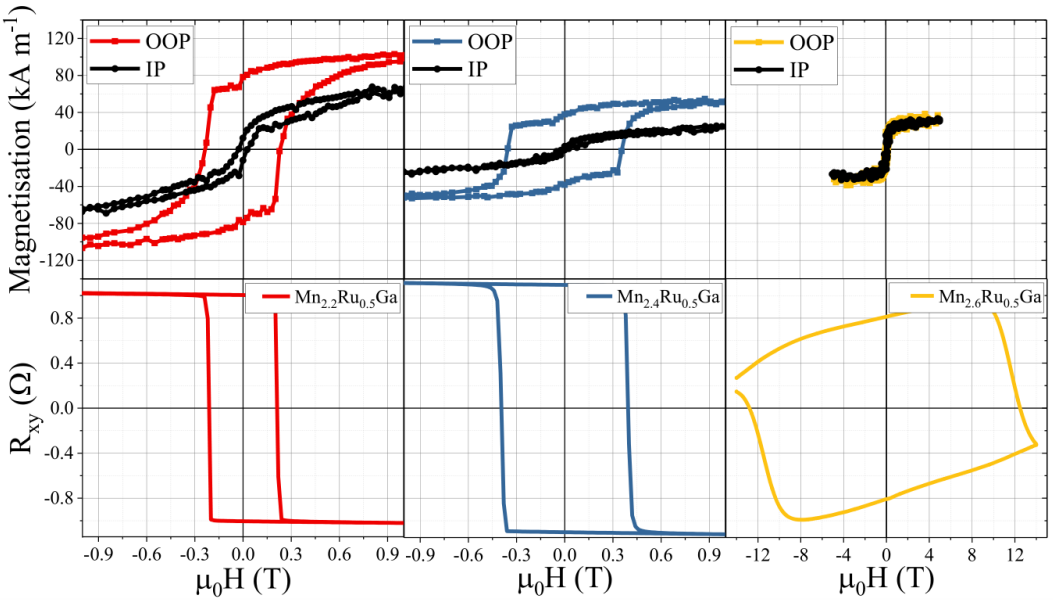

Figure 4.8: Series 1 - Top panel: SQUID net magnetisation at 300 K with field applied out-of-plane (OOP) and in-plane (IP) relative to the sample surface. Bottom panel: Anomalous Hall effect measurements at 300 K.

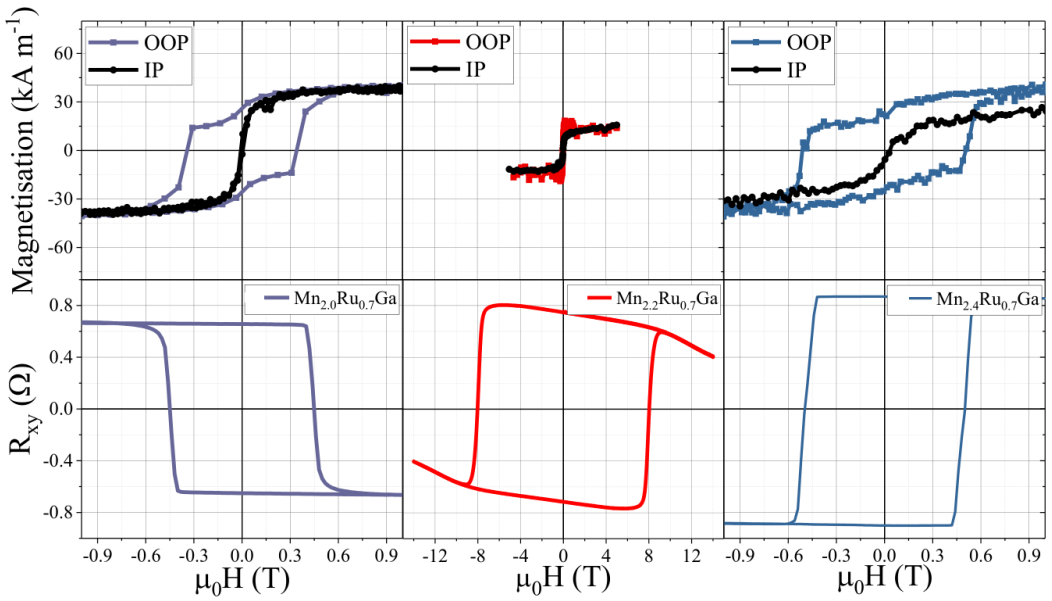

Figure 4.9: Series 2 - Top panel: SQUID net magnetisation at 300 K with field applied out-of-plane (OOP) and in-plane (IP) relative to the sample surface. Bottom panel: Anomalous Hall effect measurements at 300 K.

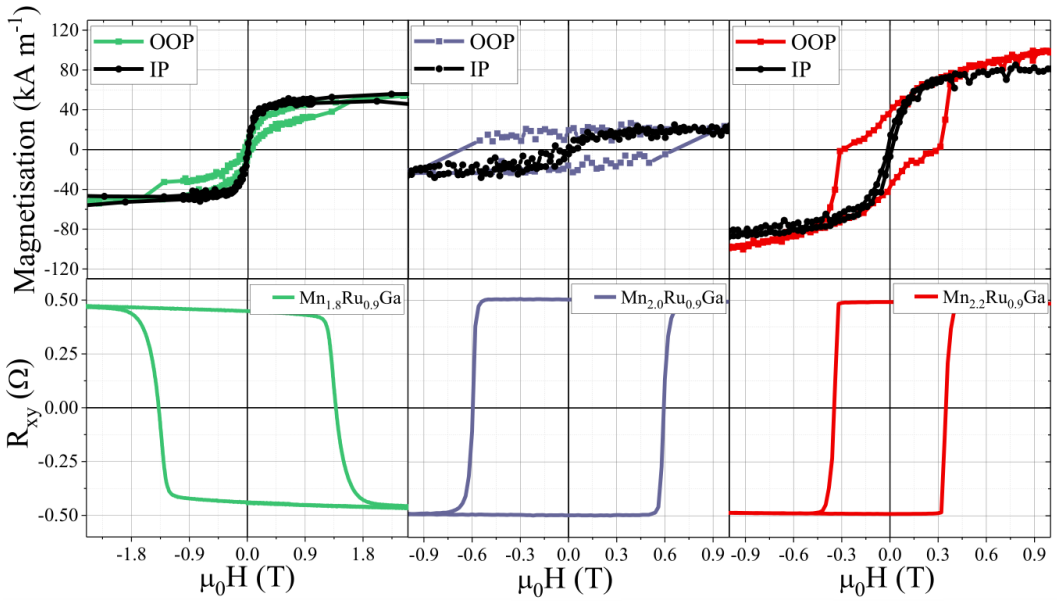

Figure 4.10: Series 3 - Top panel: SQUID net magnetisation at 300 K with field applied out-of-plane (OOP) and in-plane (IP) relative to the sample surface. Bottom panel: Anomalous Hall effect measurements at 300 K.

Comparison of SQUID and AHE loops, shown in Figures 4.8, 4.9 and 4.10, provides a further insight into the magnetism of the samples. The AHE loop reflects the magnetisation of the Mn^{4c} sublattice, whereas the SQUID measures the small net magnetisation. In all samples, AHE loops have high remnance however the out-of-plane SQUID loops exhibit a soft and a hard component. This behaviour will be discussed in Section 4.4. The SQUID magnetometry data of samples $Mn_{2.6}Ru_{0.5}Ga$ and $Mn_{2.2}Ru_{0.7}Ga$ are taken where the out-of-plane moment is virtually zero. However there remains an uncompensated in-plane component which is soft and isotropic.

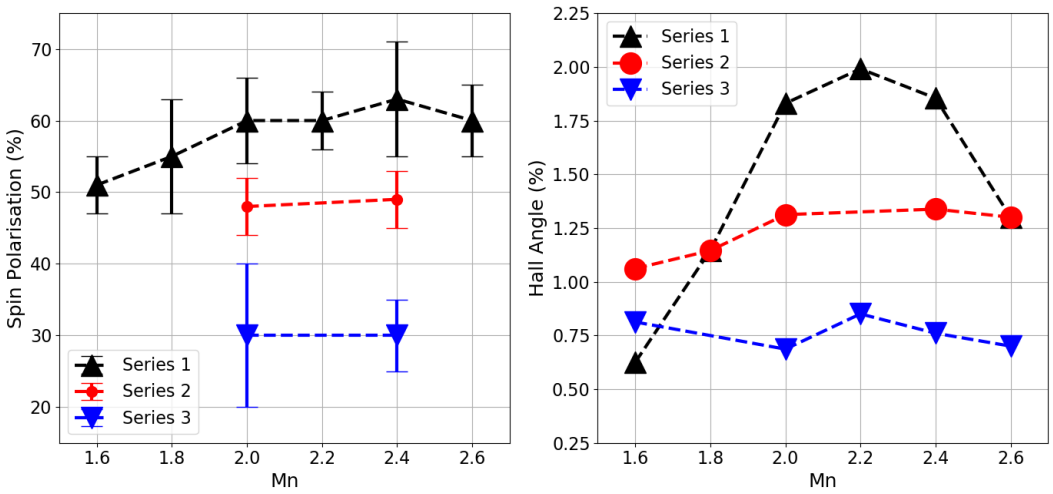

Figure 4.11: Left: Spin polarisation measured by PCAR versus Mn content. **Right**: Anomalous Hall angle measured at 300 K versus Mn.

Figure 4.11 shows the spin polarisation and θ_{AH} as a function of Mn content and θ_{AH} versus Mn content. The anomalous Hall angle at room temperature reaches a maximum of 2 % for the $x = 0.5$ series when $y = 2.2$, as shown in Figure 4.11. Spin polarisation data determined by point contact Andreev reflection are summarised in Figure 4.11. The $x = 0.5$ series (in black) shows a maximum spin polarisation at the Fermi level of 63 % for $y = 2.4$. Alloys with a higher ruthenium content have a considerably smaller spin polarisation. The spin polarisation results are still quite far from the 100 % expected from an ideal half-metal. However, in reality this is close to the maximal value that can be observed using PCAR on Heusler alloy thin films [13]. The spin polarisation is linearly dependent on the anomalous Hall angle θ_{AH} for $x = 0.5$ and $y = 2.0$, 2.4 as shown in Figure 4.12. This demonstrates that the band

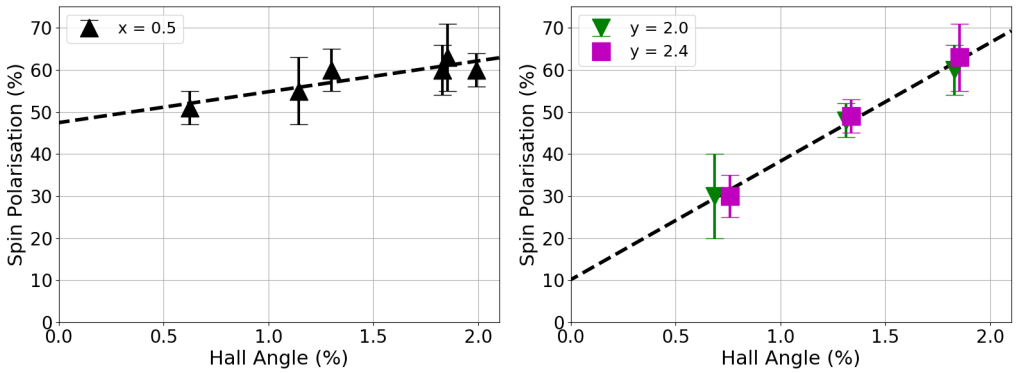

Figure 4.12: The spin polarisation versus anomalous Hall angle for constant (Left) $x = 0.5$ and (Right) $y = 2.0, 2.4$.

structure accounts for θ_{AH}, which is dominated by the lowest concentration of carriers and confirms that Mn^{4c} sublattice electrons dominate the transport.

4.3.3 Mean field theory calculations

Zero-field thermal scans of net magnetisation measured by the SQUID obtained after saturating the magnetisation at 400 K were fitted using a two-sublattice Weiss molecular mean field model of colinear ferrimagnetism described by the system of non-linear equations

$$\begin{aligned} \mathbf{H}^{4a} &= n_W^{aa}\mathbf{M}^{4a} + n_W^{ac}\mathbf{M}^{4c} \\ \mathbf{H}^{4c} &= n_W^{ac}\mathbf{M}^{4a} + n_W^{cc}\mathbf{M}^{4c} \end{aligned} \tag{4.1}$$

where H^{4a} and H^{4c} are the internal sublattice molecular fields M^{4a} and M^{4c} are the magnetisations of the two sublattices, which are modelled by Brillouin functions and n_W^{aa}, n_W^{ac} and n_W^{cc} are the three Weiss coefficients. They are related to Heisenberg exchange constants $\mathscr{J}$ by the expression

$$\mathscr{J}^{ij} = \frac{n_W^{ij}\rho\mu_0(g\mu_B)^2}{Z^{ij}} \tag{4.2}$$

where ρ is the number of the Mn atoms on the i^{th} sublattice per unit cell volume, μ_0 is permeability of free space, g is the Landé g-factor for spin, μ_B is the Bohr magneton and Z is the coordination number, where $Z^{aa} = Z^{cc} = 12$ and $Z^{ac} = 8$ for Mn_2Ru_xGa.

When more than half the sites per formula unit are manganese, we assume the excess populates the 4*d* sites which are symmetrically equivalent to the 4*c* sites. The 4*a* and 4*b* sites which accommodate Mn and Ga atoms are assumed to be fully occupied. The spin angular momentum quantum numbers for Mn atoms on each site, $S^{4a,4c}$, are multiples of $\frac{1}{2}$. The upper bound for $S^{4a,4c}$ is the sum of spins in a half-filled 3*d* orbital (5 spins). The lower bound is based on the Mn moment in similar compounds. (3 spins), so the quantum numbers in the Brillouin functions are chosen in the range $1.5 \leq S^{4a,4c} \leq 2.5$, and the sublattice magnetization is scaled to best represent the data. In metals, the spin moment per atom is rarely an integral number of Bohr magnetons and the sublattice moments at $T = 0$ K cannot be directly calculated from the $S^{4a,4c}$ quantum numbers appropriate for localised electrons due to orbital overlap and mixing. We found by density functional theory calculation that the Mn^{4a} sublattice moment at $T = 0$ K is nearly independent of Ru content for $0.5 \leq x \leq 1.0$ with a value of $m_0^{4a} = 2.70\ \mu_B$/Mn, corresponding to a sublattice magnetisation $M_0^{4a} = 465\ \mathrm{kAm^{-1}}$.[14] The net magnetisation at $T = 0$ K was extrapolated from the SQUID magnetometry data, shown in Figure 4.6. Using this value, the magnetisation of the Mn^{4c} sublattice was inferred.

MOKE microscopy at a fixed wavelength ($\lambda = 632\,\mathrm{nm}$) measures the Kerr rotation, which for MRG is essentially proportional to the magnetisation of the Mn^{4c} sublattice. Temperature-dependent MOKE data is compared with M_z of the Mn^{4c} sublattice calculated from the model, validating our approach. We use MOKE to determine T_C, since it covers the appropriate temperature range, and the Curie temperatures are then used as constraints in the fits.[22] The SQUID data, MFT fits and MOKE data for all three Ru series are shown in Figures 4.13, 4.14 and 4.15.

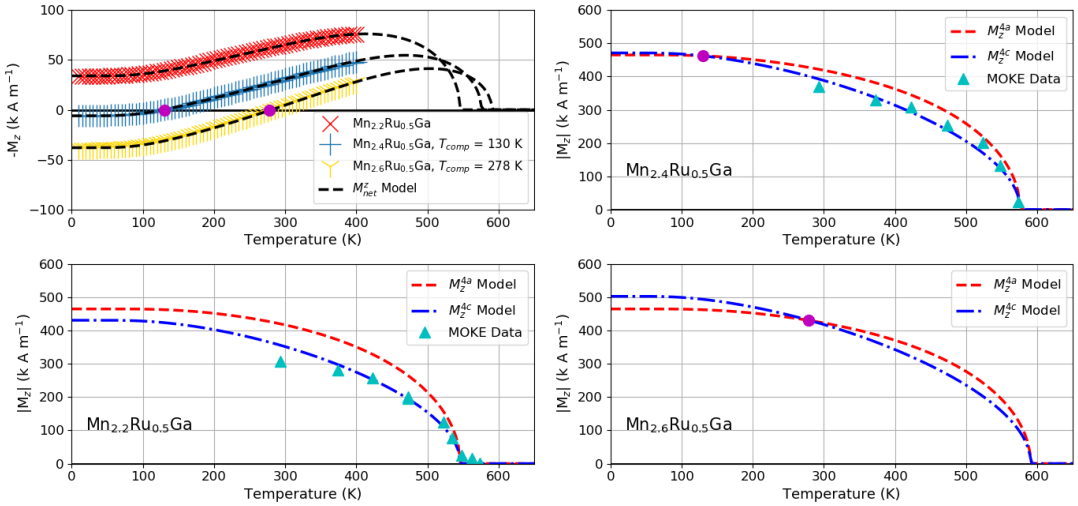

Figure 4.13: $Mn_{2.2}Ru_{0.5}Ga$, $Mn_{2.4}Ru_{0.5}Ga$ and $Mn_{2.6}Ru_{0.5}Ga$ thin films. Upper Left: MFT fit of net magnetisation versus temperature in zero field SQUID data. Lower left and right: Calculated Mn^{4a} and Mn^{4c} magnetisation curves with scaled MOKE data.

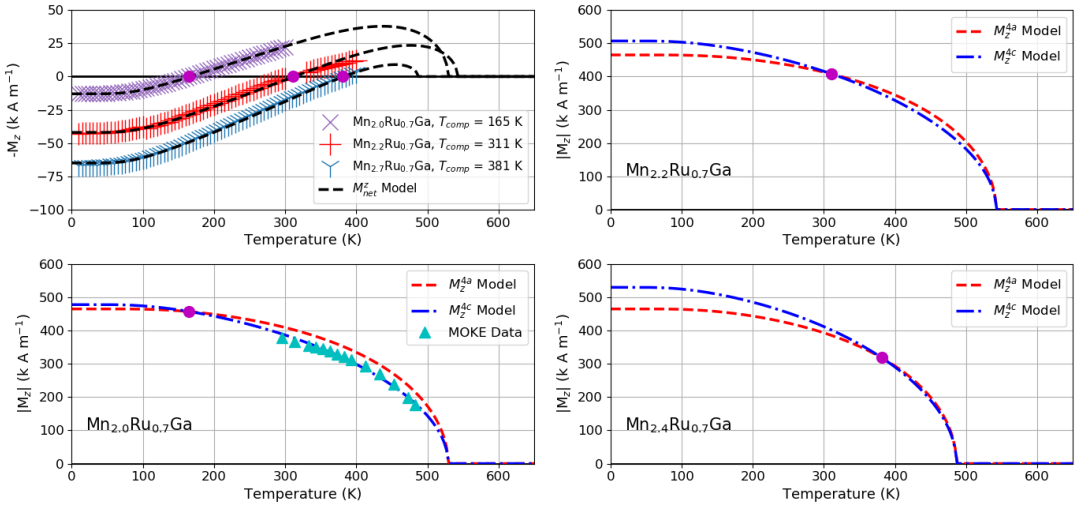

Figure 4.14: $Mn_{2.0}Ru_{0.7}Ga$, $Mn_{2.2}Ru_{0.7}Ga$ and $Mn_{2.4}Ru_{0.7}Ga$ thin films. Upper Left: MFT fit of net magnetisation versus temperature in zero field SQUID data. Lower left and right: Calculated Mn^{4a} and Mn^{4c} magnetisation curves with scaled MOKE data.

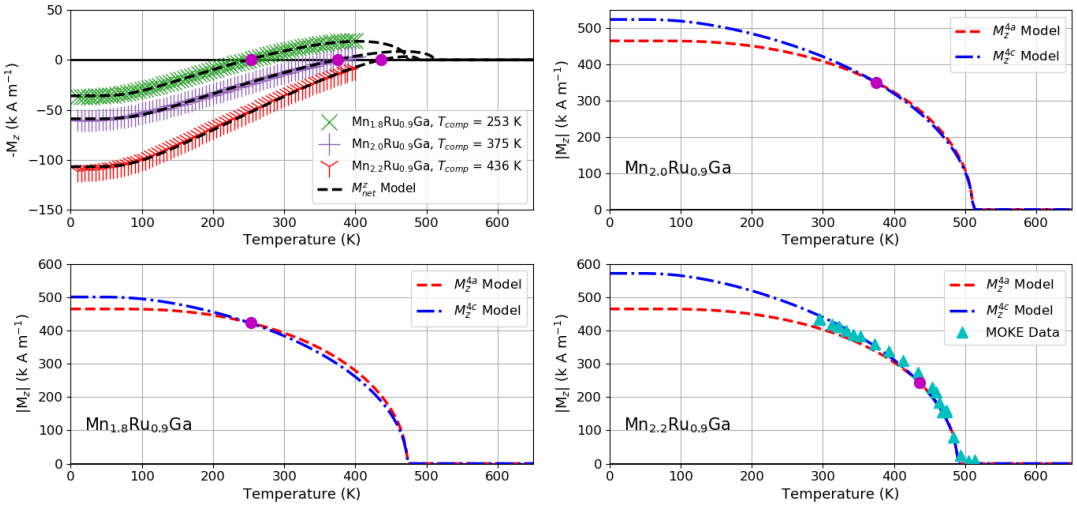

Figure 4.15: $Mn_{1.8}Ru_{0.9}Ga$, $Mn_{2.0}Ru_{0.9}Ga$ and $Mn_{2.2}Ru_{0.9}Ga$ thin films. Upper Left: MFT fit of net magnetisation versus temperature in zero field SQUID data. Lower left and right: Calculated Mn^{4a} and Mn^{4c} magnetisation curves with scaled MOKE data.

Sample	S^{4a}	S^{4c}	M_0^{4c} (kA/m)	$\mathcal{J}^{aa}$ (K)	$\mathcal{J}^{ac}$ (K)	$\mathcal{J}^{cc}$ (K)	Ratio
$Mn_{2.2}Ru_{0.5}Ga$	2.0	2.0	431	22.0	-24.5	11.6	10.0 : -7.4 : 5.3
$Mn_{2.4}Ru_{0.5}Ga$	2.5	2.5	471	19.7	-20.2	10.3	10.0 : -6.8 : 5.3
$Mn_{2.6}Ru_{0.5}Ga$	2.5	2.5	503	19.4	-20.1	9.6	10.0 : -6.9 : 5.0
$Mn_{2.0}Ru_{0.7}Ga$	2.0	2.5	478	21.6	-20.5	10.4	10.0 : -6.3 : 4.8
$Mn_{2.2}Ru_{0.7}Ga$	2.0	2.5	508	21.7	-19.7	10.5	10.0 : -6.1 : 4.8
$Mn_{2.2}Ru_{0.7}Ga$	2.0	2.5	532	19.2	-16.1	10.0	10.0 : -5.6 : 5.2
$Mn_{1.8}Ru_{0.9}Ga$	1.5	2.5	501	21.8	-23.2	7.0	10.0 : -7.1 : 3.2
$Mn_{2.0}Ru_{0.9}Ga$	1.5	2.5	526	23.0	-23.8	7.2	10.0 : -6.9 : 3.1
$Mn_{2.2}Ru_{0.9}Ga$	1.5	2.5	576	22.4	-20.6	6.2	10.0 : -6.4 : 2.8

Table 4.4: Summary of sublattice magnetisation at $T = 0$ K (M_0), spin angular momenta ($S^{4a,4c}$), Heisenberg exchange parameters from molecular field theory analysis of magnetisation data on the nine MRG thin films. The last column shows the ratio of the product of exchange constants with the coordination number $\mathcal{J}^{aa}Z^{aa} : \mathcal{J}^{ac}Z^{ac} : \mathcal{J}^{cc}Z^{cc}$.

4.4 Discussion

We define the Mn^{4c} moment as positive, coupled magnetically to the negative Mn^{4a}. In a previous study it was shown that well below T_C the Mn^{4a} moment is almost tem-

perature independent whereas the Mn^{4c} moment varies nearly linearly as a function of temperature.[16] Therefore, adding (subtracting) atoms on the Mn^{4c} sublattice is expected to raise (lower) T_{comp}, whereas adding (subtracting) Mn atoms on the Mn^{4a} will increase (decrease) the sublattice moment, but since this moment is negative it results in a decrease (increase) of T_{comp}.

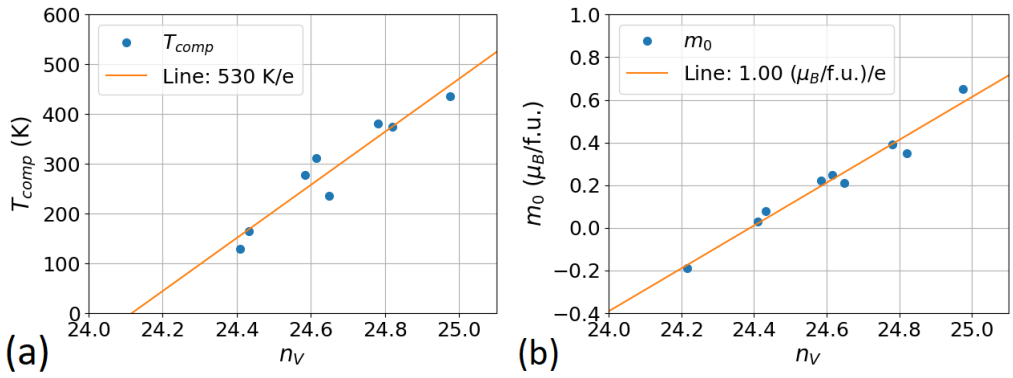

Figure 4.16: (a) T_{comp} versus n_V: adding an electron (e) raises T_{comp} by 530 K. (b) m_0 versus n_v: adding an electron (e) raises m_0 by $1\mu_B$/f.u. in agreement with the Slater-Pauling rule for a half-metal.

Increasing Ru raises T_{comp} [13] and within each Ru series increasing Mn also increases T_{comp}. Figure 4.16a shows the relationship between T_{comp} and the number of valence electrons (n_v), with a slope of 530 K per electron. We conclude that the added Mn predominantly increases the Mn concentration on the $Mn^{4c/4d}$ sublattice. This is supported by the analysis of the densities of the thin films plotted in Figure 4.5, which shows that there is no appreciable vacancy concentration for any composition in the series. Figure 4.16b shows the linear relationship between m_0 and n_v with a slope of $1\mu_B$/f.u. per electron. The Slater-Pauling behaviour confirms the half-metallicity of all the MRG thin films.

The magnetometry data in Figure 4.6, was recorded after magnetically saturating the samples perpendicular to their surface at $T = 400$ K. The z-projection of the net magnetisation was measured in zero field as a function of temperature during cool down. An ideal data set would include all three components of the sublattice specific moments which might be obtained using neutron diffraction or, if two components

would suffice, by x-ray magnetic circular dichroism (XMCD). [23] Here we first discuss the magnetic mode of MRG first in the simplified model of two collinear sublattices, based on known variations of the Mn-Mn exchange parameters with the distance between interacting atoms.

Table 4.4 summarises the fit parameters for the series. For all compositions, the model agrees well with the magnetisation data measured along the easy axis, perpendicular to the film plane. The ratios of Heisenberg exchange constants are similar to those was reported previously for an MRG film with a comparable composition. [10] The main trend that emerges from the data is that as the Ru content of MRG increases, $\mathscr{J}^{cc}$ decreases and while $\mathscr{J}^{aa}$ and $\mathscr{J}^{ac}$ remain almost constant. We explain the results as follows: $\mathscr{J}^{aa}$ does not depend on Ru content because Mn^{4a} does not have much overlap with Ru^{4d}. When the number of Mn atoms in the unit cell exceeds 16, some Mn fills the 4*d* positions, giving rise to Mn^{4c} - Mn^{4d} interactions, thereby the weakening $\mathscr{J}^{cc}$.

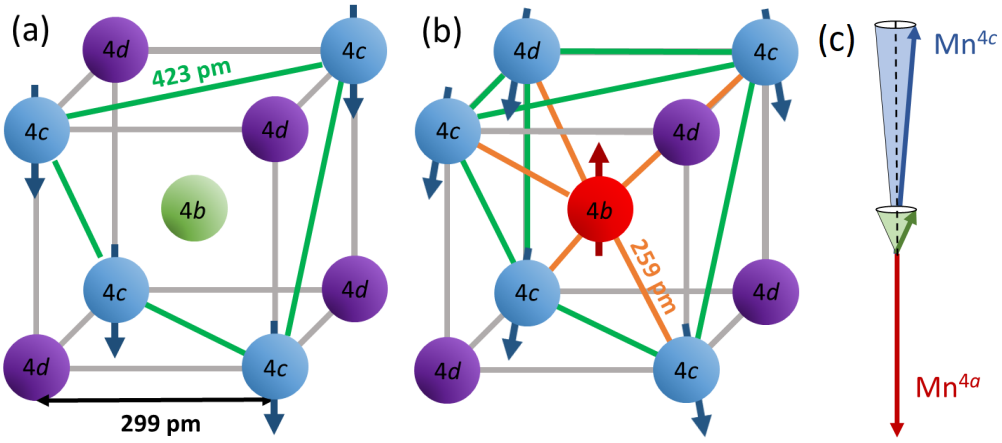

Figure 4.17: Left: Inner cube (Mn^{4c} sublattice) in the cubic unit cell of the inverse Heusler structure *XA* (Figure 1.18) showing the (a) 4*c* and 4*d* sites occupied by Mn atoms (blue with arrow) and Ru atoms (purple) with Ga (green) in the center, (b) one Ru atom is replaced with an Mn atom on a 4*d* site and Ga is replaced with Mn on the 4*b* site (red with arrow). Nearest neighbour ferromagnetic and antiferromagnetic couplings are represented by green and orange lines, respectively. The competition between exchange couplings can induce non-collinearity of sublattice moments locally. (c) Illustration of canting of net moment due to Mn^{4c} sublattice non-collinearity.

It is known that Mn-Mn distances in the range 250 pm - 280 pm generally lead

to antiferromagnetic coupling that decreases in magnitude as the distance increases, whereas at distances greater than 290 pm the coupling becomes ferromagnetic. [24] In an unstrained Mn_2RuGa film, $a_0 = 598$ pm. The intra-sublattice distances between Mn atoms, where each site forms an fcc sublattice, are $a_0/\sqrt{2} \approx 423$ pm and the inter-sublattice Mn^{4a} - Mn^{4c} or Mn^{4b} - Mn^{4c} distance is $a_0\sqrt{3}/4 \approx 259$ pm, as indicated in Figure 4.17. These distances correspond to ferromagnetic and antiferromagnetic exchange coupling, respectively. They are changed a little by the tetragonal distortion Since the densities indicate that all sites are occupied, chemical disorder will arise in the unit cell. A first type of disorder arises from Mn^{4a}-Ga^{4b} antisites and a second is the presence of Mn atoms on 4*d* sites. The Mn^{4c} sublattice portion of the unit cell is shown for Mn_2RuGa and $Mn_{2.25}Ru_{0.75}Ga$ in Figs. 4.17a and 4.17b, respectively, where the latter illustrates both types of disorder. The presence of Mn on 4*d* sites gives rise to FM coupling, marked with green lines in Figure 4.17b. Changing the positions of Ga^{4b} and Mn^{4a} results in AFM coupling because the Mn^{4b} - Mn^{4c} distance is ≈ 259 pm. This leads to random competing exchange on the Mn^{4c} sublattice, which will tend to give rise to a non-collinear spin structure. The local Mn^{4c} macroscopic sublattice moment may be expected to cant away from the anisotropy axis, forming an easy cone if four-fold in-plane anisotropy is negligible. The cone angle is the angle between the anisotropy axis and the moment. Local atomic environments differ on account of the random site occupancies that follow from the composition of the films, adding an element of randomness to the competing interactions, and the local canting angle.

In-plane applied field SQUID magnetometry data in Figures 4.8, 4.9 and 4.10, shows a component of the net moment which easily saturates along the *in-plane* field direction, unlike the hard component which normally extrapolates to the anisotropy field. For films with higher Ru content, which are closer to compensation at room temperature, the soft component dominates, and the determination of the anisotropy field is problematic. From the data on the first two samples in Figure 4.8 we deduce a cone angle for the net moment of 21°. We have measured the cone angle in other MRG thin films by vector SQUID magnetometry and find values that can be as large as 40°. A feature of the *out-of-plane* loops is the step in magnetisation near remanence that corresponds to 40 % of the weak moment. We associate this with a closing of the

Mn^{4c} cone and a simultaneous opening of a cone on the Mn^{4a} sublattice, for which we have seen evidence in XMCD data which is discussed in chapter 6. [23]

From the analysis of exchange energies and lattice parameters, it follows that sublattice non-collinearity results from competing positive and negative exchange coupling for the Mn^{4c} sublattice. This case has previously been argued for Mn^{2d} sites in tetragonal $D0_{22}$ Mn_2RhSn.[25] A picture that represents our experimental observations well appears on the right hand side of Figure 4.17c. We note that the Mn^{4c} cone angle needs to be only a few degrees to result in canting of the net moment by tens of degrees, because the net moment is more than an order of magnitude smaller than the sublattice moments, depending on how close the temperature is to compensation. The AHE loops, where R_{xy} is proportional to the perpendicular component of the Mn^{4c} sublattice magnetisation, exhibit high remanence and we conclude that the very small in-plane moment of the Mn^{4c} sublattice cannot be detected.

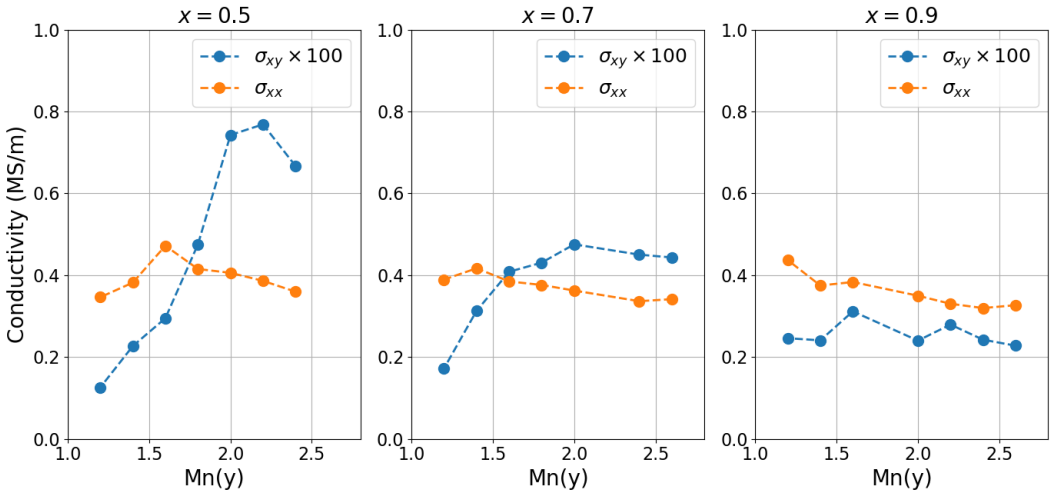

Figure 4.18: Transverse (σ_{xy}) and longitudinal (σ_{xx}) conductivities of MRG thin films at 300 K for three Ru(x) series versus Mn(y) content. Note that σ_{xy} was calculated at magnetic saturation in $\mu_0 H = 1$ T at $T = 300$ K and in the data in the graph has been multiplied by a factor of 100.

The longitudinal (σ_{xx}) and transverse (σ_{xy}) conductivities of MRG thin films are plotted for three Ru(x) series versus Mn(y) in Figure 4.18. The magnitude of σ_{xx} in the absence of a magnetic field is proportional to the conduction electron scattering. In all samples, σ_{xx} is almost constant whereas σ_{xy} shows a strong dependence on both Mn and Ru. To explain the observations, we need to consider the origins of AHE. There

are two types of contributions to the anomalous conductivity. The first is the extrinsic contribution which is scattering dependent. There are two distinct mechanisms, skew scattering and side jump, where the former is proportional to σ_{xx} and the latter is independent of σ_{xx}. The second contribution is scattering independent (intrinsic) arising from Berry curvature and is independent of σ_{xx}. [21]

In Figure 4.18, σ_{xy} exhibits a decrease with increasing Ru content. When Mn is varied with low x, σ_{xy} is seen to be independent of σ_{xx}, but for $x = 0.9$ σ_{xy} is approximately constant. The independence of σ_{xy} on σ_{xx} and its strong dependence on Ru content x suggests that for low x films the main contribution to AHE has an intrinsic origin. Impurity scattering, which depends on spin-orbit interaction, would be expected to increase with x. We find a maximal anomalous Hall angle $\theta_{AH} = 2$ % for $Mn_{2.2}Ru_{0.5}Ga$, which is ≈ 10 times higher than in conventional ferromagnets measured at 300 K. [26] Such large Hall angles are consistent with a large intrinsic contribution. While this could be a Berry phase effect, we are unable to disentangle the possible contributions of band structure (Weyl points), non-collinearity, Fermi surface effects and the influence of the incipient spin flop, which is expected for a ferrimagnet near compensation [27], and which is complete in $Mn_{2.2}Ru_{0.7}Ga$ at 7.65 T [23].

4.5 Conclusion

At the outset $Mn_2Ru_{0.5}Ga$ was assumed to have vacancies on the 4*d* sites. Here we have shown from the observed densities that all four sites in MRG are all practically full, which implies that $Mn_2Ru_{0.5}Ga$ has 24 valence electrons, not 21 as originally thought. Full occupancy of the 4*a* and 4*c* sites by Mn leads to a collinear ferrimagnetic structure, which accounts for the magnetic material properties.

The substantial absence of vacancies implies the presence of chemical disorder. Specifically, the presence of some Mn on 4*b* and 4*d* sites promotes antiferromagnetic intra-sublattice exchange coupling on the Mn^{4c} sublattice, which leads to a non-collinear ferrimagnetic structure. The non-collinearity or the the small net moment is much more pronounced than of the Mn^{4c} sublattice moment. The discrepancy between the AHE and measurements of magnetisation in Figures 4.8, 4.9 and 4.10 can therefore be explained. The independence of longitudinal and transverse conductivities indicates the dominance of the intrinsic contribution to AHE, which accounts for the

large anomalous Hall angle observed in MRG films with low x . The reduction in spin polarisation with increasing Ru corresponds to a narrowing of the spin gap in the density of states. The half-metallicity of MRG in the range of compositions investigated is confirmed by Slater-Pauling behaviour of the net moment.

The magnetisation, spin polarisation and compensation point of MRG can be tuned to match the requirements of a specific application by varying the composition of the films. Highly crystalline, textured thin films with magnetic compensation ranging from $T = 0$ K up to the magnetic ordering temperature can be produced. The coercivity near compensation that can exceed 10 T, could permit the incorporation of single MRG layers in thin film stacks without any additional antiferromagnetic layers. [12]

References

[1] D. Betto, K. Rode, N. Thiyagarajah, Y.-C. Lau, K. Borisov, G. Atcheson, M. Žic, T. Archer, P. Stamenov, and J. M. D. Coey, "The zero-moment half metal: How could it change spin electronics?," *AIP Adv.*, vol. 6, no. 5, p. 055601, 2016. (Cited on page: 125, 126, 127)

[2] J. Finley and L. Liu, "Spintronics with compensated ferrimagnets," *Appl. Phys. Lett.*, vol. 116, no. 11, p. 110501, 2020. (Cited on page: 125)

[3] T. Graf, C. Felser, and S. S. Parkin, "Simple rules for the understanding of heusler compounds," *Prog. Solid State Ch.*, vol. 39, no. 1, pp. 1 – 50, 2011. (Cited on page: 125)

[4] G. Bonfiglio, K. Rode, K. Siewerska, J. Besbas, G. Y. P. Atcheson, P. Stamenov, J. M. D. Coey, A. V. Kimel, T. Rasing, and A. Kirilyuk, "Magnetization dynamics of the compensated ferrimagnet Mn_2Ru_xGa," *Phys. Rev. B*, vol. 100, p. 104438, Sep 2019. (Cited on page: 125)

[5] S. Lenne, Y.-C. Lau, A. Jha, G. Y. P. Atcheson, R. E. Troncoso, A. Brataas, J. M. D. Coey, P. Stamenov, and K. Rode, "Giant spin-orbit torque in a single ferrimagnetic metal layer," 2019. (Cited on page: 125)

[6] M. Cubukcu, O. Boulle, M. Drouard, K. Garello, C. Onur Avci, I. Mihai Miron, J. Langer, B. Ocker, P. Gambardella, and G. Gaudin, "Spin-orbit torque magnetization switching of a three-terminal perpendicular magnetic tunnel junction," *Applied Physics Letters*, vol. 104, no. 4, p. 042406, 2014. (Cited on page: 126)

[7] L. Liu, O. J. Lee, T. J. Gudmundsen, D. C. Ralph, and R. A. Buhrman, "Current-induced switching of perpendicularly magnetized magnetic layers using spin

torque from the spin hall effect," *Phys. Rev. Lett.*, vol. 109, p. 096602, Aug 2012. (Cited on page: 126)

[8] J. Finley, C.-H. Lee, P. Y. Huang, and L. Liu, "Spin–Orbit Torque Switching in a Nearly Compensated Heusler Ferrimagnet," *Advanced Materials*, vol. 31, no. 2, p. 1805361, 2019. (Cited on page: 126)

[9] C. Banerjee, N. Teichert, K. Siewierska, Z. Gercsi, G. Atcheson, P. Stamenov, K. Rode, J. M. D. Coey, and J. Besbas, "Single pulse all-optical toggle switching of magnetization without gadolinium in the ferrimagnet Mn_2Ru_xGa," *Nat. Commun.*, vol. 11, p. 4444, 2020. (Cited on page: 126)

[10] C. S. Davies, G. Bonfiglio, K. Rode, J. Besbas, C. Banerjee, P. Stamenov, J. M. D. Coey, A. V. Kimel, and A. Kirilyuk, "Exchange-driven all-optical magnetic switching in compensated 3*d* ferrimagnets," *Phys. Rev. Res.*, vol. 2, p. 032044, Aug 2020. (Cited on page: 126, 143)

[11] C. Banerjee, K. Rode, G. Atcheson, S. Lenne, P. Stamenov, J. M. D. Coey, and J. Besbas, "Ultrafast double pulse all-optical reswitching of a ferrimagnet," *Phys. Rev. Lett.*, p. Accepted, 2021. (Cited on page: 126)

[12] K. Borisov, D. Betto, Y. C. Lau, C. Fowley, A. Titova, N. Thiyagarajah, G. Atcheson, J. Lindner, A. M. Deac, J. M. D. Coey, P. Stamenov, and K. Rode, "Tunnelling magnetoresistance of the half-metallic compensated ferrimagnet mn2ruxga," *Appl. Phys. Lett.*, vol. 108, no. 19, p. 192407, 2016. (Cited on page: 126, 147)

[13] H. Kurt, K. Rode, P. Stamenov, M. Venkatesan, Y. C. Lau, E. Fonda, and J. M. D. Coey, "Cubic Mn_2Ga thin films: Crossing the spin gap with ruthenium," *Phys. Rev. Lett.*, vol. 112, no. 2, p. 027201, 2014. (Cited on page: 126, 127, 137, 142)

[14] M. Žic, K. Rode, N. Thiyagarajah, Y.-C. Lau, D. Betto, J. M. D. Coey, S. Sanvito, K. J. O'Shea, C. A. Ferguson, D. A. MacLaren, and T. Archer, "Designing a fully compensated half-metallic ferrimagnet," *Phys. Rev. B*, vol. 93, no. 14, p. 140202, 2016. (Cited on page: 126, 139)

[15] N. Thiyagarajah, Y.-C. Lau, D. Betto, K. Borisov, J. M. D. Coey, P. Stamenov, and K. Rode, "Giant spontaneous Hall effect in zero-moment Mn_2Ru_xGa," *Appl. Phys. Lett.*, vol. 106, no. 12, p. 122402, 2015. (Cited on page: 126, 134)

[16] D. Betto, N. Thiyagarajah, Y.-C. Lau, C. Piamonteze, M.-A. Arrio, P. Stamenov, J. M. D. Coey, and K. Rode, "Site-specific magnetism of half-metallic Mn_2Ru_xGa thin films determined by x-ray absorption spectroscopy," *Phys. Rev. B*, vol. 91, no. 9, p. 094410, 2015. (Cited on page: 126, 142)

[17] I. V. Soldatov and R. Schäfer, "Advanced MOKE magnetometry in wide-field kerr-microscopy," *J. Appl. Phys.*, vol. 122, no. 15, p. 153906, 2017. (Cited on page: 127)

[18] P. Stamenov, "Point contact Andreev reflection from semimetallic bismuth—the roles of the minority carriers and the large spin-orbit coupling," *J. Appl. Phys.*, vol. 113, no. 17, p. 17C718, 2013. (Cited on page: 128)

[19] K. Borisov, C.-Z. Chang, J. S. Moodera, and P. Stamenov, "High Fermi-level spin polarization in the $(Bi_{1-x}Sb_x)_2Te_3$ family of topological insulators: A point contact Andreev reflection study," *Phys. Rev. B*, vol. 94, p. 094415, Sep 2016. (Cited on page: 128)

[20] H. Kurt, K. Rode, P. Stamenov, M. Venkatesan, Y. . Lau, E. Fonda, and J. M. D. Coey, "Cubic Mn_2Ga thin films: Crossing the spin gap with ruthenium," *Phys. Rev. Lett.*, vol. 112, no. 2, 2014. (Cited on page: 130)

[21] N. Nagaosa, J. Sinova, S. Onoda, A. H. MacDonald, and N. P. Ong, "Anomalous Hall effect," *Rev. Mod. Phys.*, vol. 82, no. 2, pp. 1539–1592, 2010. (Cited on page: 134, 146)

[22] J. Smart, *Effective Field Theories of magnetism*. London: Saunders, 1966. (Cited on page: 139)

[23] K. Siewierska, D. Betto, N. Teichert, G. Atcheson, N. Brookes, and K. Rode, "XMCD investigation of sublattice non-collinearity in compensated ferrimagnetic half-metallic thin films," *Unpublished*, 2021. (Cited on page: 143, 145, 146)

[24] J. Coey, *Magnetism and Magnetic Materials*. Cambridge University Press, New York, 2010. (Cited on page: 144)

[25] O. Meshcheriakova, S. Chadov, A. K. Nayak, U. K. Rößler, J. Kübler, G. André, A. A. Tsirlin, J. Kiss, S. Hausdorf, A. Kalache, W. Schnelle, M. Nicklas, and C. Felser, "Large noncollinearity and spin reorientation in the novel Mn_2RhSn Heusler magnet," *Phys. Rev. Lett.*, vol. 113, no. 8, p. 087203, 2014. (Cited on page: 145)

[26] T. Seki, S. Iihama, T. Taniguchi, and K. Takanashi, "Large spin anomalous Hall effect in $L1_0-$FePt: Symmetry and magnetization switching," *Phys. Rev. B*, vol. 100, p. 144427, Oct 2019. (Cited on page: 146)

[27] T. Fu, S. Li, X. Feng, Y. Cui, J. Yao, B. Wang, J. Cao, Z. Shi, D. Xue, and X. Fan, "Complex anomalous Hall effect of CoGd alloy near the magnetization compensation temperature," *Phys. Rev. B*, vol. 103, p. 064432, Feb 2021. (Cited on page: 146)

5

Magnetic Domain Structure and Reversal in Mn_2Ru_xGa

5.1 First Demonstration of Magnetic Domain Structure in Mn_2Ru_xGa near Compensation

5.1.1 Background

Magnetic domains in antiferromagnets and compensated ferrimagnets are difficult to observe, because the materials create no stray field. Methods available to image domains or domain walls in a ferromagnet, at least at the surface of a specimen, include sensing the stray field distribution by atomic force or scanning Hall microscopy, or colloid methods, imaging the magnetic induction B in very thin films by Lorentz transmission electron microscopy, and recording the polarisation of light transmitted or reflected from a specimen using the magneto-optic Faraday effect or magneto-optic Kerr effect (MOKE). However, none of these methods work in an antiferromagnet. Imaging magnetic domains in materials with no stray field is possible via techniques such as polarized neutron beam tomography [1; 2] or X-ray linear magnetic dichroism at synchrotron light sources [3; 4], or by using auxiliary Fe monolayers and spin-polarized

scanning tunneling microscopy [5]. Methods depending on magnetostriction [6], optical second-harmonic generation [7; 8], or magnetoelectric effects [9] have also been proposed. Here, we show that it is possible to use the magneto-optic Kerr microscope to image domains directly in a zero-moment half-metal material class that produce no stray field. Such materials are insensitive to external fields and demagnetising effects, yet electronically they resemble a perfect spin polarised ferromagnetic metal. Films of MRG grown on MgO (100) substrates exhibit perpendicular magnetic anisotropy due to a small 1% tetragonal elongation induced by biaxial substrate-induced strain. The electronic band structure exhibits a spin gap, and it is the $4c$ sublattice that predominantly contributes spin-polarised conduction electrons at the Fermi energy. The allows for imaging of the domains of MRG directly by polar MOKE, thereby opening up new imaging possibilities for domains in magnetically ordered materials with no net moment. In this paper, we use MOKE to measure the magnetic hysteresis and image the magnetisation processes of low-moment MRG films close to the compensation point. This serves as a proof of concept for imaging magnetic domains in spin-polarised, fully compensated ferrimagnets.

5.1.2 Methodology

The epitaxial thin film of MRG was grown on 10×10 mm^2 MgO (001) substrate by DC magnetron sputtering, using our Shamrock sputtering system. The film was co-sputtered in argon from two 75 mm targets of Mn_2Ga and Ru onto the MgO substrate maintained at 380 °C. The film was capped in situ with a 3 nm layer of AlO_x deposited at room temperature from an Al_2O_3 target in order to prevent oxidation and post-annealed ex-situ at 350 °C in vacuum for 30 min. The film was deposited with a nominal composition of $Mn_2Ru_{0.4}Ga$ and a magnetisation < 30 kAm^{-1} corresponding to a moment $< 0.16\mu_B$ per formula unit. Field- and temperature-dependent magnetometry data of similar samples are published in [10]. The composition $Mn_2Ru_{0.4}Ga$ was chosen so that the film has a low enough coercivity to be saturated at room temperature in the 300 mT magnet in the polar Kerr microscope. However, due to some Mn evaporation in the post-annealing process, the actual composition is slightly different.

A Bruker D8 X-ray diffractometer with a copper tube emitting $K_{\alpha 1}$ X-rays with wavelength 154.06 pm and a double-bounce Ge [220] monochromator was used to de-

termine the diffraction patterns of the thin films. Low-angle X-ray reflectivity (XRR) was measured using a PANalytical X'Pert Pro diffractometer, and thickness was found by fitting the interference pattern using X'Pert Reflectivity software with a least-squares fit. Anomalous Hall effect was measured using the four-point van der Pauw method with indium contacts and an applied current of 5 mA.

Atomic force microscopy was performed using multi-mode atomic force microscope in the contact mode. For Kerr imaging, a wide-field Kerr microscope with a $10\times/0.25$ objective lens was used. All loops have been measured with polar sensitivity and a control feature which readjusts the analyzer position with the help of a reference mirror in order to compensate the Faraday rotation in the objective lenses caused by the magnetic field applied perpendicular to the film [11]. The domain contrast was optimised by the means of an analyzer and a rotatable compensator (quarter-wave plate) [12]. Creeping behavior was observed by changing the magnetic field, so the images were recorded after the domain structure had stabilised. The grayscale domain images were converted to binary images using ImageJ software, and the fractal dimension of the domains was calculated by the box-counting method using the Fractalyse [13] software.

5.1.3 Results and Discussion

The X-ray diffraction pattern of the $Mn_2Ru_{0.4}Ga$ thin film shows (002) and (004) reflections, together with peaks from the MgO substrate (Figure 5.1). The ratio of (002) and (004) peak intensities (I(002)/I(004)) was 0.06, and this small value is indicative of a high degree of atomic order in the inverted $L2_1$ Heusler structure [14]. The c lattice parameter was calculated to be 606.4 pm, hence the percentage of tetragonal distortion

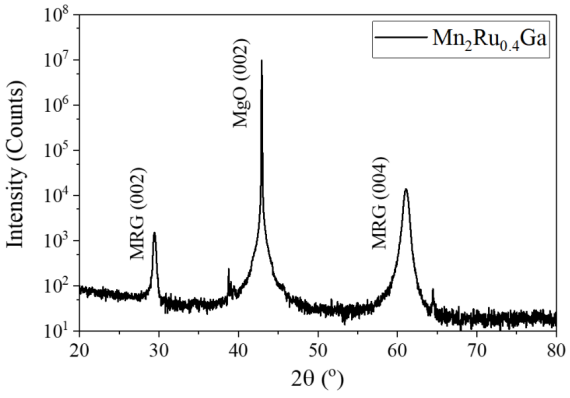

Figure 5.1: X-ray diffraction pattern of a film of $Mn_2Ru_{0.4}Ga$ on MgO(001) single crystal substrate.

of the cubic unit cell, given by $(c-a)/a$, is approximately 1% [15]. A least-squares fit to the XRR pattern yielded a thickness t for the MRG thin film of 40.2 nm. Atomic force microscopy of the film shows an RMS surface roughness of 1.3 nm.

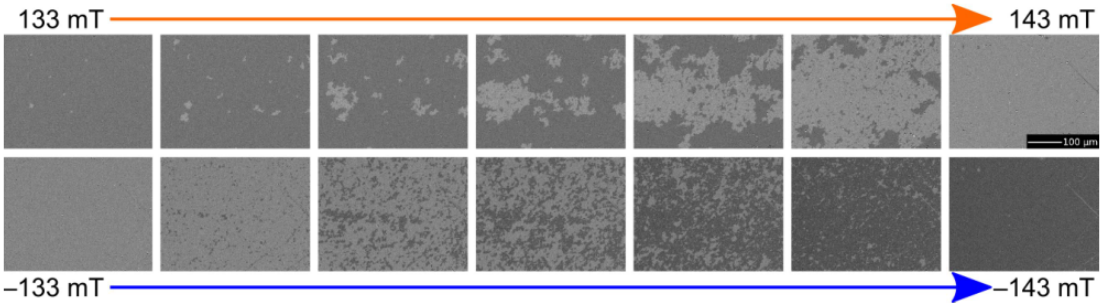

Figure 5.2: Kerr imaging of the magnetisation reversal process of nearly compensated $Mn_2Ru_{0.4}Ga$ with the out-of-plane easy axis. The contrast changes from dark (light) to light (dark) with increasing the positive (negative) field caused by nucleation and growth of magnetic domains during the switching process.

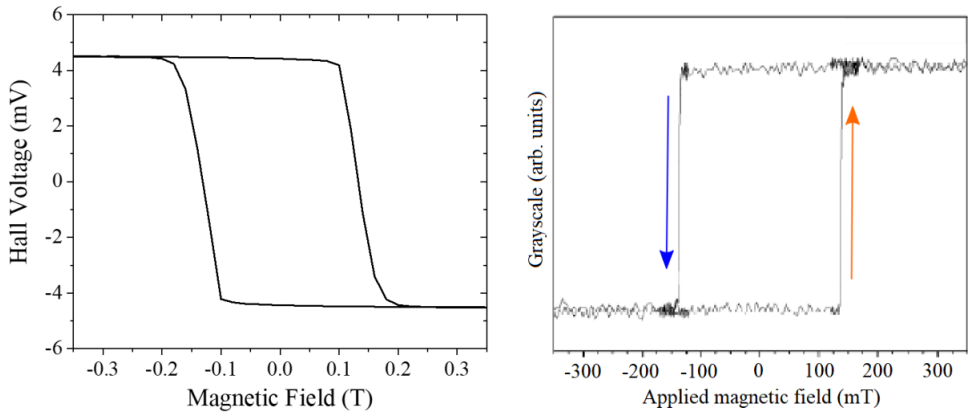

Figure 5.3: Hysteresis loops of $Mn_2Ru_{0.4}Ga$ obtained via anomalous Hall effect (left) and Kerr microscopy (right). The sharp switching observed by MOKE on a sub-millimeter-sized image contrasts with the broader switch measured by the Hall effect on a blanket 10×10 mm^2 film in the van der Pauw configuration.

Polar Kerr microscope was used to follow the magnetic 140 switching process of the perpendicular $Mn_2Ru_{0.4}Ga$ film. The domain images in a 400×300 μm^2 window are presented in Figure 5.2 as a function of the applied field around the negative and positive coercive fields. The magnetic hysteresis loops obtained by measurement of

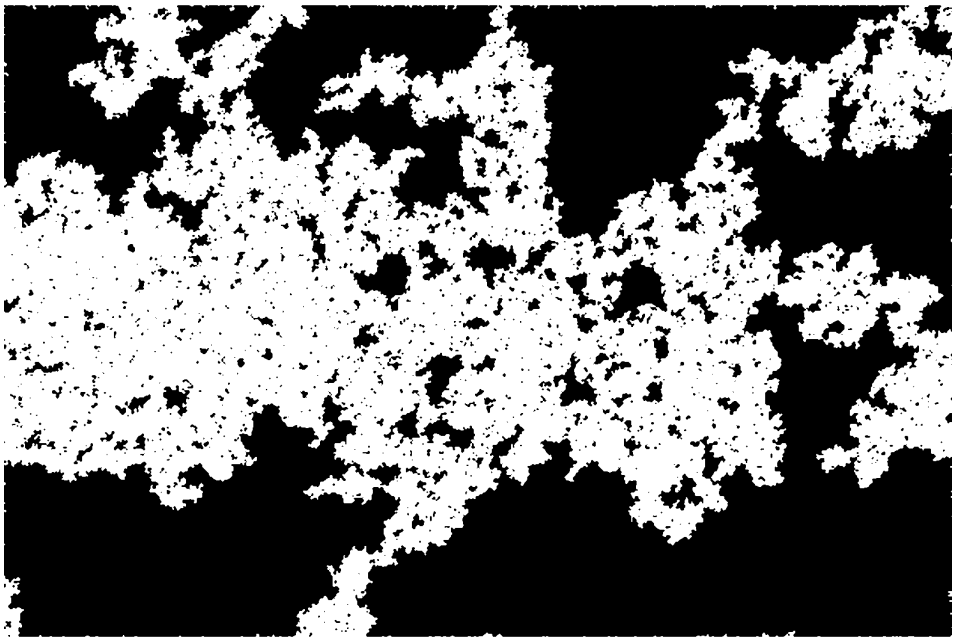

Figure 5.4: Fractal analysis. Fifth image (from left) of the top panel in Figure 5.2, converted from grayscale to binary. The image has a fractal dimension $D_f = 1.85$.

the anomalous Hall effect and analysis of the Kerr microscopy images are compared in Figure 5.3. Switching fields of both measurements coincide, but the switching process observed by MOKE is sharper. We attribute this to slight inhomogeneities in the film that are less visible in MOKE due to the smaller probing area of the measurement (10×10 mm^2 blanket film for the Hall measurement versus a sub-millimeter-sized image for MOKE). According to the AHE Loop in Figure 5.3, the coercive field $\mu_0 H_C = 137$ mT and onset of magnetisation switching are at $\mu_0 H_{SW} = 133$ mT. Domain creep is observed in the vicinity of the coercive field. The arrows indicate the direction of magnetisation change. The emerging domains (bright contrast) are seen to have irregular outlines, with dimensions of order 20 μm. They appear to nucleate randomly. With increasing the negative field, the reverse domains grow, and more new ones appear until the entire film has switched. We anticipate that defects or surface roughness of the film may play a part in pinning domain walls. The evolution of the domain pattern around negative H_C [Figure 5.2 (bottom: from left–right)] is similar and also involves the nucleation and growth of irregularly shaped domains (dark contrast) with a fractal structure. The same domain patterns are not reproduced on field

cycling to saturation. They do not nucleate in the same places, and nucleation does not appear to be primarily controlled by a set of non-magnetic defects in the crystal.

Fractal-like magnetic domains have previously been observed in thin films [16; 17] and at surfaces [18] of strong uniaxial ferromagnets. Fractal antiferromagnetic domains have been reported in NiO using spectroscopic photoemission and low-energy electron microscopy [19]. Figure 5.4 reproduces the fifth image of the top panel in Figure 5.2 after binary conversion using ImageJ. The fractal dimension of the domains determined by the box-counting method is $D_f = 1.85$. The irregular, fractal-like outlines of the domains suggest that the domain wall energy (per unit area) may be smaller than in typical ferromagnets.

5.1.4 Conclusion

Imaging of magnetic domains in low moment ferrimagnetic thin films with high spin polarization via MOKE has been demonstrated. Our approach offers an opportunity to investigate the domain structure of ZMHM materials at T_{comp} by the Kerr microscopy. The method can be extended to provide insight into domain dynamics in the absence of the stray field. Due to the uniaxial anisotropy in MRG thin films, at compensation this material magnetically resembles a uniaxial antiferromagnet, and therefore it is a candidate for investigating nucleation and to study spin-flop transitions on a microscopic scale. Domains can also be observed at compensation by varying the sample temperature.

5.2 Magnetic Domain Reversal and Domain Wall Pinning in Mn_2Ru_xGa

5.2.1 Background

In this section the aim is to compare the magnetic domain patterns and time dependence of the magnetic reversal process depending on the tetragonal distortion of the material. This was modified by variation of the substrate temperature during deposition while maintaining composition, film thickness and surface roughness. Increased substrate temperatures lead to relaxation of the material hence reducing the degree of tetragonal distortion.

Depending on the deposition temperature we observed two distinct magnetisation reversal processes, one dominated by domain wall motion and the other by domain nucleation, similar to those observed in other perpendicular thin films. [20; 21] We analysed them by time-dependent measurements of the magnetic after-effect, yielding estimations of the involved activation volumes and activation energy distributions, whereby a strong dependence on the deposition temperature was ascertained. The distribution of activation energies is the underlying cause of reversal and it is due to crystalline defects such as misfit dislocations that locally alter the distortion and thereby the anisotropy of the material. The defects act as pinning centres for the magnetic domains.

Virgin domain patterns in MRG thin films are also characterised. We explore the temperature dependence of the domain pattern and find that it does not change once it nucleates just below T_C. Also, we demonstrate a method to visualise pinning centres by analysing virgin domain patterns after repeated thermal demagnetisation.

5.2.2 Methodology

Epitaxial thin films of MRG were grown by DC magnetron co-sputtering on 10×10 mm^2 MgO(100) substrates using a Shamrock sputtering system. The films were deposited from three 75 mm diameter targets of Mn_2Ga, Mn_3Ga and Ru in argon atmosphere. A series of samples with the same composition of $Mn_{2.2}Ru_{0.5}Ga$ were prepared at different substrate temperature during deposition, T_{dep}, set by a heating coil behind the substrate and varied from 240 °C to 350 °C. The MgO substrates were back-coated with tantalum for constant infrared absorption during thin film deposition. Two of those samples were chosen for deeper characterisation, because they exhibit two different magnetisation reversal mechanisms. The chosen samples from the series were prepared with T_{dep} =300 °C (sample A) and T_{dep} =320 °C (sample B). Another sample considered in the study has a composition of $Mn_{2.2}Ru_{0.9}Ga$ and was deposited at nominally 340 °C, but without tantalum back coating (sample C). This sample demonstrates that it is possible for the reversal mechanism to be a mixture of the two processes identified in samples A and B. All films have a thickness of 52 nm and were capped in-situ with a 2 nm layer of AlO_x deposited at room temperature in order to prevent oxidation.

A Bruker D8 High-Res X-ray diffractometer with a Cu tube (λ=1.59 Å) and a double-bounce Ge[220] monochromator was used to determine the reciprocal space maps of the thin films. Other diffraction patterns and low angle X-ray reflectivity (used to confirm the film thickness) was measured with a Panalytical X'Pert Pro diffractometer using Cu Kα_1 radiation.

Domain imaging, magnetic hysteresis and after-effect measurements were performed in an out-of-plane-field electromagnet using an Evico polarization microscope illuminated by either red (central wavelength λ=632 nm) or blue (λ=455 nm) light from an LED array. For high-resolution imaging at room temperature, a 100× immersion lens ($NA = 1.3$) combined with the blue light option was used. Lower resolution imaging and magnetic hysteresis and after-effect measurements were done using red light and 20× magnification. For magnetic hysteresis measurements the polar Faraday effect was compensated using the mirror technique described in [11]. For temperature-dependent measurements the films were covered by a protective 10 nm film of SiO_2. A 50× non-immersion lens ($NA = 0.8$), blue light, and a lab built heating stage were used, while keeping the sample in a nitrogen gas-flow chamber.

Atomic force microscopy was performed using multi-mode atomic force microscope in the tapping mode. Magnetotransport is measured using Van der Pauw method in a 1 T GMW magnet. Saturation magnetisation and anisotropy field were obtained by in-plane and out-of-plane SQUID magnetometry magnetisation versus applied field measurements.

5.2.3 Theory - Magnetisation Reversal in Ferrimagnetic Thin Films

In 1962, E. Fatuzzo published his theory to describe the polarisation reversal in ferroelectric materials. [22] This process is analogous to magnetisation reversal in ferromagnetic alloys such as rare-earth - transition in thin films.[23] This model can also be extended to ferrimagnets to understand the shapes of the curves of magnetisation reversal as a function of time observed for MRG and hence identify the dominant reversal mechanism. The model assumes that the nuclei of domains are formed at random on the surface of the crystal according to a statistical process. To calculate the area covered by the switched domains as a function of time, the model neglects both (a) possibility of overrunning of nucleation sites by the sideways growth of domains and

(b) merging of the domains due to their sideways expansions. It is noted that those assumptions are not realistic, however this calculation of restricted area A is needed to calculate the unrestricted area θ.

Let N_0 the total number of nucleation sites and $N(t)$ be the total number of nuclei at time t. Considering the magnetisation reversal via nucleation occurs according to a statistical process in a random way with a probability R per unit time, hence we obtain

$$\frac{dN}{(N-N_0)} = Rdt \tag{5.1}$$

$$N(t) = N_0\left(1-e^{-Rt}\right) \tag{5.2}$$

where separation of variables was applied to the differential equation and then integrated. The area A has the form

$$A = \left[\int_0^t ds\left(\frac{dN}{dt}\right)_s (\sigma_n)_{t-s}\right] + \frac{\pi r_c^2}{T}N(t) \tag{5.3}$$

where the first term is an integral which finds the area due to the growth of domains and the second term is the area covered by N nuclei, which form over an area T (Note: in Fatuzzo's model this is the total electrode area). In the integral, $(\sigma_n)_{t-s}$ represents the amount that the domain has expanded through sideways motion at time $(t-s)$. In the second term r_c is the radius of the nucleus, modelled as a disk, at its birth and it can grow by velocity v_0. Evaluating the integral, the expression for A becomes

$$\begin{aligned} A = \frac{2N_0v_0^2}{TR^2}&\left[1-R(t_0+t)+\frac{1}{2}R^2(t_0+t)^2-e^{-Rt}\left(1-Rt_0+\frac{1}{2}R^2t_0^2\right)\right] \\ &-\frac{\pi r_c^2N_0}{T}\left(1-e^{-Rt}\right)+\frac{\pi r_c^2}{T}N(t) \end{aligned} \tag{5.4}$$

Examining the above expression it is clear that in the limit where $t\to\infty$, $A\to\infty$, which is unphysical because of the two assumptions made earlier. However, the more accurate area θ can be calculated using A, as a consequence of the theorem by Avrami [24], summarised by equation

$$\theta = 1-\exp(-A) \tag{5.5}$$

where θ is the true surface coverage and it is expressed as a function of the extended

surface coverage A, which is a convolution of the growth and nucleation process. Therefore, in the limit of $t \to \infty$, $\theta \to 1$, i.e. it is finite and unity represents the entire area of the surface of the thin film. It should be noted that the theorem neglects the area of the nucleus at it's birth, however Fatuzzo modifies the Avrami equation to incorporate it, hence θ becomes

$$\theta = 1 - \exp\left[-\left(A + \frac{\pi r_c^2 N_0 R t}{T} - \frac{\pi r_c^2}{T} N(t)\right)\right] \tag{5.6}$$

and substituting equation 5.4 into the above yields

$$\theta = 1 - \exp\left(-2k^2\left[1 - (\tau + k^{-1}) + \frac{1}{2}(\tau + k^{-1})^2 - e^{-\tau}(1 - k^{-1}) - \frac{1}{2}k^{-2}(1 - \tau)\right]\right) \tag{5.7}$$

where

$$k = \frac{1}{Rt_0}$$
$$\tau = Rt$$

and τ can be considered as a dimensionless time and $t_0 = r_c/v_0$. Now the fractional area $B(\tau)$ that has not been switched at time τ can be defined as

$$B(\tau) = \exp\left(-2k^2\left[1 - (\tau + k^{-1}) + \frac{1}{2}(\tau + k^{-1})^2 - e^{-\tau}(1 - k^{-1}) - \frac{1}{2}k^{-2}(1 - \tau)\right]\right) \tag{5.8}$$

Figure 5.5 is an illustration of the magnetisation reversal curve shapes in equation 5.8 for various values of the parameter k. From the theory, for small values of k the magnetisation reversal process is dominated by nucleation. Large k values indicate a domain wall propagation dominated reversal mechanism.

Magnetisation reversal in hard ferrimagnets requires applying a magnetic field H and the number of domains N nucleated over an area S during time t is given by

$$N = N^* S t e^{\beta H} \tag{5.9}$$

where N^* is a constant characteristic to the magnetic alloy at a given temperature. For applied fields lower than coercivity H_C, magnetisation reversal is thermally activated

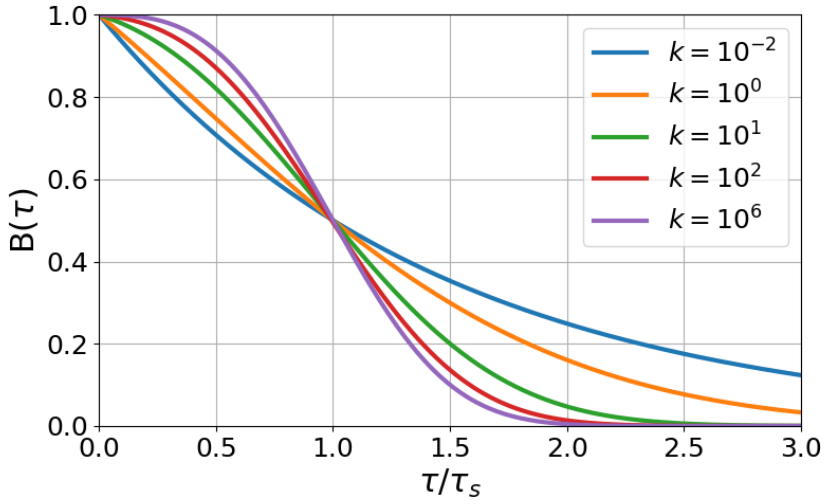

Figure 5.5: Theoretical magnetisation reversal curves described by equation 5.8 for different values of k, where t_{50} is the time it takes to reverse 50% of the domains.

and for a fixed temperature, the domain wall velocity v_0 is given by

$$v_0 = v^* \exp\left(\frac{H}{H_C}\right) \tag{5.10}$$

where v^* is a constant.

Quantitative Analysis

Considering the case of $\tau = Rt << 1$, then $N = N_0 Rt$ and now comparing this to equation 5.9 leads to the expression for nucleation probability R

$$R = \frac{N^* S}{N_0} e^{\beta H} \tag{5.11}$$

Now using the expression for k and equation 5.10 yields

$$k = \frac{v_0}{R r_c} \tag{5.12}$$

$$k = \frac{v^* N_0}{N^* S r_c} \exp\left(\left(\frac{1}{H_C} - \beta\right) H\right) \tag{5.13}$$

Let the switching time t_{50} can be defined as the time needed to switch 50 % of the domains, meaning $\theta(\tau_s) = 0.5$, where $\tau_s = R t_{50}$. Empirical expression for t_{50} is given

by

$$t_{50} = t_0 \exp\left(\alpha\left(H_C^* - H\right)\right) \tag{5.14}$$

where t_0 is the activation time ($\approx 10^{-10}$ s), α and H_C^* are fitting parameters, with the latter expected to be close or equal to H_C. To find tau_s in terms of k, the expression for θ in terms of $B(\tau)$ for $\tau = \tau_s$

$$\theta(\tau_s) = 1 - B(\tau_s) = 0.5$$
$$B(\tau_s) = 0.5$$

can be used. This analysis will be applied to the two mechanisms of magnetisation reversal.

(i) Domain wall propagation only ($k >> 1$)

Since $B(\tau)$ from equation 5.8 has the form $\exp(-\zeta(\tau))$, first evaluate the argument of the exponential function in the limit $k \to \infty$, and small $\tau = \tau_s << 1$

$$\zeta(\tau_s) = 2k^2\left(1 - \tau_s + \frac{1}{2}\tau_s^2 - e^{-\tau_s}\right) \tag{5.15}$$

$$\zeta(\tau_s) = 2k^2\left(1 - \tau_s + \frac{1}{2}\tau_s^2 - \left(1 - \tau_s + \frac{1}{2}\tau_s^2 - \frac{1}{6}\tau_s^3 + ...\right)\right) \tag{5.16}$$

$$\zeta(\tau_s) \approx \frac{1}{3}k^2\tau_s^3 \tag{5.17}$$

where the Tailor expansion formula, $\exp(-\tau_s) \approx 1 - \tau_s + \frac{1}{2}\tau_s^2 - \frac{1}{6}\tau_s^3$, was used. Therefore the expression $B(\tau)$ reduces to

$$B(\tau_s) = \exp\left(-\frac{1}{3}k^2\tau_s^3\right) \tag{5.18}$$

Using the above expression $B(\tau_s) = 0.5$, an analytical expression for τ_s can be obtained

$$\exp(-\zeta(\tau_s)) = \frac{1}{2} \tag{5.19}$$

$$\zeta(\tau_s) = \ln(2) \tag{5.20}$$

$$\frac{1}{3}k^2\tau_s^3 = \ln(2) \tag{5.21}$$

$$\tau_s = \left(\frac{3\ln(2)}{k^2}\right)^{\frac{1}{3}} \tag{5.22}$$

where it is clear that $k \to \infty$ implies $\tau_s \to 0$. Also, since $\tau_s = Rt_{50}$, it follows that

$$t_{50} \propto \exp(-\beta H) k^{\frac{-2}{3}} \tag{5.23}$$

$$t_{50} \propto \exp(-\beta H) \exp\left(\frac{-2}{3}\left(\frac{1}{H_C} - \beta\right) H\right) \tag{5.24}$$

$$t_{50} \propto \exp\left(-\frac{1}{3}\left(\beta - \frac{2}{H_C}\right) H\right) \tag{5.25}$$

(ii) Nucleation only ($k << 1$)

In the limit of small k, $B(\tau)$ reduces to

$$B(\tau) = \exp(-\tau) \tag{5.26}$$

Following a similar method to the one in the previous case, we find τ_s

$$\exp(-\tau_s) = \frac{1}{2} \tag{5.27}$$

$$\tau_s = \ln(2) \tag{5.28}$$

and also

$$t_{50} \propto \exp(-\beta H) \tag{5.29}$$

Activation Energy

As mentioned above, when the applied field H is less than the coercive field H_C, magnetisation reversal is thermally activated. As before the two reversal mechanisms of nucleation and domain wall propagation will be considered and the expressions for the respective activation energies and volumes will be derived. The starting point in this calculation is assuming a single activation energy for each mechanism and write down expressions for nucleation probability R and domain wall velocity v

$$R \approx R_0 \exp\left[-\frac{(W_N - 2HMV_N)}{k_B T}\right]$$

and (5.30)

$$v \approx v_0 \exp\left[-\frac{(W_P - 2HMV_P)}{k_B T}\right]$$

where W_N and W_P are activation energies for nucleation and domain wall propagation and their corresponding activation volumes V_N and V_P.

(i) Nucleation only ($k << 1$) In this limit, we consider an assembly of isolated nucleated domains of volume V and the reversal process requires overcoming an energy barrier E. This is done thermally and the mean waiting time Γ before the energy jump occurs can be defined as

$$\Gamma = \left(\frac{1}{F_0}\exp\left(\frac{E}{k_BT}\right)\right) \tag{5.31}$$

where F_0 is a frequency factor and $E = W - 2HMV$ with W being the activation energy. Using equation 5.26 and relation $\tau = Rt$, obtain

$$B(t) = \exp(-Rt) = \exp\left(-\frac{t}{\Gamma}\right) \tag{5.32}$$

Letting $t = t_{50}$ and using equation 5.14 with equation 5.31 with specified nucleation activation energy and volume gives

$$\begin{aligned}
B(t_{50}) = \exp\left(-\frac{t_{50}}{\Gamma}\right) &= \frac{1}{2} \\
t_{50} &= \Gamma\ln(2) \\
\exp(\alpha(H_C^* - H)) &= \left(\frac{\ln(2)}{F_0}\right)\exp\left(\frac{W_N - 2HMV_N}{k_BT}\right) \\
(\alpha(H_C^* - H)) &= \ln\left(\frac{\ln(2)}{F_0}\right) + \left(\frac{W_N - 2HMV_N}{k_BT}\right) \\
W_N(H) &= k_BT\left(\alpha(H_C^* - H) + \ln\left(\frac{F_0}{\ln(2)}\right)\right) + 2HMV_N
\end{aligned}$$

Let $H = 0$ and $H_C^* = H_C$, then the above expression for W_N in the absence of external fields becomes

$$W_N = k_BT\left(\alpha H_C + \ln\left(\frac{F_0}{\ln(2)}\right)\right) \tag{5.33}$$

and $\alpha = \frac{2MV_N}{k_BT}$ found from solving $\frac{dW_N(H)}{dH} = 0$.

The nuclei can be modelled as cylinders with radius $r_c \approx \delta_W$ and height equal to the thickness of the thin film (D). For the energy of the nucleus, it can either be assumed that the contribution is purely anisotropic hence $W_N = KV_{ACT}$, or a domain wall contribution meaning $W_N = 2\pi r_c D\sigma$, where σ is domain wall energy. For the case of MRG, the former is more appropriate than the latter.

A last short note, a crude approximation to obtain an analytical expression for parameter N^* is given by

$$N^* = \left(\frac{F_0}{\delta^2}\exp\left(-\frac{W_N}{k_BT}\right)\right) \tag{5.34}$$

(ii) Domain wall propagation only ($k >> 1$)

Using a similar approach as above, with $v_0 \approx F_0 r_c$ and assuming no field dependence in parameter k meaning $V_N \approx V_P = V_{ACT}$

$$B(t) = \exp\left(-\frac{1}{3}k^2(Rt)^3\right) = \exp\left(-\frac{1}{3}k^2\left(\frac{t}{\Gamma}\right)^3\right) \tag{5.35}$$

Letting $t = t_{50}$ and using equation 5.14 with equation 5.31 with specified domain wall propagation activation energy and active volume V_{ACT} gives

$$\begin{aligned}
\exp\left(-\frac{1}{3}\left(\frac{t_{50}}{\Gamma}\right)^3\right) &= \frac{1}{2} \\
\frac{1}{3}\left(\frac{t_{50}}{\Gamma}\right)^3 &= \ln(2) \\
t_{50} &= \Gamma\left(3\ln(2)\right)^{\frac{1}{3}} \\
\exp(\alpha(H_C^* - H)) &= \exp\left(\frac{W_P - 2HMV_{ACT}}{k_BT}\right)\frac{(3\ln(2))^{\frac{1}{3}}}{F_0} \\
\alpha(H_C^* - H) &= \left(\frac{W_P - 2HMV_{ACT}}{k_BT}\right) + \ln\left(\frac{(3\ln(2))^{\frac{1}{3}}}{F_0}\right) \\
W_P(H) &= k_BT\left(\alpha(H_C^* - H) + \ln\left(\frac{F_0}{(3\ln(2))^{\frac{1}{3}}}\right)\right) + 2HMV_{ACT}
\end{aligned}$$

Let $H = 0$ and $H_C^* = H_C$, then the above expression for W_P in the absence of external fields becomes

$$W_P = k_BT\left(\alpha H_C + \ln\left(\frac{F_0}{(3\ln(2))^{\frac{1}{3}}}\right)\right) \tag{5.36}$$

and $\alpha = \frac{2MV_{ACT}}{k_BT}$.

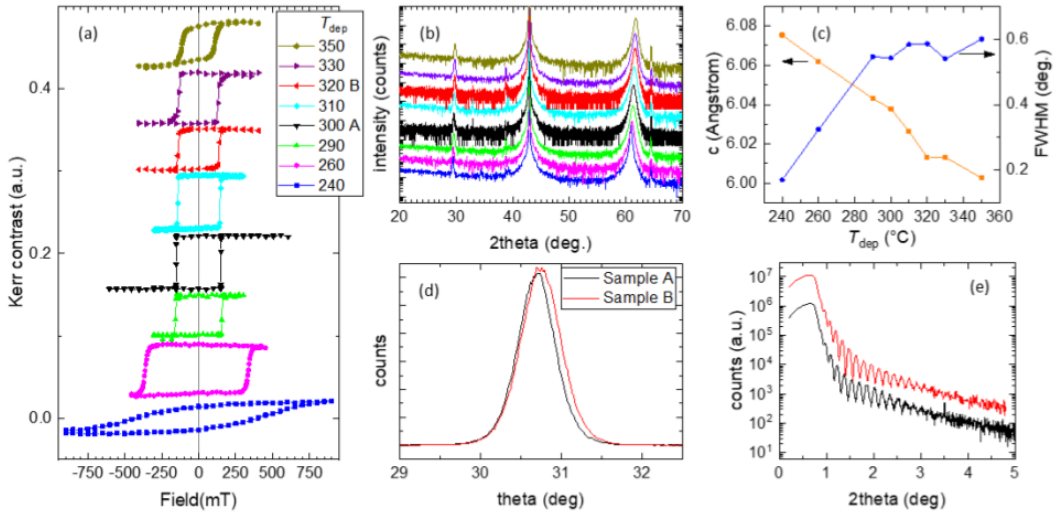

Figure 5.6: MOKE hysteresis loops and structural characterisation. MOKE measurements (a) yield hysteresis loops with high squareness and similar coercivity for 290 °C $\leq T_{dep} \leq$ 350 °C. XRD patters (b) reveal a peak shift of the (002) and (004) reflections to higher 2θ angles with increasing T_{dep}. The corresponding lattice parameters are shown in (d) together with rocking curve widths of the (004) reflection. Selected rocking curves and XRR measurements are shown in (d) and (e), respectively.

Sample	T_{dep} [°C]	c [pm]	a [pm]	$c/a-1$ [%]	l_x [nm]	l_z [nm]
A	300	604	598	1.0	16.5	25.0
B	320	601	599	0.3	11.9	13.8

Table 5.1: Structural parameters of samples A and B.

5.2.4 Characterisation of Samples I: Samples A and B

Figure 5.6 (a) shows polar magneto-optical Kerr effect (MOKE) hysteresis loops of a series of $Mn_{2.2}Ru_{0.5}Ga$ thin films deposited using different deposition temperatures T_{dep}. For temperature 290 °C $\leq T_{dep} \leq$ 330 °C the samples exhibit square hysteresis loops with similar coercive fields around 150 mT. Lower deposition temperatures resulted in less sharp loops with increased coercive field. The loop for $T_{dep} = 350$ °C is also less sharp with decreased coercivity. A further sample deposited at 365 °C does not show any polar MOKE. Therefore, deposition temperatures between 290 °C and 330 °C seem to be favourable for the growth or MRG. However, between 300 °C and 320 °C the magnetisation reversal behaviour was found to change changes from do-

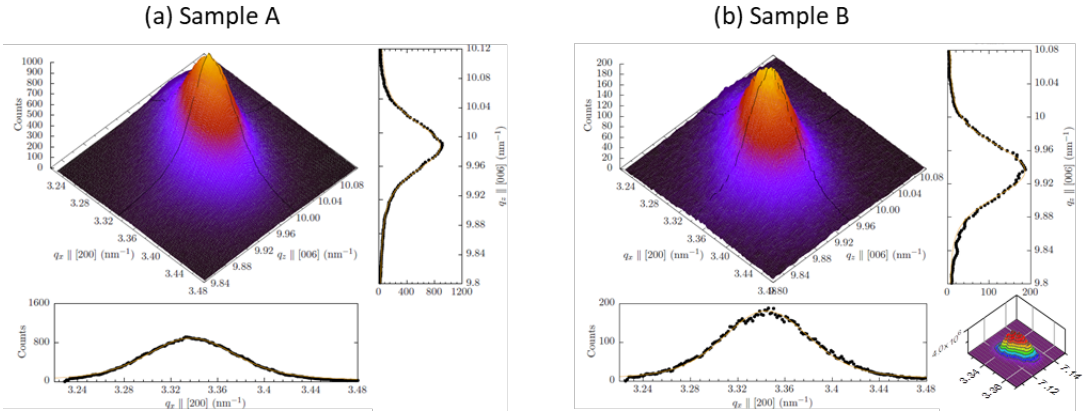

Figure 5.7: Reciprocal space maps of the MRG (206) reflection of samples A (a) and B (b). The 3-D plot is the full peak in the $q_x - q_z$ plane and the curves in the bottom and right panels are cross sections used for peak fitting (orange lines) in q_x and q_z, respectively, through the maximum. The bottom right graph in (b) shows the reciprocal space map of the MgO(113) peak.

Sample	T_{dep} [°C]	M_S [kA/m]	$\mu_0 H_A$ [T]	K_u [kJ/m^3]	δ [nm]
A	300	75	2.5	94	20
B	320	82	1.3	53	26

Table 5.2: Magnetic characterisation at $T = 300$ K. Saturation magnetization M_S, anisotropy fields $\mu_0 H_A$ and constants K_u, and estimated Bloch wall widths δ for samples A and B.

main wall motion dominated to nucleation dominated, which is why we focus on these temperature points in the main manuscript.

Figure 5.6 (b) shows X-ray diffraction patterns in dependence of the MRG films with different deposition temperatures. All samples clearly show the (002) and (004) reflections of MRG, indicating epitaxial growth on the MgO substrates in [001] direction. A shift in the peak positions indicates a decrease of the c-parameter for higher deposition temperatures, which is shown in Figure 5.6 (c). This happens because tetragonal distortion of the MRG lattice, caused by the epitaxial strain due to the smaller MgO lattice parameter, is released at higher deposition temperatures. To analyse the crystallography further, we compare the rocking curves of the (004) MRG peaks (see Figure 5.6 (c)), which are indicative for the mosaicity of the films. The full width at half maximum (FWHM) are plotted in Figure 5.6 (c) (blue curve, right

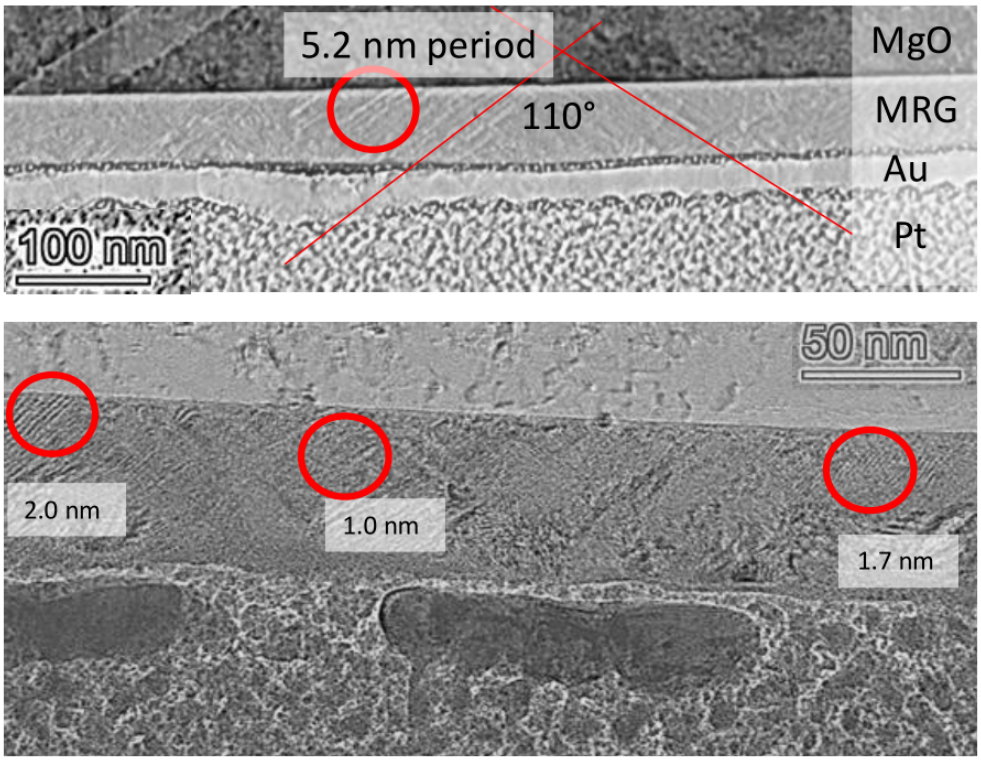

Figure 5.8: TEM cross sections of sample B. The spacings and angles obtained from the contrast fit to the expected values of the (112) lattice planes.

axis) and is almost constant in the range 290 °C $\leq T_{dep} \leq$ 330 °C with values between 0.53° $<$ FWHM $<$ 0.60°. At lower deposition temperatures the FWHM decreases strongly indicating a lower density of dislocations and grain boundaries.

In order to characterise film thickness and roughness, X-ray reflectivity (XRR) measurements have been performed and are shown for samples A and B in Figure 5.6 (e). They are almost identical and modelling using the Parrott algorithm yields similar roughness below 1 nm and film thickness of 52 nm for both films. Lower deposition temperatures results in an increased roughness of up to 2.6 nm (not shown). Since rocking curves and XRR measurements did not reveal significant differences between samples A and B, reciprocal space maps (RSMs) have been measured for the (206) reflections and fit by Voight functions to reveal the structural coherence length in in-plane and out-of- plane directions. The RSMs are shown in Figure 5.7 for samples A and B and reveal less tetragonal distortion and shorter structural coherence lengths in both x and z directions for sample B, as discussed in the main text.

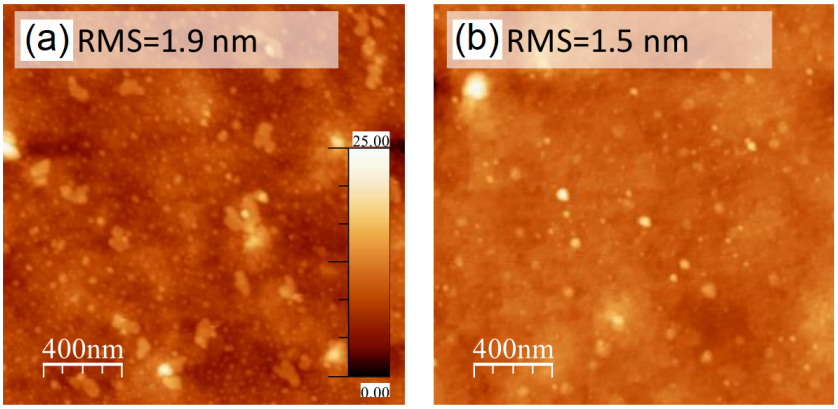

Figure 5.9: AFM micrographs of (a) sample A and (b) sample B.

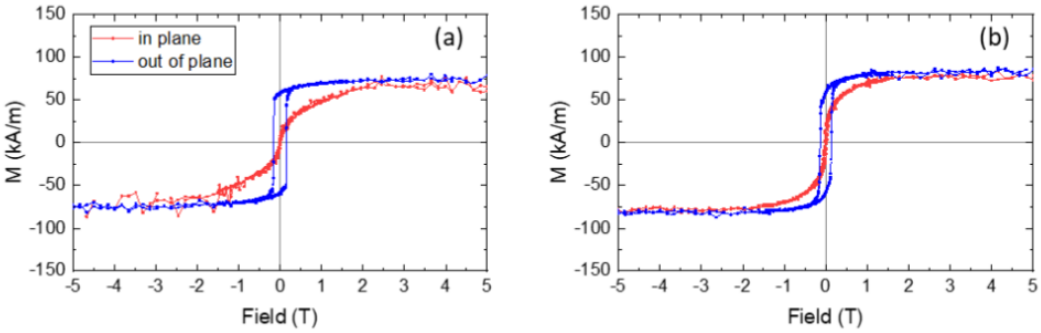

Figure 5.10: Magnetic hysteresis loops of (a) sample A and (b) sample B.

For further structural analysis, TEM cross sections of sample B have been prepared in MRG(110) orientation and images are shown in Figure 5.8. The visible stripe contrast in the red circle shows periodicity of multiples of 1.0 nm and angles with respect to the surface normal of around 55°. Therefore, the contrast originates from distorted $\{112\}$ lattice planes. Structural defects, leading to these distortions may include twin boundaries, and misfit dislocations due to relaxation of the MRG lattice grown on the smaller MgO lattice.

Figure 5.9 (a) and (b) show atomic force micrographs of samples A and B, showing that both films are continuous, with similar roughness values of 1.9 nm and 1.5 nm RMS (root mean square), respectively. In summary, in the deposition temperature range 290 °C $\leq T_{\text{dep}} \leq$ 330 °C, which includes the films A and B, investigated in the main text, the values of roughness, film thickness, and rocking curve FWHM values are similar. However, structural coherence lengths decrease, and c parameter and

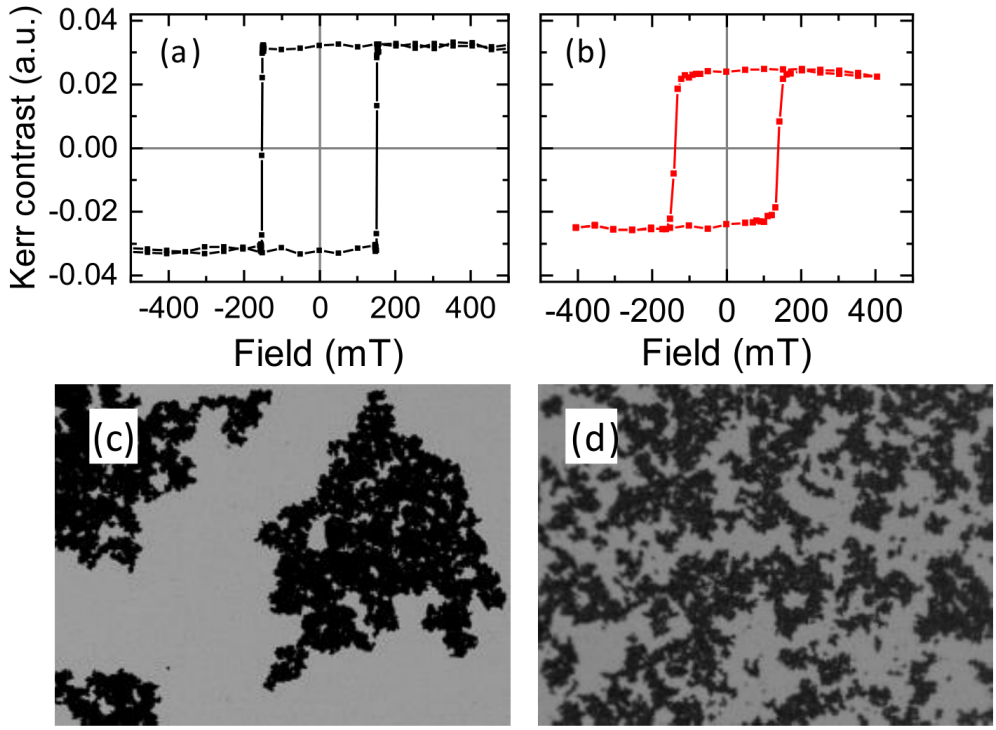

Figure 5.11: MOKE hysteresis loops and corresponding MOKE domain images during magnetisation reversal for sample A in (a) and (c), and sample B in (b) and (d). The applied fields to obtain the domain patterns were in (c) -151 mT and (d) -139 mT. Fields of view are (c) 370 μm and (d) 74 μm

tetragonal distortion decrease with higher deposition temperature.

Figure 5.10 show the magnetic hysteresis loops of samples A and B, taken at 300 K. From this the values of saturation magnetisation M_S and anisotropy fields $\mu_0 H_A$ are extracted. The magnetic exchange constant is estimated using the Curie temperature $T_C \approx 550$ K and the lattice parameters (around 6 Å) to be $A = 4 \times 10^{-12}$ Jm^{-1}. With these values the uniaxial anisotropy constants K_u and magnetic domain wall width $\delta \approx \pi A/K_u$ can be estimated. The results are summarised in Table 5.2.

Figure 5.11 shows the magnetic hysteresis loops, obtained by Kerr microscopy for samples A and B. Both samples exhibit similar coercive fields H_C of 151 mT for sample A and 139 mT for sample B and near perfect squareness. The magnetisation reversal is sharper in sample A and occurs within 3 mT while it takes around 30 mT for sample B. The visible negative slope in the saturation region of sample B is an artefact of the polar Faraday effect of the polarisation microscope [12]. Shown in Figure 5.11

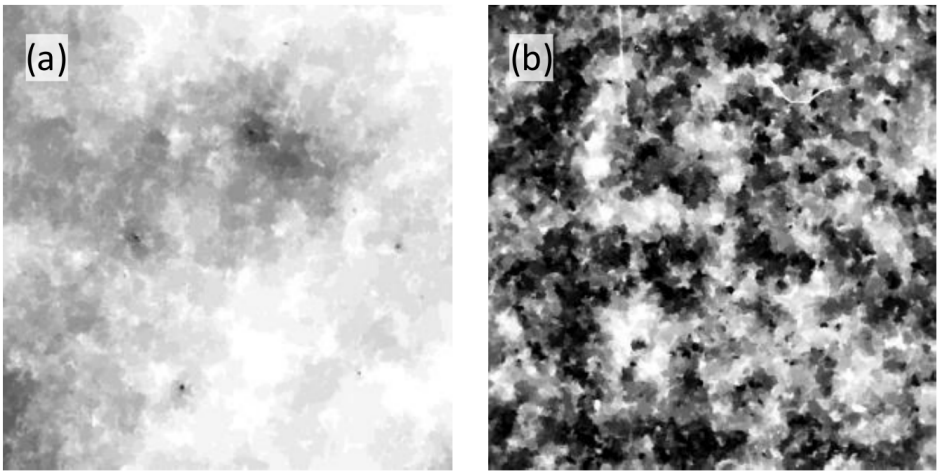

Figure 5.12: Average of several domain images taken under the same conditions for (a) sample A averaging of 21 images taken at -151 mT (320 μm field of view) and (b) sample B averaging of 23 images taken at -139 mT (64 μm field of view).

(c) and (d) are corresponding domain images taken during the magnetisation reversal at negative coercivity after saturation in + 800 mT. The applied field is removed after 5 s to stop domain wall creep during image acquisition. A few large domains of order 100 μm with irregular outlines are visible for sample A and many domains with sizes down to the sub-micron resolution limit of the microscope are seen for sample B.

To check if the domain formation was deterministic, we repeated this process and averaged over several images taken in the same way. The results are shown in Figure 5.12. All images were binarised before averaging, so any white areas remain unchanged in all repetitions and black areas reverse every time. For sample A, a few black or dark grey spots can be identified, which indicate soft centres where the domains nucleate. The domain growth, however, is not really deterministic, as seen by the varying grey tones across the image. For sample B, nucleation sites are much denser and form visible patterns across the image with features parallel to the image borders. These directions correspond to [110] directions of the MRG lattice and is the same direction where strain contrast was seen in TEM images (see Figure 5.8) and corresponds to the easier in-plane axis of the second order magnetic anisotropy term.[14]

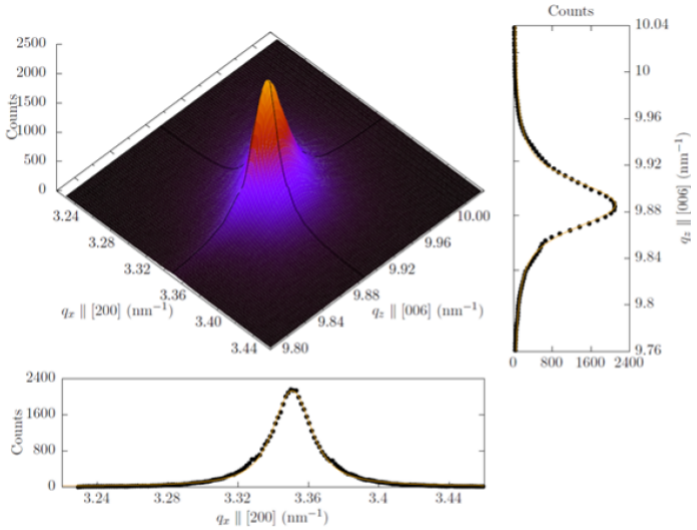

Figure 5.13: Reciprocal space map of the (206) peak of sample C. The 3-D plot is the full peak in the $q_x - q_z$ plane and the curves in the bottom and right panels are cross sections used for peak fitting (orange lines) in q_x and q_z, respectively, through the maximum.

c [pm]	a [pm]	$c/a-1$ [%]	l_x [nm]	l_z [nm]
607	597	1.7	29.8	20.8
T_{dep} [°C]	M_S [kA/m]	$\mu_0 H_A$ [T]	K_u [kJ/m^3]	δ [nm]
340	92	1.0	46	29

Table 5.3: Structural and magnetic characterisation at $T = 300$ K. Lattice parameters a, c, tetragonal distortion, coherence lengths l_x, l_z, saturation magnetisation M_S, anisotropy fields $\mu_0 H_A$ and constants K_u, and estimated Bloch wall widths δ for sample C.

5.2.5 Characterisation of Samples II: Sample C

Figure 5.13 shows the reciprocal space map of the (206) peak of sample C. This was used to extract the tetragonal distortion and structural coherence lengths in in-plane and out-of-plane directions. With a tetragonal distortion of 1.7 % it is more strained than samples A and B. It also shows the largest in-plane coherence length of all investigated samples with $l_x = 29.8$ nm and an out-of-plane coherence length comparable to that of sample A with $l_z = 20.8$ nm.

The magnetic and magneto-optic characterisation of sample C is shown in Figure 5.14. The sample exhibits a coercivity of 340 mT and saturation magnetization of 92 kA/m and remanent magnetisation of 33 kA/m (Figure 5.14 (a,c)). The tempera-

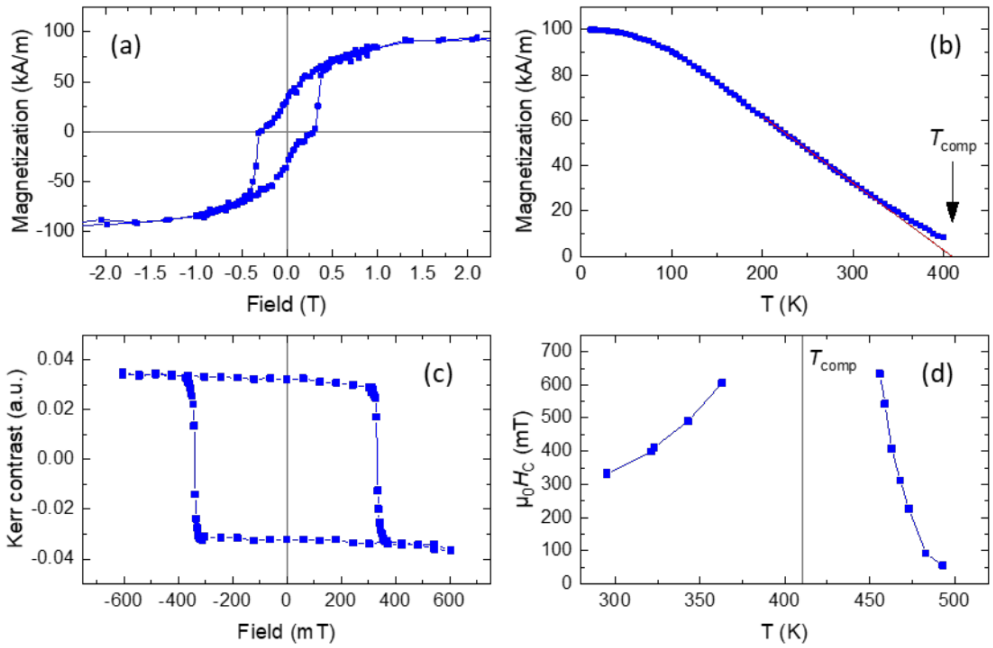

Figure 5.14: SQUID magnetometry of Sample C: (a) Magnetic hysteresis loop measured at 300 K and (b) magnetisation versus temperature with zero applied field after saturation at 10 K. MOKE microscopy of Sample C: (c) MOKE hysteresis loop measured at 300 K and (d) coercive fields versus temperature measured from MOKE loops.

ture dependence of the magnetization measured during zero field cooling from 400 K is shown in Figure 5.14 (b) and indicates a magnetic compensation point at 410 K, obtained by extrapolation of the linear region of the M(T) plot (red line). The sign of the MOKE hysteresis loop (Figure 5.14 (c)) is reversed as compared to samples A and B because the compensation temperature is above room temperature for this sample, which results in an opposite alignment of the 4*c* magnetic sublattice. This compensation point causes a divergence of the coercive field, as seen in Figure 5.14 (d), where it was not possible to reach coercivity in a magnetic field of 1 T between 370 and 460 K. The stepped behaviour of the magnetic hysteresis loop in Figure 5.14 (a) can most likely be explained by canting effect of both magnetic sublattices, as discussed in Chpater 4 and Chapter 6.

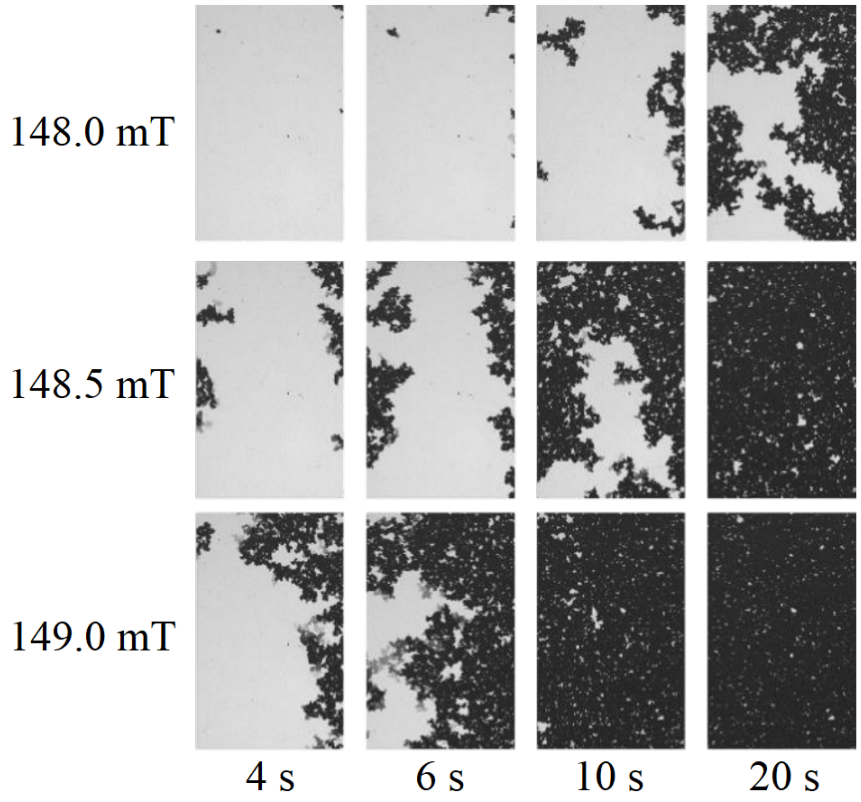

Figure 5.15: Magnetisation reversal: Magnetic domain patterns of sample A at different applied fields as a function of time. Width of imaged area is 350 μm.

5.2.6 Magnetic Domain Reversal

For a quantitative analysis of the magnetisation reversal, we studied the time evolution of magnetic domains at constant negative field after saturation in a large positive field. The results are shown in Figures 5.15, 5.16 and 5.17 for samples A, B and C, respectively.

For sample A the magnetic reversal occurs by dendritic growth of several irregularly shaped domains meaning the process is domain wall motion dominated. The rate of domain growth increases substantially when increasing the field by 1 mT, where for applied fields 148 mT, 184.5 mT and 185 mT the times to reverse half of domains are $t_{50} = 20$ s, $t_{50} = 10$ s and $t_{50} = 6$ s, respectively. Some areas in the panels of Figure 5.15 show parts of the domains in a lighter grey scale, most pronounced in the second panel of the last row. These regions are reversed during image acquisition and obtaining one

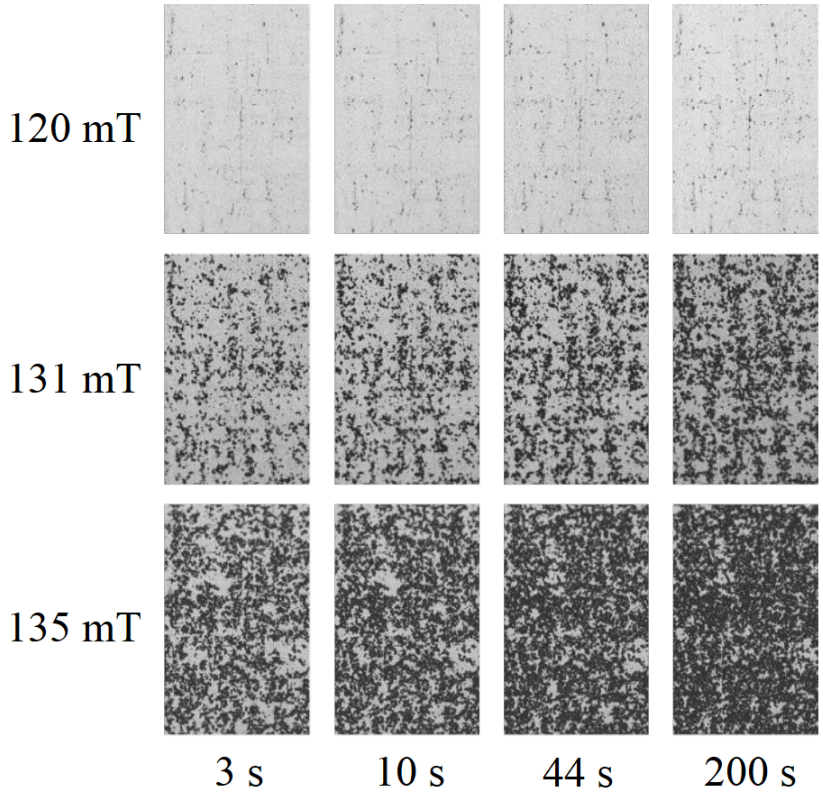

Figure 5.16: Magnetisation reversal: Magnetic domain patterns of sample B at different applied fields as a function of time. Width of imaged area is 100 μm.

image involves averaging over four exposures of 40 ms each. The few non-reversed (light) spots seen in the last panel at 149 mT did not switch within the timeframe of the measurement (140 s). They are hard centres and require a higher applied field and several seconds to reverse. Magnetisation reversal in sample B, shown in Figure 5.16, at constant field occurs by nucleation and growth of small domains. The timeframe for the magnetisation reversal is much longer than for sample A and full magnetisation reversal could not be observed for any field value because either the first recorded frame after field application is already partly reversed or the last frame after up to 800 s is not fully reversed. The compensation point of sample C is above room temperature at $T_{\mathrm{comp}} = 420$ K, hence this sample reverses from dark to bright contrast using the same measurement protocol as for samples A and B. There is a large number of small bright domains visible in the first panel, resulting from a higher density of soft centres, as compared with sample A. The reversal then mainly happens through the growth of

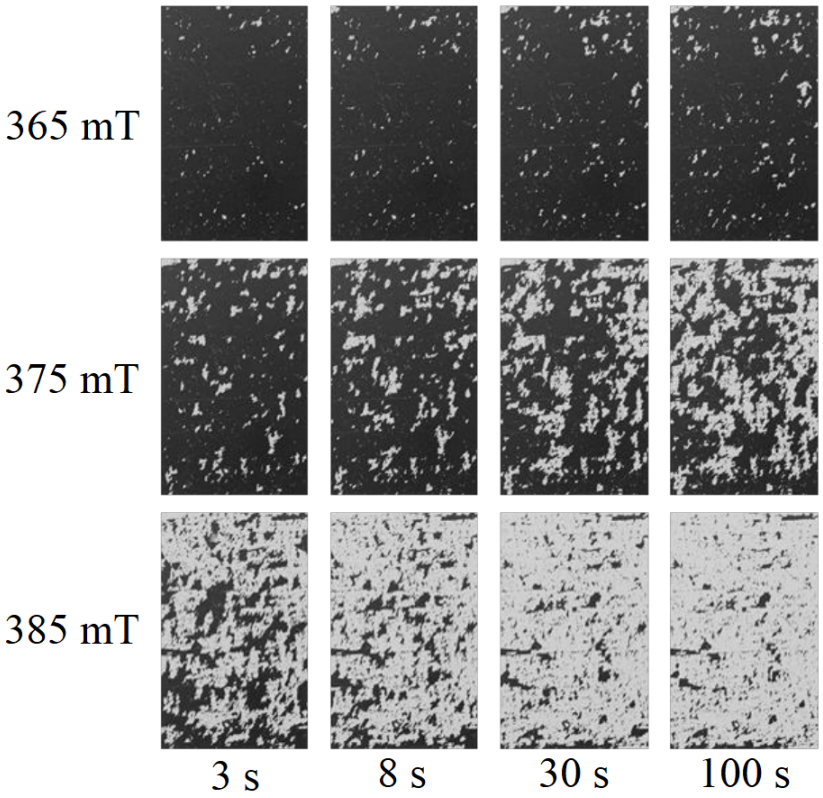

Figure 5.17: Magnetisation reversal: Magnetic domain patterns of sample C at different applied fields as a function of time. Width of imaged area is 350 μm.

those small domains over time, but a few nucleation events can be observed as well. Therefore, this sample seems to be on the transition between reversal dominated by domain wall motion and nucleation. Typical domain sizes are in the tens of microns in width and growth of current domains as well as nucleation of new domains can be observed throughout the reversal process. Therefore, the magnetic reversal process of sample C cannot be attributed as either domain wall motion, or nucleation dominated, but is a competition of both mechanisms.

The curves are based on Kerr contrast, but can be interpreted as $m(t) = \frac{M(t)+M_S}{2M_S}$ with M_S the saturated magnetisation at $t = 0$. The magnetisation reversal characteristics are modelled and analysed based on a model developed by by Fatuzzo [22] for polarisation relaxation in ferroelectric materials and first used by Labrune *et al.* for perpendicular GdTbFe films [23]. Magnetisation relaxation curves for various applied magnetic fields shown in Figure 5.18, are used to analyse activation volumes and en-

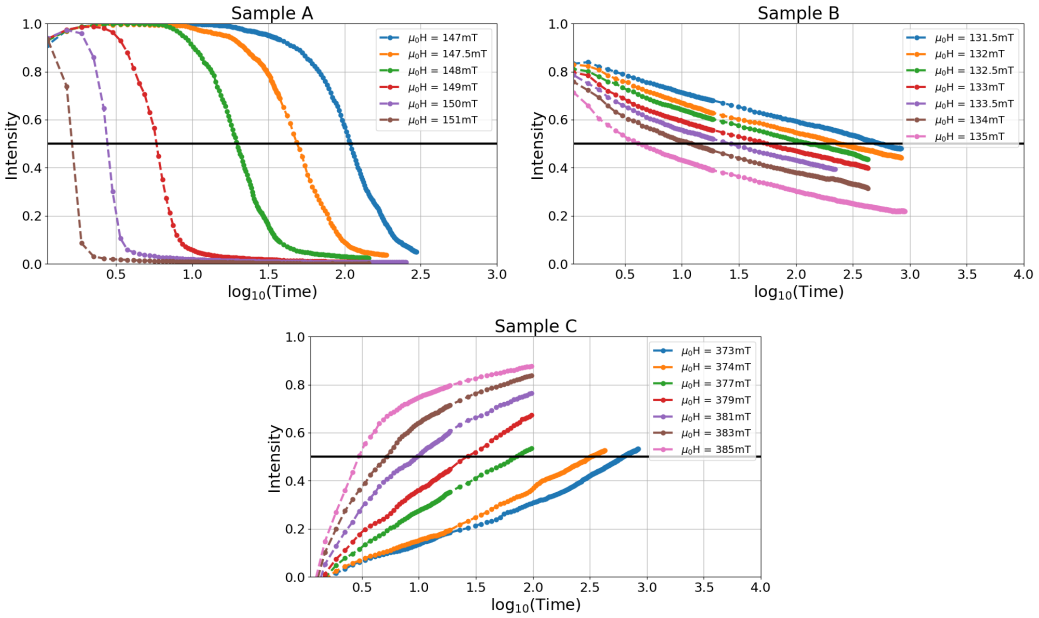

Figure 5.18: Magnetic after-effect: Relaxation curves versus $\log_{10}$(time) for different applied fields for sample A, sample B and sample C.

ergies. The increase of intensity for times under 1 s is related to the polar Faraday effect during the ramping of the magnetic field with a time constant of around 0.4 s. The shape of the magnetic relaxation curves differs fundamentally between the samples A and B. The "S"-shaped curves in the $m(t) - t/t_{50}$ plot with decreasing width for increasing fields for sample A and almost linear behaviour for sample B across most of the investigated time frames. Such different domain behaviours are common for thin films with perpendicular anisotropy and were already described for Au/Co/Au [20; 25] and rare earth-transition metal thin films [26; 27]. The differences are based on different activation energy distributions causing reversal dominated either by domain wall propagation or by nucleation. In the case of sample C, magnetic after-effect measurements were carried out the same way as for the other samples. Since sample C's compensation temperature is above RT, the relaxation commences from zero to one, as seen the data in Figure 5.19, along with the reversed sign of the MOKE hysteresis loop. The $m(\log_{10}(t))$ curves show neither the typical S-shape or linear behaviour that is observed for samples A and B, respectively.

The time dependent normalised magnetisation relaxation curves for samples A, B and C for selected applied fields are shown in Figure 5.19. These curves were modelled

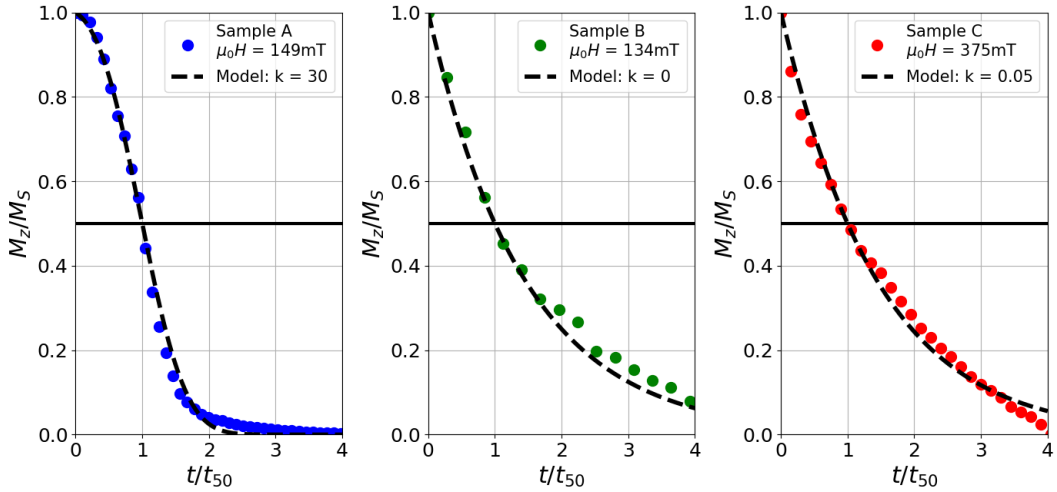

Figure 5.19: Magnetic after-effect modelling: Normalised relaxation curves versus t/t_{50} for selected applied fields for sample A, sample B and sample C. Samples B and C have been normalised to decay faster to illustrate how well the Fatuzzo-Labrune model can reproduce the data at short timescales and determine the k values.

using equation 5.8 from the Fatuzzo-Labrune model. For sample A the model and data are in agreement. For the other two samples, only at short time scales the data can be modelled, however it was possible to deduce the value of k which is consistent with the theory. As described in the model above, high k values indicate domain wall motion dominated reversal and $k = 0$ indicates nucleation dominated reversal. The k values found support the MOKE data where we see for sample A reversal is domain wall motion dominated, for sample B it's nucleation driven reversal. For sample C the k value is not zero and it is not large because domain reversal is a mixture of contributions from both mechanisms. The characteristic time, for which half the samples magnetisation is reversed (t_{50}) follows an phenomenological relation, already introduced in the theory section,

$$t_{50} = t_0 \exp(\alpha(H_C^* - H)) \tag{5.37}$$

with the activation time t_0 (taken as 10^{-10} s), H_C^* the sample's intrinsic coercivity (without thermal activation, H_C^* is in general larger than H_C, which is the coercivity read off magnetic hysteresis loops), H is the applied field, and μ_0 the vacuum permeability. The α parameter can be read off linear fits to the $\ln(t_{50})$-H-plots in Figure 5.21.

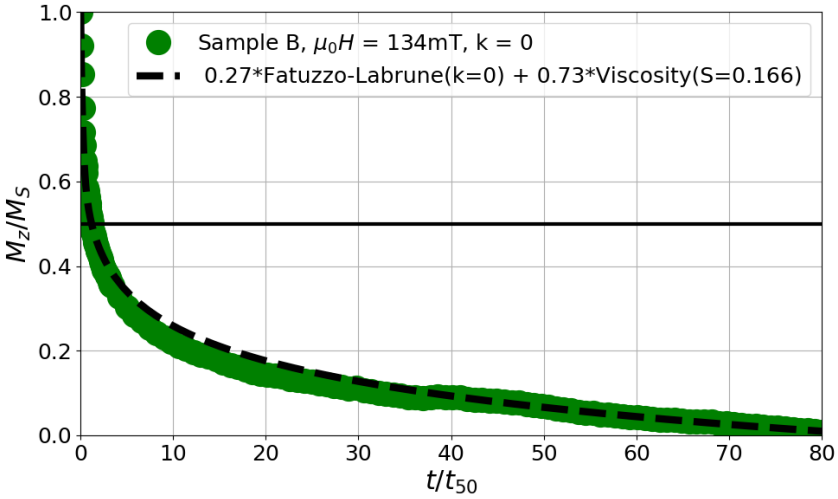

Figure 5.20: Magnetic after-effect: Normalised relaxation curve versus t/t_{50} for $\mu_0 H =$ 134 mT for sample B. Linear combination of Labrune-Fatuzzo model, with $k = 0$, and magnetic viscosity model, with $S = 0.166$ were found by numerical minimisation to fit the data. This combination allows to model the data accurately at both short and long timescales.

Comparison of equation 5.37 with the Néel-Arrhenius equation given by

$$\tau = \tau_0 \exp\left(\frac{E_A - \mu_0 H M_S V^*}{k_B T}\right) \tag{5.38}$$

and we infer that $t_0 = \tau_0 \approx 10^{-10}$ s and $\alpha = \frac{M_S V^*}{k_B T}$ where E_A is the activation energy, k_B is the Boltzmann constant, T is the measurement temperature and V^* is the Barkhausen volume. For zero applied field ($H = 0$) the energy barrier for the thermally activated nucleation process is given by equation 5.39. The activation volume V^* and activation length l^* are found from equations 5.40 and 5.41.

$$E_A = k_B T(\alpha \mu_0 H_C^*) \tag{5.39}$$

$$\alpha = \frac{M_S V^*}{k_B T} \tag{5.40}$$

$$l^* = \sqrt{\frac{V^*}{d}} \tag{5.41}$$

$$\delta = \pi \sqrt{\frac{A}{K_u}} \tag{5.42}$$

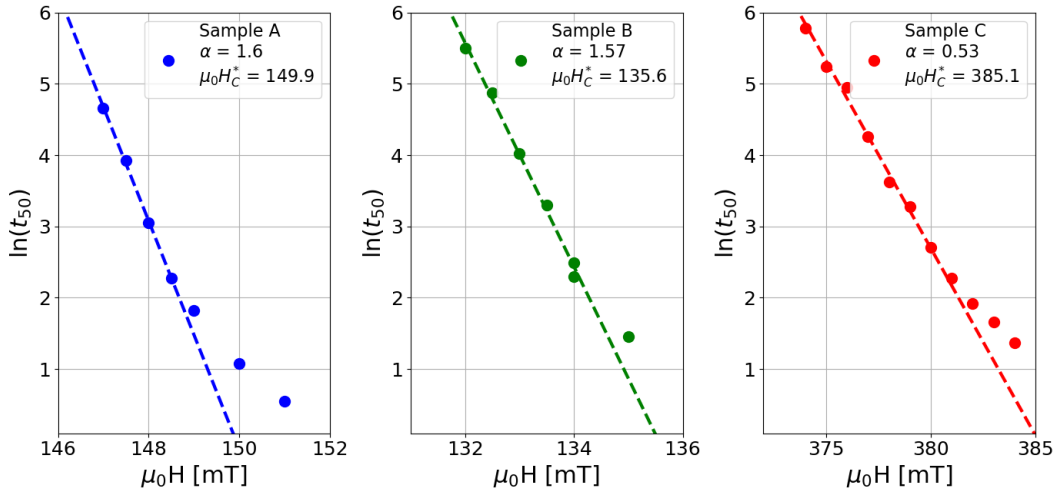

Figure 5.21: Field dependence of $\ln(t_{50})$ extracted from relaxation curves for sample A, sample B and sample C with fits to the linear regions.

Parameters	Sample A	Sample B	Sample C
M_S [kAm^{-1}]	75	82	92
α [mT^{-1}]	1.60	1.57	0.53
$\mu_0 H_C^*$ [mT]	149.9	135.6	385.1
$E_A \pm \Delta E_A$ [eV]	6.2 ± 0.029	5.5 ± 0.52	5.3 ± 0.22
V^* [μm^3]	8.8×10^{-5}	7.9×10^{-5}	2.4×10^{-5}
l^* [nm]	42	40	22
δ [nm]	20	26	29

Table 5.4: Summary of parameters found from experiments and calculated from the Fatuzzo-Labrune model for samples A, B and C.

where d is the film thickness and $A \approx 4 \times 10^{-12}$ Jm^{-1} is the exchange stiffness. The values of calculated parameters for all three samples are summarised in Table 5.4.

We obtain values of $\alpha = 1.54$ mT^{-1} for film A and $\alpha = 1.56$ mT^{-1} for film B are very similar despite the different magnetisation reversal behaviour, however the samples have the same composition. For sample C with higher Ru content than A and B, with the magnetisation reversal not clearly dominated by either mechanism, the value $\alpha = 0.53$ mT^{-1} was found. In the model a single activation energy was assumed which allowed for the determination of the order of magnitude of V^*, however it fails to provide more accurate information about the observed relaxation phenomena. It is important to check if this assumption is valid for each sample and explicitly find the

distribution of activation energies by evaluating the maximum slope of the $m(t)$ curves from Figure 5.18 derived by Bruno *et al.* [28]

$$\left(-\frac{dm(t)}{d\ln(t)}\right)_{max} = \frac{k_B T}{\Delta E_A} \tag{5.43}$$

where ΔE_A is the width of the distribution around the central value E_A. The respective activation energy ranges for samples A, B and C were found to be 6.2 ± 0.029 eV, 5.5 ± 0.52 eV and 5.3 ± 0.22 eV. For sample A, the magnetic reversal is governed by domain wall motion, which implies that an area of film can only switch if there is domain wall present in its vicinity. Therefore, the real distribution of activation energies, which are the domain wall propagation energies, is likely to be even narrower. The wider distribution of activation energies of sample B is supported by the linear behaviour at large times in the curves of Figure 5.18, which corresponds to the widely used model for magnetic viscosity with $M(t) = M_S - S\ln\left(1+\frac{t}{t_0}\right)$ with viscosity coefficient S. The logarithmic, instead of exponential decay, results from the assumption of a wide range of activation energies, prohibiting the system to reach thermal equilibrium even at long time scales.[29] This is explicitly demonstrated in Figure 5.20, where a linear combination of the F-L model term (M_{F-L}) and magnetic viscosity model term (M_V) was used to fit the data. In this case, the total magnetisation $m(t) = 0.27M_{F-L}(t, k = 0) + 0.73M_V(t, S = 0.166)$ and is in good agreement with the data. Strikingly, ΔE_A is exactly in the range where the transition between the two magnetic reversal process occurs, which is between 0.1 and 0.5 eV as determined from the deposition temperature series.

5.2.7 Magnetic Domain Pinning and Virgin State Domains

In order to further investigate the distribution of pinning centres based on domain observations in epitaxial MRG thin films, the discussion will focus on sample C because it has a larger domain wall coherence length of $l_{wc} = 240$ nm, which simplifies the analysis via optical methods. The aim is to produce virgin domain patterns by thermal demagnetisation. Firstly, the formation of the domain pattern during a controlled cool-down from above T_C, at a rate of ≈ 3 K/min, is analysed. In the second step, the film is repeatedly thermally demagnetised and images are taken at exactly the same position

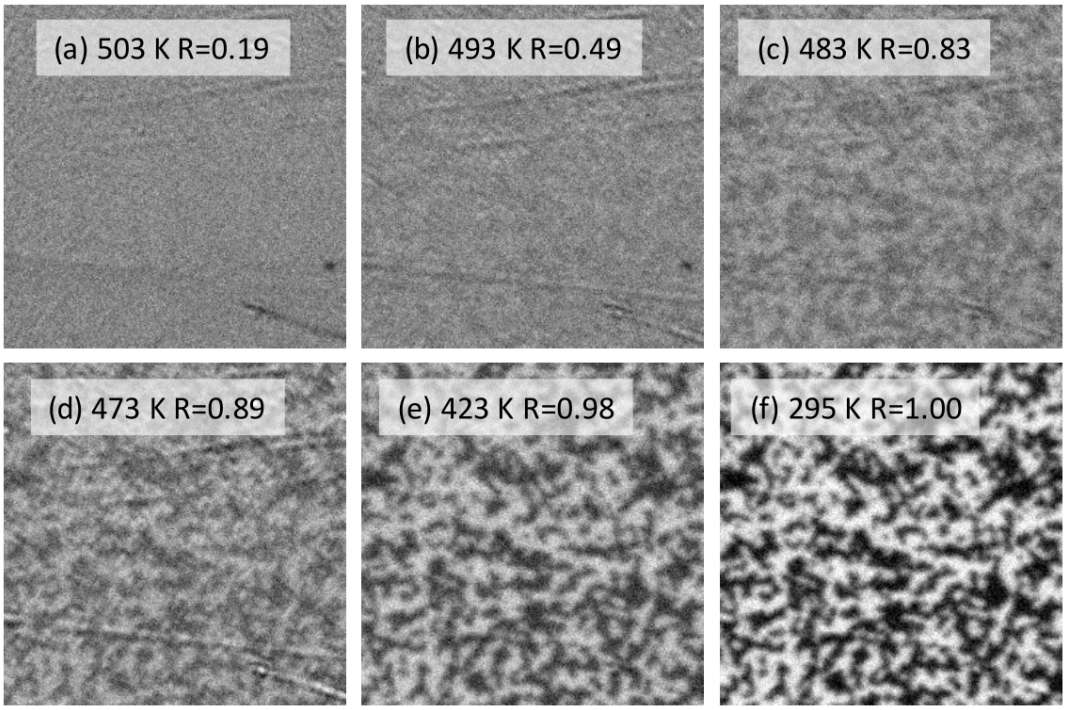

Figure 5.22: Thermal demagnetisation: (a-f) MOKE images of the magnetic domain structure at different temperatures during cool-down from Curie temperature. The width of the images is 24 μm.

after each demagnetisation in order to generate a 'probability map' of the domain wall locations.

Figure 5.22 shows the domain structure during cool-down after thermal demagnetisation. At $T = 503$ K, the film is demagnetised and no domain pattern is visible in the Kerr image as depicted in Figure 5.22(a). Figure 5.22(b) shows that a domain structure emerges during cool-down and is clearly visible below $T = 483$ K as seen in Figures 5.22(b)-(f). Both net magnetisation and anisotropy of the sample changes with temperature, hence it was expected that the domain pattern will change to accommodate for the temperature dependence of domain wall energy and demagnetising field. However, this is not the case because of domain wall pinning as mentioned in the previous section. The domain pattern begins to form just below $T_C = 500$ K and remains unchanged down to $T = 295$ K. Analysis of the images demonstrates this behaviour in Figure 5.23, where the Kerr contrast (left axis) and the correlation coefficient (right axis) are plotted against temperature. The Kerr contrast increases gradually with

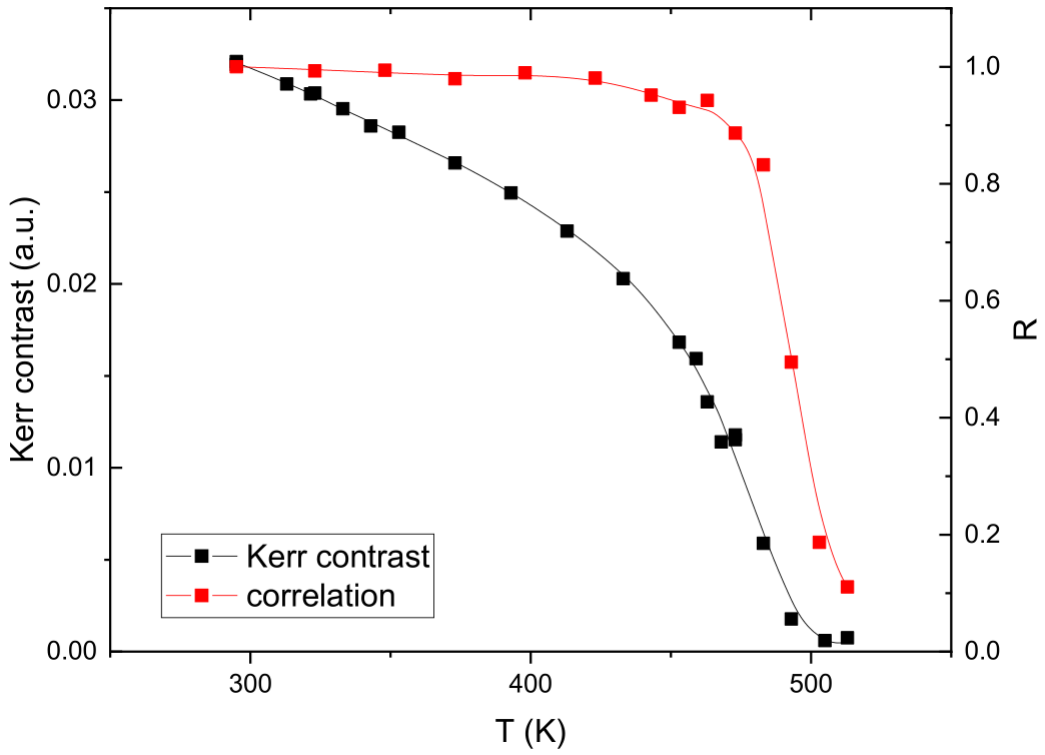

Figure 5.23: Temperature dependence of Kerr contrast between light and dark domains (black curve, left scale) and the image correlation coefficient (R) between images of virgin domain structures taken at temperatures from 295 K to 510 K (red curve).

decreasing temperature and following the z-projection of the Mn^{4c} sublattice magnetisation [30]. The correlation coefficient jumps from 0.19 to 0.83 between 503 K and 483 K, clearly indicating that the domain pattern at 483 K is essentially the same as the one at 295 K. Differences from a correlation coefficient of unity are due to the loss of contrast at high temperatures.

Virgin state domain patterns are utilised to visualise prominent domain wall pinning sites by means of Kerr microscopy. For this purpose images are taken after thermal demagnetisation repeatedly at the same spot. Initially the domains have a random orientation as shown in the background frame in Figure 5.24. The correlation between subsequent images at the same spot was determined to be close to zero. The tracing of the domain walls can be achieved using image analysis and is depicted in the center frame of Figure 5.24. An overlay of 33 traced domain wall images yields the foreground frame of Figure 5.24. The brightness at each spot maps the probability to find a

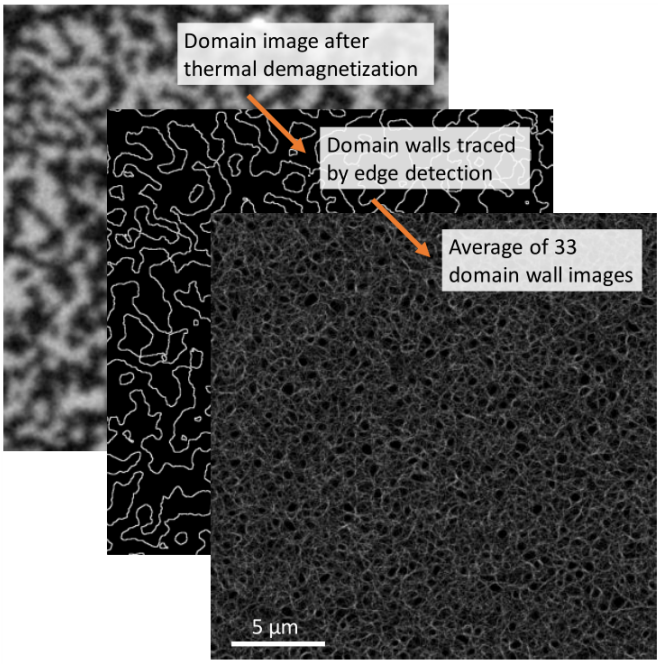

Figure 5.24: Visualisation of pinning sites by MOKE imaging of magnetic domains. *Background frame*: Domain images are repeatedly taken following thermal demagnetisation. *Center frame*: Domain walls are traced by edge detection. *Foreground frame*: Averaging of multiple domain wall images, in this case 33 images, from the same sample area to obtain a "heat map" highlighting the domain wall pinning sites.

domain wall at that pixel. It is clear that the averaged domain wall pattern in the image is not random, suggesting that domain wall tension alone is not the origin of the length scale of the domains. Black areas are avoided entirely by domain walls where there are no effective pinning sites. Bright lines traced by domain walls in multiple images show the locations of pinning sites.

The size and distribution of the brightness minima can be used to quantify regions lacking effective pinning centres. For simplicity, the analysis is focused on the black regions. Due to the continuous nature of the domain walls, the pinning sites themselves are hidden at the nodes of the network of white lines in the foreground frame in Figure 5.24. Those are harder to analyse using image analysis software, but their length scale is of the same order. The majority of apparent pinning sites are surrounded by regions of low pinning. The width of the black areas in Figure 5.24 is approximately 300 nm and therefore corresponds to l_{wc}, but it is an order of magnitude larger than

the structural coherence length $l_x = 29.8$ nm and the length scales determined from the Barkhausen nucleation volume $l^* = 22$ nm. Therefore, the magnetic pinning sites can be mapped by means of Kerr microscopy and the 240 nm auto-correlation length scale of the domain walls is shown to correspond to the average distance between prominent pinning centres. This level of information about structural defects in the thin films can otherwise be obtained only by cross sectional TEM because pinning centres lie within the volume of the film.

5.2.8 Conclusion

The analysis of magnetic domain patterns during magnetisation reversal for a set of MRG thin films with deposited at different deposition temperatures shows that the magnetisation reversal behavior changes from domain-wall-motion dominated process for $T_{\text{dep}} = 300\,^{\circ}\text{C}$ to nucleation-dominated process for $T_{\text{dep}} = 320\,^{\circ}\text{C}$, which is quite a narrow range.Analysis of the magnetic after-effect using the Fatuzzo-Labrune model found that all investigated films show similar activation volumes with dimensions of $22 - 42$ nm, and activation energies between 5.3 eV and 6.2 eV. The main differences were found in the distribution of activation energies where films with $\Delta E_A \leq 0.52$ eV show reversal dominated by nucleation, while samples with $\Delta E_A \leq 0.10$ eV show reversal dominated by domain wall motion. Magnetisation reversal in sample C with a ΔE_A value in the range $0.1 < \Delta E_A < 0.52$ was found to be a competition of the two mechanisms.

Analysis of virgin state domains prepared by thermal demagnetisation and cool-down demonstrated the important role of pinning in domain structure formation. Comparing the structural parameters of the samples, it is likely that structural defects such as misfit dislocations are responsible for the range of activation energy since they locally disturb the anisotropy and act as pinning centres for domain walls.

In the context of spintronic applications, domain-wall dominated magnetisation reversal behaviour is desirable for race-track memory devices. The study highlights the important role of deposition temperature in minimising structural defects. Further study into the dependence of MRG composition on crystalline defects and thus magnetisation reversal mechanisms is required. This will allow for optimisation in an

attempt to narrow the activation energy distribution and maximise domain wall coherence length as well as maintain high spin polarisation.

References

[1] M. Schlenker and J. Baruchel, "Neutron techniques for the observation of ferro- and antiferromagnetic domains," *J. Appl. Phys*, vol. 49, no. 3, pp. 1996–2001, 1978. (Cited on page: 153)

[2] M. Schlenker, J. Baruchel, J. F. Pétroff, and W. B. Yelon, "Observation of subgrain boundaries and dislocations by neutron diffraction topography," *Appl. Phys. Lett.*, vol. 25, no. 7, pp. 382–384, 1974. (Cited on page: 153)

[3] M. J. Grzybowski, P. Wadley, K. W. Edmonds, R. Beardsley, V. Hills, R. P. Campion, B. L. Gallagher, J. S. Chauhan, V. Novak, T. Jungwirth, F. Maccherozzi, and S. S. Dhesi, "Imaging current-induced switching of antiferromagnetic domains in cumnas," *Phys. Rev. Lett.*, vol. 118, p. 057701, Jan 2017. (Cited on page: 153)

[4] F. Nolting, A. Scholl, J. Stohr, J. W. Seo, J. Fompeyrine, H. Siegwart, J. P. Locquet, S. Anders, J. Luning, E. E. Fullerton, M. F. Toney, M. R. Scheinfein, and H. A. Padmore, "Direct observation of the alignment of ferromagnetic spins by antiferromagnetic spins," *Nature*, vol. 405, pp. 767–769, 2000. (Cited on page: 153)

[5] M. Bode, E. Y. Vedmedenko, K. von Bergmann, A. Kubetzka, P. Ferriani, S. Heinze, and R. Wiesendanger, "Atomic spin structure of antiferromagnetic domain walls," *Nat. Mater.*, vol. 5, pp. 477–481, 2006. (Cited on page: 154)

[6] B. K. Tanner, "Antiferromagnetic domains," *Contemp. Phys.*, vol. 20, pp. 187–210, 1979. (Cited on page: 154)

[7] M. Fiebig, D. Fröhlich, B. B. Krichevtsov, and R. V. Pisarev, "Second harmonic generation and magnetic-dipole-electric-dipole interference in antiferromagnetic cr_2o_3," *Phys. Rev. Lett.*, vol. 73, pp. 2127–2130, Oct 1994. (Cited on page: 154)

[8] M. Fiebig, D. Fröhlich, G. Sluyterman v. L., and R. V. Pisarev, "Domain topography of antiferromagnetic cr_2o_3 by second-harmonic generation," *Appl. Phys. Lett.*, vol. 66, no. 21, pp. 2906–2908, 1995. (Cited on page: 154)

[9] P. Schoenherr, L. Giraldo, M. Lilienblum, M. Trassin, D. Meier, and M. Fiebig, "Domain topography of antiferromagnetic cr_2o_3 by second-harmonic generation," *Materials*, vol. 10, no. 9, p. 1051, 2017. (Cited on page: 154)

[10] K. E. Siewierska, G. Atcheson, K. Borisov, M. Venkatesan, K. Rode, and J. M. D. Coey, "Study of the Effect of Annealing on the Properties of Mn_2Ru_xGa Thin Films," *IEEE Trans. Magn.*, vol. 53, no. 11, pp. 1–5, 2017. (Cited on page: 154)

[11] I. V. Soldatov and R. Schäfer, "Advanced MOKE magnetometry in wide-field kerr-microscopy," *J. Appl. Phys.*, vol. 122, no. 15, p. 153906, 2017. (Cited on page: 155, 160)

[12] R. Schäfer, *Investigation of Domains and Dynamics of Domain Walls by the Magneto-optical Kerr-effect*. ACS, 2007. (Cited on page: 155)

[13] "Fractalyse - Fractal Analysis Software." `http://www.fractalyse.org/`. Accessed: 2020-11-12. (Cited on page: 155)

[14] D. Betto, K. Rode, N. Thiyagarajah, Y.-C. Lau, K. Borisov, G. Atcheson, M. Žic, T. Archer, P. Stamenov, and J. M. D. Coey, "The zero-moment half metal: How could it change spin electronics?," *AIP Adv.*, vol. 6, no. 5, p. 055601, 2016. (Cited on page: 155)

[15] H. Kurt, K. Rode, P. Stamenov, M. Venkatesan, Y. C. Lau, E. Fonda, and J. M. D. Coey, "Cubic Mn_2Ga thin films: Crossing the spin gap with ruthenium," *Phys. Rev. Lett.*, vol. 112, no. 2, p. 027201, 2014. (Cited on page: 156)

[16] D.-H. Kim, Y.-C. Cho, S.-B. Choe, and S.-C. Shin, "Correlation between fractal dimension and reversal behavior of magnetic domain in Co/Pd nanomultilayers," *Appl. Phys. Lett.*, vol. 82, no. 21, pp. 3698–3700, 2003. (Cited on page: 158)

[17] D. Navas, N. Soriano, F. Béron, C. T. Sousa, K. R. Pirota, J. Torrejon, C. Redondo, R. Morales, and C. A. Ross, "Microscopic reversal magnetization mechanisms in CoCrPt thin films with perpendicular magnetic anisotropy: Fractal structure versus labyrinth stripe domains," *Phys. Rev. B*, vol. 96, p. 180403, Nov 2017. (Cited on page: 158)

[18] A. Kreyssig, R. Prozorov, C. D. Dewhurst, P. C. Canfield, R. W. McCallum, and A. I. Goldman, "Probing Fractal Magnetic Domains on Multiple Length Scales in $Nd_2Fe_{14}B$," *Phys. Rev. Lett.*, vol. 102, p. 047204, Jan 2009. (Cited on page: 158)

[19] J. Das and K. S. Menon, "On the evolution of antiferromagnetic nanodomains in nio thin films: A leem study," *J. Magn. Magn. Mater.*, vol. 449, pp. 415 – 422, 2018. (Cited on page: 158)

[20] J. Pommier, P. Meyer, G. Pénissard, J. Ferré, P. Bruno, and D. Renard, "Magnetization reversal in ultrathin ferromagnetic films with perpendicular anistropy: Domain observations," *Phys. Rev. Lett.*, vol. 65, pp. 2054–2057, Oct 1990. (Cited on page: 159, 179)

[21] A. Kirilyuk, J. Ferré, V. Grolier, J. Jamet, and D. Renard, "Magnetization reversal in ultrathin ferromagnetic films with perpendicular anisotropy," *J. Magn. Magn. Mater.*, vol. 171, no. 1, pp. 45 – 63, 1997. (Cited on page: 159)

[22] E. Fatuzzo, "Theoretical considerations on the switching transient in ferroelectrics," *Phys. Rev.*, vol. 127, pp. 1999–2005, Sep 1962. (Cited on page: 160, 178)

[23] M. Labrune, S. Andrieu, F. Rio, and P. Bernstein, "Time dependence of the magnetization process of re-tm alloys," *J. Magn. Magn. Mater.*, vol. 80, no. 2, pp. 211 – 218, 1989. (Cited on page: 160, 178)

[24] M. Avrami, "Kinetics of phase change. i general theory," *J. Chem. Phys.*, vol. 7, no. 12, pp. 1103–1112, 1939. (Cited on page: 161)

[25] J. Ferré, V. Grolier, P. Meyer, S. Lemerle, A. Maziewski, E. Stefanowicz, S. V. Tarasenko, V. V. Tarasenko, M. Kisielewski, and D. Renard, "Magnetization-reversal processes in an ultrathin co/au film," *Phys. Rev. B*, vol. 55, pp. 15092–15102, Jun 1997. (Cited on page: 179)

[26] C. Lin, J. C. Suit, and R. H. Geiss, "Micromagnetics of magnetization reversal in amorphous tb-fe films by lorentz microscopy," *J. Appl. Phys*, vol. 63, no. 8, pp. 3835–3837, 1988. (Cited on page: 179)

[27] H. D. Shieh and M. H. Kryder, "High resolution measurement of coercivity variations in magneto-optical recording media," *IEEE Trans. Mag.*, vol. 24, no. 6, pp. 2464–2466, 1988. (Cited on page: 179)

[28] P. Bruno, G. Bayreuther, P. Beauvillain, C. Chappert, G. Lugert, D. Renard, J. P. Renard, and J. Seiden, "Hysteresis properties of ultrathin ferromagnetic films," *J. App. Phys.*, vol. 68, no. 11, pp. 5759–5766, 1990. (Cited on page: 183)

[29] G. Bertotti, *Hysteresis in Magnetism*. Elsevier, 1998. (Cited on page: 183)

[30] D. Betto, N. Thiyagarajah, Y.-C. Lau, C. Piamonteze, M.-A. Arrio, P. Stamenov, J. M. D. Coey, and K. Rode, "Site-specific magnetism of half-metallic Mn_2Ru_xGa thin films determined by x-ray absorption spectroscopy," *Phys. Rev. B*, vol. 91, no. 9, p. 094410, 2015. (Cited on page: 185)

6

Site-specific magnetism study of Mn_yRu_xGa thin films by XMCD

6.1 Background and Motivation

In Chapter 4, the analysis of SQUID magnetometry hysteresis loops of MRG thin films showed that the net moment is canted relative to the anisotropy axis in the absence of a magnetic field. In AHE measurements, transverse resistance is proportional to the M_z^{4c} and the AHE loops show high remnance. Sublattice magnetisations are between 1-2 orders of magnitude higher than the net moment, which means that weak canting of the Mn^{4c} moment, difficult to observe in AHE, can give rise to large canting angles of the net moment. The canting of the net moment is hypothesised to result from sublattice non-collinearity. This non-collinearity could originate from competing positive and negative exchange on one or both Mn sublattices. The Heisenberg exchange energies extracted from MFT fits of thermal scans of the net moment, suggest that competing exchange is more likely to occur on the Mn^{4c} sublattice, because the its intra-sublattice exchange energy is the weakest.

Non-collinearity is difficult to demonstrate in thin films. Magnetometry only measures the projection of the net moment on one axis and varies between $10-100\,\mathrm{kA}m^{-1}$,

due to the compensated nature of MRG. AHE is sensitive to the z-projection of magnetisation of only one sublattices. A technique which is sensitive to both site specific Mn sublattice moments in thin films is required. The ideal techniques are thin film neutron diffraction and x-ray magnetic circular dichroism (XMCD). In this work the focus is on XMCD, described in detail in Chapter 2 Section 2.7.

Firstly, XMCD spectra taken normal incidence to the thin film surface will determine the sublattice moment projections onto the z-axis. The compensation temperature will be found from temperature dependent XMCD scans. Assuming anisotropy is negligible, the inter-sublattice exchange can be extracted and compared with the value obtained from MFT. At compensation, MRG magnetically resembles a uniaxial antiferromagnet, therefore applying a sufficiently strong perpendicular field induces a spin-flop transition. To probe magnetic anisotropy, the usual approach involves applying the field along the hard axis and measuring the moment. In XMCD this is not possible because rotating the sample by 90° means the beam cannot probe the sample surface. Instead, XMCD measurements will be performed at two incidence angles ϕ^1 and ϕ^2, such that $|\phi^1 - \phi^2| = 90°$. Using trigonometry, the moments projected onto the x-ray beam propagation vector **k** can be related to perpendicular and parallel components of the sublattice moments. From this a two dimensional projection of sublattice moments can be obtained in the $x-z$ plane. This approach allows hard axis measurements and the results can be used to find anisotropy constants, assuming uniaxial anisotropy.

6.2 Sample Preparation and Characterisation

For the XMCD study, samples A and B were deposited by DC magnetron sputtering at $T_{\text{dep}} = 350\,°\text{C}$ with nominal compositions $Mn_{2.2}Ru_{0.7}Ga$ and $Mn_{2.0}Ru_{0.8}Ga$, respectively. Before the XMCD measurements, the structural and magnetic properties of the samples were measured and the results are shown below.

Sample A - $Mn_{2.2}Ru_{0.7}Ga$

Reciprocal space map around MgO (113) peak shown in Figure 6.1 confirm that the films are strained by the substrate with lattice parameters $a = 597$ pm and $c = 602$ pm giving rise to $\approx 1\%$ tetragonal distortion of the unit cell and PMA.

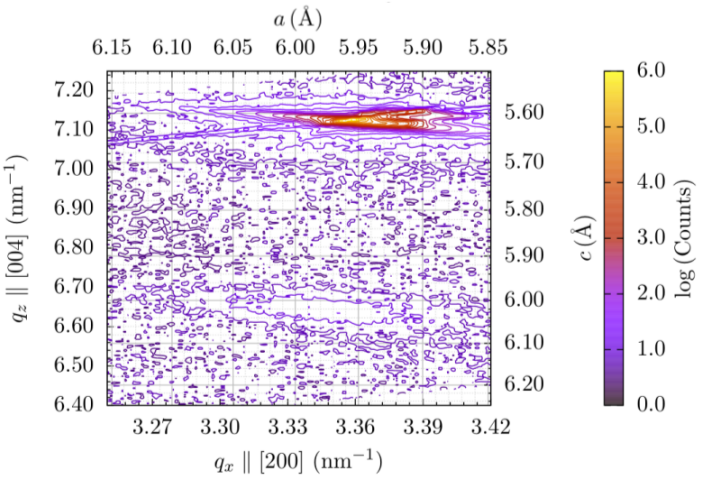

Figure 6.1: Reciprocal Space Map: MgO(113) and MRG(204) peaks of $Mn_{2.2}Ru_{0.7}Ga$ grown epitaxially on MgO(001). The real lattice parameters a and c are reported in the basis of the unit cell of MRG.

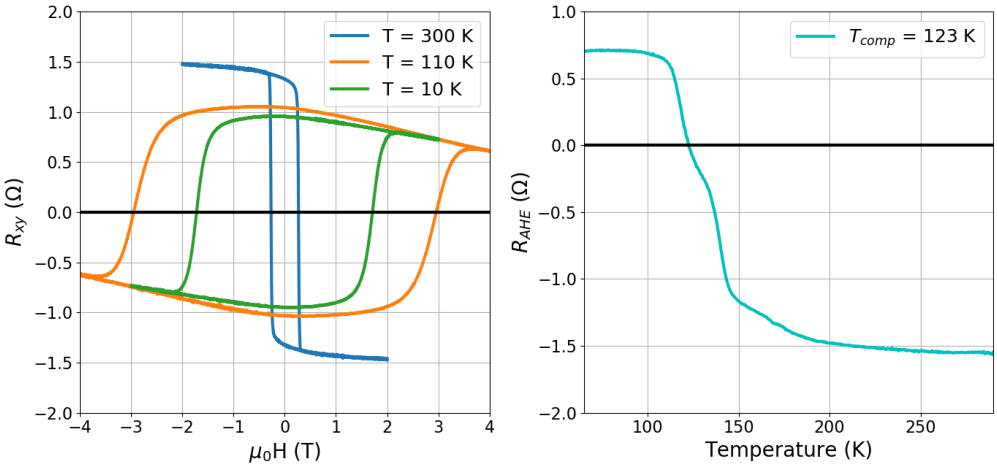

Figure 6.2: Anomalous Hall Effect: (Left) Field loops at $T = 300$ K, 110 K and 10 K. Loops change sign upon crossing T_{comp}. (Right) Anomalous Hall resistance as a function of temperature showing $T_{\text{comp}} = 123$ K determined from the difference of AHE vs T in positive and negative saturation.

Figure 6.2 shows Anomalous Hall effect field loops at various temperatures. As expected, there is a change of sign of the AHE coefficient upon crossing he compensation point, as demonstrated in Chapter 4. Thermal scans of R_{xy} were taken in + 4 T and -4 T saturation field. The two contributions to R_{xy} will be magnetoresistance (even in

field) and AHE (odd in field). Therefore the AHE contribution can be extracted using $R_{xy}(+4T) + R_{xy}(-4T) = 2R_{\mathrm{AHE}}$. R_{AHE} crosses zero at compensation which is found to be $T_{\mathrm{comp}} = 123$ K.

From a 0-field temperature scan shown in Figure 6.3 compensation occurs at 123 K, which corresponds to the value found from AHE. Mean field theory fitting of the data allows for extraction of the Weiss constants and calculation of the exchange energies. Figure 6.3 also shows SQUID magnetometry field loops of the net moment for both out-of-plane and in-plane geometries measured at 300 K and 200 K. For comparison, the AHE loop at 300 K is plotted with the SQUID. The coercivity of the hard magnetic phase in both AHE and SQUID hysteresis loops are in agreement. The net moment in SQUID appears to have a soft phase at low field, absent in AHE as previously seen in Chapter 4. Moreover, for the loop measured closer to T_{comp}, at $T = 200$ K, this apparent soft component is more pronounced. This is not surprising because as compensation is approached the out-of-plane moment becomes smaller, hence the effects of sublattice non-collinearity are expected to be more noticeable.

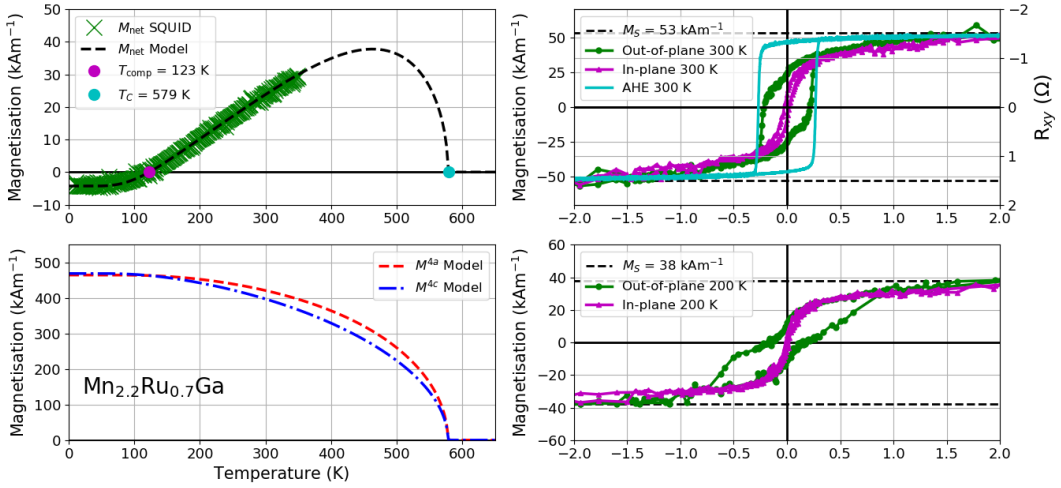

Figure 6.3: SQUID magnetometry: (Left panel) Mean field theory fitting of magnetisation versus temperature. (Right panel) SQUID magnetometry hysteresis loops at 300 K and 200 K and AHE loop at 300 K.

Sample B - $Mn_{2.0}Ru_{0.8}Ga$

$Mn_{2.0}Ru_{0.8}Ga$ has a higher Ru content than the previous sample, which increases the c parameter while substrate strain maintains the in-plane lattice parameter close

to $a = \sqrt{2}a_{\mathrm{MgO}}$. The reciprocal space map in Figure 6.4 shows $a = 595$ pm and $c = 608$ pm producing a tetragonal distortion of $\approx 2\%$. Figure 6.5 shows the SQUID and AHE data. The MFT fit of the zero field temperature scan shows $T_{\mathrm{comp}} = 367$ K. The SQUID loop at $T = 200$ K is very similar to the to the AHE loop at $T = 300$ K with the main difference in the coercive field which increases closer to T_{comp}.

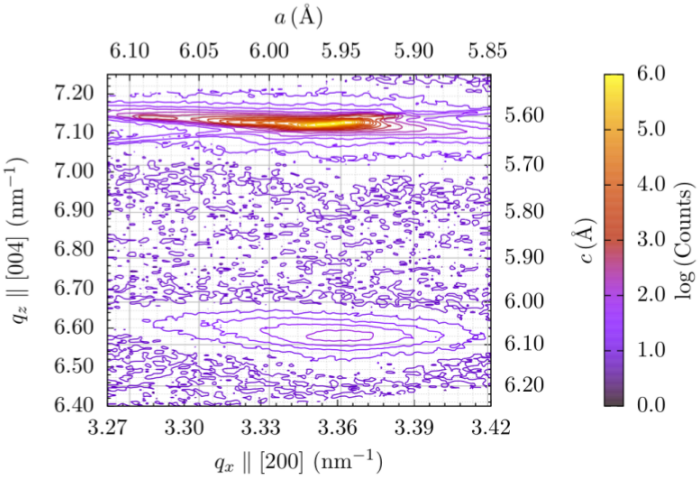

Figure 6.4: Reciprocal Space Map: MgO(113) and MRG(204) peaks of $Mn_{2.0}Ru_{0.8}Ga$ grown epitaxially on MgO(001). The real lattice parameters a and c are reported in the basis of the unit cell of MRG.

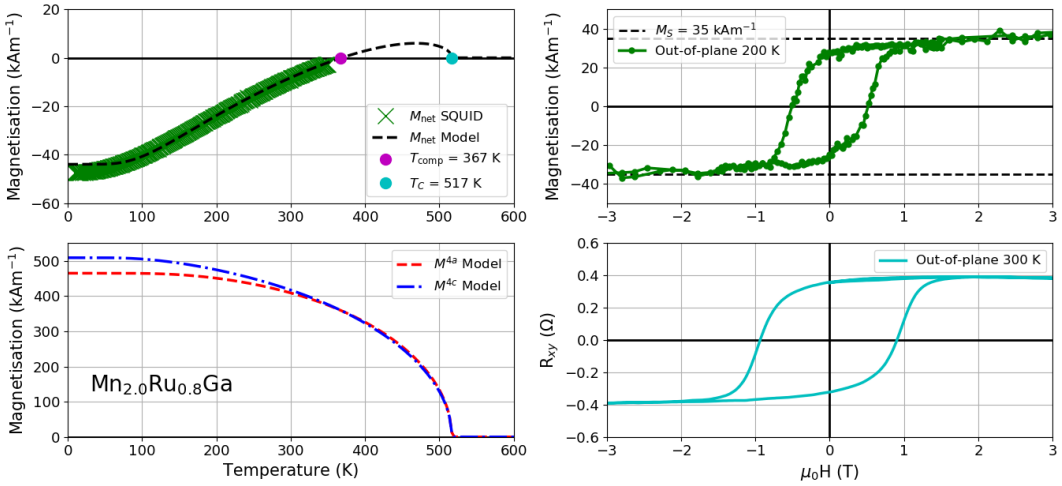

Figure 6.5: SQUID magnetometry: (Left panel) Mean field theory fitting of magnetisation versus temperature. (Right panel) SQUID magnetometry hysteresis loop at 200 K and AHE loop at 300 K.

Summary

The structural and magnetic parameters of both MRG thin films are summarised in Table 6.1 and the mean field theory input and output parameters are shown in Table 6.2. Comparing Samples A and B, there is a small difference of 1.2 %, 0.4 % for $\mathscr{J}^{aa}$, $\mathscr{J}^{ac}$, respectively. The relatively large 36 % decrease observed in the Mn^{4c} intra-sublattice exchange $\mathscr{J}^{cc}$, going from Sample A to B, could be attributed to a decrease in Mn content which depopulates the Mn^{4c} sublattice as demonstrated in Chapter 4.

At $T = 200$ K, sample A and B show a saturation magnetisation of $M_S = 38$ kA/m and $M_S = 35$ kA/m, respectively, while the canting of the net moment at remnance in sample A is larger than in sample B. This could be because the tetragonal distortion in sample B is larger than in sample A, producing a stronger anisotropy field which pins the net moment to the anisotropy axis more effectively.

Sample A - $Mn_{2.2}Ru_{0.7}Ga$			Sample B - $Mn_{2.0}Ru_{0.8}Ga$		
c (pm)	a (pm)	$\frac{c-a}{a} \cdot 100$	c (pm)	a (pm)	$\frac{c-a}{a} \cdot 100$
602	597	0.8	608	595	2.2
T_{comp} (K)	T_C (K)	M_0^{Net} (Am^{-1})	T_{comp} (K)	T_C (K)	M_0^{Net} (Am^{-1})
123	579	4000	367	517	47000

Table 6.1: Summary of structural and magnetic parameters of the MRG thin films: lattice parameters c and a, tetragonal distortion $\left(\frac{c-a}{a} \cdot 100\right)$, net magnetisation at $T = 0$ K (M_0^{Net}), compensation (T_{comp}) and Curie temperatures (T_C).

Sample A - $Mn_{2.2}Ru_{0.7}Ga$			Sample B - $Mn_{2.0}Ru_{0.8}Ga$		
$J^{4a} = 2.0$, $J^{4c} = 2.0$			$J^{4a} = 1.5$, $J^{4c} = 2.5$		
$M_0^{4a} = 465$ kA/m $M_0^{4c} = 469$ kA/m			$M_0^{4a} = 465$ kA/m $M_0^{4c} = 509$ kA/m		
n_W^{aa}	n_W^{ac}	n_W^{cc}	n_W^{aa}	n_W^{ac}	n_W^{cc}
449	-348	203	452	-352	149
$\mathscr{J}^{aa}$	$\mathscr{J}^{ac}$ (K)	$\mathscr{J}^{cc}$	$\mathscr{J}^{aa}$	$\mathscr{J}^{ac}$ (K)	$\mathscr{J}^{cc}$
21.8	-24.2	9.9	21.9	-25.6	7.2
Ratio = 10.0 : -8.1 : 5.0			Ratio = 10.0 : -7.8 : 3.3		

Table 6.2: Summary of the total angular momenta ($J^{4a,4c}$), magnetisation at T = 0 K (M_z^0), extracted Weiss constants and Heisenberg exchange energies from MFT fitting for $Mn_{2.2}Ru_{0.7}Ga$ and $Mn_{2.0}Ru_{0.8}Ga$ thin films. The last column shows the ratio of the product of exchange parameters with their coordination numbers $\mathscr{J}^{aa}Z^{aa} : \mathscr{J}^{ac}Z^{ac} : \mathscr{J}^{cc}Z^{cc}$

6.3 XMCD Experimental Set-up and Calculations

This section consists of four parts. Subsection 6.3.1 discusses the main features of the XAS and XMCD spectra measured at the Mn L-edges of MRG thin films and how it is possible to distinguish the moments of Mn sublattices and calculate their magnitudes. Subsections 6.3.2 and 6.3.3 describe the experimental details of measurements at normal and grazing incidence of the x-ray beam on the surface of the sample with the aid of diagrams. Subsections 6.3.4 and 6.3.5 show the mathematical equations used to calculate $m_{\perp}$ and $m_{\parallel}$ components from k-projections of moments (m_k) obtained from XMCD spectra collected at different angles of incidence, and a balancing of torques based on the magnetic free energy, assuming uniaxial anisotropy.

6.3.1 XAS and XMCD Spectra

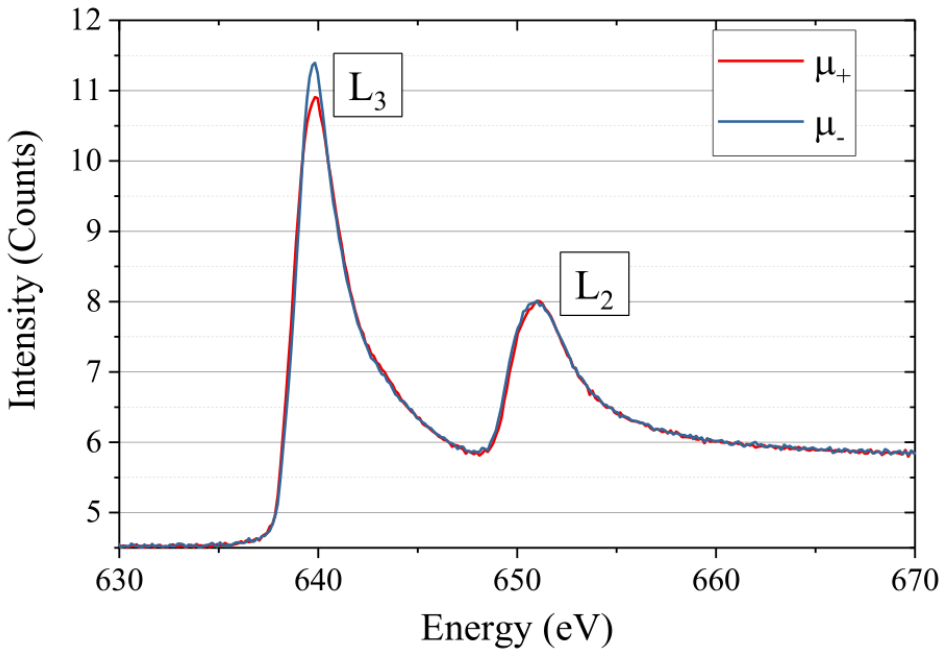

Figure 6.6: Typical Mn L-edge XAS spectra of an MRG thin film, performed with LCP (μ_+) and RCP (μ_-) X-rays.

The magnetism in MRG originates from two antiferromagnetically coupled Mn sublattices. Therefore, circularly polarised XAS measurements were performed at the

L-edges of Mn. L-edge absorption corresponds to the resonant excitation of core electrons from $2p$ states to unoccupied valence states in the Mn $3d$ band. Typical circularly polarised XAS spectra are shown in Figure 6.6. Using quantum mechanical core-hole corrected multiplet calculations [1; 2], the theoretical absorption and dichroism spectra were found by Betto *et al.* [3]. The measured XAS is different from the calculated spectra for several reasons. Firstly, the metallic nature of Mn causes a broadening of the L_3 and L_2 peaks. Secondly, the 2p spin-orbit coupling in MRG ($\approx$ 10 eV) is not sufficient to ensure pure $P_{\frac{3}{2}}$ and $P_{\frac{1}{2}}$ character of the L_3 and L_2 peaks, respectively.

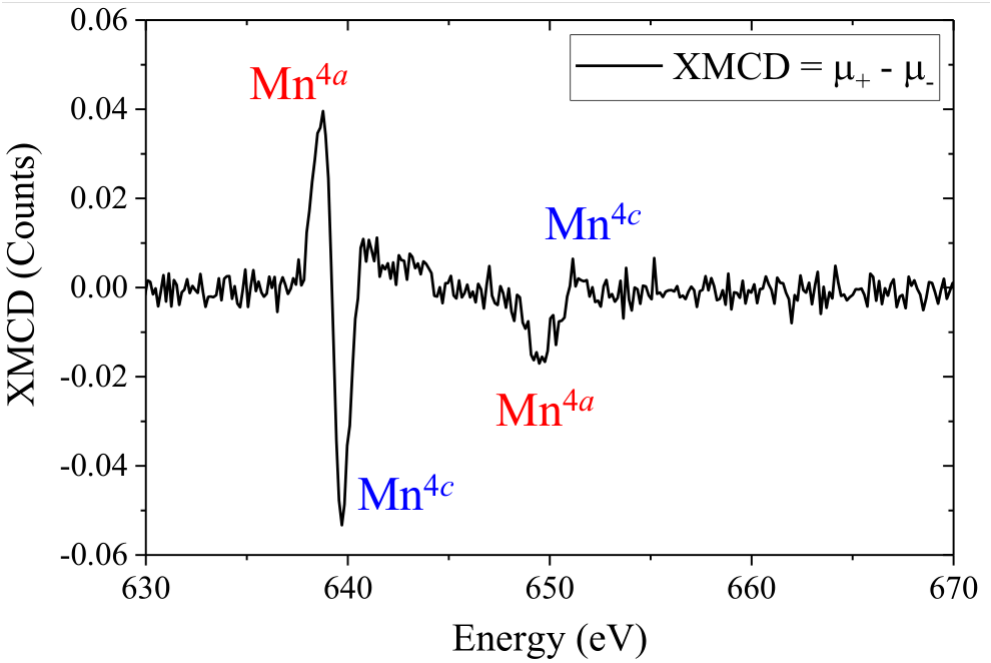

Figure 6.7: Typical Mn L-edge XMCD spectrum of an MRG thin film.

The difference in circularly polarised XAS is the XMCD spectrum shown in Figure 6.7. The Mn occupies inequivalent sites which will give rise to a small shift in X-ray absorption energy, which is $\approx$ 1 eV as seen in the spectrum. Magnetic selectivity of circularly polarised XAS implies that XMCD peaks corresponding to the site specific moments have the opposite sign. This allows to differentiate between the two Mn sublattice moments. The orbital and magnetic components of the net moments are related to the integrals of isotropic XAS and XMCD spectra via sum rules [4; 5; 6] as discussed in Chapter 2 subsection 2.7.3 .

The sum rules assume that the transition from 2p core states to 3d valence states are well defined and that the 3d valence states are separable from other final states. However, as discussed above, the L_3 and L_2 absorption edges are not pure in character and intermixing of 3d and 4s valence states means the final states are not well defined. These factors lead to a 5-10 % error in the sum rules. [7; 8] The m^{4a} and m^{4c} sublattice moments are assumed to be proportional to the peak areas integrated in the ranges 638.2 eV - 639.1 eV and 639.3 eV - 640 eV, respectively. This is in violation of the sum rules, which require the integration of the entire XMCD spectrum. Furthermore, the chosen integrated regions in the XMCD spectrum cannot be normalised by isotropic XAS, as it is the case in sum rule calculations, and the peaks have a significant overlap. Considering all the factors, the sublattice moments obtained are in arbitrary units (arb. unit) and need to be normalised using magnetometry data to convert from arb. unit to μ_B/Mn.

6.3.2 Normal Incidence

The diagram in Figure 6.8 depicts the simplest measurement geometry with the x-ray beam propagation vector **k** incident normal to the film surface. The blue arrows indicate the two available field directions, one parallel to the beam, i.e. longitudinal field ($\mu_0\mathbf{H}_\mathrm{L}$), and perpendicular to the beam i.e. transverse field ($\mu_0\mathbf{H}_\mathrm{T}$). Before the measurements, the films were saturated in $+9$ T field longitudinal field at temperatures far away from compensation such that the coercive field satisfies $\mu_0 H_C < 9$ T.

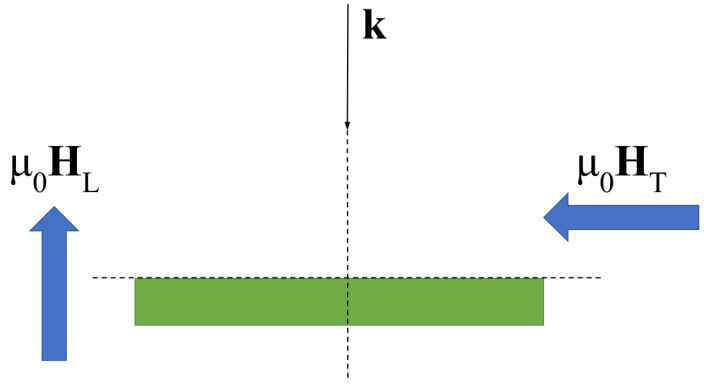

Figure 6.8: Normal incidence showing longitudinal ($\mu_0\mathbf{H}_\mathrm{L}$) and transverse ($\mu_0\mathbf{H}_\mathrm{T}$) field directions.

6.3.3 Grazing Incidence

The XMCD measurements were performed in different sample orientations and applied field directions with respect to the beam in order to construct 2-D projections of sublattice moments. The four geometries are:

1. Normal incidence & Longitudinal field
2. Grazing incidence & Transverse field
3. Normal incidence & Transverse field
4. Grazing incidence & Longitudinal field

Two different sample orientations are needed to give two equations for two unknowns which are $m_\perp$ and $m_\parallel$. Figures 6.9 and 6.10 are diagrams showing pairs of

sample orientations and applied fields relative to the beam for easy axis and hard axis measurements. Counter clockwise (clockwise) rotations are positive (negative).

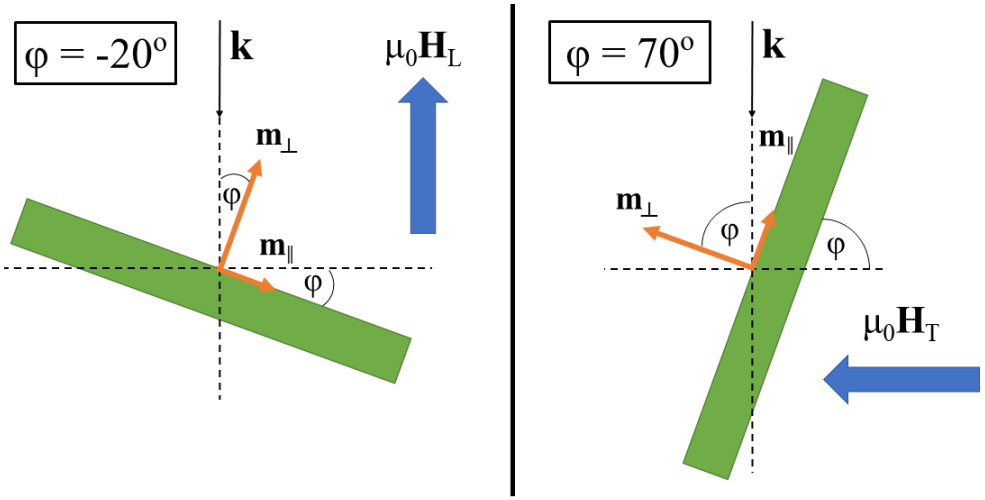

Figure 6.9: Left: Normal incidence & Longitudinal field ($\phi = -20°$). Right:Grazing incidence & Transverse field ($\phi = 70°$).

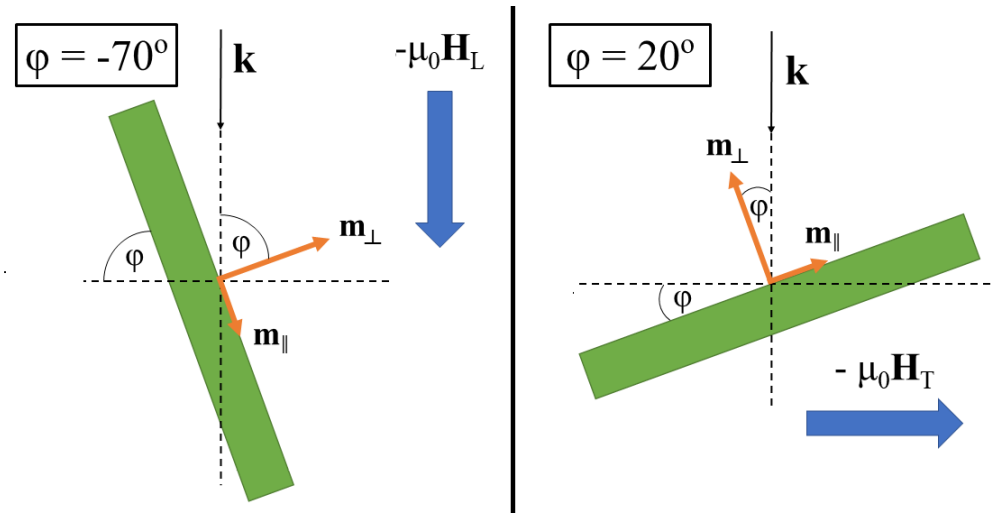

Figure 6.10: Left: Normal incidence & Transverse field ($\phi = -70°$). **Right:** Grazing incidence & Longitudinal field ($\phi = 20°$).

For a pair of sample geometries, the sample is first rotated $\phi = \phi^1$ and for the second measurement is performed at $\phi = \phi^2$, such that $|\phi^2 - \phi^2|$ 90°. The choice of angles is determined by finding the minimal angle at which XMCD signal can be detected and

used for calculations in a transverse applied field. In this case, 20° was found to be the most appropriate choice. Before each measurement, the samples were saturated in an out-of-plane field of +9 T with sample rotated to $\phi = -20°$ at a temperature far from compensation such that $\mu_0 H_C < 9$ T.

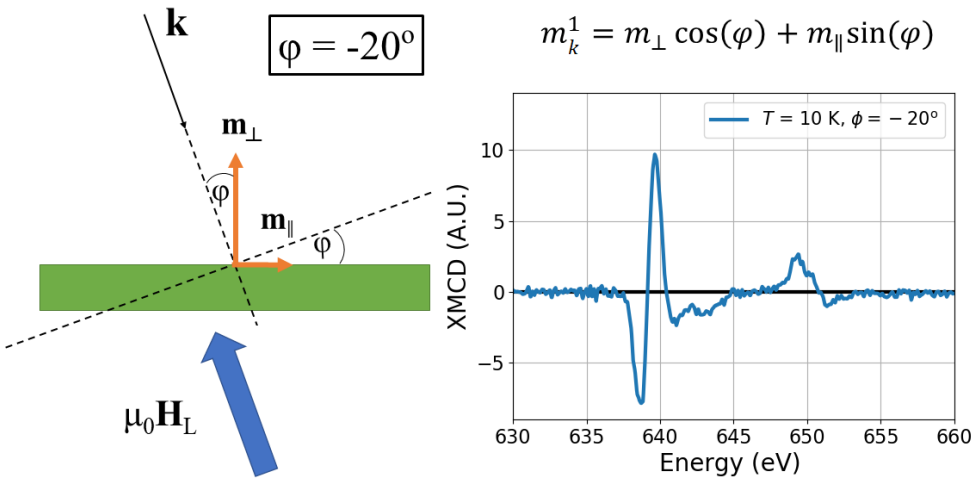

Figure 6.11: Normal incidence & Longitudinal field: Diagram in the frame of the sample and a sample XMCD spectrum.

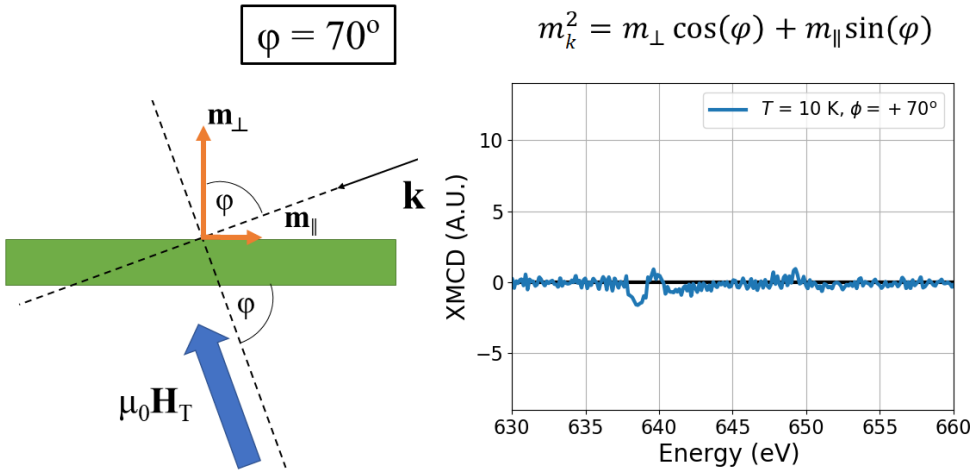

Figure 6.12: Grazing incidence & Transverse field: Diagram in the frame of the sample and a sample XMCD spectrum.

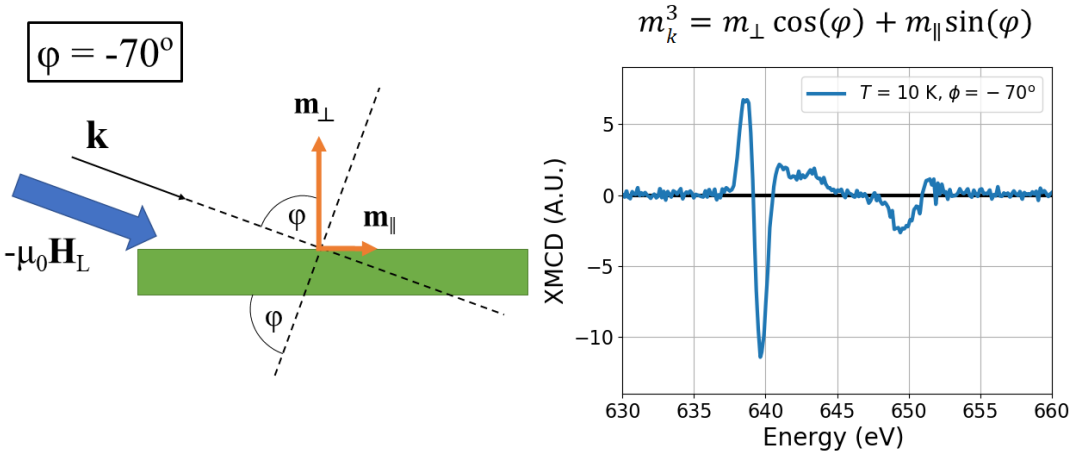

Figure 6.13: Normal incidence & Transverse field: Diagram in the frame of the sample and a sample XMCD spectrum.

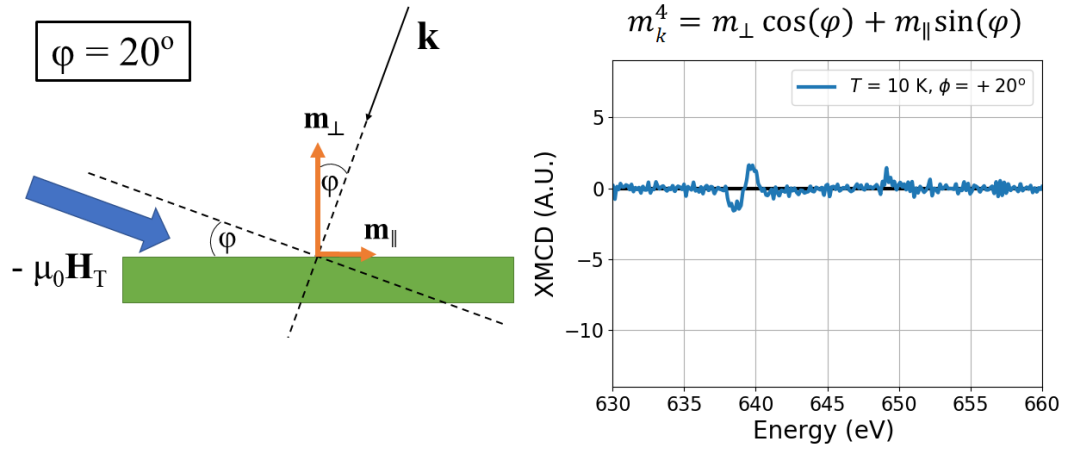

Figure 6.14: Grazing incidence & Longitudinal field: Diagram in the frame of the sample and a sample XMCD spectrum.

To visualise the projections the incidence angles of x-rays and the applied field directions, diagrams in the frame of the sample are shown in Figures 6.11, 6.12, 6.13, 6.14. Each figure includes an XMCD spectrum of sample A taken at $T = 10$ K and $|\mu_0 \mathbf{H}| = 4$ T. The measured moment (m_k) is a linear combination of the perpendicular ($m_\perp$) and parallel ($m_\parallel$) components, with coefficients found using trigonometry. The derivation of the equations used to analyse the data is shown in section 6.3.4.

6.3.4 Calculation of Moment Components

Let m_k^i and m_k^j be the k-vector projections of the magnetic moment measured in the ith and jth geometries, where $i, j = 1,2,3,4$ with the sample at respective angles of ϕ^i and ϕ^j such that $|\phi^i - \phi^j| = \frac{\pi}{2}$. The projections can be expressed in term of their parallel $m_\parallel$ and perpendicular $m_\perp$ components, as seen in the figures above, by

$$m_k^i = m_\perp \cos(\phi^i) + m_\parallel \sin(\phi^i) \qquad (6.1) \qquad m_k^j = m_\perp \cos(\phi^j) + m_\parallel \sin(\phi^j) \qquad (6.2)$$

For the out-of-plane field, in the first geometry the sample is rotated clockwise by an angle $\phi^1 = -20^o$ and in the second the rotation is counter clockwise by $\phi^2 = 70^o$. Let $\phi^1 = \phi$, then $\phi^2 = \frac{\pi}{2} + \phi$. Rewriting the equations 6.1 and 6.2 with ϕ angle gives

$$m_k^1 = m_\perp \cos(\phi) + m_\parallel \sin(\phi) \qquad (6.3) \qquad m_k^2 = m_\perp \sin(\phi) - m_\parallel \cos(\phi) \qquad (6.4)$$

Using equations 6.3 and 6.4 to find $m_\perp$ and $m_\parallel$

$$m_\perp = m_k^1 \cos(\phi) + m_k^2 \sin(\phi) \qquad (6.5)$$

$$m_\parallel = m_k^1 \sin(\phi) - m_k^2 \cos(\phi) \qquad (6.6)$$

For the in-plane field, $\phi^3 = -70^o$ and $\phi^4 = 20^o$. Let $\phi^3 = \phi$, then $\phi^4 = \frac{\pi}{2} + \phi$.

$$m_\perp = m_k^3 \cos(\phi) + m_k^4 \sin(\phi) \qquad (6.7)$$

$$m_\parallel = m_k^3 \sin(\phi) - m_k^4 \cos(\phi) \qquad (6.8)$$

Then the final moment vector in x-z plane is given by

$$\mathbf{m} = m_\parallel \hat{\mathbf{x}} + m_\perp \hat{\mathbf{z}} \qquad (6.9)$$

6.3.5 Magnetic Free Energy and Torques

At equilibrium, torques exerted on the sublattice moments by an applied field B and by the crystal lattice must vanish. The simplest case of uniaxial anisotropy is used. More experimental data is required for a more complicated model with more free parameters. Equating the torques on sublattice moments with the field in-plane along the hard axis allows us to obtain sublattice anisotropy constants ($K_1^{4a,4c}$) and the inter-sublattice exchange ($\mathscr{J}^{ac}$). The magnetic free energy density of each Mn sublattice is given by

$$E^{4a,4c}(\theta^{4a},\theta^{4c}) = K_1^{4a,4c}\sin^2(\theta^{4a,4c}) - \mathscr{J}^{ac}\cos\left(\theta^{4a}-\theta^{4c}\right) \tag{6.10}$$

The torque exerted on the sublattice moments by the anisotropy and exchange fields is

$$\tau_A^{4a,4c}(\theta^{4a},\theta^{4c}) = -\frac{\partial E^{4a,4c}(\theta^{4a},\theta^{4c})}{\partial\theta^{4a,4c}} = -K_1^{4a,4c}\sin\left(2\theta^{4a,4c}\right) \mp \mathscr{J}^{ac}\sin\left(\theta^{4a}-\theta^{4c}\right) \tag{6.11}$$

The torque exerted by the applied magnetic field is

$$\tau_B^{4a,4c}(\mathbf{B}) = |\mathbf{M}^{4a,4c}\times\mathbf{B}| \tag{6.12}$$

At equilibrium, all torques must vanish and using equations 6.11 and 6.12 we obtain two equations to be solved numerically for θ^{4a} and θ^{4c}

$$|\mathbf{M}^{4a}\times\mathbf{B}| = K_1^{4a}\sin\left(2\theta^{4a}\right) + \mathscr{J}^{ac}\sin\left(\theta^{4a}-\theta^{4c}\right) \tag{6.13}$$

$$|\mathbf{M}^{4c}\times\mathbf{B}| = K_1^{4c}\sin\left(2\theta^{4c}\right) - \mathscr{J}^{ac}\sin\left(\theta^{4a}-\theta^{4c}\right) \tag{6.14}$$

To find the optimal K_1^{4a}, K_1^{4c} and $\mathscr{J}^{ac}$ the following minimisation condition Δ is used

$$\Delta = \sqrt{(\theta_{XMCD}^{4a}-\theta^{4a})^2 + (\theta_{XMCD}^{4c}-\theta^{4c})^2} \tag{6.15}$$

where $\theta_{XMCD}^{4a,4c}$ are the $\mathrm{Mn}^{4a,4c}$ sublattice moment angles found from XMCD data. The corresponding anisotropy fields can be found using

$$\mu_0 H_A = \frac{2K_1}{M_S} \tag{6.16}$$

where M_S is the saturation magnetisation.

6.4 Results

6.4.1 Normal Incidence

In this section all measurements were performed at normal incidence and in longitudinal magnetic field. The measurements demonstrate the dependence of the z-projection of sublattice moments on i) temperature in the presence of $\mu_0 H_L = 9$ T and ii) $\mu_0 H_L$ from 0 T to 9 T at $T = 145$ K.

6.4.1.1 Sample A: Temperature Dependence

Since Sample A has a $T_{comp} = 123$ K it is possible to investigate the sublattice moment behaviour at temperatures above, below and at compensation using a cryostat. The relative magnitudes of sublattice moments as a function of temperature are

- $T < T_{comp}$: $|m^{4c}| > |m^{4a}|$
- $T = T_{comp}$: $|m^{4c}| = |m^{4a}|$
- $T > T_{comp}$: $|m^{4c}| < |m^{4a}|$

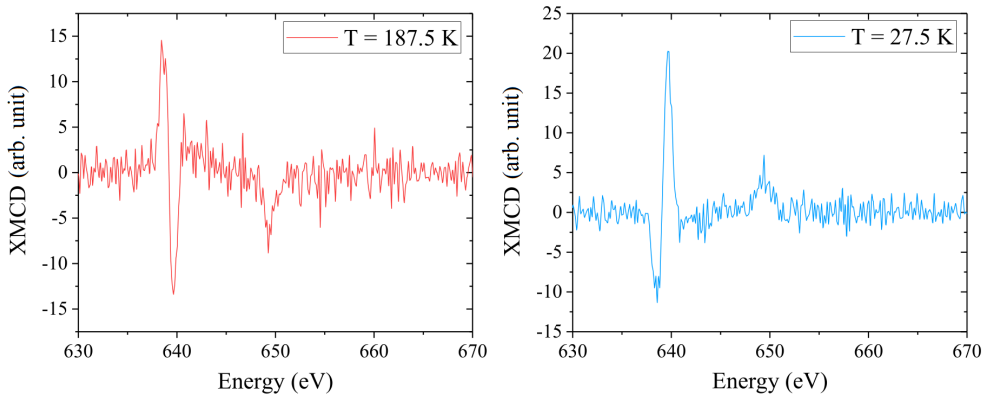

Figure 6.15: Sample A: XMCD spectra in $\mu_0 H_L = +9$ T taken above and below compensation at $T = 187.5$ K and $T = 27.5$ K, respectively.

XMCD spectra measured in a perpendicular +9 T field at $T > T_{comp}$ and $T < T_{comp}$ are shown in 6.15. The peaks in the L_3 and L_2 regions change sign confirming that compensation was crossed.

Temperatures $T = 290$ K and $T = 25$ K are far above and below compensation, respectively. In an applied field of $\mu_0 H_L = +9$ T along the z-axis, the dominating sublattice moments at those temperatures are assumed to be pinned along the easy axis. Therefore the magnitudes of the z-projections of the dominating sublattice moments at temperatures far from compensation are assumed to be equal to the values found from MFT fits of net moment measured by SQUID magnetometry. The temperature dependence of the magnitude of sublattice moments calculated from both MFT and XMCD are shown in Figure 6.16.

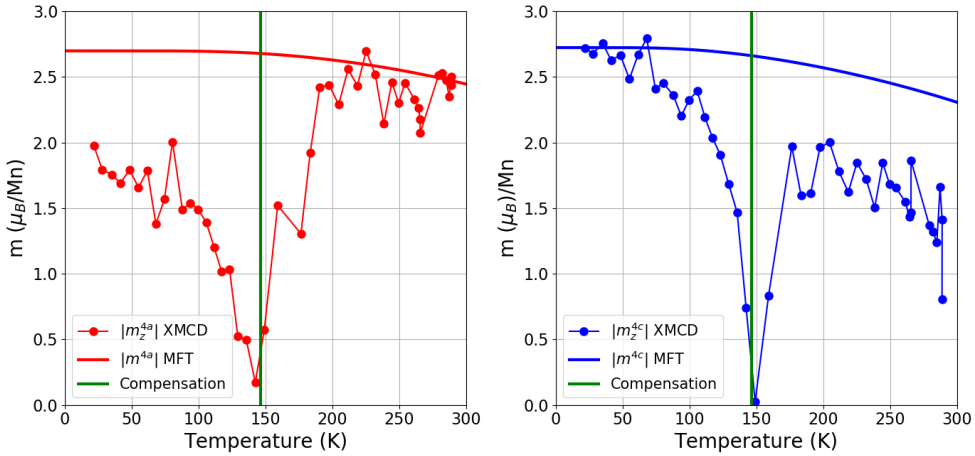

Figure 6.16: Sample A: The z-projection of absolute sublattice moments versus temperature in $\mu_0 H_L = +9$ T calculated from XMCD and sublattice moments calculated from MFT with $\mu_0 H = 0$ T. Compensation point found in XMCD is marked with a green vertical line.

Away from compensation, the dominant sublattice moments from XMCD show a similar temperature dependence to MFT model. This validates the assumption that they are aligned with the applied field in those temperatures. The weaker sublattice, which is antiparallel to the dominant one, is expected to tilt in the applied field. Close to compensation, both sublattice moments rotate relative to the anisotropy axis and their z-projection decreases. A sharp decrease in z-projection is found at $T = 145$ K which is indicative of a spin-flop transition at compensation. Analysing the variation of magnitude of sublattice moments in XMCD relative to the MFT, enables the calculation of the canting angles of the moments.

Figure 6.17 shows the moments versus temperature with vector diagrams of directions of sublattice moments at seven different temperatures. As temperature is increased from 20 K towards compensation, the z-projection of sublattice moments decreases to zero with the Mn^{4c} sublattice being dominant. Upon crossing compensation the Mn^{4a} sublattice begins to dominate, the z-projections of moments increase in magnitude. The vector diagrams illustrate the rotation of sublattice moments, relative to the easy axis direction, due to the variation in temperature.

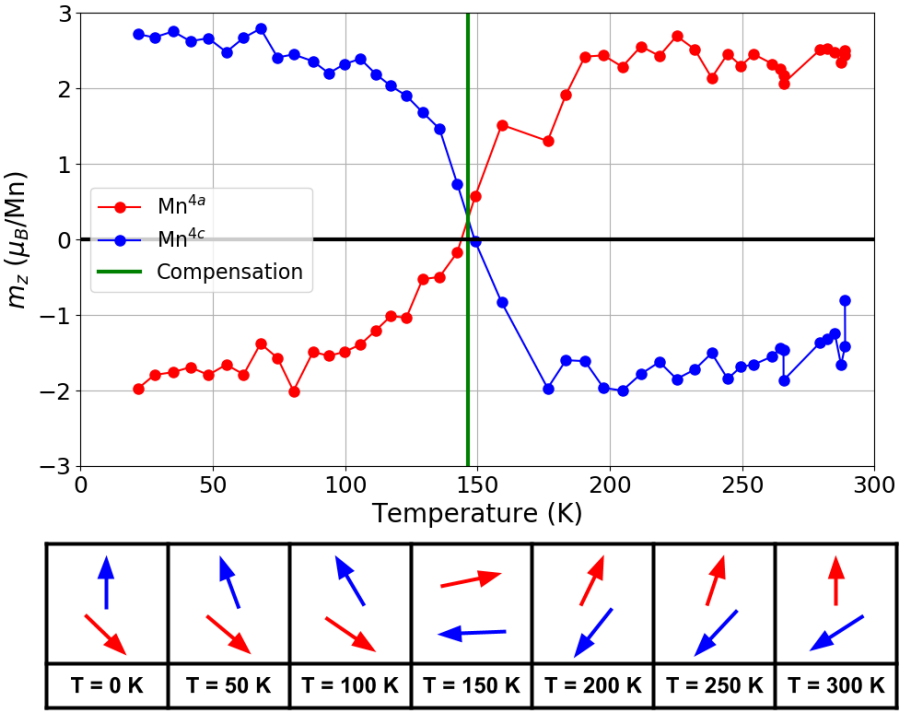

Figure 6.17: Sample A: The z-projection of sublattice moments versus temperature in $\mu_0 H_L = +9$ T from XMCD and illustration of sublattice moment directions.

The data in 6.17 can be used to extract the inter-sublattice exchange energy $\mathscr{J}^{ac}$, which is constant with temperature, by assuming that the sublattice anisotropy can be ignored, so the condition can be written as $|\mathscr{J}^{ac}| >> |K_1^{4a,4c}|$. Considering the variation in torque, the $\mathscr{J}^{ac}$ can be calculated using

$$\Delta\tau_B(\mathbf{B}) = \Delta\tau_A(\theta^{4a}, \theta^{4c}) \tag{6.17}$$

$$|\mathbf{M}^{4a} \times \mathbf{B}| - |\mathbf{M}^{4c} \times \mathbf{B}| = -2\mathscr{J}^{ac} \sin\left(\theta^{4a} - \theta^{4c}\right) \tag{6.18}$$

The result of the calculation, shown in Figure 6.18, shows that $\mathscr{J}^{ac}$ is almost constant away from compensation, as expected, but diverges at compensation. In the temperature range where $\mathscr{J}^{ac}$ is constant, the value is 20 times smaller than $\mathscr{J}^{ac} = 17.46$ meV obtained from MFT. These findings suggest that the anisotropy is sufficiently large such that the condition $|\mathscr{J}^{ac}| >> |K_1^{4a,4c}|$ does not hold.

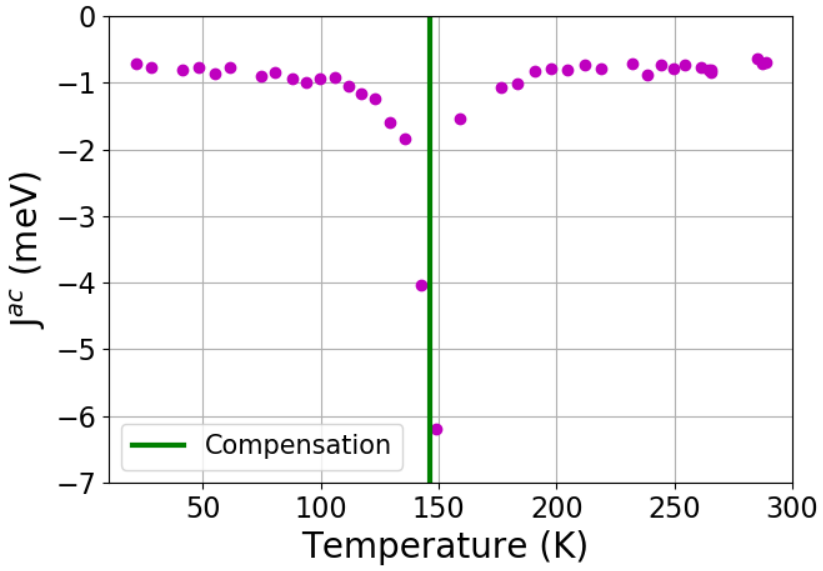

Figure 6.18: Variation in $\mathscr{J}^{ac}$ calculated from the temperature dependent sublattice moments in XMCD.

In the next section, field dependent data taken near compensation where a spin-flop transition was observed will be used to calculate the anisotropy constants and compare them to the inter-sublattice exchange.

6.4.1.2 Sample A: Spin-flop at T = 145 K

In uniaxial antiferromagnets (AFMs), a spin-flop is a metamagnetic transition where by applying a sufficiently high magnetic field along the easy axis, known as a spin-flop field ($\mu_0 H_{sf}$), it is energetically more favourable for the sublattice moments to reorient perpendicular to the applied field. The magnetic susceptibility in in uniaxial AFMs is not isotropic and the perpendicular magnetic susceptibility $\chi_\perp$ is always larger than

the parallel magnetic susceptibility $\chi_{\parallel}$. Thus, in the perpendicular field H the magnetostatic energy is lower by $\Delta E(H)$

$$\Delta E(H) = \frac{1}{2}\mu_0(\chi_{\perp} - \chi_{\parallel})H^2 \tag{6.19}$$

This favours the moments to be in a transverse 'spin-flopped' state relative to the easy axis. However, magnetocrystalline anisotropy pins the moments along the easy axis and to overcome this a sufficient perpendicular field must be applied, known as the spin-flop field (H_{sf}), given by

$$\mu_0 H_{\mathrm{sf}} = \sqrt{\frac{2K\mu_0}{(\chi_{\perp} - \chi_{\parallel})}} \tag{6.20}$$

where K is the magnetocrystalline anisotropy.

The perpendicular susceptibility can be derived by assuming canting of antiferromagnetically coupled sublattice moments $|\mathbf{M}^A| = M^A$ and $|\mathbf{M}^B| = -M^B$ by a small angle δ away from the easy axis in an applied perpendicular field H. The perpendicular component of the magnetisation is $M_{\perp} = 2M^{\alpha}\cos(\delta)$, where $\alpha = A, B$. Ignoring anisotropy, the two torques acting on the system are due to the applied field and the inter-sublattice exchange field. At equilibrium, the torques on each sublattice are zero. Using this information $\chi_{\perp}$ is derived

$$|\mathbf{M}^A \times \mathbf{H}| = -n_W^{AB} M^A M^B \sin(2\delta) \tag{6.21}$$

$$M^A H \sin(\delta) = -n_W^{AB} M^A M^B \left(2\sin(\delta)\cos(\delta)\right) \tag{6.22}$$

$$H = -n_W^{AB}\left(2M^B\cos(\delta)\right) \tag{6.23}$$

$$H = -n_W^{AB} M_{\perp} \tag{6.24}$$

$$\therefore \chi_{\perp} = \frac{M_{\perp}}{H} = \frac{-1}{n_W^{AB}} \tag{6.25}$$

Equation 6.25 highlights that $\chi_{\perp}$ is constant and independent of temperature, up to the Néel magnetic ordering temperature (T_N). The calculation of parallel susceptibility involves the expansion of the Brillouin functions $B_J(x)$ around the argument x_0 in the absence of an applied field. The expression for $\chi_{\parallel}$, derived in detail [9], has the form

$$\chi_{\parallel} = \frac{2\beta B_J'(x_0)}{T - n_W^{AB}\beta B_J'(x_0)} \tag{6.26}$$

where β is a constant and $B'_J(x_0) = \left(\frac{\partial B_J(x)}{\partial x}\right)_{x=x_0}$. In the limit of $T \to 0$, $B'_J(x_0) \to 0$ and therefore $\chi_{\parallel} \to 0$. At $T = T_N$, $\chi_{\parallel} = \chi_{\perp}$ and for $T < T_N$ $\chi_{\parallel} < \chi_{\perp}$.

Experimental characteristics of a spin-flop transition in a uniaxial AFM:

- $0 \leq H < H_{\mathrm{sf}}$: The sublattice moments are pinned to the easy axis by magnetocrystalline anisotropy and compensate perfectly, hence the net moment is zero.
- $H = H_{\mathrm{sf}}$: A large and sharp increase in the net moment occurs because the moments rotate away from the easy axis into the basal plane with slight canting giving rise to a non-zero net moment.
- $H > H_{\mathrm{sf}}$: The net moment increases linearly with applied until the cone between the moments is closed.

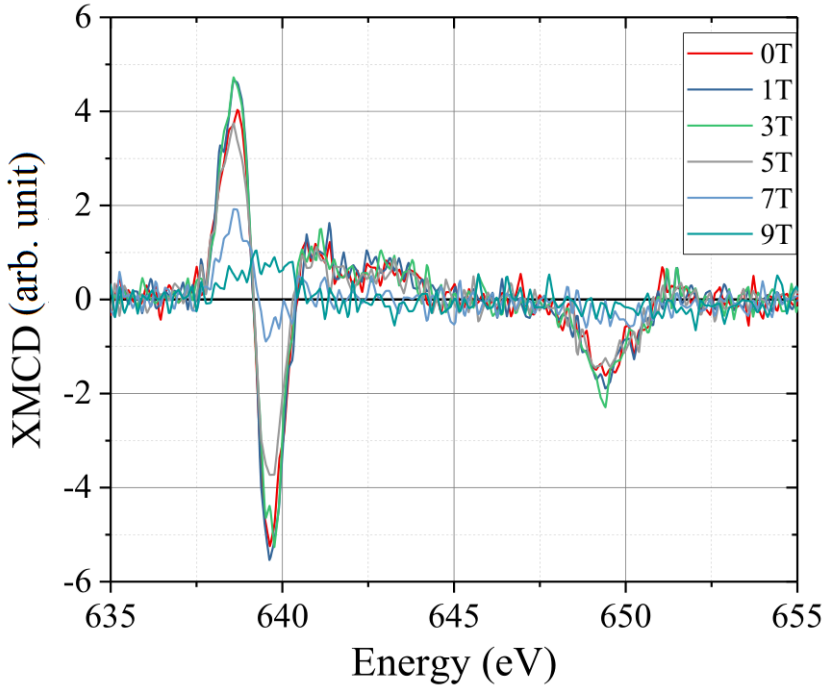

Figure 6.19: $Mn_{2.2}Ru_{0.7}Ga$: XMCD spectra taken at $T = 145$ K at various fields applied out-of-plane.

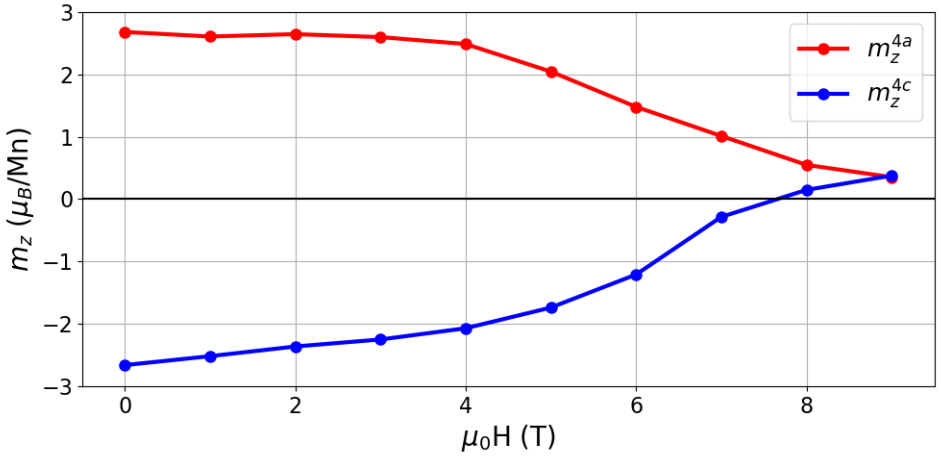

Figure 6.20: $Mn_{2.2}Ru_{0.7}Ga$: The z-projection of sublattice moments versus applied magnetic field at $T = 145$ K from XMCD.

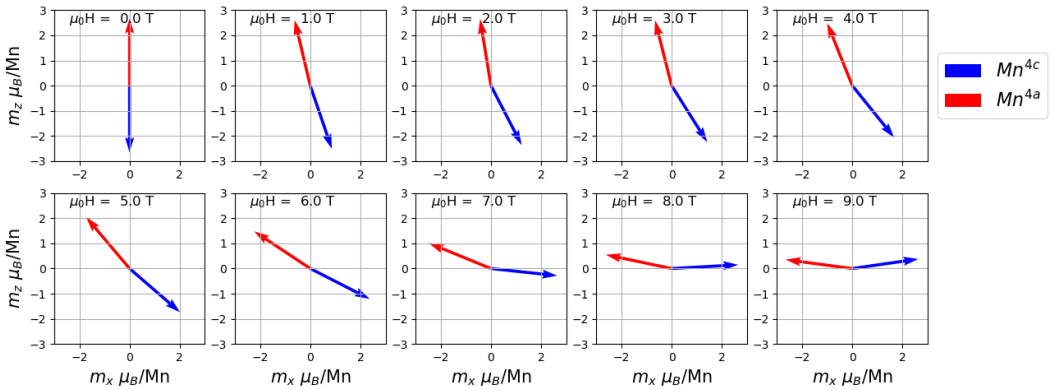

Figure 6.21: $Mn_{2.2}Ru_{0.7}Ga$: 2-D representation of sublattice moment directions with field applied along the easy axis.

In the case of MRG, close to or at T_{comp} the net moment is very small or zero and magnetically it resembles a uniaxial antiferromagnet. Therefore, at compensation MRG is expected to exhibit a spin-flop transition. From the temperature scan in 9 T, the compensation was determined to be at $T = 145$ K. XMCD spectra shown in 6.19 were measured with **k** normally incident on the surface of the sample, in a perpendicular field of up to +9 T. Prior to the measurement the sample was saturated in +9 T at $T > T_{\text{comp}}$. Figure 6.20 shows the z-projection of the sublattice moments calculated from the XMCD. The sample was saturated above compensation, therefore the m^{4a}

moment is positive. The bottom of the figure shows vector illustrations of magnetic sublattice moment directions at selected fields. The units of moment were converted from arb. unit to μ_B/Mn using values calculated by MFT calculations shown above in Figure 6.3. The data in Figure 6.20 was used to construct 2D vector representation of the orientations of sublattice moments shown in 6.21.

The XMCD spectra at low fields show that in the L_3 region large oppositely oriented peaks. This means the sublattice moments have finite moments and are oppositely aligned. At zero-applied field, the two sublattices are assumed to be approximately collinear. As external magnetic field is increased from 0 to 3 T, the m_z^{4a} is approximately constant and m_z^{4c} slowly decreases as it rotates away from the easy axis. At higher fields, the XMCD peaks begin to get smaller indicating the that the increasing field causes both sublattices to bend together. The last spectrum 9 T shows a small broad positive peak which indicates a reorientation of sublattice moments via a spin-flop transition. The Mn^{4c} moment is fully in the plane when m_z^{4c} is zero which occurs at the spin-flop field $\mu_0 H_{\mathrm{sf}} = 7.65$ T. The transition observed in MRG is not sharp as in typical AFMs. This is because in MRG the Mn sublattices are not symmetrically equivalent and have higher magnetocrystalline anisotropy.

To estimate the value of the magnetocrystalline constant from the spin-flop field, equation 6.20 is rearranged for K

$$K = \frac{1}{2\mu_0}(\chi_\perp - \chi_\parallel)(\mu_0 H_{\mathrm{sf}})^2 \tag{6.27}$$

where $\mu_0 H_{\mathrm{sf}} = 7.65$ T, $\chi_\perp = (-n_W^{ac})^{-1} = (348.2)^{-1}$ and assuming that $\chi_\parallel \approx 0$ at $T = 145$ K, gives an effective anisotropy constant $K = 6.69 \times 10^4$ Jm^{-3}. This corresponds to an anisotropy energy 0.02 meV, which is almost 3 orders of magnitude lower than inter-sublattice exchange. This value is typical of cubic ferromagnetic and ferrimagnetic materials. SQUID magnetometry data taken at $T = 140$ K, shows the saturation magnetisations is $M_S^{\mathrm{net}} = 20$ kAm^{-1}, therefore the anisotropy field is $H_A^{\mathrm{net}} = 6.7$ T. This is consistent with large anisotropy fields of the net moment recorded in AHE measurements at temperatures close to T_{comp} presented in Chapter 4. Calculating the individual sublattice anisotropies requires hard axis measurements of sublattice magnetisations which will be presented in the next section.

6.4.2 Grazing Incidence

In this section, the 2-D projections of sublattice moments are presented and discussed. Sublattice moments are expressed as vectors in the $x-z$ plane, $\mathbf{m}^{4a,4c} = (m_{\parallel}^{4a,4c})\hat{\boldsymbol{x}} + (m_{\perp}^{4a,4c})\hat{\boldsymbol{z}}$. The moments cannot be probed in three dimensions, therefore at zero or low fields it is possible that the moments have a y-projection that is not accessible. This will result in an uncertainty in both magnitude and direction of sublattice moments. The magnitudes of the sublattice moments are constant at a fixed temperature and it was assumed that at $|\mu_0\mathbf{H}| = 4$ T there is no component in the y-direction. Therefore, for each applied field the moments were scaled such that the absolute of their magnitudes are constant and equal to those measured in $|\mu_0\mathbf{H}| = 4$ T. Then the sublattice moments were converted from arbitrary units to μ_B/Mn using MFT data.

To determine the anisotropy constants of the sublattice moments, the torques exerted on them at equilibrium were calculated and set to zero. The data taken at zero field was not included in the minimisation because in that case there is no torque on the sublattices. The zero field case was treated separately, where the optimal angles are found by minimising the free magnetic energy density with optimised constants.

6.4.2.1 Vector Diagrams

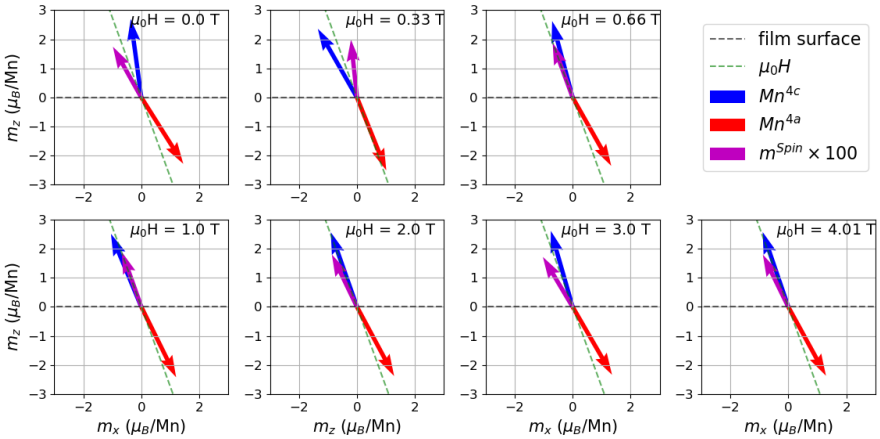

Figure 6.22: Field applied out-of-plane: m_z vs m_x of Mn^{4a}, Mn^{4c} sublattices and the spin moment m^{Spin}.

Figure 6.22 shows the $z-x$ projection of sublattice moments at $T = 10$ K and with field applied out-of-plane along the green dashed line. In the measurement, the field is ramped close to the easy axis of the net moment. The spin moment (m^{Spin}) is proportional to the net moment and it is shown together with the sublattice moments. The spin moment was multiplied by 100 to make its magnitude similar to the sublattice moments. At higher fields, m^{Spin} and m^{4c} are in good agreement with each other and are saturated along the applied field direction for $|\mu_0\mathbf{H}| > 0.66$ T.

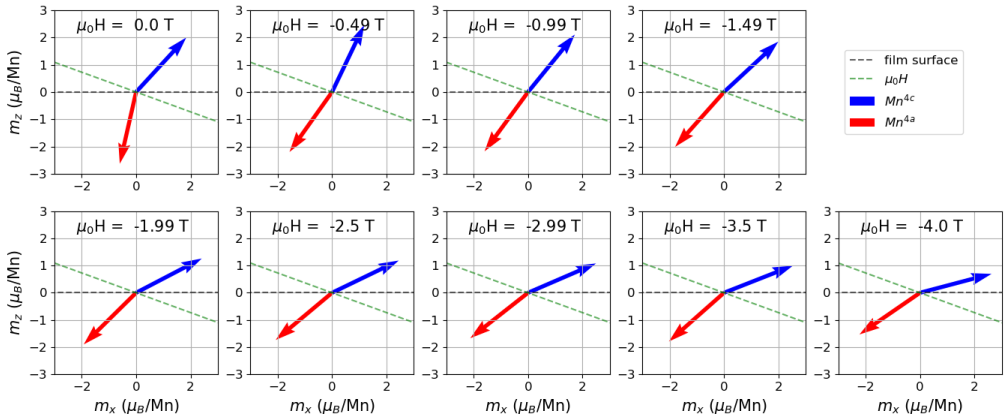

Figure 6.23: Sample A - $T = 10$ K - Field applied in-plane: m_z vs m_x of Mn^{4a} and Mn^{4c} sublattices. Green dashed line indicated the applied field axis.

Figure 6.23 shows a selection of the 2-D projections of sublattice moments with field applied along the dashed green line. Data at 0-field shows large canting of sublattices and is not reliable for the reason described above. From $|\mu_0\mathbf{H}| > 0$, the moments rotate towards the applied field direction. At the maximal applied field, moments are strongly canted away from the easy axis and are non-collinear. No switch is observed because the net moment is very low. Sublattice moments do not saturate along the field axis which indicates that the field applied is not sufficient to overcome the magnetocrystalline anisotropy. The next section shows the quantitative analysis of the 2-D in-plane field data, using the angles of the sublattice moments with respect to the anisotropy axis and their perpendicular component.

6.4.2.2 Quantitative Analysis

In the first step, the angles and perpendicular moments of the Mn4a (red) and Mn4c (blue) sublattices are calculated from the vector diagram. Then using the balancing of torques and the minimisation condition the anisotropy and inter-sublattice constants are found. Figures 6.24, 6.25 and 6.26 show the fitted angles and perpendicular moments for three cases:

- Case 1: Sample A and $T = 10$ K
- Case 2: Sample B and $T = 10$ K
- Case 3: Sample B and $T = 200$ K

The optimised anisotropy and intersublattice constants for each case, summarised in Table 6.3, were substituted into the uniaxial anisotropy model equations to calculate the optimised angles and the perpendicular moments (black broken lines) for fields > 0 T. Our findings demonstrate that the uniaxial anisotropy model was successful in reproducing the XMCD data. Since the net moment is larger in the case of Sample B, the switching of the net moment is accompanied by switching of the Mn sublattices.

Case 1:

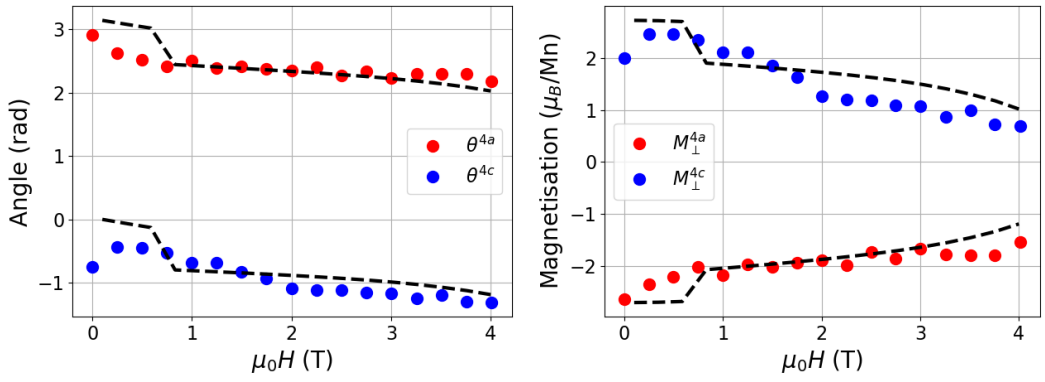

Figure 6.24: Sample A - $T = 10$ K: (Left) angles (Right) $m_\perp$ components of Mn^{4a} (red) and Mn^{4c} (blue) sublattice moments. Black lines are fits for optimised constant parameters of the uniaxial model.

Case 2:

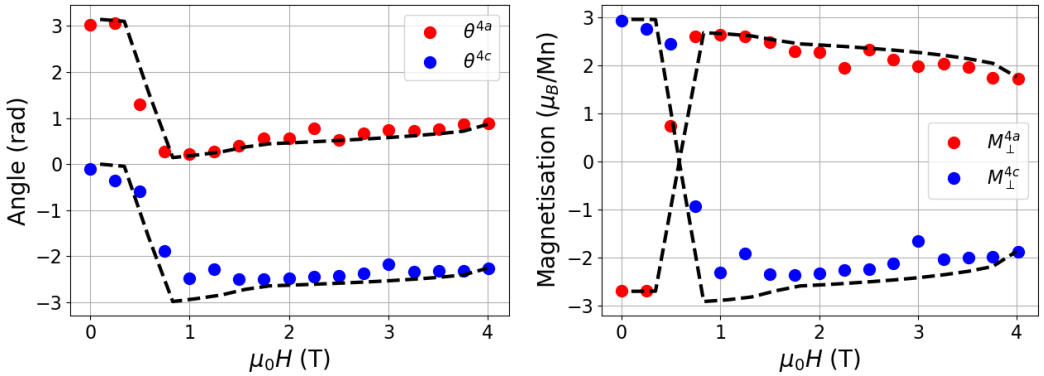

Figure 6.25: Sample B - $T = 10$ K: (Left) angles (Right) $m_\perp$ components of Mn^{4a} (red) and Mn^{4c} (blue) sublattice moments. Black lines are fits for optimised constant parameters of the uniaxial model.

Case 3:

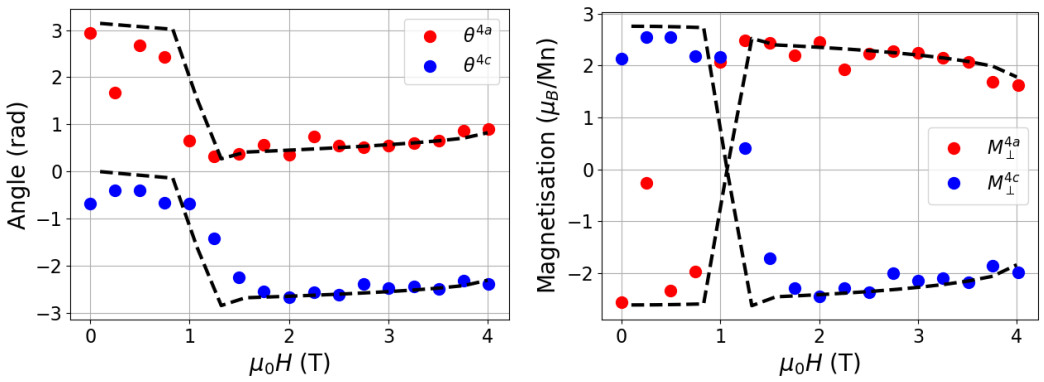

Figure 6.26: Sample B - $T = 200$ K: (Left) angles (Right) $m_\perp$ components of Mn^{4a} (red) and Mn^{4c} (blue) sublattice moments. Black lines are fits for optimised constant parameters of the uniaxial model.

We report large sublattice anisotropy constant magnitudes of the order of MJm^{-3}, which is not typical in cubic materials. The signs of K_1^{4a}, K_1^{4c} are positive and negative, respectively, meaning that Mn4a sublattice has easy-axis anisotropy and Mn^{4c} sublattice has easy-plane anisotropy. The question arises is it possible to have such large

	T (K)	K_1^{4a} (MJm^{-3})	K_1^{4c} (MJm^{-3})	$\mathscr{J}^{ac}_{XMCD}$ (MJm^{-3})	$\mathscr{J}^{ac}_{MFT}$ (MJm^{-3})
Sample A	10	1.1	-1.0	-9	-13
Sample B	10	2.1	-1.9	-13	-13
Sample B	200	1.9	-1.8	-14	-13

Table 6.3: Summary of sublattice anisotropy constant, K_1^{4a} and K_1^{4c}, and inter-sublattice exchange, $\mathscr{J}^{ac}_{XMCD}$ and $\mathscr{J}^{ac}_{MFT}$, obtained from XMCD and MFT, respectively.

anisotropy constants in MRG. To gain insight, we can compare MRG to another Mn-based Heusler alloy Mn_3Ga. It has a tetragonal $D0_{22}$ structure, with a c/a ratio of 1.8, and two antiferromagnetically coupled Mn sublattices. The anisotropy of this alloy is ≈ 2 MJm^{-3}, which is the same order of magnitude as our sublattice anisotropies. [10] Considering that Mn sublattices in Mn_3Ga have similar chemical environments as those in MRG and that in the tetragonal representation of MRG unit cell the c/a ratio is 1.4, it is conceivable to achieve the sublattice anisotropy constants we have calculated from XMCD. To determine the impact of these results on the presence of sublattice canting and non-collinearity in the absence of an external field, we find the set of angles that minimise the magnetic free energy density (equation 6.10) with the values anisotropy and inter-sublattice exchange constants from Table 6.3.

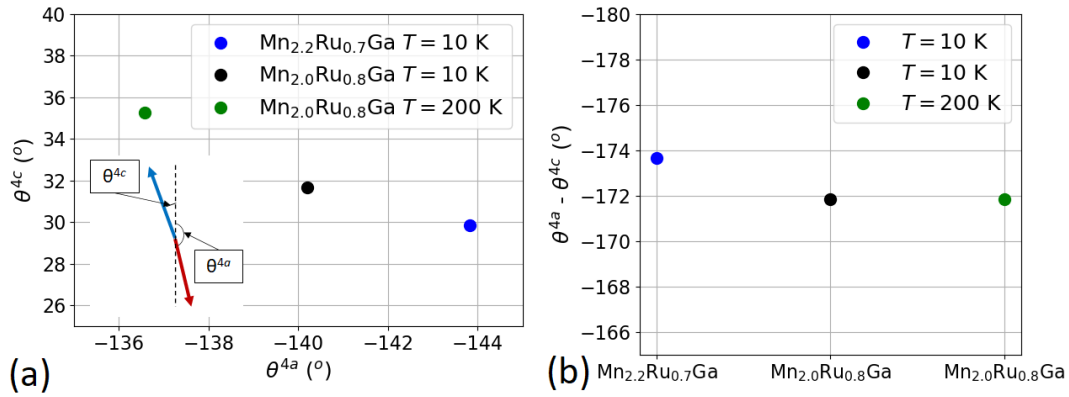

Figure 6.27: Minimising the magnetic free energy density: (a) sublattice angles θ^{4a} and θ^{4c} defined with respect the the z-axis as shown in the bottom right diagram, (b) the difference between θ^{4a} and θ^{4c}.

Figure 6.27 (a) shows that in the absence of an applied field, the anisotropy favours canting of both sublattices by 30° - 36° and the angles are larger when measured closer

to T_{comp}. This is an interesting result because we did not expect canting in both sublattices and for the angles to be larger than about 5° [11]. Canting of both sublattices away from the z-axis explains the observed soft component in the out-of-plane and in-plane hysteresis loops of the net moment (see Figures 6.3) i.e. the canted magnetic state is destroyed when an external magnetic field is applied. Examining the difference between the angles shown in Figure 6.27 (b) we find that $(180° - |\theta^{4a} - \theta^{4c}|) \approx 7°$ and is independent of temperature. From Figure 6.22 it is follows that applying a magnetic field less than the spin-flop field also does not affect the non-collinearity. Both canting and non-collinearity of sublattices is expected to contribute to the already low threshold for magnetic switching observed in single pulse all optical toggle switching [12; 13], which occurs at timescales of < 10 ps. [14]. The results can also be used to determine the frequencies of current-induced SOT oscillations from magnon dispersion simulations.

6.5 Conclusion

Two MRG thin films, sample A ($Mn_{2.2}Ru_{0.7}Ga$) with $T_{\text{comp}} < 300$ K and sample B ($Mn_{2.0}Ru_{0.8}Ga$) with $T_{\text{comp}} > 300$ K were measured in XMCD to determine their sublattice anisotropy fields. A temperature scan in +9 T of Sample A with out-of-plane applied field showed the moments switch at about $T = 145$ K which is an indication of crossing compensation. The inter-sublattice exchange $\mathscr{J}^{ac}$ was calculated from the data, assuming anisotropy is much less than exchange. The results showed that $\mathscr{J}^{ac}$ diverged near T_{comp} and values were too small. This demonstrated that the sublattice anisotropy cannot be neglected. At compensation, a spin-flop transition was observed with a spin-flop field of $\mu_0 H_{\text{st}} = 7.65$ T. The transition is not sharp as in typical antiferromagnets, because the Mn sublattices are not symmetrically equivalent and have a stronger magnetocrystalline anisotropy. The expression for the spin-flop field was used to calculate the effective anisotropy constant of the net moment which is shown in Table 6.4. The constant is two orders of magnitude lower than $\mathscr{J}^{ac}$ and is positive indicating easy-axis anisotropy, as expected.

The two dimensional projections of sublattice moments were calculated. At lower fields the moments vary in an unexpected way, which is attributed to the moments not being saturated in the plane of the applied field. The anisotropy of Mn^{4a} and Mn^{4c}

sublattices in MRG were found to be easy-axis and easy plane, respectively. All calculated constants, fields and energies of sublattice anisotropy are summarised in Table 6.4. The anisotropy constants were calculated based on uniaxial anisotropy model, because two out of three spatial components of sublattice moments are measured in XMCD. This limits the number of free parameters allowed in the model, therefore using a more complicated model to analyse the data is not useful.

Sample A: $Mn_{2.2}Ru_{0.7}Ga$				
Spin-flop ($T = 145$ K)				
	K_1 (Jm^{-3})	H_A (T)	E_A (K)	$\lvert\mathscr{J}^{ac}/K_1\rvert$
M^{Net}	6.69×10^4	6.7	0.02	8.7×10^2
Hard-axis measurement ($T = 10$ K)				
	K_1 (Jm^{-3})	H_A (T)	E_A (K)	$\lvert\mathscr{J}^{ac}/K_1\rvert$
M^{4a}	1.1×10^6	4.6	4.2	8.2
M^{4c}	-1.0×10^6	-4.4	-4.0	9.0
Sample B: $Mn_{2.0}Ru_{0.8}Ga$				
Hard-axis measurement ($T = 10$ K)				
	K_1 (Jm^{-3})	H_A (T)	E_A (K)	$\lvert\mathscr{J}^{ac}/K_1\rvert$
M^{4a}	2.1×10^6	8.8	8.0	6.2
M^{4c}	-1.9×10^6	-7.6	-7.5	6.8
Hard-axis measurement ($T = 200$ K)				
	K_1 (Jm^{-3})	H_A (T)	E_A (K)	$\lvert\mathscr{J}^{ac}/K_1\rvert$
M^{4a}	1.9×10^6	8.5	7.5	7.4
M^{4c}	-1.8×10^6	-7.6	-7.0	7.8

Table 6.4: Summary of anisotropy constants, fields and energies for samples A and B.

There are four main results which need to be discussed:

1. In data with field applied close to the easy-axis, the relative canting between sublattice moments was found to be up to 10°, which suggests non-collinearity is present.

2. K_1^{4a} is positive implying easy-axis anisotropy and K_1^{4c} is negative implying easy-plane anisotropy.

3. The anisotropy constants of sample B were about two times bigger than those found for sample A.

4. The magnitudes of sublattice anisotropy constants are 10^6 Jm^{-3}.

At a first glance, the observed sublattice non-collinearity appears to be a consequence of positive and negative anisotropy on Mn^{4a} and Mn^{4c} sublattices, respectively. From RSM data for samples A and B, shown in section 6.2, the $a_A > a_B$ and $c_A < c_B$, which results in a larger tetragonal distortion of the unit cell of sample B. This is consistent with the relative increase in the magnitudes of anisotropy constants between the two samples. Magnetocrystalline anisotropy constants of the order 10^6 Jm^{-3} are typically observed for tetragonal crystal structures, e.g. $D0_{22}$ structure where $\frac{c}{a} = 2$. In the case of MRG, $1.00 < \frac{c}{a} < 1.02$, because it is a cubic crystal and biaxial strain due to the substrate causes a small tetragonal distortion of up to 2 %. Therefore, the magnitudes derived from the simple uniaxial anisotropy model are reflecting a contribution to the free energy that is not included in the model.

There are two interactions that favour non-collinearity in magnetically ordered systems:

- Dzialoshinskii - Moriya interaction (DMI).
- Competing positive and negative exchange between nearest and next-nearest neighbour spins.

DMI is an asymmetric exchange contribution to the Hamiltonian. The point group for the cubic inverted Heusler is $\bar{4}$3m and in this case bulk DMI is not allowed. However it is allowed in tetragonal systems. It is a short-range interaction giving rise to canting of spins and long range magnetic order. A famous example is Hematite (α-Fe_2O_3), which is a canted antiferromagnet due to DMI arising from the crystal structure symmetry. The unit cell of MRG has a small tetragonal distortion and typically in ferrimagnets, DMI is much weaker than anisotropy [15] and therefore is very unlikely to give rise to canting angles $\theta^{4a,4c} = 180° \pm 10°$.

A more similar example to MRG is the tetragonal Mn_2RhSn Heusler alloy, which exhibits large ground state non-collinearity. [15] The lattice parameters are $a = 6.026$ Å and $c = 6.261$ Å, hence the tetragonal distortion is $\frac{c}{a} \approx 1.04$. The large non-collinearity in this system, where at $T = 1.8$ K $\theta^{1,2} = 180° \pm 55°$, is due to competing exchange.

Consider competing exchange as the origin of sublattice non-collinearity in MRG. Since $K_1^{4c} < 0$, it is likely that competing exchange takes place on the Mn^{4c} sublattice. A comparison of a collinear and non-collinear spin structure, resulting from negative and positive nearest and next nearest neighbour coupling is illustrated in Figure 6.28. To justify this kind of magnetic order in MRG, the Mn-Mn distances in the unit cell can be calculated and examined because they largely determine the type of magnetic coupling. For Mn-Mn distance $\Delta > 290$ pm the interaction is FM and for 250 pm $<$ $\Delta < 280$ pm the coupling is AFM.

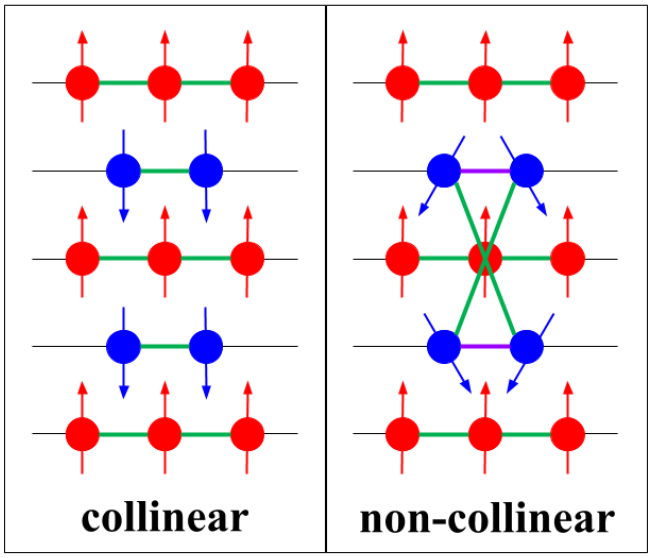

Figure 6.28: Example of two antiferromagnetically coupled inequivalent sublattices (red and blue atoms). **Left**: A collinear structure where atoms of each sublattice show FM (green) coupling. **Right**: A non-collinear spin structure: The red sublattice spins are all FM (green) coupled. Blue sublattice spins show AFM (purple) nearest neighbour and FM (green) next-nearest neighbour couplings. This competition of exchange interactions produces a local canting of the blue spins.

The results presented in Chapter 4 show that all sites of MRG are fully occupied which gives rise to chemical disorder including Mn-Ga antisites. The Mn-Mn distance calculations for the MRG unit cell show that the distance between Mn^{4b} - Mn^{4c} is ≈ 259 pm, which leads to AFM coupling. The Mn^{4c} - Mn^{4c} distance is > 290 pm which indicates ferromagnetic coupling. Therefore the most likely scenario is that the nearest neighbour Mn^{4b}-Mn^{4c} exchange coupling is antiferromagnetic (AFM) and

next-nearest neighbour Mn^{4c}-Mn^{4c} is ferromagnetic (FM) and also larger in magnitude. This could explain the relatively low and positive values of $\mathscr{J}^{cc}$ found from MFT. This is a crude approximation, however preliminary DFT calculations, which take into account the presence of Ru on the 4*d* sites, support the presence of such magnetic order. The nearest neighbour exchange ($\mathscr{J}_1^{cc}$) is negative and next nearest neighbour exchange ($\mathscr{J}_2^{cc}$) is positive with $|\mathscr{J}_1^{cc}| < |\mathscr{J}_2^{cc}|$, thus a non-collinear order is plausible.

It seems that competing exchange can explain the non-collinearity, the negative sign of K_1^{4c}, and the large magnitudes of anisotropy constants. The increase in the anisotropy constants of between samples A and B can also be explained in the context of the competing exchange hypothesis. As mentioned earlier, $a_A > a_B$, which indicates that the crystal structure favours shorter Mn^{4b}-Mn^{4c} distance and stronger AFM coupling. The MFT data supports this hypothesis showing a decrease in $|\mathscr{J}^{cc}|$. Thus the resultant effect could be that the sublattice moments require higher field to saturate along the hard direction. In the uniaxial anisotropy model, this will result in larger magnitude of anisotropy constants. In addition to non-collinearity, it is possible that at zero field the sublattices are canted relative to the c-axis thus the net moment forms a cone that is tilted. In order to test this hypothesis experimentally, measurements of all three spatial components of sublattice moments is required as a function of temperature and field. This can be achieved in a neutron diffraction experiment suitable for thin film samples. A more complicated model with more fitting parameters, allowing for sublattice non-collinearity can then be used to describe the results. The accurate determination of sublattice anisotropy and exchange fields are important for the development of nano-oscillators and prediction of ferromagnetic resonance frequencies.

6. SITE-SPECIFIC MAGNETISM STUDY OF MN_YRU_XGA THIN FILMS BY XMCD

References

[1] B. Thole, G. Van Der Laan, and P. Butler, "Spin-mixed ground state of Fe phthalocyanine and the temperature-dependent branching ratio in X-ray absorption spectroscopy," *Chem. Phys. Lett.*, vol. 149, no. 3, pp. 295 – 299, 1988. (Cited on page: 200)

[2] R. D. Cowan, *Theory of Atomic Structure and Spectra, Los Alamos Series in Basic and Applied Sciences*. University of California Press,Berkeley, CA, 1981. (Cited on page: 200)

[3] D. Betto, N. Thiyagarajah, Y.-C. Lau, C. Piamonteze, M.-A. Arrio, P. Stamenov, J. M. D. Coey, and K. Rode, "Site-specific magnetism of half-metallic Mn_2Ru_xGa thin films determined by x-ray absorption spectroscopy," *Phys. Rev. B*, vol. 91, no. 9, p. 094410, 2015. (Cited on page: 200)

[4] B. T. Thole, P. Carra, F. Sette, and G. van der Laan, "X-ray circular dichroism as a probe of orbital magnetization," *Phys. Rev. Lett.*, vol. 68, pp. 1943–1946, Mar 1992. (Cited on page: 200)

[5] M. Altarelli, "Orbital-magnetization sum rule for x-ray circular dichroism: A simple proof," *Phys. Rev. B*, vol. 47, pp. 597–598, Jan 1993. (Cited on page: 200)

[6] P. Carra, B. T. Thole, M. Altarelli, and X. Wang, "X-ray circular dichroism and local magnetic fields," *Phys. Rev. Lett.*, vol. 70, pp. 694–697, Feb 1993. (Cited on page: 200)

[7] W. L. O'Brien and B. P. Tonner, "Orbital and spin sum rules in x-ray magnetic circular dichroism," *Phys. Rev. B*, vol. 50, pp. 12672–12681, Nov 1994. (Cited on page: 201)

[8] C. Piamonteze, P. Miedema, and F. M. F. de Groot, "Accuracy of the spin sum rule in xmcd for the transition-metal *l* edges from manganese to copper," *Phys. Rev. B*, vol. 80, p. 184410, Nov 2009. (Cited on page: 201)

[9] J. Coey, *Magnetism and Magnetic Materials*. Cambridge University Press, New York, 2010. (Cited on page: 212)

[10] K. Rode, N. Baadji, D. Betto, Y.-C. Lau, H. Kurt, M. Venkatesan, P. Stamenov, S. Sanvito, J. M. D. Coey, E. Fonda, E. Otero, F. Choueikani, P. Ohresser, F. Porcher, and G. André, "Site-specific order and magnetism in tetragonal Mn_3Ga thin films," *Phys. Rev. B*, vol. 87, p. 184429, May 2013. (Cited on page: 220)

[11] K. Siewierska, D. Betto, N. Teichert, G. Atcheson, N. Brookes, and K. Rode, "XMCD investigation of sublattice non-collinearity in compensated ferrimagnetic half-metallic thin films," *Unpublished*, 2021. (Cited on page: 221)

[12] C. Banerjee, N. Teichert, K. Siewierska, Z. Gercsi, G. Atcheson, P. Stamenov, K. Rode, J. M. D. Coey, and J. Besbas, "Single pulse all-optical toggle switching of magnetization without gadolinium in the ferrimagnet Mn_2Ru_xGa," *Nat. Commun.*, vol. 11, p. 4444, 2020. (Cited on page: 221)

[13] C. S. Davies, G. Bonfiglio, K. Rode, J. Besbas, C. Banerjee, P. Stamenov, J. M. D. Coey, A. V. Kimel, and A. Kirilyuk, "Exchange-driven all-optical magnetic switching in compensated 3*d* ferrimagnets," *Phys. Rev. Res.*, vol. 2, p. 032044, Aug 2020. (Cited on page: 221)

[14] C. Banerjee, K. Rode, G. Atcheson, S. Lenne, P. Stamenov, J. M. D. Coey, and J. Besbas, "Ultrafast double pulse all-optical reswitching of a ferrimagnet," *Phys. Rev. Lett.*, p. Accepted, 2021. (Cited on page: 221)

[15] O. Meshcheriakova, S. Chadov, A. K. Nayak, U. K. Rößler, J. Kübler, G. André, A. A. Tsirlin, J. Kiss, S. Hausdorf, A. Kalache, W. Schnelle, M. Nicklas, and C. Felser, "Large noncollinearity and spin reorientation in the novel Mn_2RhSn Heusler magnet," *Phys. Rev. Lett.*, vol. 113, p. 087203, Aug 2014. (Cited on page: 223)

7
Conclusion and Outlook

After the theoretical prediction of zero-moment half-metals, it took almost 20 years before the first member of this materials class, Mn_2Ru_xGa(MRG) was discovered. Extensive studies of MRG, both experimental and theoretical, including those in this thesis, reveal the secrets of the special combination of its constituent elements and suggest the recipe to prepare other alloys in this material class. Mn is the element responsible for the magnetism of MRG. Other alloys that have since been found to belong to the same class were also Mn based. One reason is that the s-d coupling of Mn allows for a spin-gap in the density of states and AFM coupling of the two sublattices. If elements to the right of Mn in the periodic table are used, the s-d coupling leads to ferromagnetic ordering and no compensation. On the other had, replacing Mn with Cr means s-d coupling is weak and proposed spin polarisation is low. The second reason is that many candidate materials from DFT did not crystallise in the correct structure. This poses a big limitation on the application of zero-moment half-metal materials in spintronic devices. If all or most are Mn-based, they all face the problem of Mn diffusion through the device structure after annealing, which is a necessary step in the fabrication of magnetic tunnel junctions. The possible solutions to this problem is the deposition of an ultra-thin protective layer between MRG and MgO. The ideal material for this purpose should have a close lattice match to MRG and allow for crystalline MgO to

grow on top to achieve coherent tunnelling and high TMR. The layer must stop Mn from diffusing into MgO and any diffusion of the material into MRG should not have an effect on its spin polarisation and PMA. The layer must be ultra-thin and have a long spin diffusion length to minimise the negative impact on TMR.

Finding a way of mitigating Mn diffusion from MRG into the MgO barrier in magnetic tunnel junctions is of paramount importance. In the study of the effects of annealing both blanket MRG films and MRG based spin-valve structures in Chapter 3, annealing shows no significant impact on crystalline and magnetic properties up to 350 °C, but annealing at 400 °C causes a large shift in compensation temperature and an increase in the in-plane magnetic moment. The study of annealing of MRG based spin-valve structures with various spacer layers demonstrates that any one spacer can have a positive impact on one of the film properties at the expense of other. The key is to find a balance to maximise the gain and minimise the loss. Spacer materials were selected based on their lattice parameter and the potential to act as a diffusion barrier. At one extreme is the TiN spacer layer in which no diffusion is possible, but relaxation of the MRG crystal lattice results in loss of PMA. At the other extreme is the V spacer layer, which has a perfect lattice match, causing the V atoms diffuse strongly into MRG. This causes a complete disordering of the crystal and full loss of PMA. Hf and Mo spacers represent a compromise, as a small degree of inter-diffusion stabilises the crystal structure by the filling of defects. A fully or mostly oxidised HfO_x spacer layer appears to behave like TiN. The behaviour of the heterostructure with a partially oxidised Hf spacer layer resembles the one with a Hf spacer, due to available diffusive species. Both Hf and Mo may be useful as ultra-thin dusting layers in future active devices. The presence of those layers can have a negative impact on TMR, however Mo is promising due to its large spin diffusion length of ≈ 235 nm.

The next key element in the MRG compound is the transition metal Ru. The addition of Ru improves the wetting of the thin film, adds both states and electrons to the density of states which positions the Fermi level in the spin gap allowing for high spin polarisation. The last element is Ga which also plays an important role in the properties of MRG. Namely, in DFT calculations demonstrate the impact of Mn-Ga antisite defects on opening of the spin gap at the density of states, non-volume conserving tetragonal elongation of the cubic unit cell and the magnitude of the net magnetic moment.

Extensive study of MRG properties had been carried out as a function of Ru content, but the Mn content had not been varied. Our exploration of variation of the Mn content in Mn_2Ru_xGa thin films in Chapter 4 shows the influence of Mn composition on the population of the Mn^{4c} sublattice. The molecular field theory models the increase of T_{comp} is when Mn was added onto the 4*c* site. This is supported by density data which indicates the presence of vacancies which are assumed to be on the 4*d* sites. Presence of vacancies adds an extra degree of freedom and stability to the Heusler structure, although there are fewer than $1-x$ vacancies predicted from the chemical formula. Addition of Ru increases c-parameter, decreases anomalous Hall angle and decreases spin polarisation meaning the Fermi level is pushed upwards out of the spin gap hence reducing spin polarisation. The highest anomalous Hall angles and spin polarisation were found for $x = 0.5$ and $y > 2$. Using this information, compositions can be selected to suit a required application. For example, MRG can be used as a fixed layer in a magnetic tunnel junction without any need for an antiferromagnet to pin the magnetisation. In this case, T_{comp} of MRG should be close to room temperature giving to give a huge coercivity and exhibit high spin polarisation at Fermi level. Those criteria are fulfilled by $Mn_{2.6}Ru_{0.5}Ga$ with spin polarisation of about 60% and an coercivity in excess of 12 T at 300 K. Another example is single pulse all optical toggle switching at room temperature, where $T_{comp} >$ room temperature is required and large tetragonal distortion. For this purpose MRG with $x = 0.9$ best suits the criteria because of the high *c* parameter and the suitable value of T_{comp}.

There is a prospect for using MRG thin films in spintronic memory devices that depend on moving magnetic domain walls by electrical current (such as spin-orbit torque-driven domain-wall logic gates). The analysis of magnetic domain patterns during magnetisation reversal for a set of MRG films is presented in Chapter 5. Magnetisation reversal behavior changes radically from domain wall motion dominated process to nucleation dominated. By analysing the magnetic after-effect, films show similar activation volumes with dimensions of 34–40 nm. Comparison of structural parameters of the samples shows that structural defects such as misfit dislocations are responsible for the range of activation energies ΔE_A . The samples with $\Delta E_A > 0.52$ eV show reversal dominated by nucleation, while samples with $\Delta E_A < 0.10$ eV show reversal dominated by domain wall motion. The defects act as pinning centres for domain walls and cause local variation in the anisotropy. The next step in the research is to

demonstrate movement of a domain wall with an electrical current in a Hall-bar structure. Results indicate that the track width should be less than 240 nm, which requires patterning using electron beam lithography. The switching in such devices will occur at timescales comparable with the inverse of the ferromagnetic resonance frequency, that is shorter than 10 ps. The single layer MRG-based magneto-optical devices, utilising single-pulse all optical toggle switching as well as moving of domain walls do not face the Mn diffusion issue and hence have a higher prospect of success.

The detailed study of MRG films with various chemical compositions in Chapter 4 revealed that the magnetic ordering is not simply ferrimagnetic. The difference between hysteresis loops measured by SQUID magnetometry and AHE at 300 K is perhaps the most striking experimental result in the thesis. AHE measures very square loops reflecting the Mn^{4c} sublattice magnetisation, but SQUID measures the small resultant, and amplifies the effect of any non-colliearity between sublattices.

XMCD measurements on MRG thin films in chapter 6, allow for sublattice specific moments to be were calculated from XMCD spectra and normalised using the results of MFT fitting of the net moment measured by SQUID magnetometry. Temperature dependent measurements in +9 T showed crossing of compensation at 145 K. The data suggests that anisotropy is relatively large compared to inter-sublattice exchange. A spin-flop transition near compensation with a spin-flop field of 7.65 T was observed. The anisotropy field of the net moment was estimated to be 6.7 T. By performing angular XMCD scans with field applied close to the easy and hard axes, two dimensional projections of sublattice moments were found. Using a uniaxial anisotropy model, the torques on the sublattice moments with field applied along the hard axis were calculated. At equilibrium the net torque vanishes, which allows sublattice anisotropy constants to be determined. The calculations show that uniaxial magnetocrystalline anisotropy constants are of the order 10^6 Jm^{-3}, which is typical of tetragonal systems and is unusually large for a near cubic crystal. The Mn^{4a} and Mn^{4c} sublattice showed easy-axis and easy-plane anisotropies, respectively. Non-collinearity of sublattices was observed, with the canting angle of sublattices $(\theta^{4a,4c} - 180°) < \pm 10°$. The most plausible explanation of the results is that the non-collinearity of the sublattice moments is due to competing exchange on the Mn^{4c} sublattice. The uniaxial anisotropy model and two sublattice mean field model, which only provides three exchange constants, are too simple to account for sublattice non-collinearity.

Neutron diffraction measurements on the thin films have the advantage that all three spacial components of sublattice moments can be measured. The disadvantage is that such a measurement is difficult on thin films due to a small interaction volume. To minimise this problem, films will be deposited on a large square substrate. The large sample can be diced into four equal pieces and stacked on top of each other on the sample holder thus increasing the interaction volume. Sufficient signal-to-noise ratio of the diffraction patterns can be achieved with an intense neutron beam and long integration times. With complete information about the magnitudes and directions in three spacial dimensions of sublattice moments as a function of temperature and field, it will be possible to develop a more detailed model and verify the presence of competing exchange in MRG. This experiment was originally scheduled for May 2020, however due to the Covid-19 pandemic it has been rescheduled to February 2021.